# Imagerie d'objets enfouis en utilisant la décomposition de l'opérateur de retournement temporel.

Ting Zhang

# ÉCOLE CENTRALE DE MARSEILLE

École Doctorale - ED 352

Institut Fresnel UMR 7249, équipe SEMOX

# THÈSE DE DOCTORAT

pour obtenir le grade de

DOCTEUR de l'ÉCOLE CENTRALE de MARSEILLE

Discipline: *physique et sciences de la matière*

# Electromagnetic wave imaging of targets buried in a cluttered medium using an hybrid Inversion-DORT method


Par

**ZHANG Ting**

**Directeur de thèse:** Chaumet Patrick
**Co-directeur de thèse:** Belkebir Kamal


*Soutenue le 03 Mars 2014*
*devant le jury composé de*

| | | |
|---|---|---|
| Saillard Marc | Professeur des Universités, MIO | Président |
| Prada-julia Claire | Directeur de Recherches, Institut Langevin | Rapporteur |
| Lambert Marc | Chargé de Recherches, LSS-SUPELEC | Rapporteur |
| Pichot Christian | Directeur de Recherches, LEAT | Examinateur |
| Giovannini Hugues | Professeur des Universités, Institut Fresnel | Examinateur |
| Chaumet Patrick | Maître de Conférences, Institut Fresnel | Directeur de thèse |
| Belkebir Kamal | Maître de Conférences, Institut Fresnel | Co-directeur de thèse |

# Remerciement

Je tiens à adresser en premier lieu mes plus chaleureux remerciements à mon directeur de thèse, Patrick CHAUMET. Les mots me manquent pour exprimer ma gratitude. Il s'est toujours soucié de m'offrir, de tout point de vue, les meilleures conditions de travail possibles. Je le remercie en particulier pour ses multiples conseils, sa grande disponibilité, ses grandes qualités scientifiques et la confiance qu'il m'a accordée.

Je voudrais également exprimer toute ma reconnaissance à Kamal BELKEBIR, mon codirecteur de thèse. Sa compétence, sa rigueur et sa vision scientifique m'ont beaucoup appris, en particulier ses talents d'inverseur.

J'aimerais aussi remercier Anne SENTENAC. Je n'oublie pas son aide précieuse dans la relecture, la correction des publications et de ce tapuscrit. La justesse de ses critiques a été très constructive et utile. Son enthousiasme permanent et sa compétence scientifique sont très impressionnants et charmants.

Je voudrais aussi remercier, Mme Claire PRADA-JULIA, Directeur de recherche à l'Institut Langevin, et Monsieur Marc LAMBERT, Chargé de recherche au Laboratoire des Signaux et Systèmes, d'avoir accepté d'être mes rapporteurs, et pour l'intérêt qu'ils ont manifesté pour cette étude. Je tiens également à remercier Monsieur Christian PICHOT, Monsieur Marc SAILLARD, et Monsieur Hugues GIOVANNINI, d'avoir accepté l'invitation de participer à ce jury de thèse.

Je remercie le CSC (China Scholarship Counscil) pour m'avoir financé pendant les trois annés de mon doctorat, l'école doctorale 352 et l'École Centrale de Marseille pour l'avoir supervisé, et surtout l'Institut Fresnel qui m'a permis d'accomplir ce travail dans un cadre agréable. Je dois aussi remercier l'Université d'Aix-Marseille qui m'a donné quatre mois de financement, et Monsieur Hugues GIOVANNINI qui m'a donné deux mois de financement sur son projet SURMITO. Ceux-ci m'ont permis de continuer ma recherche pendant la prolongation de cette thèse.

En particulier, pendant ma période sensible de la grossesse et surtout après l'accouchement, mes deux chers directeurs et Anne SENTENAC ont été très compréhensifs et m'ont donné beaucoup de conseils utiles. Il y a aussi Anne-laure FEHREMBACH et Virginie CHAMARD, qui ont toujours été à mes côtés pour m'aider et me conseiller.

Je voudrais aussi remercier toute l'équipe SEMOX. En particulier, Guillaume, qui est toujours prêt à répondre à mes questions sur les résultats expérimentaux et qui est très patient pour expliquer les différents problèmes inhérents à la manipulation. Merci à Gabriel, Nicolas, Emeric, David, Slimane, Jules, Charan, Pierre et Anastasios.

Je remercie toutes les personnes formidables que j'ai rencontrées à l'Institut Fresnel. Frédéric ZOLLA, André NICOLET, Marc TRAVERSARI, Frédéric FORESTIER, et Jean CAYZAC. Un merci particulier à Nelly et Claire, qui ont assuré les demandes administratives et surtout la vie quotidienne.

Pour m'avoir accompagnée pour mes premiers pas en France, je suis reconnaissante aux amis chinois, Xinghai FU, Da SHU, Yi ZHANG, Yan LIU, Xiao WANG, Xiaoyun SI, Guowei YANG, Tao LIN, Xueqin CHEN, Yuan ZHANG, Di GAO, Xianbin XU, Mingxuan ZHU, Zhiyong Xiao, Ningning SONG, Siwei LIU, Xuefeng LIU.

Enfin, je souhaite remercier ma famille et ma belle famille pour leurs soutiens constants. En particuler, ma mère, qui m'a beaucoup soutenue. Pour conclure, je souhaite bien évidemment remercier mon extraordinaire mari Yi RUAN et notre petit amour, Jing Yuan, qui m'a toujours donné beaucoup de bonheurs et de courage pour continuer.

# Contents

# List of Figures

# Résumé en Français

## Contents



# Le mot du directeur de thèse

Une règle a été établie par le conseil scientifique (CS) de l'université Aix-Marseille. Le CS exige pour les thèses écrites en anglais, qu'au moins 10% de la thèse soit rédigée en Français. Mme Zhang est chinoise et malgré tout a décidé de rédiger elle même ce résumé. Je n'ai fait que peu de corrections sur ce résumé et je tiens donc à souligner la qualité de son Français dont beaucoup d'étudiants pourraient s'inspirer.

# 1) Introduction

Ce travail de thèse porte sur la détection et la caractérisation d'objets tridimensionnels localisés en espace homogène, ou en présence d'une interface. Mais avant de rentrer dans le vif du sujet, nous allons définir la terminologie utilisée dans ce tapuscrit. Nous définissons deux classes de problèmes: le problème direct et le problème inverse. La diffusion d'une onde électromagnétique par un objet de permittivité relative et de forme arbitraire est ce que nous définissons comme étant le problème direct, *i.e.* l'objet étant supposé connu, le champ diffracté est calculé en un ou plusieurs points d'observation donnés. Le problème inverse consiste à "déterminer l'objet", à partir de la seule mesure du champ diffracté en différents points d'observation. Le terme "déterminer l'objet" est mis entre guillemets, car il peut avoir différentes significations suivant la problématique posée:

- détection et localisation: repérer le nombre de diffuseurs et connaître la position de ceux-ci.

- reconnaissance de forme: déterminer la forme d'objets inconnus.
- caractérisation: accéder à la forme et à la permittivité relative des diffuseurs.

Dans ce travail de thèse, nous nous sommes intéressés au problème de la détection, localisation et caractérisation des objets. Nous nous sommes également intéressés au problème de la caractérisation d'objets présents dans des milieux désordonnés, *i.e.* le voisinage des cibles présentes des fluctuations de la permittivité. Une des nombreuses applications de ce domaine recherche est le sondage du sous-sol, où les cibles sont enfouies dans un milieu comportant des hétérogénéités et les antennes émettrices et réceptrices sont au dessus de l'interface. Dans ce cas les méthodes d'inversion classique (linéaires et non linéaires) distinguent difficilement les cibles à détecter des inhomogénéités du milieu. De nombreuses études ont été consacrées à la compréhension de l'influence des hétérogénéités autour de l'objet d'intérêt sur la réponse du signal de l'objet, et différentes techniques ont vu le jour pour améliorer le rapport signal sur bruit. En régime harmonique, nous nous proposons d'utiliser la méthode de Décomposition de l'Opérateur de Retournement Temporel (DORT), développée d'abord dans le domaine acoustique[1,2], puis appliquée à l'electromagnétisme[3–5]. Cela consiste à analyser les valeurs propres et les vecteurs propres de l'opérateur de retournement temporel (TRO), qui nous permet de dénombrer et de localiser les cibles les plus échogènes. Cette méthode est efficace quand le ou les objets sont en présences d'hétérogénéités faiblement contrastées et où la diffusion simple domine, mais trouve sa limite dans le régime de la diffusion multiple. En particulier, lorsque seulement des données monochromatiques sont utilisées[6,7]. Cette technique a l'inconvénient de localiser les cibles sans les caractériser. Pour ces raisons nous nous proposons de combiner les avantages des méthodes d'inversion non-linéaire et DORT. Cette approche d'imagerie combinée sera étudiée sur des données synthétiques. Deux configurations d'intérêt seront prises en compte. Première, les diffuseurs sont présents dans un milieu infini et entourés d'hétérogénéités, alors que dans la seconde, les diffuseurs sont enfouis sous une interface plane. La méthode DORT sera développée pour des champs tridimensionnels vectoriels, où les antennes peuvent dont prendre trois orientations différentes.

Ensuite, nous allons exploité les capacités focalisantes de DORT dans le domaine de l'imagerie optique à haute résolution. Cette partie nous permettra de tester et valider les nouveaux algorithmes sur des données expérimentales. Nous allons montrer que la méthode DORT permet de bien focaliser et caractériser chaque diffuseur présent sur une interface et ce sélectivement.

Enfin, nous présenterons les résultats obtenus à partir de données transitoires, en considérant une approche mono-source et multiples fréquences. Nous présenterons trois façons de traiter les données transitoires:

- Marche-récurrente-en-fréquence: nous résolvons séquentiellement plusieurs problèmes inverses. Plus précisément, nous résolvons le problème inverse à une fréquence et utilisons le résultat final pour l'inversion aux fréquences plus élevées.
- Multiples fréquences: nous considérons les champs diffractés à toutes les fréquences en même temps.
- Inversion en régime transitoire: les champs diffractés mesurés sont recueillis dans le temps.

Dans cette partie, nous allons d'abord tester les algorithmes d'inversion avec des données synthétiques. Ensuite, nous comparerons les différentes méthodes développées avec des mesures expérimentales effectuées dans une chambre anéchoïque dans le domaine des hyper-fréquences.

# 2) Problème direct et problème inverse

## 2.1) En régime harmonique

La géométrie générale du problème de diffraction que nous nous proposons d'étudier est illustrée par Fig. 1. Un diffuseur tridimensionnel de forme arbitraire avec la permittivité $\epsilon(\boldsymbol{r}) = \varepsilon(\boldsymbol{r})\varepsilon_0$ et supposé non-magnétique ($\mu = \mu_0$) est contenu dans un domaine $W$, linéaire, isotrope et non

magnétique ($\varepsilon_0$ et $\mu_0$ sont la permittivité et perméabilité du vide, respectivement). Les ondes électromagnétiques qui sondent le milieu, où sont localisés les diffuseurs, sont générées par des antennes, considérées comme des dipôles électriques ponctuels. Les champs diffractés sont évalués aux points de réception régulièrement distribués sur la surface de mesure $\Gamma$.

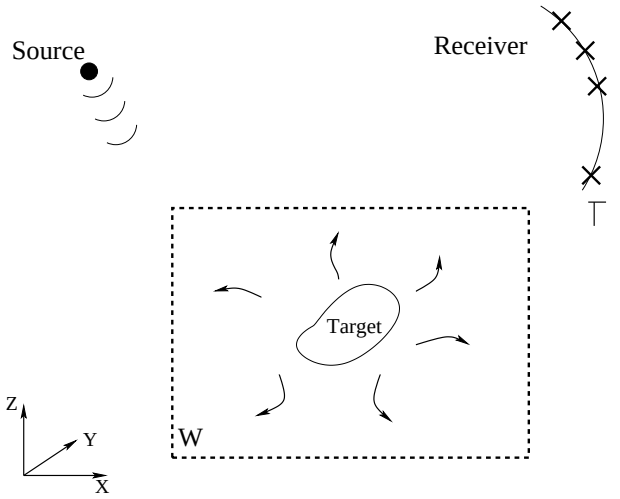


**Figure 1 :** *Géométrie du problème de diffraction. Les diffuseurs sont confinés dans le domaine $W$. $\Gamma$ est la surface de mesure.*

### 2.1.1) Problème direct

Nous utilisons la méthode des dipôles couplés (CDM) pour calculer le champ diffracté par l'objet considéré. Le domaine $W$ contenant l'objet est éclairé par une onde électromagnétique incidente de longueur d'onde $\lambda$ ($k_0 = 2\pi/\lambda$). Le principe de la CDM consiste à représenter l'objet en un ensemble de $N$ petits cubes d'arête $a$ (par petits, nous entendons plus petits que la longueur d'onde dans l'objet : $a \ll \frac{\lambda}{\sqrt{\|\varepsilon\|}}$). Chacun de ces petits cubes, sous l'action de l'onde incidente, se polarise, et donc acquiert un moment dipolaire, dont la valeur dépend du champ incident et de son interaction avec les dipôles voisins. Ces dipôles induits rayonnent donc un champ électromagnétique. Le champ électromagnétique à la position $\boldsymbol{r}$, $\boldsymbol{E}(\boldsymbol{r})$, est donc la somme de l'onde incidente et du champ rayonné par les $N-1$ autres dipôles,

$$\boldsymbol{E}^{\mathrm{loc}}(\boldsymbol{r}_i) = \boldsymbol{E}^{\mathrm{inc}}(\boldsymbol{r}_i) + \sum_{j=1, j\neq i}^{N} \boldsymbol{G}(\boldsymbol{r}_i, \boldsymbol{r}_j)\alpha^0(\boldsymbol{r}_j)\boldsymbol{E}^{\mathrm{loc}}(\boldsymbol{r}_j), \tag{1}$$

où $\boldsymbol{E}^{\mathrm{inc}}$ est le champ incident, $\boldsymbol{G}$ la fonction Green du champ en espace homogène, et $\alpha^0$ la polarisabilité de chaque élément de discrétisation obtenue à partir de la relation de Claussius-Mossotti. Une fois le système d'équations linéaires résolu, le champ diffracté par l'objet à une position $\boldsymbol{r}$ arbitraire, est obtenu en faisant la somme de tous les champs rayonnés par chacun des dipôles,

$$\boldsymbol{E}^{\mathrm{sca}}(\boldsymbol{r}) = \sum_{j=1}^{N} \boldsymbol{G}(\boldsymbol{r}, \boldsymbol{r}_j)\alpha^0(\boldsymbol{r}_j)\boldsymbol{E}^{\mathrm{loc}}(\boldsymbol{r}_j). \tag{2}$$

Le tenseur de Green (aussi appelé fonction de Green) en espace homogène est donné par

$$\boldsymbol{G}(\boldsymbol{r}, \boldsymbol{r}_j) = \frac{e^{ik_0 R}}{4\pi k_0^2}\left[(3\widehat{\boldsymbol{R}}\otimes\widehat{\boldsymbol{R}} - \boldsymbol{I})\left(\frac{1}{R^3} - \frac{ik_0}{R^2}\right) + (\boldsymbol{I} - \widehat{\boldsymbol{R}}\otimes\widehat{\boldsymbol{R}})\frac{k_0^2}{R}\right], \tag{3}$$

où $\widehat{\boldsymbol{R}} = \boldsymbol{R}/R$, $\boldsymbol{R} = \boldsymbol{r} - \boldsymbol{r}_j$, $\boldsymbol{I}$ la matrice unité. Quand l'objet est en présence d'un substrat plan, ou dans un multicouche, la même approche peut être adoptée. Il suffit de remplacer la fonction Green de l'Eq. 3 par celle du système de référence.

### 2.1.2) Problème inverse

Le problème inverse est de déterminer les positions, les formes et les matériaux constitutifs des objets à partir de leurs réponses (champs diffractés) à une excitation électromagnétique connue. Nous limitons notre étude à une méthode itérative non-linéaire. Nous utilisons une approche itérative, où le paramètre d'intérêt, à savoir la distribution de la permittivité relative $\varepsilon = \chi + 1$, est mise à jour progressivement en minimisant une fonction coût $\mathcal{F}$ décrivant l'écart entre les données mesurées $\boldsymbol{f}_l^{\text{mes}}$ et celles qui seraient obtenues par le calcul direct ayant la meilleure estimation disponible de la permittivité relative

$$\begin{aligned}\mathcal{F}_n(\chi_n, \boldsymbol{E}_{1,n}, \cdots, \boldsymbol{E}_{N,n}) &= \mathcal{F}_n(\chi_n, \boldsymbol{E}_{\bullet,n}) \\ &= W_\Gamma \sum_{l=1}^{N} \|\boldsymbol{f}_l^{\text{mes}} - \overline{\overline{\boldsymbol{B}}}\chi_n \boldsymbol{E}_{l,n}\|_\Gamma^2 + W_\Omega \sum_{l=1}^{N} \|\boldsymbol{E}_l^{\text{inc}} + \chi_n \overline{\overline{\boldsymbol{A}}}\boldsymbol{E}_{l,n} - \boldsymbol{E}_{l,n}\|_\Omega^2,\end{aligned} \tag{4}$$

où, $n$ est le nombre d'itération, les coefficients de normalisation étant définis par

$$W_\Gamma = \frac{1}{\sum_{l=1}^{N} \|\boldsymbol{f}_l^{\text{mes}}\|_\Gamma^2}, \qquad W_\Omega = \frac{1}{\sum_{l=1}^{N} \|\boldsymbol{E}_l^{\text{inc}}\|_\Omega^2}, \tag{5}$$

avec $\boldsymbol{E}_l$ est le champ total dans le domaine d'investigation. $\overline{\overline{\boldsymbol{A}}}$ est la matrice contenant toutes les fonctions Green du champ permettant d'accéder au champ dans l'objet, et $\overline{\overline{\boldsymbol{B}}}$ la matrice permettant de calculer le champ diffracté par l'objet. $\boldsymbol{E}_l^{\text{inc}}$ est le champ incident correspondant à chaque illumination $l = 1, \cdots, N$.

Afin d'améliorer la procédure d'inversion, nous injectons une information *a priori* stipulant que la partie réelle de $\varepsilon$ est supérieure à $\varepsilon_b$ que sa partie imaginaire est positive[8]. La fonction complexe $\chi_n$ est alors transformée en deux fonctions auxiliaires $\xi_n$ et $\eta_n$ réelles telles que

$$\chi_n = 1 + \xi_n^2 + i\eta_n^2 - \varepsilon_b, \tag{6}$$

où $\varepsilon_b$ est la permittivité relative du milieu. L'estimation initiale de $\chi$ est obtenue par une procédure de rétro-propagation.

## 2.2) En régime temporel

Le régime temporel est obtenu *via* un passage dans le domaine fréquentiel. Le ou les antennes émettrices rayonnent un champ ayant une enveloppe gaussienne modulée à la fréquence $f_0$ de la forme

$$\mathcal{F}(t) = A \ \exp\left[-16\left(\frac{t - t_{\text{trans}}}{\tau}\right)^2\right] \ \cos(2\pi f_0 t), \tag{7}$$

où $\tau$ est lié à la durée de l'impulsion. Plus $\tau$ est petit, plus large est le spectre. Le décalage temporel $t_{\text{trans}}$ est choisi suffisamment grand pour avoir $\mathcal{F}(t) = 0$ pour $t \leq 0$ et ainsi assurer la causalité.

Un exemple de $\mathcal{F}(t)$ est présenté en Fig. 2 avec $f_0 = 5.5$ GHz ($\lambda_0 \approx 54.5$ nm), $\tau = 2$ ns et $t_{\text{trans}} = 4$ ns. Le nombre de fréquences utilisées pour décrire l'impulsion dans le domaine fréquentiel est $P = 21$, et nous avons vérifié que le nombre de fréquences est suffisant pour décrire correctement l'impulsion.

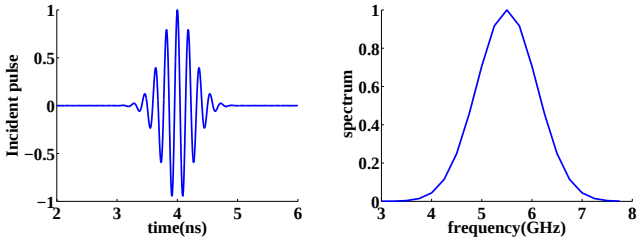


(a) (b)

**Figure 2 :** *(a) Évolution du champ incident en fonction de temps. (b) Spectre du champ incident.*

Donc, pour le problème direct, nous devons résoudre successivement $P$ harmoniques problèmes et après passage en temporel. Cette méthode a quelques avantages par rapport à des méthodes numériques qui travaillent directement dans le domaine temporel comme par exemple la méthode des différences finies. En effet, le domaine de calcul se limitant au support du diffuseur, et donc la précision du calcul est déterminée principalement par la taille de la maille de la discrétisation. Ensuite, la condition d'onde sortante est intrinsèquement satisfaite à travers la fonction de Green, et enfin, il est plus facile de prendre en compte la dispersion des milieux.

Pour le problème inverse, nous travaillons aussi dans le domaine fréquentiel. Deux possibilités s'offrent à nous. Premièrement, nous pouvons résoudre successivement le problème inverse à une fréquence donnée ou l'estimation initiale est donnée par le résultat obtenu à la fréquence précédente. Cette méthode est appelée "marche-récurrente-en-fréquence". La fonction coût reste la même que celle donnée par l'Eq. 5, mais nous devons la minimiser successivement à toutes les fréquences. Deuxièmement, nous pouvons choisir d'inverser toutes les fréquences en même temps. Dans ce cas la fonction coût à minimiser est définie comme

$$\begin{aligned}\mathcal{F}_n(\chi_{1,n},\cdots,\chi_{P,n},\boldsymbol{E}_{1,1,n},\cdots,\boldsymbol{E}_{1,P,n},\cdots,\boldsymbol{E}_{N,1,n},\cdots,\boldsymbol{E}_{N,P,n}) &= \mathcal{F}_n(\chi_{\bullet,n},\boldsymbol{E}_{\bullet,\bullet,n}) \\ &= W_\Gamma \sum_{l=1}^{N}\sum_{p=1}^{P} \|\boldsymbol{h}^{(2)}_{l,p,n}\|^2_\Gamma + W_\Omega \sum_{l=1}^{N}\sum_{p=1}^{P} \|\boldsymbol{h}^{(1)}_{l,p,n}\|^2_\Omega,\end{aligned} \tag{8}$$

avec

$$W_\Gamma = \frac{1}{\sum_{l=1}^{N}\sum_{p=1}^{P} \|\boldsymbol{f}^{\text{mes}}_{l,p}\|^2_\Gamma}, \qquad W_\Omega = \frac{1}{\sum_{l=1}^{N}\sum_{p=1}^{P} |\boldsymbol{E}^{\text{inc}}_{l,p}\|^2_\Omega}. \tag{9}$$

# 3) Détection et caractérisation de diffuseurs en trois dimensions dans un milieu désordonné

## 3.1) La méthode DORT

La méthode DORT est une méthode en régime harmonique de retournement temporel qui permet de détecter et de localiser des diffuseurs présents dans un milieu désordonné, c'est-à-dire un milieu comportant des hétérogénéités. Dans notre simulation, $\varepsilon_f$, la permittivité relative du milieu au voisinage les diffuseurs, peut être suivant la relation ci-dessous

$$\varepsilon_f(\boldsymbol{r}) = \varepsilon_b + C(\boldsymbol{r}), \tag{10}$$

$$C(\boldsymbol{r}) = \sigma_f^2 \exp\left(-\frac{\|\boldsymbol{r}\|^2}{l_c^2}\right), \tag{11}$$

avec $\varepsilon_b$ la permittivité moyenne du milieu et $C(\boldsymbol{r})$ une fonction de corrélation gaussienne de moyenne nulle et d'écart-type $\sigma_f$. Plus $\sigma_f$ est grand, plus la fluctuation est forte. Les hétérogénéités varient suivant les trois dimensions de l'espace. $l_c$ est la longueur de corrélation de $C(\boldsymbol{r})$.

Dans la configuration tridimensionnelle vectorielle étudiée, les antennes peuvent prendre trois orientations possibles. Pour un couple émetteur-récepteur $(i, j)$, une sous-matrice $3 \times 3$ peut être construite,

$$\boldsymbol{K}_{ij} = \begin{pmatrix} K_{ij}^{xx} & K_{ij}^{xy} & K_{ij}^{xz} \\ K_{ij}^{yx} & K_{ij}^{yy} & K_{ij}^{yz} \\ K_{ij}^{zx} & K_{ij}^{zy} & K_{ij}^{zz} \end{pmatrix}. \tag{12}$$

Les éléments diagonaux de la matrice décrivent la relation entre les récepteurs et émetteurs avec la même orientation. Les éléments hors diagonale décrivent les polarisations croisées. Une fois toutes les mesures effectuées, nous obtenons une matrice $\boldsymbol{K}$

$$\boldsymbol{K} = \begin{pmatrix} \boldsymbol{K}_{11} & \boldsymbol{K}_{12} & \dots & \boldsymbol{K}_{1N} \\ \boldsymbol{K}_{21} & \boldsymbol{K}_{22} & \dots & \boldsymbol{K}_{2N} \\ \vdots & \vdots & \ddots & \vdots \\ \boldsymbol{K}_{N1} & \boldsymbol{K}_{N2} & \dots & \boldsymbol{K}_{NN} \end{pmatrix}. \tag{13}$$

Chaque élément $\boldsymbol{K}$ de la matrice correspond au champ diffracté mesuré sur un récepteur, quand un autre émet. En vertu du théorème de la réciprocité, $\boldsymbol{K}$ est symétrique. Dans un cadre monochromatique, l'opération de retournement temporel consiste à conjuguer la phase et à permuter le rôle des sources et des récepteurs. Matriciellement cela correspond à conjuguer et à transposer la matrice $\boldsymbol{K}$. L'opérateur de Retournement Temporel est donc représenté par la matrice $\boldsymbol{L} = \boldsymbol{K}^{\dagger}\boldsymbol{K}$. Les invariants de cet opérateur nous fournissent deux renseignements principaux:

1. D'abord, le nombre de valeurs propres émergentes est lié au nombre de diffuseurs dans le milieu sondé. A noter qu'en présence d'un seul diffuseur le nombre de valeurs et vecteurs propres associés varient suivant la configuration, voir Tab. 1 pour le nombre de valeurs propres suivant la configuration.

| | Complète | Limite-homogène | Limite-demi-espace |
|---|---|---|---|
| Illumination scalaire | 1 | 1 | 1 |
| Illumination vectorielle | 3 | 3 | 2 |

**Table 1 :** *Nombre de valeurs propres pour un diffuseur suivant la configuration choisie. Configuration complète signifie que les antennes sont disposées tout autour du diffuseur. Configuration limite-homogène signifie que la mesure se fait sur un plan au dessus du diffuseur sans présence d'interface. Configuration limite-demi-espace signifie que la mesure se fait sur un plan au-dessus d'une interface plane quand le diffuseur est placé en dessous de cette même interface. Illumination scalaire signifie que les antennes ne prennent qu'une seule orientation tandis que vectorielle signifie que chaque antenne prend les trois orientations possibles de l'espace.*

2. Ensuite, si nous analysons les vecteurs propres associés, ils nous donnent des informations sur la location des diffuseurs: Si on alimente les antennes par un courant ayant l'amplitude et la phase donnés par le vecteur propre, alors le champ présentera un maximum là où se trouve le diffuseur. La méthode DORT est une technique très efficace pour localiser les objets situés dans un environnement hétérogène.

## 3.2) Résultats numériques en espace homogène

Nous reportons sur la Fig. 3 la configuration du problème étudié. Un réseau bidimensionnel plan d'antennes ($N = 9 \times 9$, de la longueur $8\lambda$) situé à $z = 2\lambda$ est utilisé pour illuminer successivement le domaine et mesurer le champ diffracté. L'interdistance entre deux antennes voisines est de $\lambda$. Les diffuseurs étudiés sont deux sphères diélectriques de rayon $r_1 = \lambda/6$ et $r_2 = \lambda/4$, avec comme permittivité relative $\varepsilon = 3\varepsilon_b$, où $\varepsilon_b$ est la moyenne de la permittivité relative du milieu dans lequel les diffuseurs sont immergés. La distance entre les diffuseurs est de $0.5\lambda$ et $0.7\lambda$, suivant les axes $x$ et $z$, respectivement. $\lambda$ est la longueur d'onde d'illumination. Le plus grand diffuseur est le plus éloigné des sources. Le domaine $W$ représenté dans Fig. 3 est une boîte de taille $5\lambda \times 5\lambda \times 4\lambda$, centrée à $z = -\lambda$. Le milieu dans lequel les diffuseurs sont immergés à une variation de permittivité

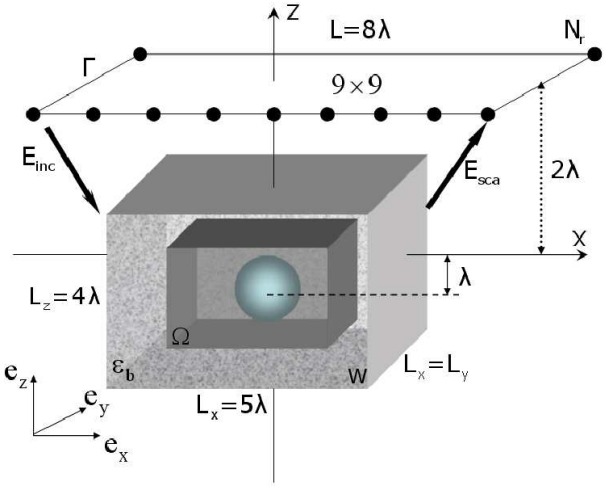


**Figure 3 :** *Géométrie du problème. Les sources et récepteurs sont distribués régulièrement sur un plan, au dessus des diffuseurs. Les diffuseurs sont confinés dans un domaine $W$.*

relative avec les caractéristiques suivantes : une faible longueur de corrélation ($l_c = \lambda/10$), un écart type $\sigma(\varepsilon_f)$=$0.068\varepsilon_b$ et un régime de diffusion simple entre les diffuseurs et les hétérogénéités. Si nous observons les différentes valeurs propres, Fig. 4, nous pouvons voir que pour chaque diffuseur, il y a bien trois valeurs propres dominantes associées. Les autres valeurs propres appartiennent à l'espace du bruit.

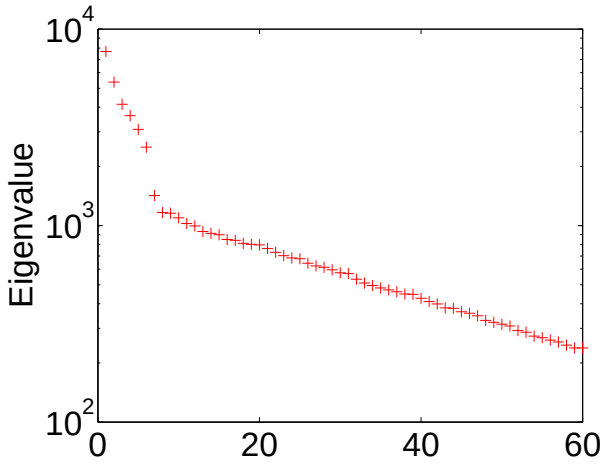


**Figure 4 :** *Évolution des valeurs propres pour la configuration détaillée dans Fig. 3. Illuminations vectorielles en présence d'un bruit de structure ayant les caractéristiques statistiques suivantes:* $l_c = \lambda/10$ *et* $\sigma(\varepsilon_f)$=$0.068\varepsilon_b$.

Dans la Fig. 5 nous observons respectivement les cartes d'intensité du champ focalisant dans le plan $(x, y)$ et le plan $(x, z)$, champ focalisant formé par les vecteurs propres de l'opérateur du retournement temporel. Les trois premières valeurs propres forment un champ focalisant sur le diffuseur dont la signature sur les antennes est dominante. Les trois valeurs propres suivantes (4, 5 et 6) correspondent à la signature du deuxième diffuseur le plus échogène. Celui-ci est situé loin des antennes. Grâce à la méthode DORT, le domaine d'investigation utilisé pour le problème d'inversion peut être limité à la région donnée par les champs focalisants, qui est environ 10 fois plus petite que le domaine où les champs retournés ont été calculés. Sans cette information nous devrions utiliser une boîte d'investigation nettement plus grande demandant alors un temps calcul prohibitif.

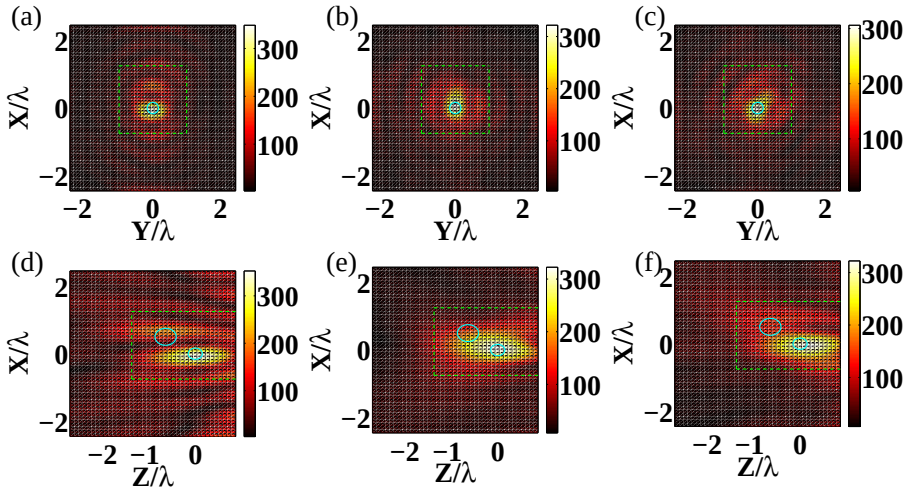


**Figure 5 :** *Intensité des champs retournés pour les trois premières valeurs propres, avec $l_c = \lambda/10$ et $\sigma(\varepsilon_f)$=0.068$\varepsilon_b$. Ces trois vecteurs propres focalisent sur le diffuseur qui est le plus proche des antennes. (a), (b) et (c) plan $(x, y)$ à $z = 0$. (d), (e) et (f) plan $(x, z)$ à $y = 0$. Chaque colonne correspond à la première, la deuxième et la troisième valeur propre. La boîte en pointillée indique le domaine d'investigation $\Omega$ utilisé dans l'inversion.*

Ici, nous nous proposons d'introduire les champs focalisants (champs dortiens) comme champ incident dans la procédure d'inversion pour améliorer le rapport signal sur bruit. Le nombre total des incidences est alors réduit au nombre des valeurs propres dominantes correspondant aux diffuseurs, et donc la taille du problème est grandement diminué. Notons que nous n'avons pas besoin de mesurer le nouveau champ diffracté correspondant aux nouvelles incidences dortiennes. En effet, il peut être déduit en utilisant une combinaison linéaire des mesures avec comme coefficients de la combinaison les composantes du vecteur propre. Figure 6 présente les résultats de la reconstruction en trois dimensions avec HM-DORT et HM. La reconstruction utilisant les champs dortiens (HM-DORT) est meilleure que celle obtenue sans DORT (HM) et évite les fausses alarmes autour des objets d'intérêts. La fonction coût, Fig. 6(c), converge plus rapidement avec HM-DORT, et la valeur finale de celle-ci est environ un ordre de grandeur plus petite qu'avec HM seul, ce qui donne une meilleure caractérisation des diffuseurs. Les intérêts principaux de la méthode DORT dans ce cas réside dans le temps de calcul, qui est environ 36 fois plus long sans DORT qu'avec DORT, en raison de la diminution du nombre des incidences et d'une meilleur reconstruction des diffuseurs.

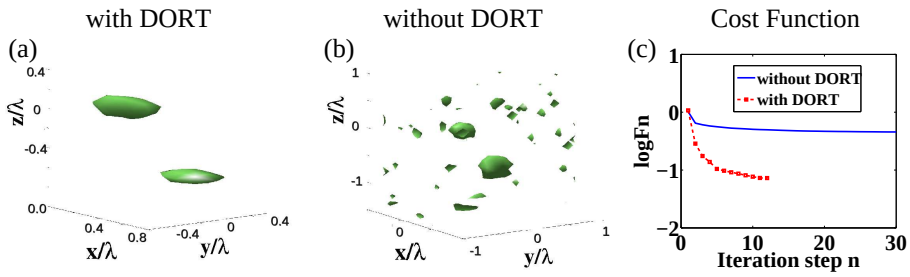


**Figure 6 :** *Même configuration que Fig. 5. (a) Carte de permittivité reconstruite en utilisant HM-DORT, vue en Iso-surface à $\varepsilon = 2$. (b) même que (a) avec HM. (c) Évolution des fonctions coûts: HM-DORT (- -) et HM (-).*

Nous avons vérifié que HM-DORT présente des images satisfaisantes des cibles, avec des écarts-types élevés jusqu'à $0,125\varepsilon_b$, la présence de diffusion multiple et de grandes longueurs de corrélation où les champs dortiens sont détériorés. Les diffuseurs sont mieux localisés avec HM-DORT qu'avec DORT seul, surtout suivant la direction $z$. Notons l'importance de l'utilisation d'une inversion non-linéaire et de données vectorielles complètes pour obtenir des reconstructions de bonne qualité.

## 3.3) Résultats numériques en demi-espace

En demi-espace, les sources et les objets à détecter sont situés dans deux milieux différents, séparés par une interface plane. Les objets sont dans un milieu de permittivité $\varepsilon_f$ et les antennes sont dans l'air. Cette configuration réaliste a pour première conséquence d'avoir un système d'imagerie ayant une ouverture numérique faible à cause de la réflexion du champ rayonné par les antennes sur la surface qui augmente avec l'éloignement de l'antenne par rapport au diffuseur. Dans ce cas avec une seule longueur d'onde $\lambda_{\text{ref}}$, deux structures différentes peuvent donner le même champ diffracté, avec une interdistance $d = \lambda_{\text{ref}}/2$, comme montré dans la Ref.5. Il n'y a donc pas unicité de la solution. En utilisant des données synthétiques, sans bruit, nous avons vérifié qu'une marche-récurrente-en-fréquence est indispensable pour obtenir des reconstructions précises. L'estimation initiale pour résoudre le problème inverse à une fréquence est donnée par la solution obtenue à basse fréquence. Pour la fréquence la plus basse, l'estimation initiale est obtenue par la rétro-propagation.

La configuration choisie est de deux diffuseurs sphériques tels que $r_1 = \lambda_{\text{ref}}/8$, situé à $(0.5\lambda_{\text{ref}}, 0.4\lambda_{\text{ref}}, 0.5\lambda_{\text{ref}})$, et $r_2 = \lambda_{\text{ref}}/6$, centré à $(-0.5\lambda_{\text{ref}}, 0.4\lambda_{\text{ref}}, -0.5\lambda_{\text{ref}})$. Leurs permittivités relatives sont toutes égales à 5. La taille du domaine $W$ est de $(3\lambda_{\text{ref}} \times 3\lambda_{\text{ref}} \times 3\lambda_{\text{ref}})$ m$^3$. Le milieu dans lequel les deux diffuseurs sont immergés est de permittivité relative 3. La distribution des antennes est la même que la configuration sans interface vue précédemment. Le plan qui sépare les antennes et les diffuseurs est situé en $z = \lambda_{\text{ref}}$. Les données sont simulées pour trois longueurs d'onde différentes $\lambda_1 = 3\lambda_{\text{ref}}$, $\lambda_2 = 1,5\lambda_{\text{ref}}$ et $\lambda_{\text{ref}}$. Notons que ces illuminations supplémentaires à des longueurs d'onde plus grandes n'augmentent pas l'ouverture numérique et ne donnent pas plus d'informations en terme de hautes fréquences spatiales. Nous considérons un désordre de l'écart type $\sigma(\varepsilon_f) = 0.058$ et de longueur de corrélation $l_c = \lambda_{\text{ref}}/18$. A la fréquence la plus haute $\lambda_{\text{ref}}$, pour chaque diffuseur, il existe donc deux valeurs propres associées à chaque diffuseur. Les résultats des reconstructions sont reportés dans Fig. 7.

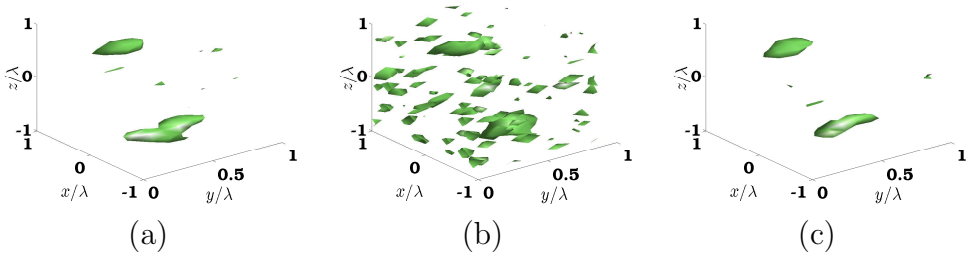


**Figure 7 :** *Cartes de permittivités reconstruites en présence d'une interface entre les antennes et les diffuseurs. (a) Iso-surface à $\varepsilon = 3.5$ avec HM-DORT. (b) même que (a) mais obtenue avec HM. (c) même que (a) dans le cas où le bruit de structure est généré dans un domaine $W$ plus grand avec la taille de $(6\lambda_{\text{ref}} \times 6\lambda_{\text{ref}} \times 3\lambda_{\text{ref}})$ $m^3$.*

Les résultats des reconstructions montrées sur la Fig. 7 sont tous obtenus en utilisant la marche-récurrente-en-fréquence. HM-DORT donne des résultats similaires à ceux obtenus en espace-homogène. Les améliorations apportées par HM-DORT sont particulièrement évidentes en vue de l'iso-surface, où avec HM seule beaucoup de fausses alarmes apparaissent dans le domaine

d'investigation dissimulant ainsi les objets à reconstruire, Fig. 7 (b). Grâce à HM-DORT, les effets liés à la présence des hétérogénéités sont remarquablement diminués et seuls les deux objets échogènes sont extraits. La valeur de la fonction coût est un ordre de grandeur inférieur avec la méthode HM-DORT que celle obtenue avec HM. En outre, le temps de calcul avec HM-DORT (qui utilise, dans ce cas, seulement 4 champs incidents à chaque inversion) à la longueur d'onde $\lambda_{\text{ref}}$ est de 287 s, soit environ 80 fois inférieur à la méthode HM (22201 s).

Notons que les hétérogénéités données par $C(\boldsymbol{r})$ sont seulement dans le domaine $W$, et qu'au delà c'est le substrat de permittivité uniforme $\varepsilon_b$. Mais la méthode présentée peut être utilisée pour déduire le comportement du système d'imagerie dans une situation réaliste où les hétérogénéités sont présentes dans un milieu plus étendu. En effet, les résultats présentés ne changent pas lorsque la taille de $W$ est grandie par un facteur quatre, *i.e.* $W = (6\lambda_{\text{ref}} \times 6\lambda_{\text{ref}} \times 3\lambda_{\text{ref}})$ m$^3$ en gardant la même distribution de bruit de structure et les mêmes statistiques. Les deux diffuseurs sont toujours bien localisés par DORT et les reconstructions obtenues sont similaires à celles avec un $W$ plus petit, voir Fig. 7 (c). La propriété focalisante de DORT permet de diminuer considérablement l'influence des hétérogénéités loin des cibles d'intérêts et la taille de $W$ n'a pas d'influence sur les reconstructions.

Nous avons aussi varié les caractéristiques du bruit de structure pour tester la robustesse de HM-DORT. Un nouveau paramètre SC est introduit pour quantifier le pouvoir diffractant des hétérogénéités:

$$\text{SC} = \sum_{l=1}^{N} \sum_{\alpha}^{x,y,z} \|\boldsymbol{f}_{l,\alpha}^{\text{clutter}}\|_{\Gamma}^{2}. \tag{14}$$

où $\boldsymbol{f}_{l,\alpha}^{\text{clutter}}$ est le champ diffracté par les hétérogénéités seules. Le comportement de SC est présenté sur la Fig. 8. Quand $l_c \ll \lambda$, le bruit de structure peut être homogénéisé ce qui conduit à un champ diffracté faible, et lorsque $l_c \gg \lambda$, la variation spatiale à grande échelle de celui-ci ne perturbe pas le signal rayonné par les diffuseurs car il est localement homogène. L'effet des hétérogénéités est donc important quand la longueur de corrélation est de l'ordre de grandeur de la longueur d'onde d'illumination, comme le confirme la Fig. 8. Notons que le comportement de SC par rapport à la longueur de corrélation diffère fortement en fonction de la configuration étudiée. En demi-espace, SC présente un pic "pointu" centré à $l_c = \lambda/10$, alors qu'en l'absence d'interface la courbe SC présente un pic "très large" avec un maximum à $l_c \approx \lambda/3$.

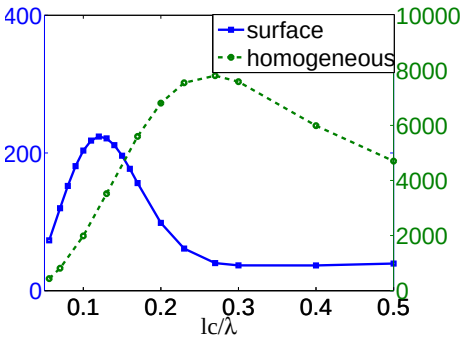


**Figure 8 :** *SC en fonction de $l_c/\lambda$, en l'absence d'interface (trait pointillé) et avec une interface (trait plein).*

Avec une longueur de corrélation fixée, en utilisant la méthode marche-récurrente-en-fréquence, il est possible que SC soit très élevé à la longueur d'onde de départ. La reconstruction obtenue est alors fortement perturbée et cette mauvaise estimation initiale compromet les inversions suivantes. Cette possibilité souligne la limitation de la marche-récurrente-en-fréquence. Selon les caractéristiques du bruit de structure, les choix des longueurs d'onde, des champs incidents utilisés

dans l'inversion doivent être adaptés. Il est probable qu'une procédure globale d'inversion avec plusieurs fréquences conduirait à de meilleurs résultats.

# 4) Application de DORT à la Microscopie tomographique par diffraction (TDM)

Nous avons précédemment étudié la méthode DORT en utilisant des données synthétiques. Dans cette partie, nous nous proposons d'étudier la possibilité de caractérisation avec HM-DORT en utilisant des données expérimentales. Dans notre équipe (SEMOX, Institut Fresnel), une technique d'imagerie optique assez récente, la Microscopie tomographique par diffraction (TDM), a été développée pour reconstruire des objets tridimensionnels déposés sur un substrat plan. Les travaux précédents étaient conduits dans la configuration scalaire, ce qui signifie que les illuminations étaient polarisées suivant une seule direction et les champs diffractés étaient détectés suivant la même direction. Dans ce travail de thèse, nous nous proposons d'appliquer HM-DORT en TDM. Grâce à DORT, nous pouvons focaliser sélectivement sur chaque diffuseur dans un milieu présentant des multiples diffuseurs. En particulier, si les diffuseurs sont présents dans un milieu désordonné, le rapport signal à bruit peut être amélioré en utilisant DORT.

## 4.1) Mesure des données vectorielles en microscopie tomographique de diffraction

Pour que la focalisation dortienne soit isotrope sur le substrat, nous avons vu précédemment que travailler en vectoriel était essentiel. Nous avons donc décidé de mesurer toutes les composantes du champ électrique diffracté. En plus, les hautes fréquences spatiales, déterminantes pour caractériser un objet de petite taille, étant sur les bords de l'ouverture numérique, seront parfaitement mesurées, ce qui on le verra, apportera une meilleure résolution par rapport à l'hypothèse scalaire, *i.e.*, seul le champ électrique diffracté parallèlement au champ incident est mesuré.

Cette mesure vectorielle du champ électrique a nécessité des modifications du montage expérimental sur l'orientation des polariseurs un peu plus compliqué qu'il n'y paraît. Les illuminations sont polarisées dans la base $(\hat{\boldsymbol{y}}, \hat{\boldsymbol{x}})$ et les champs diffractés sont détectés suivant les directions de polarisation perpendiculaires $(\hat{\boldsymbol{d}}_1, \hat{\boldsymbol{d}}_2)$ tel que $\hat{\boldsymbol{x}}.\hat{\boldsymbol{d}}_1 = \sqrt{2}/2$. La procédure de renormalisation est fortement complexifiée par cette mesure sur deux bases différentes. En effet il est nécessaire de normaliser les champs mesurés avant d'effectuer l'inversion non-linéaire. Les champs diffractés sont normalisés de sorte que, le champ spéculaire réfléchi corresponde au champ théorique calculé par le problème direct pour chaque illumination (en amplitude et en phase). Cette procédure est bien détaillée au sein de cette thèse. Ce nouveau montage permet d'accéder au champ diffracté vectoriel pour un éclairement incident en polarisation TE ou TM.

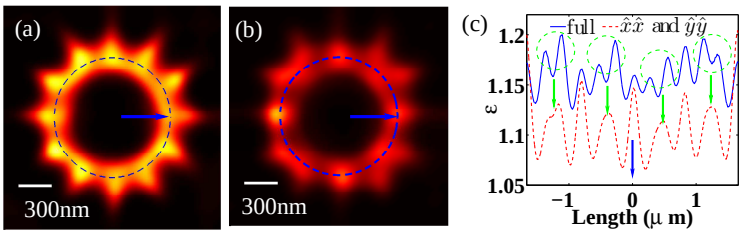


**Figure 9 :** *Carte de permittivité obtenue avec HM pour un échantillon diélectrique constitué de 12 rectangles en résine formant une structure dodécagonale. (a) Le champ diffracté est mesuré vectoriellement pour des illuminations incidentes en TE et TM. (b) Seul le champ diffracté parallèle au champ électrique incident est mesuré en $\hat{\boldsymbol{x}}\hat{\boldsymbol{x}}$ et $\hat{\boldsymbol{y}}\hat{\boldsymbol{y}}$. (c) Coupe de la permittivité suivant le cercle bleu sur (a) (trait bleu solide) et (b) (trait rouge pointillé).*

Nous considérons huit incidences, définies par un angle polaire $\theta_{\text{inc}} = 60°$ et un angle azimutal $\phi_{\text{inc}}$ régulièrement espacé sur $[0\ 2\pi]$. Nous prenons un échantillon complexe composés de douze rectangles de résine de permittivité relative $\varepsilon = 2$, de largeur 100 nm, longueur 300 nm et hauteur 140 nm. Ils sont placés radialement au sommet d'un dodécagone, sur un substrat de silicium de permittivité relative $15 + i0.15$. Figure 9 (a) montre la reconstruction quand le champ incident est orienté successivement suivant TE et TM et que le champ diffracté est mesuré vectoriellement. Dans ce cas nous sommes capable de distinguer les rectangles quelle que soit leurs orientations et même quand leurs interdistances sont inférieures à un quart de la longueur d'onde. Au contraire, l'utilisation des données scalaires combinées $\hat{\boldsymbol{x}}\hat{\boldsymbol{x}}$ et $\hat{\boldsymbol{y}}\hat{\boldsymbol{y}}$, donne une permittivité reconstruite trop faible comparée avec celle obtenue avec des données complètes, et la structure dodécagonale est perdue, Fig. 9 (b). A noter que cette amélioration est plus évidente sur la Fig. 9 (c), où la permittivité présentée est obtenue pour une coupe suivant la cercle bleu sur les Figs. 9 (a) et (b). En effet, entouré en pointillés bleu, sur la mesure vectorielle complète nous apercevons bien les deux rectangles en diagonal alors qu'en donnée scalaires combinées ces deux rectangles n'en forment plus que un. La résolution anisotrope observée dans Fig. 9 (b) est due à l'absence de la polarisation croisée. Nous avons aussi utilisé des données scalaires $\hat{\boldsymbol{x}}\hat{\boldsymbol{x}}$ ou $\hat{\boldsymbol{y}}\hat{\boldsymbol{y}}$ pour reconstruire cette structure complexe. Le résultat est très détérioré et la résolution suivant la direction perpendiculaire à la polarisation est complètement perdue. Cette réalisation expérimentale souligne l'importance d'utiliser des mesures complètes pour atteindre une super-résolution dans l'imagerie optique en champ lointain.

## 4.2) Application de DORT en TDM

Dans cette partie, nous nous proposons d'appliquer la méthode DORT en TDM. L'échantillon est constitué de 4 plots cylindriques de permittivité relative $\varepsilon = 2$ et de hauteur $h = 150$ nm déposés sur un substrat de silicium. Les diamètres des plots sont respectivement de 200 nm, 300 nm, 400 nm et 500 nm. Les champs incidents sont en TE et TM orientés suivant les axes $\hat{\boldsymbol{x}}$ et $\hat{\boldsymbol{y}}$ et les champs diffractés sont mesurés vectoriellement. Nous utilisons 88 incidences, avec $\theta_{\text{inc}}^{\max} = 61°$ et $\phi_{\text{inc}}$ distribuées régulièrement entre $[0\ 2\pi]$.

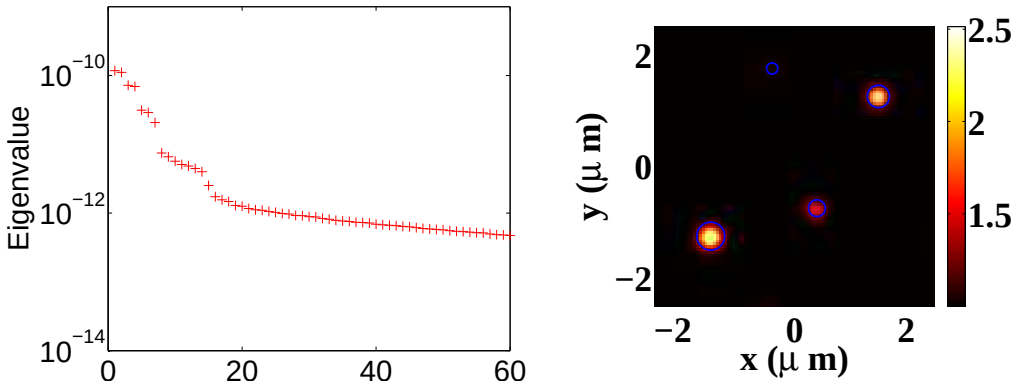


**Figure 10 :** *(a) Valeurs propres en présence de 4 plots différents, avec des illuminations polarisées en TM et TE. (b) Reconstruction de la permittivité en utilisant HM dans un domaine d'investigation très grand contenant ces 4 plots.*

Notons que sans utiliser DORT, nous devons chercher la distribution de permittivité dans une boîte très grande (5 $\mu$m $\times$ 5 $\mu$m $\times$ 200 nm). Malheureusement, le diffuseur le moins diffractant est perdu car noyé par les trois autres diffuseurs plus échogènes, Fig. 10 (b).

Avec DORT nous commençons par regarder la distribution des valeurs propres sur la Fig. 10 (a). Les sept premières valeurs propres sont nettement émergentes par rapport aux autres, puis à partir de la 15-ème valeur propre on rentre clairement dans le bruit. Pour déterminer les vecteurs propres associés à chaque diffuseur, il faut regarder les cartes d'intensités des champs retournés générés par ces vecteurs propres. Pour chaque diffuseur, il y a deux valeurs propres associées.

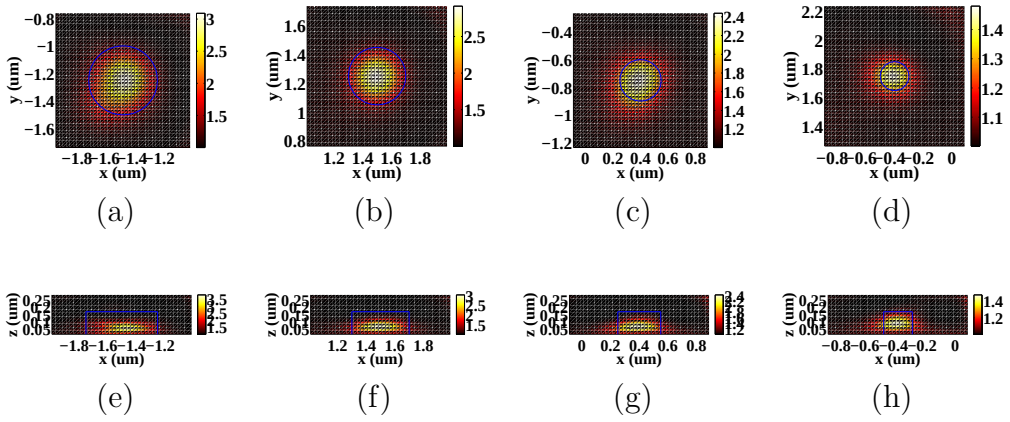


**Figure 11 :** *Reconstruction sélective en utilisant HM-DORT sur ces 4 plots. Le domaine d'investigation a été limité à une boîte autour de chaque diffuseur, de la taille de* 1 $\mu m \times$ 1 $\mu m \times$ 300 *nm.*

Comme il est possible grâce à DORT de focaliser sur des diffuseurs de manière sélective, nous nous proposons de caractériser les diffuseurs séquentiellement. Le domaine d'investigation a donc été limité à une boîte autour de chaque diffuseur et seuls les champs incidents qui focalisent sur ce diffuseur ont été utilisés dans l'inversion, c'est-à- dire ont été utilisés les deux vecteurs propres associés au diffuseur considéré. Les quatre cibles sont parfaitement reconstruites avec HM-DORT. La permittivité de la cible la moins brillante est reconstruite avec une sous-estimation de sa permittivité relative.

# 5) Inversion dans le régime transitoire

Dans cette partie, nous allons présenter les résultats obtenus à partir de données transitoires, c'est-à-dire que l'objet d'intérêt est éclairé par une seule source qui émet un champ électrique variant dans le temps. L'approche considérée est donc mono-source et multi-fréquence en utilisant la transformée de Laplace. Nous montrons des résultats à partir de champs mesurés dans une chambre anéchoïque ($14 \times 6.5 \times 6.5$ m$^3$). Les champs diffractés sont mesurés pour 21 fréquences différentes, de 3 GHz à 8 GHz, avec un pas $\Delta f = 0.25$ GHz. Les cibles sont placées dans le vide. Nous travaillons dans le régime de la transmission, c'est-à-dire que les récepteurs sont situés à l'opposé de l'émetteur, par rapport au diffuseur.

Le premier diffuseur considéré est constitué de deux cubes disposés suivant l'axe $z$, de permittivité relative $\varepsilon = 2.4$ et de côté $a = 2.5$ cm, dont les centres sont séparés par 5 cm suivant $z$. Nous comparons deux façons de traiter les données multi-fréquences. Nous pouvons soit les inverser fréquence après fréquence (marche-récurrente-en-fréquence), soit considérer tous les champs en même temps dans la procédure de minimisation (multi-fréquence).

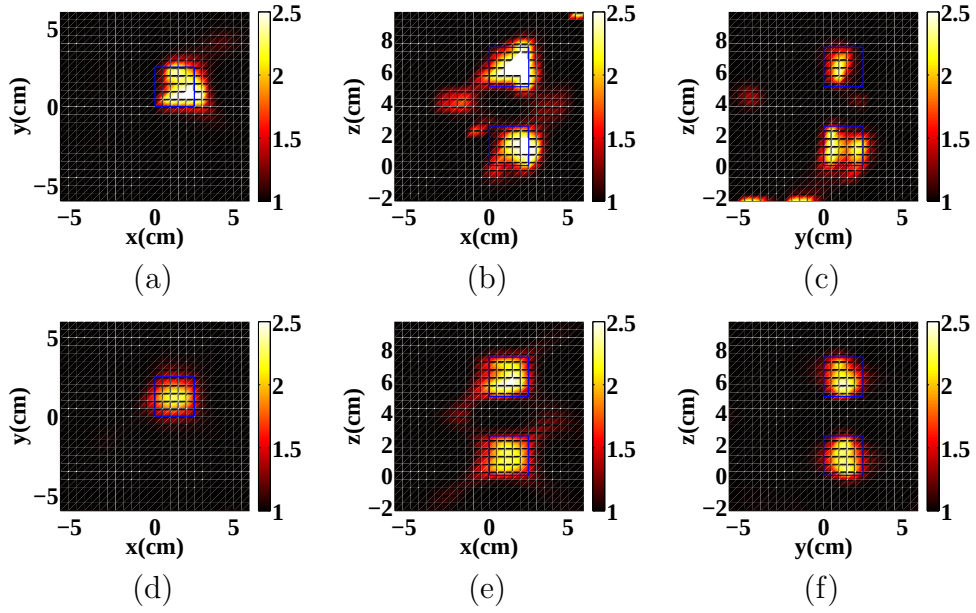


**Figure 12 :** *Carte de permittivité reconstruite pour les deux cubes disposés suivant l'axe $z$. (a)-(c) pour la marche-récurrente-en-fréquence. (d)-(f) en multi-fréquence. (a) et (d) dans le plan $(x, y)$ à $z = 1.25$ cm. (b) et (e) dans le plan $(x, z)$ à $y = 1.25$ cm. (c) et (f) dans le plan $(x, y)$ à $x = 1.25$ cm.*

Si nous comparons les résultats montrés sur la Fig. 12, nous pouvons voir que la méthode multiple-fréquence donne de bien meilleures reconstructions que la marche-récurrente-en-fréquence. En effet avec la marche-récurrente-en-fréquence, des objets fantômes apparaissent en dehors des cibles. Alors qu'avec le multi-fréquence, la permittivité reconstruite du milieu entourant les objets est parfaitement égale à l'unité et la permittivité obtenue pour chaque diffuseur est proche de sa valeur réelle. Nous pouvons alors conclure que l'inversion multi-fréquence est robuste vis-à-vis du bruit contrairement à la marche-récurrente-en-fréquence.

Maintenant, nous considérons un deuxième objet, deux cubes en contact par un bord de permittivité relative $\varepsilon = 2.4$ et de côté $a = 2.5$ cm). Cette fois ci, la reconstruction obtenue en multi-fréquence [Figs. 13 (a), (b) et (c)] est clairement très loin de l'objet réel. Nous avons vérifié que les mesures des champs diffractés étaient peu bruités. Nous avons donc toute l'information

nécessaire pour reconstruire l'objet. En fait, la contribution des hautes fréquences domine tellement dans la fonction coût que l'inversion se fait essentiellement avec les hautes fréquences, et les basses fréquences qui stabilisent l'algorithme d'inversion n'ont plus assez de poids. Nous nous proposons alors de pondérer les contributions pour chaque fréquence $f_p$ $(p = 1, \cdots, 21)$ par un coefficient $1/(f_p)^3$ pour que les contributions des hautes fréquences soient fortement atténuées. Dans ce cas, la fonction coût est modifiée à partir de l'Eq. 5, comme

$$\tilde{F}_n(\chi_n, \boldsymbol{E}_{\cdot,\cdot,n}) = \frac{\sum_{l=1}^{N}\sum_{p=1}^{P}(1/f_p)^{\alpha}\|\boldsymbol{h}^{(2)}_{l,p,n}\|^2_{\Gamma}}{\sum_{l=1}^{N}\sum_{p=1}^{P}(1/f_p)^{\alpha}\|\boldsymbol{f}^{\mathrm{mes}}_{l,p}\|^2_{\Gamma}} + \frac{\sum_{l=1}^{N}\sum_{p=1}^{P}(1/f_p)^{\alpha}\|\boldsymbol{h}^{(1)}_{l,p,n}\|^2_{\Omega}}{\sum_{l=1}^{N}\sum_{p=1}^{P}(1/f_p)^{\alpha}\|\boldsymbol{E}^{\mathrm{inc}}_{l,p}\|^2_{\Omega}}. \tag{15}$$

Nous pouvons voir que cette pondération permet d'améliorer la reconstruction, Figs. 13 (d), (e) et (f). C'est-à-dire que si nous travaillons avec des hautes fréquences non pondérées, l'algorithme d'inversion a de forte chance de ne pas converger vers la solution.

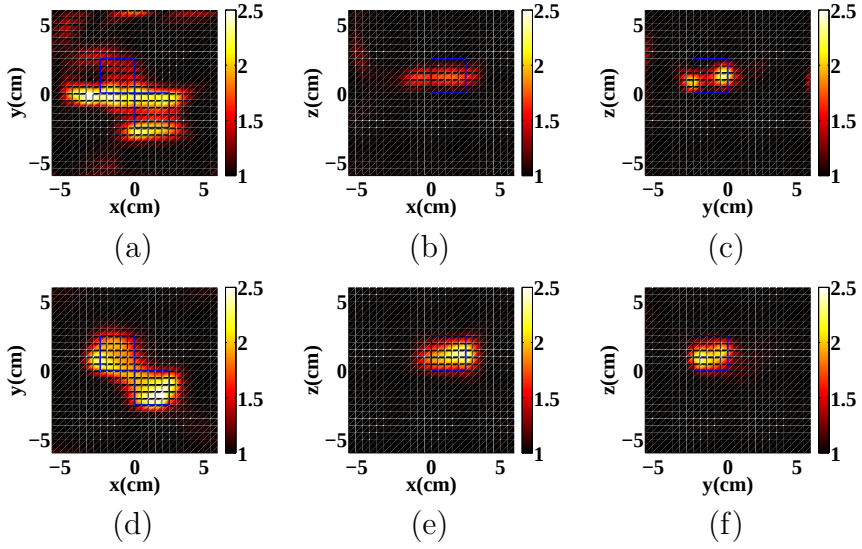


**Figure 13 :** *Carte de permittivité reconstruite pour les deux cubes en contact par un bord. (a)-(c) en utilisant le multi-fréquence. (d)-(f) en utilisant le multi-fréquence avec une fonction coût pondérée par* $(1/f_p)^3$*. (a) et (d) dans le plan* $(x, y)$ *à* $z = 1.25$ *cm. (b) et (e) dans le plan* $(x, z)$ *plane à* $y = -1.25$ *cm. (c) et (f) dans le plan* $(y, z)$ *à* $x = 1.25$ *cm.*

A noter que pour certaines objets, la pondération sur la fonction coût n'est pas indispensable, une version non pondérée de l'inversion suffit pour reconstruire correctement les cibles.

# 6) Conclusion

Dans ce mémoire de thèse nous avons étudié comment détecter et caractériser des objets en présence de bruit dans le régime harmonique et transitoire. Ces développements théoriques ont été confrontés avec succès aux données expérimentales dans le domaine de l'optique et des hyperfréquences. Les travaux futurs consistent à étendre l'inversion multi-fréquences quand les objets sont en présence d'interfaces pour pouvoir inverser des données expérimentales obtenues en TDM.

# Introduction

The electromagnetic inverse scattering problem is an important issue and of great interest in many areas, such as non-invasive testing, medical imaging or subsoil probing. It consists to determine properties of unknown targets from the knowledge of their response to an exterior electromagnetic excitation. The inverse problem is opposite to the forward scattering problem, which aims to model the interaction between electromagnetic waves and known material structures. In the forward problem, shapes, positions and constitutive materials of scatterers are assumed to be known and the scattered field is computed by solving Maxwell's equations. This problem is generally well-posed (existence, unicity and stability of the solutions are simultaneously satisfied) while the inverse scattering problem, which aims to detect and characterize these unknown objects is ill-posed and non-linear[9–13]. Under restrictive conditions, such as the Born or Rytov approximations, inverse scattering problems may be formulated as linearized problems. In these particular cases the parameter of interest is linked to the scattered fields through a simple Fourier transformation[14]. This linearized procedure includes the Newton-Kantorovich method[15,16] and the distorted-wave Born approach[17–19]. They have been shown analytically to be equivalent in Ref. 20. In case of rigorous computation, we use the non-linearized method, namely the modified gradient method[9,21] and the contrast source inversion method[22–24]. These inversion techniques which reconstruct the permittivity map of a given investigation domain and which, in their nonlinear versions, can handle configurations supporting multiple scattering[25–27] seem to be an interesting alternative, for which the Born approximation is not valid. A hybrid method combining ideas from linearized and non-linearized method is given in Ref. 28.

In practical applications, such as subsoil probing, where the targets are buried in an inhomogeneous medium, these classical inversion techniques can not distinguish the possible inhomogeneities of the host medium from the targets themselves. This strategy yields to a poor estimation of the target[5] because the inhomogeneities of the natural medium blur the signature of the targets. Many studies were devoted to understanding the clutter influence in the deterioration of the signal response of targets[29] and proposed to reduce the clutter-signal ratio. Additional possible data preprocessing such as frequency averaging[30], angular correlation[31] or Wigner-Ville transform[32] can enhance further the target signature and reduce the influence of the clutter or that of the roughness of the surface separating the embedding medium and the measurement medium[33,34]. Other techniques for diminishing the clutter influence take advantage of the properties of the Time Reversal (TR) operator. The time reversal concept was firstly studied in the acoustic domain by Mathias Fink and Claire Prada in Institut Langevin, Paris[1,2,35,36] and then extended to electromagnetic domains[3,4,37,38]. They usually perform the Singular Value Decomposition (SVD) of the response matrix and either work on the noise subspace [as in the Multiple Signal Classification (MUSIC) method[39,40]] or on the signal subspace as in the DORT (Décomposition de l'Opérateur de Retournement Temporel) method to detect and locate targets in noisy medium[41]. The sensitivities of the MUSIC and the DORT algorithms have been compared in Ref. 42.

In the time-harmonic regime, we propose to use the DORT method[43]. It consists in analysing the eigenvalues and eigenvectors of the time reversal operator (TRO), in order to synthesize incident fields that focus selectively on the targets of interest, thus improving the signal-to-noise ratio. The methods developed for detecting and localizing the targets buried in an inhomogeneous random medium are often based on the manipulation of the TRO. The simplest approach consists in simulating, in a homogeneous average medium, the intensity maps of the dominant eigenvector fields of the TRO and using these maps for pinpointing the targets. This technique has been shown to be efficient for weakly contrasted clutter where single scattering dominates but have shown their limits in configurations supporting multiple scattering, especially when using only monochromatic data[6,7,44]. Moreover, the provided images are meaningless in terms of intrinsic properties of targets such as the refractive index. In this thesis work, we propose to combine the advantages of the hybrid inversion methods with that of the DORT analysis. This imaging approach will be firstly checked on synthetic data. Similar work has been done in the two-dimensional configuration[5,45]. In the present thesis, the study is carried out in the full vectorial configuration, with the targets possibly buried in a random inhomogeneous medium. The dipole antenna array taking three different orientations is either simply plunged into the probing medium (homogeneous space background configuration)[46] or located at a medium different from that of the targets, separated by a flat interface (half-space configuration)[47], which is more realistic (this is encountered for example in medical imaging, mineral exploration or through-wall imaging).

Another exploitation of this thesis work is the application of the combination of the DORT method with the inversion algorithms in the high-resolution optical imaging domain. In the electromagnetic domain, the DORT method is always applied with microwave data for many previous work[3–5], and firstly being demonstrated in the optical domain and proved its selective focalization ability on nano-particles in Ref. 48. Another optical imaging technique, Tomographic Diffractive Microscopy (TDM) has been recently experimentally implemented in our SEMOX team (Sondage ElectroMagnétique, Optique et Rayons X) of the Institut Fresnel, Marseille[13,49]. The basic principle of TDM is to illuminate a sample with plane wave under different successive angles, both the phase and amplitude of scattered fields are recorded through a microscope setup. Then, a three-dimensional map of permittivity is reconstructed thanks to a non-linear inversion algorithm. As most analogical microscopes, TDM neglects the vectorial nature of light in the image formation process. In all present implementations, the incident and diffracted fields are projected onto one single polarization state, defined by the orientation of the incident electrical field. The inversion procedures are based on scalar approximate models which are sufficient for qualitative imaging[50,51] but fail when quantitative imaging with high resolution is sought[13]. To get the most of TDM and to achieve super-resolution, exploiting the light polarization seems a necessary and promising lead[52,53]. In the present thesis work, the full-polarization TDM setup is developed such that applying the DORT method in TDM microscopes becomes feasible, because we need the full vectorial scattered data in order to reconstruct properly the time reversal operator. This led to consider the problem of imaging 3D samples in complex medium which seems to be interesting and to exemplify the advantage of DORT, *i.e.*, we can insert an aberrating layer before the samples for imaging to simulate an heterogeneous environment[48].

The applied non-linear inverse scattering problem mentioned above is an optimization problem, where the interest parameter is sought iteratively by minimizing a cost functional involving the measured scattered fields. In order to avoid being trapped into a local minima of the non-linear cost functional, *i.e.*, which leads to a false solution of this inversion problem, the targets need to be illuminated by different incident angles and the scattered fields are collected by enough receivers[54]. Therefore, the reconstruction resolution always degrades in case of reduced effective Numerical Aperture (NA), which measures the solid angle under which the targets are illuminated and observed. Concerned with this limit, one way to improve the reconstruction resolution and simultaneously guarantee the convergence has been studied in Ref. 19, with the well-known linearized distorted-wave Born approach. The same conclusion also holds for non-linearized inversion algorithms[21]. Better convergence of the minimization procedure can be obtained at lower frequencies, while to ameliorate the reconstruction resolution, higher frequencies are needed. The two opposing criterion can be satisfied by using multiple-frequency data. The final reconstruc-

tion result obtained at lower frequency is used as the initial estimate for the inversion at higher frequencies. This approach is known as the frequency-hopping approach[19,55], which has been validated against experimental data in the two-dimensional case[56] and also in the three-dimensional case[12,57]. When disordered medium is involved, the frequency-hopping approach has to be revisited depending strongly on the clutter characteristics, and have to adjust the working wavelength to get a better initial estimate[47]. This persuade us to perform a global multi-frequency reconstruction approach. This procedure has been validated in two-dimension[58] and is extended to three-dimension in this thesis work. Another strategy is to consider an electromagnetic source radiating a transient field. The shape, the time duration and the central frequency of this source can be properly designed according to the application at hand. A short time pulse in the time domain can be transformed into a wide band frequency spectrum owing to the Parseval theorem and the inverse scattering problem is then formulated in the frequency domain as long as the Nyquist sampling theorem can be met. The inversion algorithm is of the same principle as the multiple-frequency approach, except that the incident field is shaped by a time pulse with given spectrum[59].

This thesis work will be carried out according to the research significance and purposes discussed above. It will be divided into four parts:

- In the first part, we will present some basic principles for forward and inverse scattering problems. The forward scattering problem is served to generate synthetic scattered fields in presence of scatterers with arbitrary shapes. We choose one based on the integral equation method, the Coupled Dipole Method (CDM) for solving the forward scattering problem. In order to reconstruct three-dimensional targets (shape, constitutive material), with only known measured scattered fields and incident excitations, we propose to use one of the iterative non-linear algorithm, Hybrid Method (HM). The forward and the inverse scattering problem will be discussed both in the time-harmonic regime and in the transient regime. The transient scattering problem will also be formulated in the frequency domain, through the Fourier transform.
- In the second part, we will present one of the time reversal technique, the DORT method, for detecting and focalizing three-dimensional targets using synthetic data generated by CDM. The principle of the DORT method will be illustrated with one single scatterer in the homogeneous background space configuration and in the half-space configuration. The behavior of eigenvalues and eigenvectors of the time reversal operator will be analyzed for illuminations polarized along one single direction or three vectorial directions. The DORT method will be combined with the non-linear inversion algorithm for restricting the investigating domain to a small region and thus improving the reconstruction resolution with the clutter of different characteristics. We will show that in presence of multiple scattering effects, it is mandatory to use a nonlinear inversion procedure, otherwise the reconstruction quality would be greatly deteriorated.
- In the third part, we will firstly explain how to realize a full-polarization tomographic diffractive microscopy. The aim is to retrieve the vectorial scattered field for illuminations with any polarization state. The reconstruction result will be compared to that obtained by scalar data, with only one projection. We will show that the reconstruction resolution can be ultimately improved with these full-polarized data. In the following chapter, we will apply the DORT focusing method in the framework of the full-polarization TDM in order to realize selective characterization, especially for far-separated samples. The time computation would be drastically reduced owing to the focalization ability of DORT.
- In the last part, we will briefly present the time reversal focusing procedure in the time domain using synthetic data. The transient inversion algorithm will be compared with the frequency-hopping approach in existence. Applications to experimental data are reported. Several different three-dimensional targets will be reconstructed in the frequency domain, by the multiple-frequency method and the frequency-hopping approach. Finally, a transient inversion algorithm will also be applied to reconstruct them, since the Nyquist theorem can be satisfied, with a limit number of sampling frequencies.

# Part I

# Forward and inverse electromagnetic scattering problem

# Introduction of PART I

Forward and inverse electromagnetic scattering problem

This part will present two basic research problems in electromagnetic domain: the forward problem and the inverse problem. These two problems will be discussed in the time-harmonic regime and in the time domain. As for in the time domain, the forward and the inverse problem will be formulated in the frequency domain due to the Parseval Plancherel's theorem, so that a large number of time-harmonic problems should be solved.
In the first chapter, we will choose one of the numerical calculation methods for solving the forward scattering problem: the Coupled Dipole Method (CDM). Beginning from the integral equations, the dyadic Green function will be deduced in homogeneous space configuration and in half-space configuration.
In the second chapter, we will discuss different iterative inversion methods for characterizing scatterers in three-dimension. One linearized method (Conjugate Gradient Method) and one non-linearized method (Contrast Source Inversion) will be presented. Then we will choose a hybrid method that combining the advantages of these two methods as the inversion algorithm that we use in this thesis work.

Chapter 1

# Forward scattering problem: Electromagnetic scattering by an arbitrary three-dimensional scatterers

## Contents



## 1.1 Introduction

The forward scattering problem concerns with modeling the interaction of electromagnetic fields with an arbitrary, inhomogeneous, dispersive objects. It is an important research problem in many domains such as optical forces[60], near field optics[61] and rough surface scattering problems[62]. The forward solver can also be served for the inverse scattering procedure that we choose. This problem may be formulated either in the time domain or in the time-harmonic regime. The forward scattering problem is generally solved numerically. An analytic solution exists only for cylindrical

scatterers with a circular or an elliptical cross section[63], for homogeneous spheres or for ellipsoids. Otherwise, we have to solve it numerically for scatterers of any given shape.

In the time-harmonic regime, several numerical techniques for solving the forward scattering problem were reported in Ref. 64, including the Finite Element Method (FEM), the Multiple Multipole Method (MMP), the Method Of Moments (MOM) and the Coupled Dipole Method (CDM)[65,66], also called discrete dipole approximation[67]. Both of MOM and CDM are based on the volume-surface integral representation of electromagnetic fields and their equivalence is provided in Ref. 68. The CDM is widely applied in many domains, *i.e.*, for computing optical forces[60], study of radiation dynamics[69], near field light scattering[70].

In the time domain, for solving the forward scattering problem directly in the time domain, the most popular numerical method is the Finite Difference Time Domain Method (FDTD)[71,72]. The FDTD method is based on the time iterative process, avoiding to solve large linear equations. Meanwhile it can be applied to particles with flexible shapes and electric properties. While the main drawback is that the entire computational time window must be finely discretized, leading to a large memory requirement. Moreover, in the FDTD, the boundary conditions at the edges of the computational window must be carefully handled.

To tackle the transient solution of the forward problem, another method consists in solving it via a passage into the frequency domain, through a temporal Laplace or Fourier transform. Then we resolve several time-harmonic problems for a collection of frequencies, to study the time evolution of these electromagnetic quantities. During the time-harmonic procedure, we propose to use the CDM[65,66]. The CDM has the advantage of restricting the computational domain to the support of scatterers and the computation precision is determined mainly by the mesh size over which the integral equation is discretized. Meanwhile, the boundary condition is inherently satisfied through an appropriate dyadic Green's function, and it is more easy to take into account the dispersion of the background media as well as the target under test than FDTD approach. However, a potential hurdle is the storage of the Green's function for a large number of frequencies, when the scatterers are finely discretized.

In conclusion, according to advantages and drawbacks of these different methods, in this thesis work, we propose to use the CDM, both in the time-harmonic regime and in the time domain, which permits to solve the forward scattering problem for scatterers present in dispersive medium.

## 1.2 Geometry of the problem

The general geometry of the scattering problem that we propose to study is shown in Fig. 1.1. A three-dimensional scatterer of arbitrary shape is assumed to be non-magnetic ($\mu = \mu_0$) and contained in the scattering domain $W$. The bounded domain $W$ is assumed to be linear, isotropic and non-magnetic with the permittivity $\epsilon(\boldsymbol{r}) = \varepsilon(\boldsymbol{r})\varepsilon_0$ and permeability $\mu = \mu_0$ ($\varepsilon_0$ and $\mu_0$ being the permittivity and permeability of vacuum, respectively), $\varepsilon(\boldsymbol{r})$ is the relative permittivity at each position $\boldsymbol{r}$. The incident excitation sources are either generated by the antennas, considered as electric point dipoles, or consist of several plane waves. The scattered fields are evaluated at receiver points regularly distributed on the measurement surface $\Gamma$. Depending on the distance between the scatterers and the measurement surface, both the near-field and the far field components can be considered in our work.

A right-handed Cartesian coordinate frame $(O, \boldsymbol{e}_x, \boldsymbol{e}_y, \boldsymbol{e}_z)$ is defined. The position vector $\boldsymbol{r}$ is defined as:

$$\boldsymbol{r} = x\boldsymbol{e}_x + y\boldsymbol{e}_y + z\boldsymbol{e}_z. \tag{1.1}$$

The forward scattering problem consists in calculating the scattered field measured at receiver points, and the calculation of the total field inside the scattering domain, assuming that the incident excitation and the optical and geometrical properties of the scatterers are known.

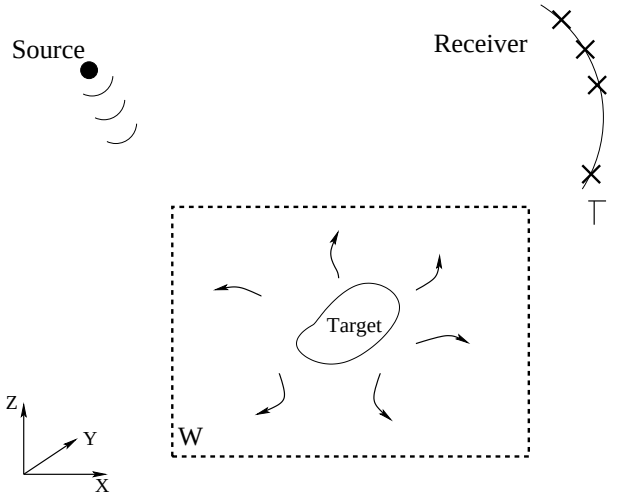


**Figure 1.1 :** *Geometry of the scattering problem. The scatterers are confined in the scattering domain $W$. $\Gamma$: measurement surface.*

## 1.3 Basic electromagnetic equation in time regime

The property of waves and fields in electromagnetic domain was formalized into four equations, and published by James Clerk Maxwell (1831-1879) in 1873[73,74]. Since then, the electromagnetic behavior had been governed fundamentally by the distribution of the charge and current that generate the electromagnetic field. In three-dimensional vector space, at the position $\boldsymbol{r}$, the Maxwell equations are

$$\nabla \times \mathscr{H}(\boldsymbol{r},t) = \frac{\partial \mathscr{D}(\boldsymbol{r},t)}{\partial t} + \mathscr{J}(\boldsymbol{r},t), \tag{1.2}$$

$$\nabla \times \mathscr{E}(\boldsymbol{r},t) = -\frac{\partial \mathscr{B}(\boldsymbol{r},t)}{\partial t}, \tag{1.3}$$

$$\nabla \cdot \mathscr{D}(\boldsymbol{r},t) = \boldsymbol{\rho}(\boldsymbol{r},t), \tag{1.4}$$

$$\nabla \cdot \mathscr{B}(\boldsymbol{r},t) = 0. \tag{1.5}$$

Where
$\mathscr{E}(\boldsymbol{r},t)$ is the electric field in V/m,
$\mathscr{B}(\boldsymbol{r},t)$ is the magnetic flux in T,
$\mathscr{H}(\boldsymbol{r},t)$ is the magnetic field in A/m,
$\mathscr{D}(\boldsymbol{r},t)$ is the electric displacement field in C/m$^2$,
$\mathscr{J}(\boldsymbol{r},t)$ is the electric current density in A/m$^2$ and
$\boldsymbol{\rho}(\boldsymbol{r},t)$ is the electric charge density in C/m$^3$.

In a linear non-dispersive and non-magnetic medium, the field intensities are related to the flux intensities by the following constitutive relations

$$\mathscr{D}(\boldsymbol{r},t) = \varepsilon(\boldsymbol{r})\varepsilon_0 \mathscr{E}(\boldsymbol{r},t), \tag{1.6}$$

$$\mathscr{B}(\boldsymbol{r},t) = \mu_0 \mathscr{H}(\boldsymbol{r},t). \tag{1.7}$$

Where $\varepsilon(r)\varepsilon_0$ is the permittivity of the medium in F/m, in which $\mu_0 = 4\pi \times 10^{-7}$ H/m, and $\varepsilon_0 = 1/(\mu_0 c^2)$ are respectively the permittivity and the permeability in the vacuum. The medium can be homogeneous with $\varepsilon(\boldsymbol{r})$ being constants or inhomogeneous with $\varepsilon(\boldsymbol{r})$ depending on the

position within the medium. In the case of non-linear or dispersive medium, this constitutive relation is not suitable.

## 1.4 Forward electromagnetic scattering problem in the time-harmonic regime

This section presents the Maxwell equations and the derivation of dyadic Green's function in the time-harmonic regime. In order to solve the forward scattering problem, we propose to choose one of the numerical integral methods, the CDM.

### 1.4.1 Harmonic Maxwell equations

For electromagnetic waves at a pulsation angular frequency $\omega$, the fields $\mathscr{U}(\boldsymbol{r},t)$ are time-harmonic and with sinusoidal time dependence, written as

$$\mathscr{U}(\boldsymbol{r},t) = \mathrm{Re}[\boldsymbol{U}(\boldsymbol{r})\exp(-i\omega t)]. \tag{1.8}$$

Where $\boldsymbol{U}(\boldsymbol{r})$ is the complex amplitude associated to $\mathscr{U}(\boldsymbol{r},t)$. The time-dependence is assumed everywhere in this manuscript to be $\exp(-i\omega t)$. The harmonic Maxwell equations read as

$$\nabla \times \boldsymbol{H}(\boldsymbol{r}) = -i\omega \boldsymbol{D}(\boldsymbol{r}) + \boldsymbol{J}(\boldsymbol{r}), \tag{1.9}$$
$$\nabla \times \boldsymbol{E}(\boldsymbol{r}) = i\omega \boldsymbol{B}(\boldsymbol{r}), \tag{1.10}$$
$$\nabla \cdot \boldsymbol{D}(\boldsymbol{r}) = \boldsymbol{\rho}(\boldsymbol{r}), \tag{1.11}$$
$$\nabla \cdot \boldsymbol{B}(\boldsymbol{r}) = 0. \tag{1.12}$$

The electric displacement field $\boldsymbol{D}(\boldsymbol{r})$ can be described by a free-space part and a part of induced electric polarization in the material, such that

$$\boldsymbol{D}(\boldsymbol{r}) = \varepsilon_0 \boldsymbol{E}(\boldsymbol{r}) + \boldsymbol{P}(\boldsymbol{r}), \tag{1.13}$$

where $\boldsymbol{P}$ is the electric linear polarization vector, represented as $\boldsymbol{P}(\boldsymbol{r}) = \varepsilon_0 \left[\varepsilon(\boldsymbol{r}) - 1\right] \boldsymbol{E}(\boldsymbol{r})$.

### 1.4.2 Integral equations

The electric field is evaluated outside the support of the current $\boldsymbol{J}(\boldsymbol{r}')$ and the charges $\boldsymbol{\rho}(\boldsymbol{r}')$. Combining Eqs. (1.9) and (1.10), we arrive at the following equation

$$\boldsymbol{\nabla} \times \boldsymbol{\nabla} \times \boldsymbol{E}(\boldsymbol{r}) - \varepsilon(\boldsymbol{r}) k_0^2 \boldsymbol{E}(\boldsymbol{r}) = i\omega\mu_0 \boldsymbol{J}(\boldsymbol{r}')\delta(\boldsymbol{r},\boldsymbol{r}'), \tag{1.14}$$

where $k_0^2 = \omega^2 \mu_0 \varepsilon_0$, $k_0$ being the wave number in vacuum. Thus we can transform Eq. (1.14) as

$$\boldsymbol{\nabla} \times \boldsymbol{\nabla} \times \boldsymbol{E}(\boldsymbol{r}) - k_0^2 \boldsymbol{E}(\boldsymbol{r}) = i\omega\mu_0 \boldsymbol{J}(\boldsymbol{r})\delta(\boldsymbol{r},\boldsymbol{r}') + k_0^2 \left[\varepsilon(\boldsymbol{r}) - 1\right] \boldsymbol{E}(\boldsymbol{r}). \tag{1.15}$$

A standard solution technique to solve Eq. (1.15) is to find the Green's function, which will be precised in the next section, the solution to the corresponding differential equation with a Dirac-delta-inhomogeneity,

$$\boldsymbol{\nabla} \times \boldsymbol{\nabla} \times \boldsymbol{G}(\boldsymbol{r},\boldsymbol{r}') - k_0^2 \boldsymbol{G}(\boldsymbol{r},\boldsymbol{r}') = \boldsymbol{I}\delta(\boldsymbol{r}-\boldsymbol{r}'), \tag{1.16}$$

where $\boldsymbol{I}$ is a unit diagonal matrix.

The incident field $\boldsymbol{E}^{\mathrm{inc}}(\boldsymbol{r})$ is the field measured without the scatterers, with $\varepsilon(\boldsymbol{r}) = 1$ elsewhere. Eq. (1.15) is written as

$$\boldsymbol{\nabla} \times \boldsymbol{\nabla} \times \boldsymbol{E}^{\mathrm{inc}}(\boldsymbol{r}) - k_0^2 \boldsymbol{E}^{\mathrm{inc}}(\boldsymbol{r}) = i\omega\mu_0 \boldsymbol{J}(\boldsymbol{r}')\delta(\boldsymbol{r},\boldsymbol{r}'). \tag{1.17}$$

With the dyadic Green's function $\boldsymbol{G}(\boldsymbol{r},\boldsymbol{r}')$ that enables one to determine the electric field $\boldsymbol{E}^{\text{inc}}(\boldsymbol{r})$ from a given source $\boldsymbol{J}(\boldsymbol{r}')$, the incident field in vacuum is evaluated as

$$\boldsymbol{E}^{\text{inc}}(\boldsymbol{r}) = i\omega\mu_0 \int \boldsymbol{G}(\boldsymbol{r},\boldsymbol{r}')\boldsymbol{J}(\boldsymbol{r}')\mathrm{d}\boldsymbol{r}', \tag{1.18}$$

where the integration extends over the volume occupied by $\boldsymbol{J}(\boldsymbol{r}')$.

The total field $\boldsymbol{E}(\boldsymbol{r})$ in presence of scatterers is the solution of Eq. (1.15),

$$\boldsymbol{E}(\boldsymbol{r}) = \boldsymbol{E}^{\text{inc}}(\boldsymbol{r}) + k_0^2 \int \boldsymbol{G}(\boldsymbol{r},\boldsymbol{r}')\chi(\boldsymbol{r}')\boldsymbol{E}(\boldsymbol{r}')\mathrm{d}\boldsymbol{r}', \tag{1.19}$$

where the integration is calculated in the support of the scatterers. $\chi(\boldsymbol{r}')$ denotes the contrast at the position $\boldsymbol{r}'$ as

$$\chi(\boldsymbol{r}') = \varepsilon(\boldsymbol{r}') - 1. \tag{1.20}$$

Eq. (1.19) is noted as the coupling near-field equation, which permits to calculate the total field at every point $\boldsymbol{r}$. The scattered field is defined as $\boldsymbol{E}^{\text{sca}}(\boldsymbol{r}) = \boldsymbol{E}(\boldsymbol{r}) - \boldsymbol{E}^{\text{inc}}(\boldsymbol{r})$, so we have

$$\boldsymbol{E}^{\text{sca}}(\boldsymbol{r}) = k_0^2 \int \boldsymbol{G}(\boldsymbol{r},\boldsymbol{r}')\chi(\boldsymbol{r}')\boldsymbol{E}(\boldsymbol{r}')\mathrm{d}\boldsymbol{r}'. \tag{1.21}$$

Eq. (1.21) is named as the observation field equation. The two equations above Eqs. (1.19) and (1.21) constitute the electromagnetic model of the forward scattering problem in the time-harmonic regime.

## 1.4.3 The dyadic Green's equation

For solving the integral equations above Eqs. (1.19) and (1.21), we have to find the dyadic Green's function $\boldsymbol{G}(\boldsymbol{r},\boldsymbol{r}')$ [75], that characterizes the response due to a point source $\delta(\boldsymbol{r}-\boldsymbol{r}')$, as in Eq. (1.16). Two different configurations are considered in this thesis work, homogeneous background space configuration and half-space configuration.

### 1.4.3.1 Homogeneous space configuration

Firstly, we try to find the solution of Green's function in the homogeneous background space configuration, meaning that the scatterers, the sources and the receivers are located in the same medium, for example in the vacuum. The scalar Green's function $g(\boldsymbol{r},\boldsymbol{r}')$ is the response to point sources $\delta(\boldsymbol{r}-\boldsymbol{r}')$, and we can determine it in the spherical coordinate system,

$$g(\boldsymbol{r},\boldsymbol{r}') = \frac{e^{ik|\boldsymbol{r}-\boldsymbol{r}'|}}{4\pi|\boldsymbol{r}-\boldsymbol{r}'|}. \tag{1.22}$$

The dyadic Green's function is written as

$$\boldsymbol{G}(\boldsymbol{r},\boldsymbol{r}') = \frac{e^{ik_0R}}{4\pi k_0^2}\left[(3\widehat{\boldsymbol{R}}\otimes\widehat{\boldsymbol{R}}-\boldsymbol{I})\left(\frac{1}{R^3}-\frac{ik_0}{R^2}\right)+(\boldsymbol{I}-\widehat{\boldsymbol{R}}\otimes\widehat{\boldsymbol{R}})\frac{k_0^2}{R}\right]. \tag{1.23}$$

Where $\boldsymbol{R} = \boldsymbol{r}-\boldsymbol{r}'$, $R = |\boldsymbol{R}|$ and $\widehat{\boldsymbol{R}} = \boldsymbol{R}/R$. The deviation of Green's function is described in detail in Appendix. A.

### 1.4.3.2 Half-space configuration

We want to present the principle to compute the dyadic Green's function brought by a more complicated configuration, namely as the half-space configuration, which can be widely applied for detecting buried objects, where the objects and the transceiver array are located at different

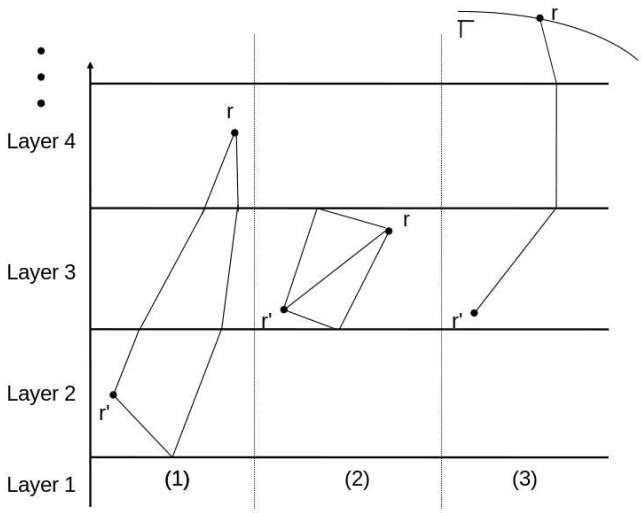


**Figure 1.2 :** *Different configurations for the dyadic Green's function of a multilayer system.*

media. Also, in the optical diffractive tomography application, the objects for imaging are generally deposited on a substrate. In this case, the dyadic Green's function response in presence of an interface has to be considered into the coupling equation and the observation equation. As shown in Fig. 1.2, the dyadic Green's function can be described in three different configurations, depending on the distribution of the source point $\boldsymbol{r}'$ and the field point $\boldsymbol{r}$.

Firstly, when the source point $\boldsymbol{r}'$ and the field point $\boldsymbol{r}$ belong to two different layers, the reflection and the transmission effects at the planar interfaces of the layers will be taken into account for calculating the Green's function [Fig. 1.2 (1)].

Secondly, for $\boldsymbol{r}$ and $\boldsymbol{r}'$ lie in the same layer, the Green function can be divided into two parts as

$$\boldsymbol{G}(\boldsymbol{r},\boldsymbol{r}') = \boldsymbol{G}^{\text{homo}}(\boldsymbol{r},\boldsymbol{r}') + \boldsymbol{G}^{\text{inter}}(\boldsymbol{r},\boldsymbol{r}'). \tag{1.24}$$

The first part $\boldsymbol{G}^{\text{homo}}(\boldsymbol{r},\boldsymbol{r}')$ corresponding to the Green's function in the homogeneous space that has been given precisely in Eq. (1.23). The second part is the Green's function by taking into account the multiple reflection effects [Fig. 1.2 (2)].

In both configurations the Green's function is computed by using an angular spectrum representation thanks to the Weyl development [76].

Notice that for a source inside the multilayer and for a scattered field computed in the far field zone, for example along a line $\Gamma$, we can calculate the dyadic Green's function through the theorem of the stationary phase [76].

### 1.4.4 Forward scattering problem in harmonic regime: Coupled dipole method

In this section, we study the electromagnetic forward scattering problem, that consists in building a scattering model and calculating the scattered field measured by the receivers, assuming

that the incident field and the electromagnetic properties of scattering domain are known. As we discussed in the introduction part of this chapter, several numerical methods are used in electromagnetic scattering theory. Considering that we work in the harmonic regime, and the scatterers are isotropic and with arbitrary shapes, we propose here to use methods based on the volume integral representation of fields, rather than the differential methods.

### 1.4.4.1 Coupled dipole method

In Ref. 68, the strong and weak forms of two volume integral methods MOM and CDM are derived for bi-anisotropic scatterers. These two techniques are shown to be completely equivalent to each other. The MOM manipulates the macroscopic field inside the scattering domain, while the CDM handles with the local one. We give the derivation procedure used in the CDM for the forward scattering problem.

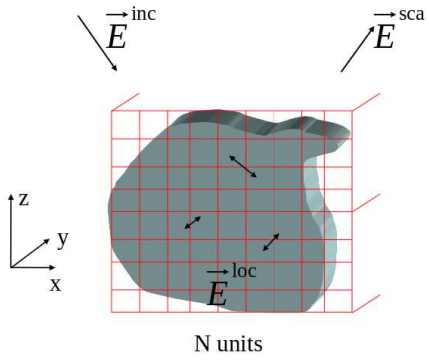


**Figure 1.3 :** *The CDM description, a three-dimensional scatterer with an arbitrary shape is discretized into $N$ cubical units, for calculating the local field inside the scatterer $\boldsymbol{E}^{\mathrm{loc}}$ and the scattered field received by the receivers $\boldsymbol{E}^{\mathrm{sca}}$.*

The CDM was introduced by Purcell and Pennypacker in 1973 to study the scattering of light by non-spherical dielectric grains in free space[77]. The incident field induces a polarization inside the scattering domain. We recall the coupling integral equation,

$$\boldsymbol{E}(\boldsymbol{r}) \ \ (\boldsymbol{r} \in W) = \boldsymbol{E}^{\mathrm{inc}}(\boldsymbol{r}) + \int_W \boldsymbol{G}(\boldsymbol{r}, \boldsymbol{r}')\chi(\boldsymbol{r}')\boldsymbol{E}(\boldsymbol{r}')\mathrm{d}\boldsymbol{r}'. \tag{1.25}$$

Notice that Eq. (1.25) differs from Eq. (1.19) by the factor $k_0^2$. This factor $k_0^2$ is included herein in $\boldsymbol{G}$. For solving numerically Eq. (1.25), the scattering domain under study is modeled by an array of $N$ polarized subunits arranged on a cubic lattice of size $d$, as shown in Fig. 1.3, hence Eq. (1.25) becomes

$$\boldsymbol{E}(\boldsymbol{r}) \ \ (\boldsymbol{r} \in W) = \boldsymbol{E}^{\mathrm{inc}}(\boldsymbol{r}) + \sum_{j=1}^{N} \int_{W_j} \boldsymbol{G}(\boldsymbol{r}, \boldsymbol{r}')\chi(\boldsymbol{r}')\boldsymbol{E}(\boldsymbol{r}')\mathrm{d}\boldsymbol{r}'. \tag{1.26}$$

In order to solve Eq. (1.26), we need to perform some approximations. Firstly, if the volume units are sufficiently small compared to the wavelength of illumination and the variation of the field inside the object is not considerable, we can assume that the field $\boldsymbol{E}$ is uniform over one cell in Eq. (1.26). Here, Eq. (1.26) can be written as

$$\boldsymbol{E}(\boldsymbol{r}_i) = \boldsymbol{E}^{\mathrm{inc}}(\boldsymbol{r}_i) + \sum_{j=1}^{N} \Big( \int_{W_j} \boldsymbol{G}(\boldsymbol{r}_i, \boldsymbol{r}')\mathrm{d}\boldsymbol{r}' \Big) \chi(\boldsymbol{r}_j)\boldsymbol{E}(\boldsymbol{r}_j). \tag{1.27}$$

To compute the volume integration of the Green's function numerically, Eq. (1.27) can be written as

$$\boldsymbol{E}(\boldsymbol{r}_i) = \boldsymbol{E}^{\text{inc}}(\boldsymbol{r}_i) + \sum_{j=1, j\neq i}^{N} \Big( \int_{W_j} \boldsymbol{G}(\boldsymbol{r}_i, \boldsymbol{r}') \mathrm{d}\boldsymbol{r}' \Big) \chi(\boldsymbol{r}_j) \boldsymbol{E}(\boldsymbol{r}_j) + \Big( \int_{W_i} \boldsymbol{G}(\boldsymbol{r}_i, \boldsymbol{r}') \mathrm{d}\boldsymbol{r}' \Big) \chi(\boldsymbol{r}_i) \boldsymbol{E}(\boldsymbol{r}_i). \quad (1.28)$$

Another approximation is made in the original form of the CDM, the Green's function $\boldsymbol{G}(\boldsymbol{r}_i, \boldsymbol{r}')$ is taken to be constant over any cell when $i \neq j$. The integrated tensor is defined as $\int_{W_j} \boldsymbol{G}(\boldsymbol{r}_i, \boldsymbol{r}') \mathrm{d}\boldsymbol{r}' = \boldsymbol{G}(\boldsymbol{r}_i, \boldsymbol{r}_j) W_j$, where $W_j = d^3$ is the volume of each cubic lattice. Here, we isolated the diagonal term ($i = j$) as it needs particular attention. For $i = j$, the dyadic Green's function presents a singularity as $\boldsymbol{G}(\boldsymbol{r}_i, \boldsymbol{r}')$ goes to infinity, $|\boldsymbol{r}_i - \boldsymbol{r}'| \to 0$. If $W_i$ shrinks down around the point $\boldsymbol{r}_i$, *i.e.*, $W_i$ approaches zero, we have

$$\lim_{W_i \to 0} \int_{W_i} \boldsymbol{G}(\boldsymbol{r}_i, \boldsymbol{r}') \mathrm{d}\boldsymbol{r}' = \boldsymbol{L}, \quad (1.29)$$

where $\boldsymbol{L}$ depends on the shape of $W_i$. In the case of a spherical or cubic shape we get [78]

$$\boldsymbol{L} = -\frac{\boldsymbol{I}}{3}. \quad (1.30)$$

Eq. (1.28) can be expressed as

$$\boldsymbol{E}(\boldsymbol{r}_i) = \boldsymbol{E}^{\text{inc}}(\boldsymbol{r}_i) + \sum_{j=1, j\neq i}^{N} \boldsymbol{G}(\boldsymbol{r}_i, \boldsymbol{r}_j) \chi(\boldsymbol{r}_j) \boldsymbol{E}(\boldsymbol{r}_j) W_j - \frac{\chi(\boldsymbol{r}_i)}{3} \boldsymbol{E}(\boldsymbol{r}_i). \quad (1.31)$$

When the number of discretization cells is large, the linear system is solved iteratively [79]. We shall use the well known conjugate gradient (CG) method which yields to the exact result beginning with an initial estimate, described as Appendix B.

Similarly, the scattered field outside the scattering domain is represented as

$$\boldsymbol{E}^{\text{sca}}(\boldsymbol{r}) = \sum_{j=1}^{N} \boldsymbol{G}(\boldsymbol{r}, \boldsymbol{r}_j) \chi(\boldsymbol{r}_j) \boldsymbol{E}(\boldsymbol{r}_j) W_j. \quad (1.32)$$

Now, if we factorize the terms corresponding to the index $i$, we can get the local field at the center of each cube expressed with the following self-consistence equation [80]

$$\boldsymbol{E}^{\text{loc}}(\boldsymbol{r}_i) = \boldsymbol{E}^{\text{inc}}(\boldsymbol{r}_i) + \sum_{j=1, j\neq i}^{N} \boldsymbol{G}(\boldsymbol{r}_i, \boldsymbol{r}_j) \alpha^0(\boldsymbol{r}_j) \boldsymbol{E}^{\text{loc}}(\boldsymbol{r}_j), \quad (1.33)$$

with

$$\alpha^0(\boldsymbol{r}_j) = 3d^3 \frac{\varepsilon(\boldsymbol{r}_j) - 1}{\varepsilon(\boldsymbol{r}_j) + 2}. \quad (1.34)$$

Eq. (1.34) represents the polarizability distribution of the subunit $j$, according to the Clausius-Mossotti expression [68], where $\varepsilon(\boldsymbol{r}_j)$ is the relative permittivity of the scattering domain at the position $\boldsymbol{r}_j$. If $d$ is small enough, the local field $\boldsymbol{E}^{\text{loc}}(\boldsymbol{r}_i)$ can be considered constant over the lattice. $\boldsymbol{E}^{\text{loc}}(\boldsymbol{r}_i) = [(\varepsilon(\boldsymbol{r}_i) + 2)/3]\, \boldsymbol{E}(\boldsymbol{r}_i)$ is the local field expressed in terms of the macroscopic field, that is equivalent to the method of moments (MOM). Equations (1.33) and (1.34) are the historical forms of the CDM which has been introduced by Purcell and Pennypacker [77].

The scattered field $\boldsymbol{E}^{\text{sca}}(\boldsymbol{r})$ at an arbitrary position $\boldsymbol{r}$ can be written as

$$\boldsymbol{E}^{\text{sca}}(\boldsymbol{r}) = \sum_{j=1}^{N} \boldsymbol{G}(\boldsymbol{r}, \boldsymbol{r}_j) \alpha^0(\boldsymbol{r}_j) \boldsymbol{E}^{\text{loc}}(\boldsymbol{r}_j). \quad (1.35)$$

In our thesis work, we use the macroscopic field for calculating the scattered field in the inversion procedure and the local field to compute the forward problem.

#### 1.4.4.2 The radiative reaction term

Notice that with the expression given in Eq. (1.30), as we do not take into account the finite size of the subunit, the energy is not conserved, *i.e.*, the optical theorem is not respected. The integration on the mesh size can be performed analytically and rigorously if the shape of the subunit is spherical[68], with the radius $a$,

$$\int_{W_i(\text{sphere})} \boldsymbol{G}(\boldsymbol{r}_i, \boldsymbol{r}')\mathrm{d}\boldsymbol{r}' = -\frac{\boldsymbol{I}}{3} + \boldsymbol{I}\frac{2}{3}\left[(1 - ik_0a)\exp(ik_0a) - 1\right] \tag{1.36}$$

$$\approx -\frac{\boldsymbol{I}}{3} + \boldsymbol{I}\left[\frac{2}{9}i(k_0a)^3\right]. \tag{1.37}$$

The approximation form of Eq. (1.37) is obtained by performing a Taylor expansion of $\exp(ik_0a)$.

If the shape of integration is a cube, the result is the same assuming that the volumes of the sphere and the cube are equivalent[68]. Hence,

$$\int_{W_i(\text{cube})} \boldsymbol{G}(\boldsymbol{r}_i, \boldsymbol{r}')\mathrm{d}\boldsymbol{r}' \approx -\frac{\boldsymbol{I}}{3} + \boldsymbol{I}\left[\frac{1}{6\pi}i(k_0d)^3\right], \tag{1.38}$$

where $a = d(3/4\pi)^{1/3}$ is the radius of a sphere having the same volume as the cube of side $d$.

The expression for Eq. (1.31) is now:

$$\boldsymbol{E}(\boldsymbol{r}_i) = \boldsymbol{E}^{\text{inc}}(\boldsymbol{r}_i) + \sum_{j=1, j\neq i}^{N} \boldsymbol{G}(\boldsymbol{r}_i, \boldsymbol{r}_j)\chi(\boldsymbol{r}_j)\boldsymbol{E}(\boldsymbol{r}_j)W_j + \left[-\frac{1}{3} + \frac{1}{6\pi}ik_0^3d^3\right]\chi(\boldsymbol{r}_i)\boldsymbol{E}(\boldsymbol{r}_i). \tag{1.39}$$

If we want to work with the local field, we have

$$\boldsymbol{E}^{\text{loc}}(\boldsymbol{r}_i) = \left[\frac{\varepsilon(\boldsymbol{r}_i) + 2}{3} - \frac{1}{6\pi}ik_0^3\chi(\boldsymbol{r}_i)W_i\right]\boldsymbol{E}(\boldsymbol{r}_i), \tag{1.40}$$

and the polarizability is now

$$\alpha(\boldsymbol{r}_j) = \alpha^0(\boldsymbol{r}_j)/\left[1 - ik_0^3\alpha^0(\boldsymbol{r}_j)/6\pi\right]. \tag{1.41}$$

Notice that the term added to the finite size of the subunit is in the magnitude of $k_0^3d^3$, and as the spacing of lattice discretization $d$ is smaller than the wavelength of illumination, $k_0^3d^3 \ll 1$. Hence, the addition of the radiative reaction term does not change much the value of the polarizability. However, in some different topics, such as optical forces domain[60,69,81], it is mandatory to take into account the radiative reaction term.

#### 1.4.4.3 Condensed form of the near field and far field equations

For the sake of simplicity, for each illumination $l$, the near field and the far field can be rewritten in a more condensed form as

$$\boldsymbol{E}_l^{\text{loc}} = \boldsymbol{E}_l^{\text{inc}} + \boldsymbol{A}\boldsymbol{p}_l, \qquad \boldsymbol{E}_l = \boldsymbol{E}_l^{\text{inc}} + \overline{\overline{\boldsymbol{A}}}\chi\boldsymbol{E}_l, \tag{1.42}$$

$$\underbrace{\boldsymbol{E}_l^{\text{sca}} = \overline{\overline{\boldsymbol{B}}}\boldsymbol{p}_l}_{\text{local field}}, \qquad \underbrace{\boldsymbol{E}_l^{\text{sca}} = \overline{\overline{\boldsymbol{B}}}\chi\boldsymbol{E}_l}_{\text{total field}}, \tag{1.43}$$

where $\boldsymbol{A}$ is a square matrix of size $3N \times 3N$ and contains all the tensors $\boldsymbol{G}(\boldsymbol{r}_i, \boldsymbol{r}_j)$ in Eq. (1.33), the vectors $\boldsymbol{p}_l = \alpha\boldsymbol{E}_l^{\text{loc}}$ represents the induced dipoles inside the scattering domain for the illumination $l$. The $3M \times 3N$ matrix $\overline{\overline{\boldsymbol{B}}}$ contains all the tensors $\boldsymbol{G}(\boldsymbol{r}_m, \boldsymbol{r}_j)$ in Eq. (1.35), while $\boldsymbol{r}_m$, $m = 1, \cdots, M$ is an observation point. The matrix $\overline{\overline{\boldsymbol{A}}}$ is different from the matrix $\boldsymbol{A}$, in which $\boldsymbol{A}$ has one as the

main diagonal term. Note that the matrices $\boldsymbol{A}$, $\overline{\overline{\boldsymbol{A}}}$ and $\overline{\overline{\boldsymbol{B}}}$ do not depend on the incident field nor on the object under study.

In Ref. 77, the original form of the CDM is given as Eq. (1.33), the local field scattered by an object of rather arbitrary shape is computed assuming that the polarizability is isotropic. In the case of anisotropic material, *i.e.*, a birefringent material, with a tensor polarizability, we would require only a trivial modification of the calculation in Eq. (1.33). In this manuscript, for the forward scattering problem, we use also the form of the local field, Eq. (1.33). While in the inversion procedure, we propose to use the macroscopic field for calculating the scattered field. The equivalence relationship is manifested by the Clausius-Mossotti expression. One reason is that if we take the polarizability as the parameter sought, it is difficult to use the *a priori* information stating that the positivity of this parameter, as performed in Ref. 25.

#### 1.4.4.4 Numerical estimated technique in CDM

In the electromagnetic scattering problem, for characterizing the scattering behavior of the scatterer, we always use the integral equation method to solve the computational problem. In the three-dimensional configuration, especially in the case of strong scatterers , solving the coupling Eq. (1.19) will become time-consuming, which persuades us to use some approximation techniques for simplifying the computation problem. The Born approximation and the renormalized Born approximation are the most widely used methods among these approximation methods[82].

The so-called Born approximation consists to assume that if the object is weakly scattering, the amplitude of the total field $\boldsymbol{E}$ inside the scattering domain is closed to that of the incident field $\boldsymbol{E}^{\text{inc}}$. Hence, the coupling Eq. (1.25) is reduced to $\boldsymbol{E} = \boldsymbol{E}^{\text{inc}}$, the calculation time of the forward scattering problem is greatly reduced under this assumption, since we do not resolve the coupling equation.

The renormalized Born approximation amounts to assimilating the local field inside the object to the incident field: hence Eq. (1.33) is reduced to $\boldsymbol{E}^{\text{loc}} = \boldsymbol{E}^{\text{inc}}$. In this case, the relationship between the total macroscopic field and the incident field reads as:

$$\boldsymbol{E} = \frac{3}{\varepsilon + 2}\boldsymbol{E}^{\text{inc}}. \tag{1.44}$$

This approximation is thus different from the classical Born approximation.

In practice, the Born approximation can be used in case that the contrast $\chi(\boldsymbol{r}')$ between the scattering point and the embedding medium is small, typically below 0.1, and the size of the scatterers is much smaller than the wavelength of illumination, so that the polarization effects induced by the scatterer can be neglected. To determine the validity of the Born approximation, an universal criterion is proposed in Ref. 83. The Born approximation can also be used in the inverse scattering problem for imaging the scatterers, in which the single scattering regime is assumed, for example, in the imaging domain for biological microscope. While for scatterers small compared to the wavelength and with moderate dielectric constant, accounting for multiple scattering in the reconstruction procedure can improve the image significantly, this point has been illustrated in Ref. 25, and one can obtain a better resolution working in the multiple scattering regime in tomographic diffractive microscopy domain.

## 1.5 Forward scattering problem in the transient regime

In the last section, we have discussed the numerical method (CDM) used for the forward scattering problem in the time-harmonic regime. In this section, we will focus on solving the forward scattering problem in the transient regime via a passage into the frequency domain.

### 1.5.1 Statement of the problem

The geometry of the problem that we propose to solve is shown in Fig. 1.1, where the emitted source is fed by a current $\mathcal{F}(t)$, thus generating a transient incident field $\boldsymbol{E}^{\text{inc}}(\boldsymbol{r},t)$. The current $\mathcal{F}(t)$ is an electromagnetic pulse with a Gaussian envelop $\mathcal{F}(t)$ and a spectrum centered at the frequency $f_0$,

$$\mathcal{F}(t) = A\ \exp\left[-16\left(\frac{t-t_{\text{trans}}}{\tau}\right)^2\right]\ \cos(2\pi f_0 t), \tag{1.45}$$

where the time duration of the pulse $\tau$ is related to the width of the envelop of the Gaussian pulse, smaller it is in the time domain, larger is the spectrum of the incident field. $f_0$ is the central frequency of the incident pulse. The shifting time $t_{\text{trans}}$ is chosen large enough to assume that we have $\mathcal{F}(t) = 0, \forall t \leq 0$.

Eq. (1.45) may be formulated in the frequency domain, using the Laplace transform defined as:

$$F(s) = \mathscr{L}[\mathcal{F}(t)] = \int_0^{+\infty} \mathcal{F}(t)\ \exp(-st)\mathrm{d}t. \tag{1.46}$$

The inverse Laplace transform is defined along a Bromwich contour as

$$\mathcal{F}(t) = \mathscr{L}^{-1}[F(s)] = \frac{1}{2i\pi}\ \int_{\beta-i\infty}^{\beta+\infty} F(s)\ \exp(st)\mathrm{d}s, \tag{1.47}$$

$$= \frac{\exp(\beta t)}{2\pi}\ \int_{-\infty}^{\infty} F(\beta+i\omega)\ \exp(i\omega t)\mathrm{d}\omega. \tag{1.48}$$

Eq. (1.47) is the inverse Laplace transform which can be evaluated numerically with the help of the form expressed in Eq. (1.48), using Fast Fourier Transform (FFT). The parameter $s$ is a complex number, $s = \beta + i\omega$, with real numbers $\beta$ and $\omega$.

To get $\mathscr{E}^{\text{sca}}(\boldsymbol{r},t)$ the transient scattered field (or the local field inside the scattering domain), we need to compute the inverse Laplace transform of $\boldsymbol{E}^{\text{sca}}(\boldsymbol{r},s)F(s)$, where $\boldsymbol{E}^{\text{sca}}(\boldsymbol{r},s)$ is obtained through Eqs. (1.33) and (1.35) with the angular frequency $\omega$ is replaced by $s$, in the expressions of the incident field, the Green's function and the polarizability. As $\beta \geq 0$, the $e^{i\omega r/c}$ dependence of the Green's function becomes $e^{-\beta r/c}e^{i\omega r/c}$, with $t = r/c$. The complex frequency imposes an exponential decay on Green's function. The introduction of complex frequencies ($\beta > 0$) into the problem via the Laplace transform allows us to handle resonant scatterers, for instance a plasmon resonance, something that the Fourier transform approach cannot do, which is provided in Ref. 84, see Appendix. G. In this manuscript, $\beta$ is assumed to be equal to 0 because we restrict our research to dielectric scatterers, where the Laplace transform coincides to the Fourier transform.

For $\beta = 0$, to obtain the Fourier transform of $\mathcal{F}(t)$ , this signal is firstly sampled in the time domain to be calculated numerically and efficiently via FFT, where the sampling number $P$ in the frequency domain is chosen in accordance with the Nyquist-Shannon sampling theorem. It should be sufficiently large in the case of the spectrum of the incident field for the highest and lowest concerned frequencies equal to zero and well represented. However, this may lead to consider a large and redundant number $P$ of time-harmonic problems. The sampling interval in the frequency domain $\Delta f$ is fixed by the observation time span $\Delta t$ during which the fields are calculated: $\Delta f \Delta t = 1$. The discretized frequency $f_p$ is simply obtained as $f_p = f_{\min} + (p-1)\times\Delta f$, with the angular frequency $\omega_p = 2\pi f_p$ and $s_p = \beta_p + i\omega_p$ ($\beta_p = 0$).

Once the $P$ time-harmonic forward scattering problems are resolved, we can obtain $P$ scattered fields $\boldsymbol{E}^{\text{sca}}(\boldsymbol{r},\omega_p)$ associated with each frequency $f_p$. The scattered field $\boldsymbol{\mathscr{E}}^{\text{sca}}(\boldsymbol{r},t)$ it then calculated through Eq. (1.48).

Here, we give an example to illustrate the form of the incident field used in this thesis, defined as Eq. (1.45). The parameters of the incident pulse are $f_0 = 5.5$ GHz ($\lambda_0 \approx 54.5$ nm) and $\tau = 2$ ns as presented in Fig. 1.4. The shifting time $t_{\text{trans}}$ is set to be equal to 4 ns. The number of

frequencies used to describe the pulse in the frequency domain is $P = 21$, and we have verified that the incident pulse can be well reformed.

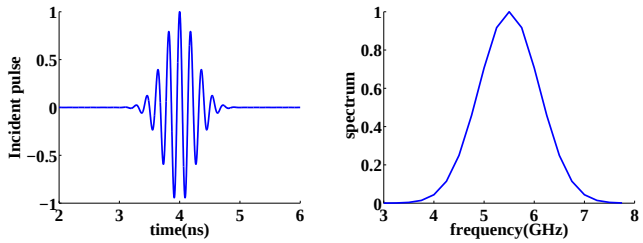


(a) (b)

**Figure 1.4 :** *Form of the incident field defined by Eq. (1.45), with $f_0 = 5.5$ GHz. (a) Normalized incident field in the time domain. (b) Normalized spectrum of the incident field.*

## 1.6 Conclusions

In this chapter, we mainly discussed about the electromagnetic scattering problem in three-dimension. The background medium is assumed to be isotropic, linear and lossless. The forward scattering problem is studied for the two different regimes: the time-harmonic regime and the time domain. The transient forward scattering problem is not directly resolved in the time domain, but transformed into the frequency domain via the Laplace transform or the Fourier transform.

The forward scattering problem concerns with the calculation of the scattered field in presence of scatterers with arbitrary shapes. Starting from basic Maxwell equations, we reported the form of dyadic Green's function corresponding to two different configurations: in homogeneous space and in presence of surface between antennas and scatterers. These two configurations are the ones used in the present thesis.

The forward scattering problem is usually time-consuming for a larger scattering domain or for a fine discretization. Under the Born approximation, the computational time can be reduced drastically. In our work, we will compare the simulation results under the Born approximation with those obtained for rigorous calculations.

In particular, for solving the forward scattering problem, there exist lots of popular numerical equation methods. We have shown the advantages and the drawbacks of these methods. And be aimed at the specific problem that we focus on, we propose to use the CDM in this thesis. The principle of this method is given in detail in this chapter.

The forward scattering problem has been studied for different configurations. Now we are interested in another research domain, the inverse scattering problem: the characterization of scatterers.

Chapter 2

# Inverse scattering problem: characterization of scatterers

## Contents



## 2.1 Introduction

The inverse scattering problem is stated as finding the position, shape and constitutive materials of objects, from their response (scattered field) to a known electromagnetic excitation. We restrict our study to iterative method. Starting from an initial estimate of permittivity distribution, one can adjust the parameters of interest by minimizing a cost function involving with the measured scattered field and the incident field. The optimization procedure can be linearized around a given estimate, or non-linearized. The literature mainly shows two approaches, depending on whether the field in the scattering domain is fixed or not. The first one is the linearized method, including the Newton-Kantorovich method[15,16], the distorted-wave Born approach[17–19] and the conjugate gradient method[82]. The total field in the investigating domain is considered fixed at each iteration step, and is the solution of the forward scattering problem for the best available estimation of the relative permittivity. The second approach is the non-linearized method, namely the modified gradient method[9,21] and the contrast source inversion method[22–24], which consist in updating simultaneously the permittivity as well as the total field inside the investigating domain. The speed of the linearized method is more advantageous, while the non-linearized method is more stable. The hybrid method combines ideas from linearized and non-linearized method. The reconstruction of several targets with different shapes and constitutive materials using experimental data was presented in Ref. 28. It was shown that the best result was obtained with the hybrid method

(HM). In Ref. 12, this method is extended to three-dimensional vectorial case. They have shown that the HM was faster than the non-linearized algorithm. In the case of noisy data or for larger objects, it is more efficient than the linearized method.

The HM works well in the time-harmonic regime when the scattered field is measured for a large number of illumination points. While the amount of sources is reduced, or for the small numerical aperture (NA), HM can not provide acceptable resolution. The quality of characterization of the scatterers is deteriorated. To circumvent this poor resolution, it is suggested to characterize scatterers using transient or multiple-frequency data[59,85]. It has been proved that when only one or a few electromagnetic sources is used, we can succeed in retrieving the unknown permittivity profile of scatterers from the measured transient field[54].

## 2.2 Different inversion scattering algorithms in the time-harmonic regime

Generally, in the time-harmonic regime, the iterative inverse techniques are mainly distinguished into two different procedures, depending on whether the total field in the investigating domain is considered as fixed (solution of the forward problem for the best available estimation of the parameter $\chi$) in each iteration step[20,86] or as an unknown that is obtained together with the parameter $\chi$ by the minimization procedure[23,28]. In this section, we will present three different inversion methods, the conjugate gradient method (CGM), the contrast source inversion method (CSI) and the hybrid method (HM), the latter one will be mainly used in our thesis work.

### 2.2.1 Description of the problem

The inverse scattering problem investigated in this thesis work is illustrated in Fig. 2.1. An unknown three-dimensional object is entirely confined in a bounded box $\Omega$, namely as the investigating domain, or the test domain. The investigating domain is generally smaller and enclosed by the scattering domain $W$ that we mentioned in Chap. 1. The test domain is illuminated successively by $l = 1, 2, \cdots, N$ electromagnetic excitation $\boldsymbol{E}_l^{\text{inc}}$. The scattered fields $\boldsymbol{f}_l^{\text{mes}}$ are measured outside the test domain $\Omega$, on a surface $\Gamma$. The issue that we are interested in is to find the relative permittivity of the unknown object using the scattered data $\boldsymbol{f}_l^{\text{mes}}$. We recall here the calculation of the total field $\boldsymbol{E}_l$ inside the investigating domain $\Omega$ and the scattered field $\boldsymbol{E}_l^{\text{sca}}$ measured on $\Gamma$,

$$\boldsymbol{E}_l(\boldsymbol{r} \in \Omega) = \boldsymbol{E}_l^{\text{inc}}(\boldsymbol{r}) + \int_{\Omega} \boldsymbol{G}(\boldsymbol{r}, \boldsymbol{r'}) \chi(\boldsymbol{r'}) \boldsymbol{E}_l(\boldsymbol{r'}) \mathrm{d}\boldsymbol{r'}, \tag{2.1}$$

$$\boldsymbol{E}_l^{\text{sca}}(\boldsymbol{r} \in \Gamma) = \int_{\Omega} \boldsymbol{G}(\boldsymbol{r}, \boldsymbol{r'}) \chi(\boldsymbol{r'}) \boldsymbol{E}_l(\boldsymbol{r'}) \mathrm{d}\boldsymbol{r'}. \tag{2.2}$$

Using an iterative approach, the basic idea of the inverse scattering problem is starting with an initial estimate $\chi_0$, we adjust the associated parameters of interest, the contrast $\chi$ and in some cases together with the total field $\boldsymbol{E}_l$, by minimizing a cost function until the calculated scattered field $\boldsymbol{E}_l^{\text{sca}}$ matches with the measured one $\boldsymbol{f}_l^{\text{mes}}$. This iterative procedure can be very different depending on the algorithm that we chooses.

For the sake of simplicity, Eqs. (2.1) and (2.2) are rewritten in a more condensed form using the notation of operators,

$$\boldsymbol{E}_l = \boldsymbol{E}_l^{\text{inc}} + \overline{\overline{\boldsymbol{A}}} \chi \boldsymbol{E}_l, \tag{2.3}$$

$$\boldsymbol{E}_l^{\text{sca}} = \overline{\overline{\boldsymbol{B}}} \chi \boldsymbol{E}_l. \tag{2.4}$$

Note that $\overline{\overline{\boldsymbol{A}}}$ and $\overline{\overline{\boldsymbol{B}}}$ do not depend on the incidences.

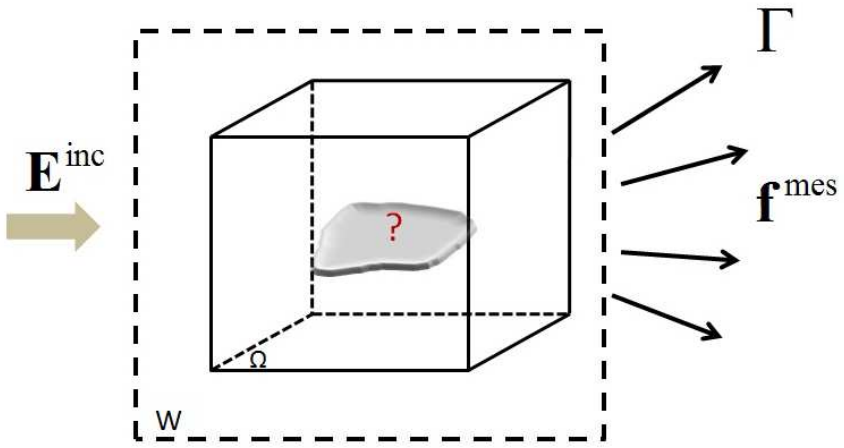


**Figure 2.1 :** *Geometry of the problem. The investigating domain used in the inversion procedure is defined as* $\Omega$*, enclosed by* $W$*.* $\Gamma$*: measurement surface.*

### 2.2.2 Conjugate gradient method (CGM)

The CGM is an iterative linearized approach, which has been presented in Ref. 57,82 for both simulated and real data. In the CGM, the forward problem is solved at each iteration step for the best available estimation of the parameter $\chi$, meaning that the total field inside $\Omega$ is considered at each iteration step as a fixed solution of Eq. (2.1), and sole the contrast permittivity $\chi$ is determined by minimizing an adequate cost function. The sequence $\chi_n$ at iteration $n$ is built up according to the following recursive relation,

$$\chi_n = \chi_{n-1} + \beta_n d_n, \tag{2.5}$$

where the updated contrast $\chi_n$ is deduced from the previous one, $\chi_{n-1}$, by adding an updated term $\beta_n d_n$. This correction term is composed of two parts: a scalar weight $\beta_n$ and an updating direction $d_n$. Once the updating direction $d_n$ is found, the scalar weight $\beta_n$ is determined by minimizing the cost functional $\mathcal{F}_n(\chi_n)$ involving the residual error $\boldsymbol{h}_{l,n}^{(2)}$ on the scattered field computed from Eq. (1.43),

$$\boldsymbol{h}_{l,n}^{(2)} = \boldsymbol{f}_l^{\text{mes}} - \overline{\overline{\boldsymbol{B}}}\chi_n \boldsymbol{E}_{l,n}. \tag{2.6}$$

The cost functional mentioned above $\mathcal{F}_n(\chi_n)$ can be expressed as

$$\mathcal{F}_n(\chi_n) = W_\Gamma \sum_{l=1}^{N} \|\boldsymbol{h}_{l,n}^{(2)}\|_\Gamma^2, \tag{2.7}$$

the subscripts $\Gamma$ are added in the norm $\|.\|$ and later in the inner product $\langle .,. \rangle$ to indicate the domain of integration. The weighting coefficient $W_\Gamma$ is

$$W_\Gamma = \frac{1}{\sum\limits_{l=1}^{N} \|\boldsymbol{f}_l^{\text{mes}}\|_\Gamma^2}. \tag{2.8}$$

In Eq. (2.6), the total field $\boldsymbol{E}_{l,n}$ is the solution of Eq. (1.43) with the contrast distribution $\chi_{n-1}$. The total field is written as

$$\boldsymbol{E}_{l,n} \approx \boldsymbol{E}_{l,n-1} = [\overline{\overline{\boldsymbol{I}}} - \overline{\overline{\boldsymbol{A}}}\chi_{n-1}]^{-1}\boldsymbol{E}_l^{\text{inc}}, \tag{2.9}$$

where $\overline{\overline{\boldsymbol{I}}}$ is an unit matrix that has the same dimension as $\overline{\overline{\boldsymbol{A}}}$ and $\overline{\overline{\boldsymbol{B}}}$. Substituting the expression of the parameter of interest $\chi_n$ derived from Eq. (2.5) into the cost functional described in Eq. (2.7) leads to a polynomial expression with respect to the scalar coefficient $\beta_n$, represented as

$$\mathcal{F}_n(\chi_n) = W_\Gamma \sum_{l=1}^{N} \left( \|\boldsymbol{h}_{l,n-1}^{(2)}\|_\Gamma^2 + \beta_n^2 \|\overline{\overline{\boldsymbol{B}}} d_n \boldsymbol{E}_{l,n}\|_\Gamma^2 - 2\beta_n Re \left\langle \boldsymbol{h}_{l,n-1}^{(2)} | \overline{\overline{\boldsymbol{B}}} d_n \boldsymbol{E}_{l,n} \right\rangle \right). \tag{2.10}$$

In this case, the unique minimum of $\mathcal{F}_n(\chi_n)$ is reached when $\frac{\partial \mathcal{F}_n(\chi_n)}{\partial \beta_n} = 0$, such that

$$\beta_n = W_\Gamma \sum_{l=1}^{N} \frac{\text{Re}\left\langle \boldsymbol{h}_{l,n-1}^{(2)} | \overline{\overline{\boldsymbol{B}}} d_n \boldsymbol{E}_{l,n} \right\rangle}{\|\overline{\overline{\boldsymbol{B}}} d_n \boldsymbol{E}_{l,n}\|_\Gamma^2}. \tag{2.11}$$

As for the updating direction $d_n$, we take the standard Polak-Ribière conjugate-gradient directions[87].

### 2.2.3 Contrast source inversion method (CSI)

Different from the linearized method, the CSI was firstly introduced in Ref. 22 for solving nonlinear tomographic microwave imaging problems, which is formulated as a minimization problem using two equations: the coupling equation and the observing equation. The total field $\boldsymbol{E}_{l,n}$ is included in the minimization procedure multiplied by the constitutive parameter $\chi$, named as the contrast source $\boldsymbol{w}_{l,n} = \chi_n \boldsymbol{E}_{l,n}$.

A second residual error with respect to the contrast source $\boldsymbol{h}_{l,n}^{(1)}$ is defined as

$$\boldsymbol{h}_{l,n}^{(1)} = \boldsymbol{E}_l^{\text{inc}} + \chi_n \overline{\overline{\boldsymbol{A}}} \boldsymbol{E}_{l,n} - \boldsymbol{E}_{l,n}. \tag{2.12}$$

This residual error is included into the cost functional with respect to the contrast source $\boldsymbol{w}_{l,n}$, given as

$$\mathcal{F}_n(\chi_n, \boldsymbol{w}_{1,n}, \cdots, \boldsymbol{w}_{N,n}) = \mathcal{F}_n(\chi_n, \boldsymbol{w}_{\bullet,n}) = W_\Gamma \sum_{l=1}^{N} \|\boldsymbol{h}_{l,n}^{(2)}\|_\Gamma^2 + W_\Omega^{\text{CSI}} \sum_{l=1}^{N} \|\chi_n \boldsymbol{h}_{l,n}^{(1)}\|_\Omega^2, \tag{2.13}$$

with the weighting coefficient given as

$$W_\Omega^{\text{CSI}} = \frac{1}{\sum\limits_{l=1}^{N} \|\chi_{n-1} \boldsymbol{E}_l^{\text{inc}}\|_\Omega^2}. \tag{2.14}$$

The unknown parameters in this inversion method are $\chi$ and $\boldsymbol{w}_l$, where $\boldsymbol{w}_l$ depends on the incidence $l$. For more details on the CSI method, see Ref. 88.

### 2.2.4 Hybrid inversion Method in harmonic regime (HM)

The HM combines the advantages of the CGM and CSI. Different from the CSI, the contrast source $\boldsymbol{w}_l$ is replaced by the total field $\boldsymbol{E}_l$ in the cost functional[21]. This method was used in the two-dimensional electromagnetic scattering case[5] and extended to the three-dimensional case in Ref. 12.

Two sequences related to the contrast and the total field inside the investigating domain, $\chi_n$ and $\boldsymbol{E}_{l,n}$, respectively, are built up according to the following recursive relations,

$$\boldsymbol{E}_{l,n} = \boldsymbol{E}_{l,n-1} + \kappa_{l,n;\boldsymbol{\nu}}\boldsymbol{\nu}_{l,n} + \kappa_{l,n;\boldsymbol{\omega}}\boldsymbol{\omega}_{l,n}, \tag{2.15}$$

$$\chi_n = \chi_{n-1} + \beta_n d_n, \tag{2.16}$$

where $\boldsymbol{\nu}_{l,n}$, $\boldsymbol{\omega}_{l,n}$ and $d_n$ are updating directions with respect to the total field $\boldsymbol{E}_{l,n}$ and the contrast $\chi_n$, respectively, and $\kappa_{l,n}$, $\beta_n$ are scalar coefficients. The updating directions $\boldsymbol{\nu}_{l,n}$ and $d_n$ are chosen as the standard Polak-Ribière conjugate-gradient directions[87], while $\boldsymbol{\omega}_{l,n}$ is given by

$$\boldsymbol{\omega}_{l,n} = \tilde{\boldsymbol{E}}_{l,n-1} - \boldsymbol{E}_{l,n-1} \quad \text{with} \quad \tilde{\boldsymbol{E}}_{l,n-1} = [\overline{\overline{\boldsymbol{I}}} - \overline{\overline{\boldsymbol{A}}}\chi_{n-1}]^{-1}\boldsymbol{E}_l^{\text{inc}}, \tag{2.17}$$

where $\tilde{\boldsymbol{E}}_{l,n-1}$ represents the total field inside the investigating domain $\Omega$, calculated from the coupling equation with contrast $\chi_{n-1}$. Indeed, the scalar weight $\kappa_{l,n}$ and $\beta_n$ are chosen at each iteration step $n$ so as to minimize the normalized cost functional $\mathcal{F}(\chi_n, \boldsymbol{E}_{l,n})$ given by

$$\mathcal{F}_n(\chi_n, \boldsymbol{E}_{1,n}, \cdots, \boldsymbol{E}_{N,n}) = \mathcal{F}_n(\chi_n, \boldsymbol{E}_{\bullet,n}) = W_\Gamma \sum_{l=1}^{N} \|\boldsymbol{h}_{l,n}^{(2)}\|_\Gamma^2 + W_\Omega \sum_{l=1}^{N} \|\boldsymbol{h}_{l,n}^{(1)}\|_\Omega^2, \tag{2.18}$$

where the normalizing coefficient $W_\Omega$ is defined as

$$W_\Omega = \frac{1}{\sum\limits_{l=1}^{N} \|\boldsymbol{E}_l^{\text{inc}}\|_\Omega^2}. \tag{2.19}$$

$W_\Gamma$ is defined the same as Eq. (2.8). The subscripts $\Omega$ and $\Gamma$ are included in the norm $\|.\|$ and later in the inner product $\langle ., . \rangle$ to indicate the domain of integration. The residual errors $\boldsymbol{h}_{l,n}^{(2)}$ and $\boldsymbol{h}_{l,n}^{(1)}$ have been defined in Eqs. (2.6) and (2.12).

To ameliorate the inversion procedure, we propose to use the *a priori* information that the the real and imaginary part of the sought relative complex permittivity are greater than unity and non-negative[8,89,90], respectively. Instead of retrieving a complex function $\chi_n$, two real auxiliary functions $\xi_n$ and $\eta_n$ are reconstructed such that

$$\chi_n = 1 + \xi_n^2 + i\eta_n^2 - \varepsilon_b. \tag{2.20}$$

The recursive relation with respect to contrast $\chi_n$ [Eq.(2.16)] becomes

$$\xi_n = \xi_{n-1} + \beta_{n;\xi} d_{n;\xi} \quad \text{and} \quad \eta_n = \eta_{n-1} + \beta_{n;\eta} d_{n;\eta}. \tag{2.21}$$

As updating directions $d_{n;\xi}$ and $d_{n;\eta}$, we take

$$d_{n;\xi} = g_{n;\xi} + \gamma_{n;\xi} d_{n-1;\xi}, \qquad \gamma_{n;\xi} = \frac{\langle g_{n;\xi}, g_{n;\xi} - g_{n-1;\xi} \rangle_\Omega}{\|g_{n-1;\xi}\|_\Omega^2}, \tag{2.22}$$

$$d_{n;\eta} = g_{n;\eta} + \gamma_{n;\eta} d_{n-1;\eta}, \qquad \gamma_{n;\eta} = \frac{\langle g_{n;\eta}, g_{n;\eta} - g_{n-1;\eta} \rangle_\Omega}{\|g_{n-1;\eta}\|_\Omega^2}, \tag{2.23}$$

where $g_\xi$ and $g_\eta$ are the gradients of the cost functional $\mathcal{F}(\xi, \eta, \boldsymbol{E}_{l,n})$ with respect to $\xi$ and $\eta$ respectively, evaluated at the $(n-1)$-th step, assuming that the total field inside the test domain does not change. These gradients are given by

$$g_{n;\xi} = 2\xi_{n-1}\text{Re}\left[ W_\Omega \sum_{l=1}^{N} \bar{\boldsymbol{E}}_{l,n-1} \overline{\overline{\boldsymbol{A}}}^{\dagger} \boldsymbol{h}_{l,n-1}^{(1)} - W_\Gamma \sum_{l=1}^{N} \bar{\boldsymbol{E}}_{l,n-1} \overline{\overline{\boldsymbol{B}}}^{\dagger} \boldsymbol{h}_{l,n-1}^{(2)} \right], \tag{2.24}$$

$$g_{n;\eta} = 2\eta_{n-1}\text{Im}\left[ W_\Omega \sum_{l=1}^{N} \bar{\boldsymbol{E}}_{l,n-1} \overline{\overline{\boldsymbol{A}}}^{\dagger} \boldsymbol{h}_{l,n-1}^{(1)} - W_\Gamma \sum_{l=1}^{N} \bar{\boldsymbol{E}}_{l,n-1} \overline{\overline{\boldsymbol{B}}}^{\dagger} \boldsymbol{h}_{l,n-1}^{(2)} \right], \tag{2.25}$$

where the overbar denotes the complex conjugation, and $\overline{\overline{\boldsymbol{A}}}^{\dagger}$ and $\overline{\overline{\boldsymbol{B}}}^{\dagger}$ are the adjoint operators of $\overline{\overline{\boldsymbol{A}}}$ and $\overline{\overline{\boldsymbol{B}}}$, respectively. The search direction $\boldsymbol{\nu}_{l,n}$ for the total field inside the test domain is similar to those chosen for the contrast functions $\xi$ and $\eta$,

$$\boldsymbol{\nu}_{l,n} = \boldsymbol{g}_{l,n;\boldsymbol{E}_l} + \gamma_{l,n;\boldsymbol{E}_l}\boldsymbol{\nu}_{l,n-1}, \tag{2.26}$$

$$\gamma_{l,n;\boldsymbol{E}_l} = \frac{\left\langle \boldsymbol{g}_{l,n;\boldsymbol{E}_l}, \boldsymbol{g}_{l,n;\boldsymbol{E}_l} - \boldsymbol{g}_{l,n-1;\boldsymbol{E}_l} \right\rangle_{\Omega}}{\|\boldsymbol{g}_{l,n-1;\boldsymbol{E}_l}\|_{\Omega}^2}, \tag{2.27}$$

where $\boldsymbol{g}_{l,n;\boldsymbol{E}_l}$ is the gradient of the cost functional $\mathcal{F}(\xi, \eta, \boldsymbol{E}_{l,n})$ with respect to the field $\boldsymbol{E}_l$, evaluated at the $(n-1)$-th step, assuming that $\xi$ and $\eta$ does not change,

$$\boldsymbol{g}_{l,n;\boldsymbol{E}_l} = W_{\Omega}\left[\boldsymbol{h}_{l,n-1}^{(1)} - \bar{\chi}_{n-1}\overline{\overline{\boldsymbol{A}}}^{\dagger}\boldsymbol{h}_{l,n-1}^{(1)}\right] - W_{\Gamma}\bar{\chi}_{n-1}\overline{\overline{\boldsymbol{B}}}^{\dagger}\boldsymbol{h}_{l,n-1}^{(2)}. \tag{2.28}$$

As initial estimate for $\xi_0$ and $\eta_0$, we use the backpropagation method provided by[56,82], that is reported in the Appendix. E.

The HM has been shown in Ref. 12 being faster and more efficient than other linear and nonlinear inversion methods, in particular, for reconstructing large objects or when dealing with noisy data. Considering this advantage, we suggest to use the HM in the thesis work, in the three-dimensional electromagnetic problem. This method will also be applied in the time domain and combined with the time reversal method for reconstructing objects buried in cluttered media.

## 2.3 Hybrid inversion method in the time domain

The HM in the time domain aims to the characterization of three-dimensional objects from knowledge of a transient scattered field. As we have described in Sec. 1.5, same as the forward scattering problem, the inversion problem is addressed in the frequency domain rather than directly in the time domain.

Assume the scatterers are illuminated by sources radiating a Gaussian incident pulse, with a time duration $\tau$ and a central frequency of its spectrum $f_0$. The definition of the incident pulse has been given in Sec. 1.5, and by taking into account the Parseval Plancherel's theorem, the inverse scattering problem can be formulated in the frequency domain. The measured transient scattered fields are transformed into the frequency domain by using the Laplace transform or the Fourier transform, depending on the choice of the value $\beta$, with the Laplace parameter $s = \beta + i\omega$. The resulting harmonic fields are $\boldsymbol{f}_{l,p}^{\text{mes}}$ $(p = 1, 2, \cdots, P)$ and the involved frequency range $(f_p)$ is accurately sampled according to the Nyquist theorem. The mathematical relationship between the sampling frequency and the time duration of the pulse was discussed in Sec. 1.5.

We are now concerned with $P$ harmonic inverse scattering problems. For each operating frequency $f_p$, we have to solve two equations deduced from Eqs. (1.42) and (1.43),

$$\boldsymbol{E}_{l,p} = \boldsymbol{E}_{l,p}^{\text{inc}} + \overline{\overline{\boldsymbol{A}}}_p\chi_p\boldsymbol{E}_{l,p}, \tag{2.29}$$

$$\boldsymbol{E}_{l,p}^{\text{sca}} = \overline{\overline{\boldsymbol{B}}}_p\chi_p\boldsymbol{E}_{l,p}. \tag{2.30}$$

In Eqs. (2.29) and (2.30), $\boldsymbol{E}_{l,p}$, $\boldsymbol{E}_{l,p}^{\text{sca}}$ and $\boldsymbol{E}_{l,p}^{\text{inc}}$ denotes the total field inside the investigating domain $\Omega$, the scattered field measured along the contour $\Gamma$ and the incident field, respectively. The tensors $\overline{\overline{\boldsymbol{A}}}_p$ and $\overline{\overline{\boldsymbol{B}}}_p$ are the susceptibility operators at the operating frequency $f_p$ for describing the field relationship from $L^3(\Omega)$ to $L^3(\Omega)$ and from $L^3(\Omega)$ to $L^3(\Gamma)$, respectively.

The inverse problem aims at finding the contrast function $\chi$ with the known transient scattered field. We propose to use the HM in the frequency domain. The updating direction and the weighting coefficients are similar to the time-harmonic problem in Sec. 2.2.4, except that the cost functional

is defined for the fields and the contrast of all frequencies,

$$\begin{aligned}\mathcal{F}_n(\chi_{1,n},\cdots,\chi_{P,n},\boldsymbol{E}_{1,1,n},\cdots,\boldsymbol{E}_{1,P,n},\cdots,\boldsymbol{E}_{N,1,n},\cdots,\boldsymbol{E}_{N,P,n}) &= \mathcal{F}_n(\chi_{\boldsymbol{\cdot},n},\boldsymbol{E}_{\boldsymbol{\cdot},\boldsymbol{\cdot},n}) \\ &= W_\Gamma \sum_{l=1}^{N}\sum_{p=1}^{P} \|\boldsymbol{h}_{l,p,n}^{(2)}\|_\Gamma^2 + W_\Omega \sum_{l=1}^{N}\sum_{p=1}^{P} \|\boldsymbol{h}_{l,p,n}^{(1)}\|_\Omega^2,\end{aligned} \tag{2.31}$$

and the normalization coefficients are defined as

$$W_\Omega = \frac{1}{\sum\limits_{l=1}^{N}\sum\limits_{p=1}^{P} \|\boldsymbol{E}_{l,p}^{\mathrm{inc}}\|_\Omega^2}, \qquad \text{and} \qquad W_\Gamma = \frac{1}{\sum\limits_{l=1}^{N}\sum\limits_{p=1}^{P} \|\boldsymbol{f}_{l,p}^{\mathrm{mes}}\|_\Gamma^2}. \tag{2.32}$$

The residual errors $\boldsymbol{h}_{l,p,n}^{(2)}$ and $\boldsymbol{h}_{l,p,n}^{(1)}$ can be deduced from Eqs. (2.6) and (2.12) at each sampling frequency $f_p$. The tensors $\overline{\overline{\boldsymbol{A}}}_p$ and $\overline{\overline{\boldsymbol{B}}}_p$ depend on the operating frequencies. The incident field $\boldsymbol{E}_{l,p}$ and the total field $\boldsymbol{E}_{l,p}$ depend on not only the operating frequencies but also the incident source $l$. Considering this inversion problem from the point of the time-harmonic regime, the scatterers are illuminated successively by $N \times P$ total harmonic incident fields for $P$ different frequencies.

In this thesis, the scatterers and the media are assumed to be non-dispersive, where the contrast $\chi_p$ does not depend on the frequency $f_p$. While our inversion method can also be supported in the dispersive case, or for example, in the microwave regime, the contrast may be frequency dependent with an Ohmic model, reads as

$$\chi_{p,n} = \xi_n^2 - \frac{i\eta_n^2}{\omega_p \varepsilon_0}. \tag{2.33}$$

Same as the harmonic problem, we propose to use the *a priori* information that the the desired real and imaginary part of the relative complex permittivity are greater than unity and non-negative. These real parameters $\xi$ and $\eta$ do not depend on the frequency and represent the actual unknowns of the inverse scattering problem. The associated gradient sought are defined in the same way as the harmonic problem, but all of the frequencies $f_p$ ($p = 1, 2, \cdots, P$) have to be considered:

$$g_{n;\xi} = 2\xi_{n-1}\mathrm{Re}\left[W_\Omega \sum_{l=1}^{N}\sum_{p=1}^{P} \bar{\boldsymbol{E}}_{l,p,n-1} \overline{\overline{\boldsymbol{A}}}_p^{\dagger} \boldsymbol{h}_{l,p,n-1}^{(1)} - W_\Gamma \sum_{l=1}^{N}\sum_{p=1}^{P} \bar{\boldsymbol{E}}_{l,p,n-1} \overline{\overline{\boldsymbol{B}}}_p^{\dagger} \boldsymbol{h}_{l,p,n-1}^{(2)}\right], \tag{2.34}$$

$$g_{n;\eta} = 2\eta_{n-1}\mathrm{Im}\left[W_\Omega \sum_{l=1}^{N}\sum_{p=1}^{P} \bar{\boldsymbol{E}}_{l,p,n-1} \overline{\overline{\boldsymbol{A}}}_p^{\dagger} \boldsymbol{h}_{l,p,n-1}^{(1)} - W_\Gamma \sum_{l=1}^{N}\sum_{p=1}^{P} \bar{\boldsymbol{E}}_{l,p,n-1} \overline{\overline{\boldsymbol{B}}}_p^{\dagger} \boldsymbol{h}_{l,p,n-1}^{(2)}\right]. \tag{2.35}$$

The updating direction with respect to the total field $\boldsymbol{E}_{l,p}$ and the gradient coefficient is the same as Eqs. (2.27), (2.17) and (2.28), we only need to calculate these parameters for each frequency. Indeed, for the transient field, we have $N \times P$ descending directions $\boldsymbol{\omega}_{l,p,n}$ and $\boldsymbol{\nu}_{l,p,n}$. The cost function $\mathcal{F}_n$ is a nonlinear expression with respect to $2 \times N \times P$ complex unknown ($\kappa_{l,p,n;\boldsymbol{\nu}}$, $\kappa_{l,p,n;\boldsymbol{\omega}}$) and two real unknown ($\beta_{n;\xi}$, $\beta_{n;\eta}$).

## 2.4 Conclusions

In this chapter, we have presented several algorithms for solving the inverse electromagnetic scattering problem. The unknown constitutive electric parameters of scatterers can be restituted using iterative methods with only known measured scattered field. Firstly, we have presented the conjugate gradient method as linearized-type method, where the total field is fixed as the solution of the forward problem corresponding to the contrast $\chi_{n-1}$ for each iteration. We introduced a non-linearized inversion method, the contrast source inversion method, where the total field is also included into the minimization procedure, multiplied by the contrast $\chi$, named as the contrast

source. Finally, we propose an hybrid inversion method that combines the advantages of non linearized and linearized inversion techniques, and that will be exploited in our thesis work for solving three-dimensional electromagnetic scattering problem.

For all of discussions above, the scatterers are illuminated successively by $l = 1, 2, \cdots, N$ sources generating an harmonic field at one fixed operating frequency. This problem is thought as working in the time-harmonic regime. The imaging resolution depends on the numerical aperture (NA). In several cases, we have to use an abundant number of illuminations sources for obtaining a well reconstructed permittivity map.

For a limited number of sources, we extended the HM to the time domain. The scatterer are excited by a small number of sources fed by a transient current. If we transform this transient field to the frequency domain according to the Nyquist sampling theorem, the scattering problem is equivalent with that the scatterers being illuminated by a large quantity of time-harmonic fields. We call it the inversion problem in the time domain.

In the following parts, the HM are reported in both the time-harmonic regime and the time domain. It will also be combined with the time reversal imaging technique for further improving the imaging resolution once the scatterers are present in cluttered medium and for reducing the computational time.

# Part II

# Detection and characterization of three-dimensional scatterers in cluttered environment

# Introduction of PART II

## Detection and characterization of three-dimensional scatterers in cluttered environment

The inverse scattering problem permits to localize and characterize targets quantitatively, to reconstruct their shapes and permittivity distributions. Assume that targets are located in a large domain, we need to obtain a small region before reconstructing them. Moreover, in the presence of a disordered medium, the signature of targets will be blurred by the strong clutter. To solve this problem, in this part, we suggest to use one of the time reversal technique, the DORT method (Décomposition de l'Opérateur de Retournement Temporel) to localize the targets and to improve signal-to-clutter ratio.
In the first chapter, we will analyze numerically the properties of the DORT method, with transceivers distributing along only one side of targets ('limited-aspect' configuration). The scalar illumination and the vectorial illumination will be compared, in which the targets and the transceivers are located in the same medium or in two different mediums, separated by an interface.
In the second chapter, we will test the focalization ability of the DORT method, using synthetic data generated by the CDM forward model, in presence of Gaussian correlated clutter with different characteristics. This reversal method will be combined with the nonlinear inversion algorithm for further improving the reconstruction. The influence of the clutter standard deviation and the correlation length will be analyzed. The homogeneous space background configuration and the half-space configuration will be studied.

Chapter 3

# Time reversal imaging in harmonic regime

## Contents



## 3.1 Introduction

In the last two chapters, we have discussed about the forward and the inverse scattering problem in electromagnetic scattering domain. In this chapter, we study the detection and the localization of objects from the measured scattered fields. This is an important issue for the characterization of buried objects. Indeed it is suitable before reconstructing buried targets to limit the investigating domain to a much smaller region. Moreover, when targets are buried in a natural medium, heterogeneities of the host medium blur the signature of objects of interest. The first task of this thesis work is to extract the significant target information from the strong clutter. We propose to use one of the time reversal approach in the frequency counterpart, *i.e.*, the DORT (Décomposition de l'Opérateur de Retournement Temporel) method for imaging the targets. It consists in analyzing the eigenvalues and eigenvectors of the Time Reversal Operator (TRO), in order to synthesize incident fields that focus selectively on targets of interest.

In this chapter, we describe a clutter model to simulate the cluttered environment. Then follows in detail the principle of the DORT technique and the application of this method using the 'limited-aspect' configuration. Scatterers are assumed to be located at either the same or different medium from the medium where the sources are located. Emitting and receiving antennas can take one or three different polarization directions.

## 3.2 Clutter model

In order to test the ability of the localization of targets using the DORT method, we assume that targets are buried in a heterogeneous medium. We aim to understand the influence of the clutter in the deterioration of the signal-response of targets. The measured scattered fields contain not only the information of the targets, but also of the response of the cluttered medium. Thanks to the time reversal technique, we can detect significant targets despite of the multiple scattering effects due to the heterogeneities of the host medium. In Ref. 30, two types of clutter are considered: discrete scatterers and continuous random inhomogeneous backgrounds. In this manuscript, we focus on the latter case, an inhomogeneous medium with relative permittivity $\varepsilon_c(\boldsymbol{r}) = \varepsilon_b + \varepsilon_f(\boldsymbol{r})$ where $\varepsilon_f(\boldsymbol{r})$ is a random function which is null outside $W$ (scattering domain) and whose average is null over $W$, where $\varepsilon_b$ is the average permittivity of the background medium. In the case of the half-space configuration, we neglect the eventual effect of the roughness of the surface separating the two media. Indeed, we assume, when dealing with the half-space configuration, that the interface is flat. The problem of the roughness of this interface has been studied in Ref. 32, where other tools than the time reversal technique have been employed.

The random permittivity of the clutter, $\varepsilon_f(\boldsymbol{r})$, is defined as a Gaussian variable with zero mean and standard deviation $\sigma_f$ and Gaussian correlation function $C(\boldsymbol{r})$ with correlation length $l_c$. The Gaussian correlation function $C$ is defined as

$$C(\boldsymbol{r}) = \sigma_f^2 \exp\left(-\frac{\|\boldsymbol{r}\|^2}{l_c^2}\right), \tag{3.1}$$

$\varepsilon_f(\boldsymbol{r})$ is implemented in the Fourier domain, as we can calculate the spectrum density function of $C(\boldsymbol{r})$. Then, we define an array of three-dimensional uniform distributed number, with the convolution of this random number and the spectrum function, we can finally get the fluctuation of the background medium $\varepsilon_f(\boldsymbol{r})$ [91,92].

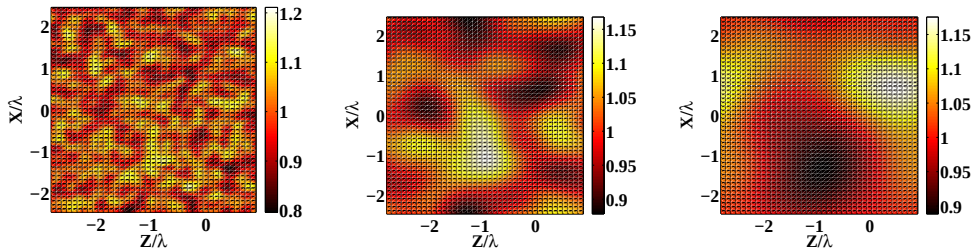


**Figure 3.1 :** *The relative permittivity distribution of inhomogeneous medium, with spatial fluctuation of the Gaussian correlation function. (a)-(c) with the same mean value $\varepsilon_b = 1$, and the same standard deviation $\sigma_f = 0.067\varepsilon_b$ but different correlation lengths. (a) $l_c = 0.1\lambda$, (b) $l_c = 0.5\lambda$, (c) $l_c = \lambda$, where $\lambda$ is the central operating wavelength of illuminations.*

We consider herein three different realizations of clutter using the spectrum method, with the same mean value and standard deviation of fluctuation, but different correlation lengths, as shown in Fig. 3.1. With a large correlation length, the peak values of permittivity are separated by a large distance on average, Figs. 3.1 (b) and (c). On the contrary, with a small correlation length, the permittivity of fluctuation varies more rapidly, Fig. 3.1 (a). The extreme case of a very small correlation length would provide a clutter that would behave as a discrete clutter, *i.e.*, composed by an assembly of point-like scatterers. On the other hand, a large value of the correlation length leads to an homogeneous background medium. Due to the finite size of the scattering domain, the

generation of clutter has a statistical error. Larger the scattering domain is, the realized standard deviation of fluctuation is more closed to the set value $\sigma_f$. The spatial average permittivity is also not equal to the theoretical value $\varepsilon_b$. This error will be diminished as the correlation length decreases or the standard deviation decreases.

To quantify more precisely the influence of the clutter with respect to parameters of the studied problem, two errors are introduced

$$\mathrm{Err}_s = \frac{\sum_{l=1}^{N} \|\boldsymbol{f}_l - \boldsymbol{f}_l^{\text{scatterers}}\|_\Gamma^2}{\sum_{l=1}^{N} \|\boldsymbol{f}_l^{\text{scatterers}}\|_\Gamma^2}, \tag{3.2}$$

$$\mathrm{Err}_d = \frac{\sum_{l=1}^{N} \|\boldsymbol{f}_l - \boldsymbol{f}_l^{\text{scatterers}} - \boldsymbol{f}_l^{\text{clutter}}\|_\Gamma^2}{\sum_{l=1}^{N} \|\boldsymbol{f}_l^{\text{scatterers}}\|_\Gamma^2}, \tag{3.3}$$

where $\boldsymbol{f}_l$ and $\boldsymbol{f}_l^{\text{scatterers}}$ denote the field scattered by the targets with or without the clutter, respectively, and $\boldsymbol{f}_l^{\text{clutter}}$ the scattered field by the clutter alone, with the illumination $l = 1, \cdots, N$. $\mathrm{Err}_s$ is used to quantify the noise level due to the clutter, and $\mathrm{Err}_d$ indicates the amount of the multiple scattering between the targets and the clutter. If $\mathrm{Err}_d$ is small, the targets and the clutter can be considered to radiate independently. Note that for the same statistical parameters, the errors $\mathrm{Err}_s$, $\mathrm{Err}_d$ may vary significantly as they depend on the specific realization of the random process.

## 3.3 Decomposition of the time reversal operator

When buried scatterers in cluttered medium are modelled, as described in the last section, we proposed to use the DORT method to detect and localize the scatterers. If one probes the cluttered medium with the measured scattered field, the re-emitting field would focus onto the brightest scatterers almost regardless to the strength of the clutter[35,93]. In this section, we discuss the principle of the DORT method and analyze the effect of the polarization of the incident field. Some simple examples on the selective focalization of scatterers are reported as well as other examples to emphasize our analysis.

### 3.3.1 Principle of DORT

Time reversal concept is based on the invariance of the wave propagation in lossless non-magnetic media,

$$\boldsymbol{\nabla}^2 \boldsymbol{\mathscr{E}}(\boldsymbol{r}, t) - \mu_0 \epsilon(\boldsymbol{r}) \frac{\partial^2}{\partial t^2} \boldsymbol{\mathscr{E}}(\boldsymbol{r}, t) = 0. \tag{3.4}$$

Where the solution of this equation $\boldsymbol{\mathscr{E}}(\boldsymbol{r}, t)$ is the vector electric field in the three-dimension space and time. $\mu_0$ and $\epsilon(\boldsymbol{r})$ are the permeability and permittivity of the medium, respectively. If we observe this propagation equation, it contains only a second order time-derivative operator with respect to the time variable $t$. This property, called *time reversal invariance*, tells us that $\boldsymbol{\mathscr{E}}(\boldsymbol{r}, -t)$ is also a solution to the same equation, implying that for any scattered field $\boldsymbol{\mathscr{E}}(\boldsymbol{r}, t)$, there exists a wave $\boldsymbol{\mathscr{E}}(\boldsymbol{r}, -t)$ which converges coherently to emitting sources. It is important to note that the time reversal concept is only valid for lossless medium. In the case of lossy medium, through a compensation method, it has been shown that we could generate a focusing wave following the time reversal technique[94].

In the frequency counterpart, the time reversal signal technique is realized by the DORT method. The three-dimensional scattering domain, made of several scatterers, is illuminated successively by $l = 1, \cdots, N_s$ electromagnetic excitation. For each source $l$, the scattered field is measured at $m = 1, \cdots, N_r$ receivers. Assuming that each antenna can play the role of source and receiver, $N_s = N_r = N$. The scattering experiment is summarized into a $N \times N$ symmetric matrix, denoted by $\boldsymbol{K}$, such that $\boldsymbol{K}_{ij}$ represents the complex amplitude of scattered field recorded by the $j$-th receiver when the $i$-th antenna is emitting.

In the case of a lossless embedding medium, time reversal and complex conjugation are equivalent operations. By virtue of the reciprocity theorem, the scattered field measured by $m$-th antenna when the $l$-th antenna is illuminating is equal to that measured by the $l$-th antenna when the $m$-th one is emitting, $\boldsymbol{K}_{lm} = \boldsymbol{K}_{ml}$ ($\boldsymbol{K}$ is symmetric). The time reversal experiment is described by the conjugate transpose matrix $\boldsymbol{K}^{\dagger}$, and the time reversal operator (TRO) is represented by the self-adjoint matrix $\boldsymbol{L} = \boldsymbol{K}^{\dagger}\boldsymbol{K}$. The DORT method consists in determining the eigenvalues and the eigenvectors of TRO. In particular according to the fact that $L$ is an hermitian operator, its eigenvalues are positive real valued and its eigenvectors are orthogonal. Two significant properties can be deduced from the invariance parameters of this diagonalizable matrix.

1. The number of dominant eigenvalues determine the number of echogeneous scatterers embedded in the medium.
2. The associated eigenvectors permit to localize these scatterers and to synthesize a wave focusing selectively on each scatterer.

In the acoustic case, it has been shown that each significant eigenvalue of the TRO is associated to a single point-like scatterer[95]. In the electromagnetism, the same rule only holds for the $s$-polarization case and for the two dimensional problem[3]. For other configurations, with three possible orientations of antennas, one may obtain more accurate information with respect to the scatterer regarding its localization and its constitutive material. The actual number of eigenvalues associated with scatterers depends on the measurements array, the polarization of the field and the configuration at hand. The localization of the scatterer can be achieved by the backpropagation of the corresponding eigenvector, which synthesizes a wave focusing on the scatterer[3,4].

### 3.3.2 Effect of polarization

In the acoustical domain, sources do not carry the polarization information. In the electromagnetic domain, there exists the possibility that we obtain full-polarized data. In Ref. 96, Chambers *et al* have shown that for a non-conducting sphere, with three possible orientations of the dipole antennas, the number of possible eigenvalues is three. For a conducting sphere, the induced magnetic dipole also contributes to the scattered field, so that the number of possible eigenvalues is up to six.

In our work, we propose to use the three-dimensional vectorial configuration, where one can build the matrix $\boldsymbol{K}$ under the three orthogonal linear polarizations in order to gain more information. More precisely, for each $\alpha$-direction ($\alpha = x, y, z$) of the polarization of the sources, three scattered field components ($\beta = x, y, z$) are measured. A $(3 \times 3)$ matrix $\boldsymbol{K}_{ij}$ can be built up as

$$\boldsymbol{K}_{ij} = \begin{pmatrix} K_{ij}^{xx} & K_{ij}^{xy} & K_{ij}^{xz} \\ K_{ij}^{yx} & K_{ij}^{yy} & K_{ij}^{yz} \\ K_{ij}^{zx} & K_{ij}^{zy} & K_{ij}^{zz} \end{pmatrix}. \tag{3.5}$$

Diagonal elements of the matrix $\boldsymbol{K}_{ij}$ describe the relation between receivers and emitters with the same orientation. The off-diagonal elements describe the cross-polarizations. $\boldsymbol{K}_{ij} = \boldsymbol{K}_{ij}^{T}$ due to reciprocity. Thus, the $3N \times 3N$ matrix $\boldsymbol{K}$ is assembled from all the matrix $\boldsymbol{K}_{ij}$ and read as

$$\boldsymbol{K} = \begin{pmatrix} \boldsymbol{K}_{11} & \boldsymbol{K}_{12} & \dots & \boldsymbol{K}_{1N} \\ \boldsymbol{K}_{21} & \boldsymbol{K}_{22} & \dots & \boldsymbol{K}_{2N} \\ \vdots & \vdots & \ddots & \vdots \\ \boldsymbol{K}_{N1} & \boldsymbol{K}_{N2} & \dots & \boldsymbol{K}_{NN} \end{pmatrix}. \tag{3.6}$$

By virtue of the reciprocity theorem, the matrix $\boldsymbol{K}$ is symmetric and the TRO is defined as $\boldsymbol{L} = \boldsymbol{K}^{\dagger}\boldsymbol{K}$. Since $\boldsymbol{L}$ is a self-adjoint matrix, one can determine the eigenvalues $\zeta$ and eigenvectors $\boldsymbol{V}$

$$\boldsymbol{L}\boldsymbol{V} = \zeta\boldsymbol{V}, \tag{3.7}$$

where the eigenvalue $\zeta$ is positive real valued and the eigenvectors $\boldsymbol{V}$ are of the form

$$\boldsymbol{V} = [V_{1,x}, V_{1,y}, V_{1,z}, \cdots, V_{N,x}, V_{N,y}, V_{N,z}]\,. \tag{3.8}$$

Each component of the eigenvector associated with the highest eigenvalue $\zeta$ provides the complex amplitudes of the emitting dipoles (former receivers) such that they synthesize an incident field $\boldsymbol{E}_{\zeta}^{\text{inc;DORT}}$ focusing on the brightest scatterer. This focusing wave can be written as

$$\boldsymbol{E}_{\zeta}^{\text{inc;DORT}}(\boldsymbol{r}) = \sum_{l=1}^{N}\sum_{\alpha}^{x,y,z} V_{l,\alpha}(\zeta)\boldsymbol{G}(\boldsymbol{r},\boldsymbol{r}_l)\hat{e}_{\alpha}, \tag{3.9}$$

where $V_{l,\alpha}(\zeta)$ corresponds to $l$-th, $\alpha$ direction component of the eigenvector associated to the eigenvalue $\zeta$. $\boldsymbol{G}(\boldsymbol{r},\boldsymbol{r}_l)$ is the Green's function describing the field received at $\boldsymbol{r}$ radiated by a point source at $\boldsymbol{r}_l$. $\hat{e}_{\alpha}$ is the unit vector co-directional with $x$, $y$ and $z$-axis, as

$$\hat{e}_x = \begin{bmatrix}1\\0\\0\end{bmatrix}, \hat{e}_y = \begin{bmatrix}0\\1\\0\end{bmatrix}, \hat{e}_z = \begin{bmatrix}0\\0\\1\end{bmatrix}. \tag{3.10}$$

The incident field $\boldsymbol{E}_{l,\alpha}^{\text{inc}}$ when each former source is emitting alone, fed by a normalized current, can be written as

$$\boldsymbol{E}_{l,\alpha}^{\text{inc}}(\boldsymbol{r}) = \boldsymbol{G}(\boldsymbol{r},\boldsymbol{r}_l)\hat{e}_{\alpha}, \tag{3.11}$$

Eq. (3.9) can be represented as

$$\boldsymbol{E}_{\zeta}^{\text{inc;DORT}}(\boldsymbol{r}) = \sum_{l=1}^{N}\sum_{\alpha}^{x,y,z} V_{l,\alpha}(\zeta)\boldsymbol{E}_{l,\alpha}^{\text{inc}}(\boldsymbol{r}). \tag{3.12}$$

With this relationship, we do not need to recalculate these new incident fields. They can be obtained by a linear combination between the eigenvector and the former incident field.

Since Maxwell's equations are linear, the corresponding scattered field is now obtained with the same linear combination than the one of the incident field, [Eq. (3.12)]:

$$\boldsymbol{E}_{\zeta}^{\text{sca;DORT}}(\boldsymbol{r}) = \sum_{l=1}^{N}\sum_{\alpha}^{x,y,z} V_{l,\alpha}(\zeta)\boldsymbol{E}_{l,\alpha}^{\text{sca}}(\boldsymbol{r}). \tag{3.13}$$

Hence, in this case, the DORT method provides a means for focusing selectively onto each target with three different incident fields. In the case of the antennas taking three orthogonal orientations in homogeneous space, for each non-conducting scatterer, there exist three possible eigenvalues. When considering the configuration with the antennas above the interface and scatterers below the interface, one can show that each point-like scatterer is associated with only two eigenvector.

## 3.4 Focalization on one single scatterer

In this section, we will present some focalization examples for both configurations: homogeneous background configuration and half-space configuration. We will begin from the simplest case, the scalar configuration, where the antennas oriented along one single direction, similar as in the acoustic domain. Then, we will focus on the vectorial configuration, with the antennas oriented along three orthogonal directions. The influence of the clutter on the behavior of the eigenvalues will also be analyzed.

### 3.4.1 Homogeneous space configuration

As we described above, the localization information of scatterers is contained in the eigenvectors which correspond to dominant eigenvalues. We have firstly tested the DORT method in a complete configuration, where a single three-dimensional target is located in a bounded medium surrounded by $N = 86$ monochromatic point sources, regularly placed along all possible directions within $4\pi$ steradians. For simplicity, we assume that there is no clutter around the target. In the case of the emitting and receiving antenna take one single orientation, only one eigenvalue focuses on the target. For the complicated vectorial case, for each target, the eigenvectors corresponding to the first three eigenvalues can generate focusing waves.

The complete configuration is not the appropriate configuration for a couple of applications, such as detecting targets under the ground or behind the wall. For these applications, emitters and receivers are always located at one side of the target, this is typically the limited-aspect configuration[4]. We will focus on this configuration.

The sketch for the limited-aspect configuration is shown in Fig. 3.2. The scattering domain is illuminated by a two-dimensional array of antennas, distributed in a square. The interval space between two antennas is $P$, the distance between antennas and the centre of scatterers is $F$, and the length of the line of antennas is $D$. Firstly, for the homogeneous space, we assume that the scatterer

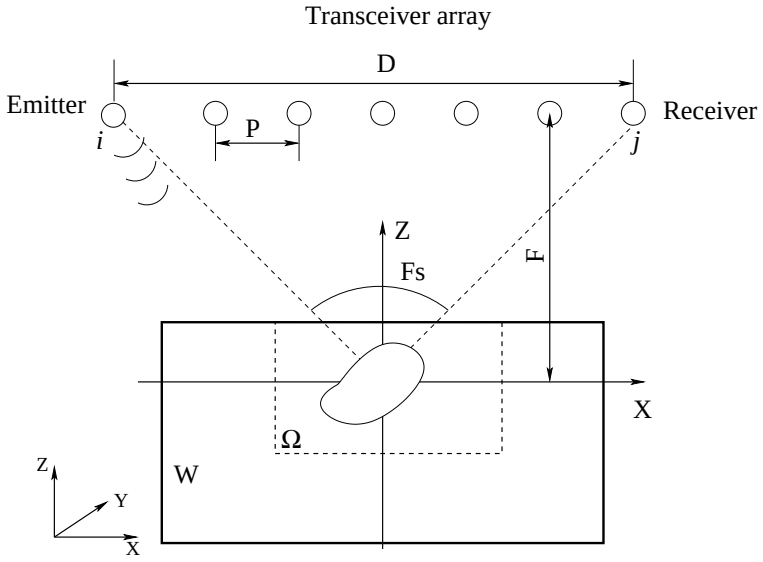


**Figure 3.2 :** *Geometry of the scattering problem in homogeneous background space. The scatterers are confined in the scattering domain $W$, in the same medium as the sources. $\Gamma$: measurement surface.*

and the antennas are located in the vacuum, with $\varepsilon_b = 1$. The transceiver array is described by a lattice of $N = 81$ dipole antennas regularly distributed on a square of side of $D = 8\lambda$, which is located at $z = 2\lambda$, where $\lambda$ is the illumination wavelength in the homogeneous lossless medium ($\lambda = 0.6$ m). The scattering domain $W$ of the imaging configuration depicted in Fig. 3.2 is a box with size $(5\lambda \times 5\lambda \times 4\lambda)$ m$^3$, centered at $(0, 0, -\lambda)$. The scattered field is generated using the CDM, with the mesh size $a = \lambda/10$. We consider a single dielectric sphere, centered at the origin, of radius $r = \lambda/6$, with relative permittivity $\varepsilon = 3\varepsilon_b$. The distance between the center of antennas and scatterer is $F = 2\lambda$, and the space between two antennas is $P = \lambda$. In this case, the angle of the maximum cone of light $F_s \approx 126°$. The product of $ka$ is about 1, where $k$ is the wavenumber of the background medium. The scattered field is measured by all receivers for successive illuminations.

#### 3.4.1.1 Scalar illumination

For the scalar case, the antennas are oriented along one single direction, for example, $x$-axis. The scattering domain is illuminated along one single direction, and the scattered field is collected along the same orientation. Firstly, we assume that there is no clutter inside the scattering domain, around the target. Then, we can construct a matrix $\boldsymbol{K}$, of the dimension $N \times N$, with only $x$-components of these measured scattered fields and determine the eigenvalue of $L = \boldsymbol{K}^{\dagger}\boldsymbol{K}$. The first four eigenvalues are 2940, 110, 62, 31, respectively, shown as the red-add line in Fig. 3.3.

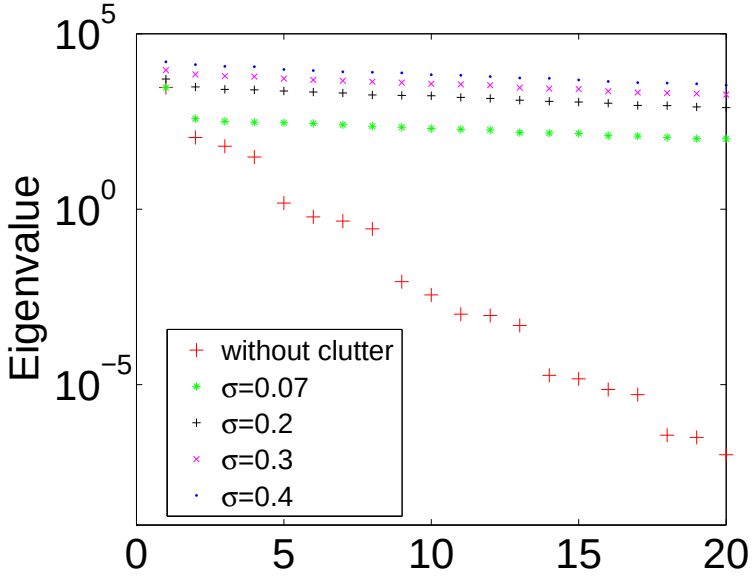


**Figure 3.3 :** *Eigenvalue of the time reversal operator in homogeneous space with scalar illumination, without clutter (red-add line) and with different levels of clutter: $\sigma = 0.07$ (green-star line), $\sigma = 0.2$ (black-add line), $\sigma = 0.3$ (magenta-cross line), $\sigma = 0.4$ (blue-solid dotted line).*

The second eigenvalue is about 30 times smaller than the first one. One can conclude that for this single scatterer, there exists one dominant eigenvalue.

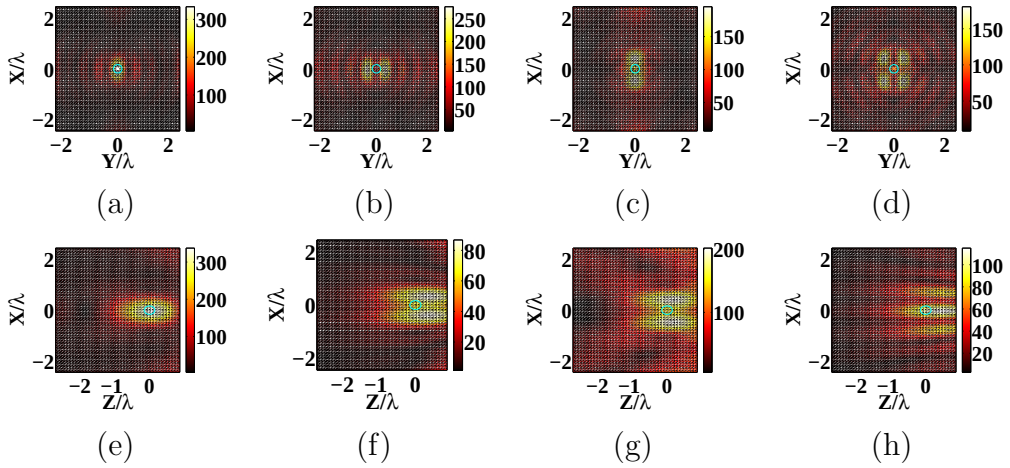


**Figure 3.4 :** *Intensity map in $W$ of the electric field deduced from four eigenvectors related to the four largest eigenvalues using illuminations at the wavelength $\lambda = 0.6$ $m$, when one single scatterer is located in the vacuum, $F_s \approx 126°$, and the antennas are oriented along $x$-direction. (a)-(d): in the $(x, y)$ plane for $z = 0$. (e)-(h): in the $(x, z)$ plane for $y = 0$. Each column corresponds to the first, the second, the third and the fourth eigenvalue. The circle represents the actual profile of the target.*

We analyze the behavior of the corresponding eigenvectors. If we use the eigenvector $V_{l,x}(1)$, $l = 1, 2, \cdots, N$, as new complex currents for each emitter, corresponding to the first largest eigenvalue, the backpropagated field is isotropic, focusing on the scatterer, as shown in Figs. 3.4 (a) and (e). On the contrary, the eigenvectors $V_{l,x}(2)$, $V_{l,x}(3)$ and $V_{l,x}(4)$ corresponding to the other three largest eigenvalues generate antisymmetric fields, which present a minimum on the scatterer [Figs. 3.4 (b)-(d)]. Up to now, we have verified numerically the analytical interpretation of the eigenvalues and of the eigenvectors reported in Ref. 4. The TRO has two types of eigenvectors for each scatterer: one generates a backpropagated field that presents maximum on the scatterer, named as the focusing fields; another generates a backpropageted field that presents a minimum on the scatterer.

We keep unchanged the other parameters, only the distance between antennas and scatterers $F$ is augmented, from $2\lambda$ to $4\lambda$. The maximum angle $F_s$ is therefore reduced to 90°.

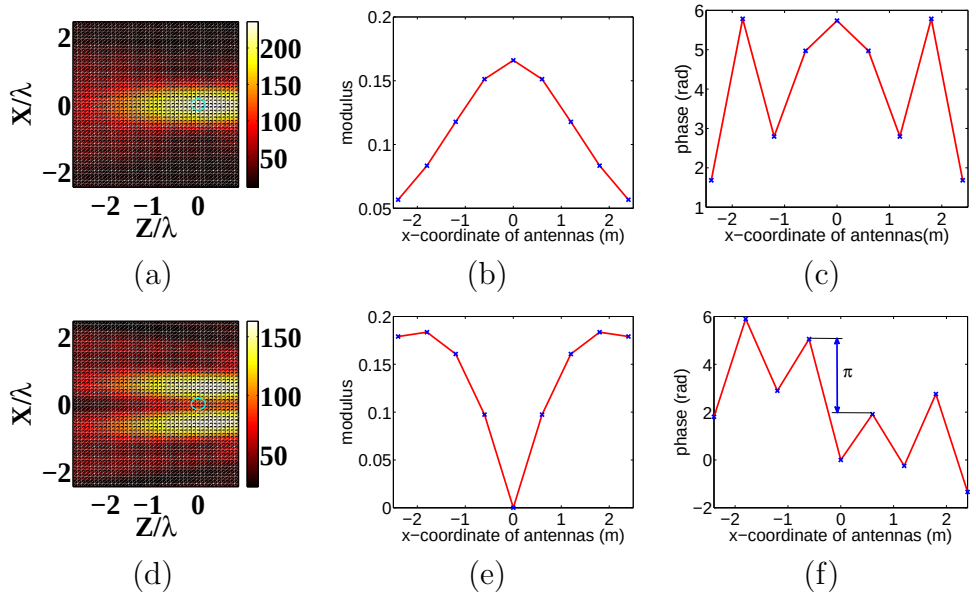


**Figure 3.5 :** *Same configuration as Figs. 3.4, except that $F$ is augmented to $4\lambda$, with $F_s = 90°$. (a)-(c): intensity map and behavior of eigenvectors corresponding to the first largest eigenvalue. (d)-(f): intensity map and behavior of eigenvectors corresponding to the second largest eigenvalue. (a) and (d): intensity map in $W$ of the electric field deduced from eigenvectors, in the $(x, z)$ plane for $y = 0$. (b) and (e): modulus of the eigenvectors versus the antenna coordinate $(x_e, y_e)$, with $y_e = 0$. (c) and (f): phase of the eigenvectors versus the antenna coordinate $(x_e, y_e)$, with $y_e = 0$.*

Comparing the intensity map of the backpropagated fields in Figs. 3.5 (a) and (d) with Figs. 3.4 (e) and (f), the focal size is prolonged along $z$-axis due to the fact that $F_s$ is reduced. The phases of the eigenvectors associated with the first and the second eigenvalues versus the antenna array are plotted in Figs. 3.5 (c) and (f). The one associated with the first eigenvalue has an axis of symmetry. For the eigenvector associated to the second eigenvalue, the phase on the left and right side present 'jumps' of value $\pi$ with respect to the central antenna situated at $x_e = 0, y_e = 0$, which is nearest to the scatterer. This is the signature of an antisymmetric eigenvector. This has also been observed for the two-dimensional case in Ref. 97. At the same coordinate, the modulus of the symmetric eigenvector is maximum [Fig. 3.5 (b)], while that of an antisymmetric eigenvector is minimum [Fig. 3.5 (e)]. In this sense, we can also determine the horizontal coordinates of scatterers by observing the modulus and the phase of the component of eigenvectors[97].

The distance between antennas and scatterers $F$ is kept at $2\lambda$, the length of the line of antennas $D$ is reduced to $4\lambda$, keeping the space between antennas $P = \lambda$. The number of antennas is reduced to $5 \times 5$, distributed in a lattice. The maximum angle $F_s = 90°$ is the same as the second case.

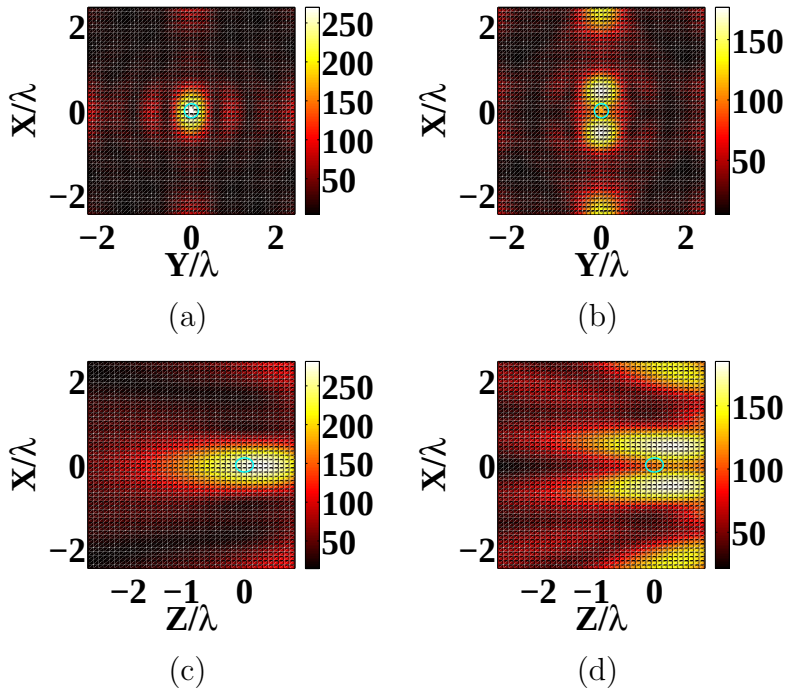


**Figure 3.6 :** *Same as Fig. 3.4 (a), (b), (e) and (f), while with a shorter measuring line, only* 25 *antennas are used. Each column corresponds to the first and the second eigenvalue.*

From Fig. 3.6, we can see that if the length of the antenna array is too small, the numerical aperture (NA) is not large enough to provide satisfactory focusing waves. The resolution of the focalization is deteriorated. As the number of antennas is reduced, several spots appear along $x$-axis. Notice that even if the NA is reduced, as it is for the second and the third case, the DORT method provide satisfactory focusing waves.

Finally, we have also varied the distance between two antennas $P$ from $\lambda$ to $\lambda/2$ or $2\lambda$, keeping the length of the measured line $D$ unchanged. The number of antennas is in this case varied. Obviously, a better resolution can be reached with a finer discretization of antennas. On the contrary, the focalization resolution would decay with a too large space between two antennas.

Now, we propose to test the robustness of focalization on different levels of noise using the DORT method with scalar illumination. The evolution of the eigenvalues without clutter and with different levels of noise is plotted in Fig. 3.3.

We present here only the highest twenty eigenvalues to illustrate the behavior of the time reversal operator versus different levels of noise. The correlation length of the correlated noise is fixed at $l_c = 0.1\lambda$, only the standard deviation $\sigma_f$ is gradually varied. The multiple scattering effect between the target and the clutter can be neglected here. From Fig. 3.3, we can see that stronger the noise is (the signal-to-noise ratio is quickly weakened), larger are the eigenvalues belonging to the noise space. Even though the eigenvalue corresponding to the target is blurred by the noise, up to $\sigma = 0.3$, the intensity map of the backpropagated field is close to what is achieved in the absence of noise. For $\sigma = 0.4$, the difference of the eigenvalues between the target and the noise is not apparent so that the target can not be recognized from the intensity map. Only the intensity map with $\sigma = 0.3$ is reported in Fig. 3.7. The backpropagated wave generated by the first eigenvector focuses yet on the target, [Figs. 3.7 (a) and (c)]. For the second eigenvector, comparing with Figs. 3.4 (b) and (f), the antisymmetric property of the eigenvector is totally blurred by the noise, [Figs. 3.7 (b) and (d)].

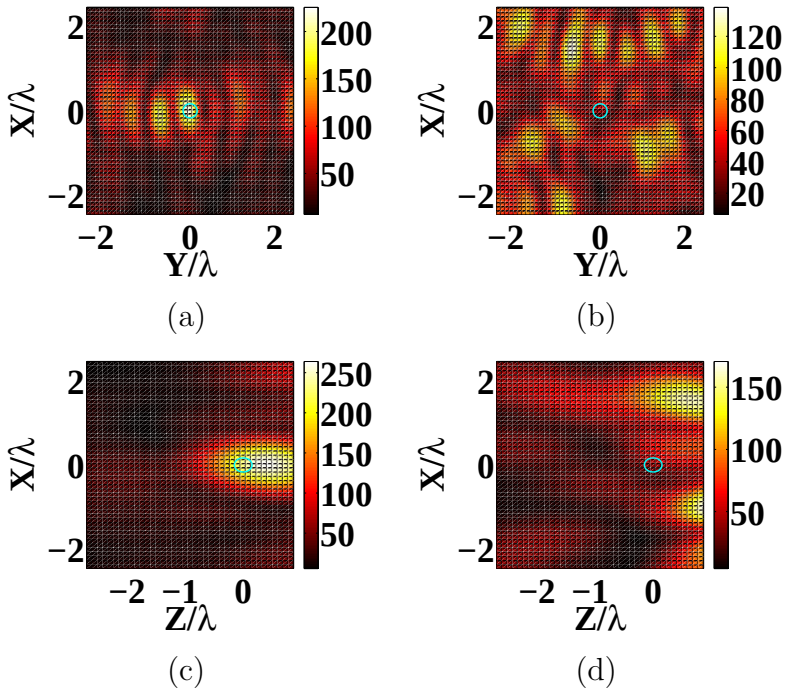


**Figure 3.7 :** *Intensity map in $W$ of the electric field deduced from two eigenvectors related to the two largest eigenvalues using the same configuration as Fig. 3.4, with $l_c = 0.1\lambda$ and $\sigma = 0.3$. (a)-(b): in the $(x, y)$ plane for $z = 0$. (c)-(d): in the $(x, z)$ plane for $y = 0$. Each column corresponds to the first and the second eigenvalue. The circle represent the actual profile of the target.*

#### 3.4.1.2 Vectorial illumination

Now, we move on to the vectorial illumination to test the focalization ability of DORT, without the presence of clutter. The eigenvalue of the time reversal operator is plotted in Fig. 3.8, in green-star line. Compared with the distribution map in scalar case, (Fig. 3.8 red-add line), there exist now three largest eigenvalues focusing on the target, instead of one for the scalar case.

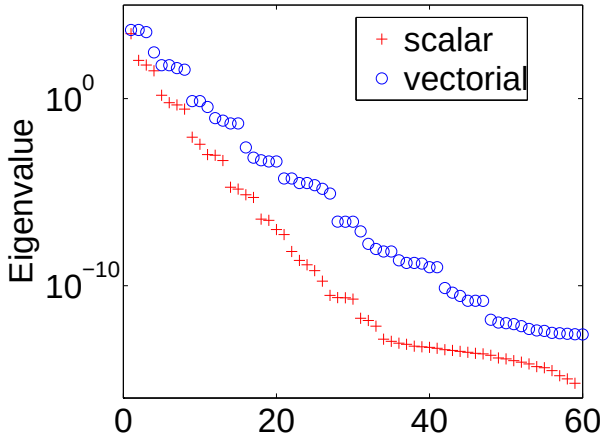


**Figure 3.8 :** *Eigenvalue of the time reversal operator in homogeneous space. Red-add line: scalar illumination, blue-circle line: vectorial illumination.*

The intensity map generated by the eigenvectors corresponding to the first three eigenvalues is shown in Fig. 3.9. As explained in the scalar configuration, the first three symmetric eigenvectors generate backpropagated waves focusing on the scatter. The fourth antisymmetric eigenvector generates a wave presenting a minimum on the scatterer. We can conclude that with the vectorial configuration, we can obtain more abundant information of the target.

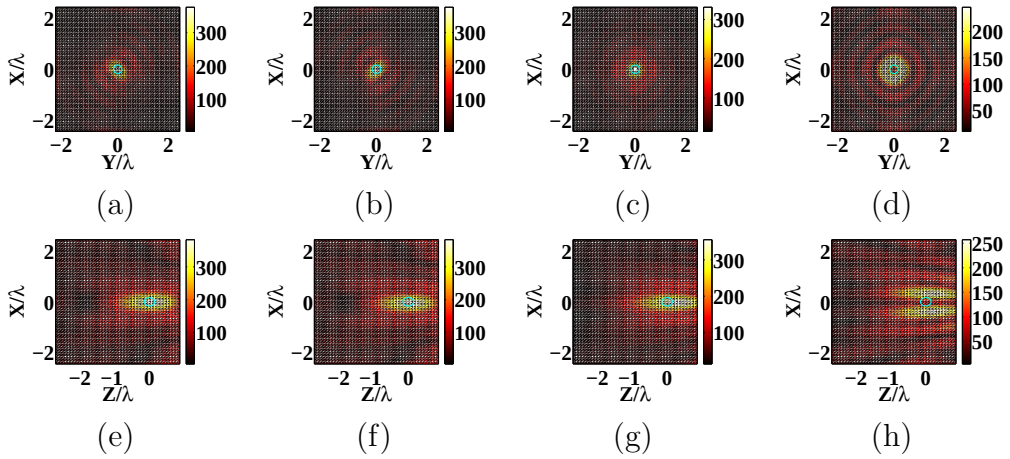


**Figure 3.9 :** *Same as Fig. 3.4, while with vectorial illumination, where the emitting and receiving antennas are oriented along three different directions.*

Up to now, with the limited-aspect data, the number of eigenvalues corresponding to each target is the same as that of complete configuration, except that the focalization along $z$-direction is better in the complete configuration than for the limited-aspect configuration. The illumination is only from one side of the target, the NA of illumination and observation is limited. One option to reduce the axial extension of the spot is to introduce the isotropic focusing concept, realized by placing a mirror in the experimental setup[98].

### 3.4.2 Half-space configuration

We propose to test the DORT method in the half-space configuration, as shown in Fig. 3.10, where the permittivities of medium 1 and 2 are different. The interface interaction has to be considered in our simulations. The measurement surface is the same as that of the homogeneous space, the data are obtained with the CDM forward solver for which the mesh size of the scattering domain $a = \lambda/18$ where $\lambda = 0.6$ m is the wavelength in vacuum. The flat interface separating the measurement medium (air) and the host medium (drive soil of relative permittivity $\varepsilon_b = 3$) where targets are buried in is at $z = \lambda$. One single sphere located at origin with radius $r = \lambda_{\text{ref}}/8$ and relative permittivity $\varepsilon = 5$ is confined entirely in a large box $W$ beneath the interface and of volume $(3\lambda \times 3\lambda \times 3\lambda)$ m$^3$. The scattering domain $W$ is centered at $(0, 0, -0.5\lambda_{\text{ref}})$. Similar as for the homogeneous space configuration, we also divide our investigation into two parts, scalar illumination and vectorial illumination. In this section, the targets are assumed to be buried in noiseless medium. The focalization ability of DORT for the half-space configuration with the presence of clutter will be investigated in the Chap. 4.

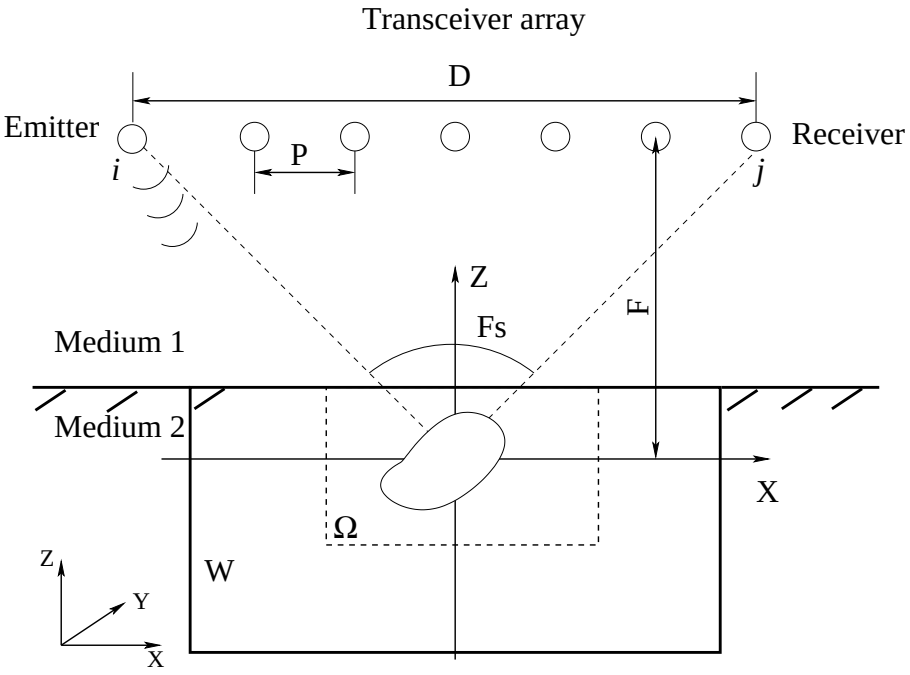


**Figure 3.10 :** *Geometry of the scattering problem in half-space. The scatterers are confined in the scattering domain $W$, separated from the antennas by an interface. $\Gamma$: measurement surface.*

#### 3.4.2.1 Scalar illumination

In this scalar case, the antennas are oriented along one single direction, for example, $x$-axis. The intensity map of the backpropagated fields for the half-space configuration with a scalar illumination is shown in Fig. 3.11. Compared with the homogeneous space case, Fig. 3.4, the spot is further extended along $z$-direction due to the limited effective numerical aperture of the imager in the half-space configuration. The focusing ability in the direction normal to the interface is significantly deteriorated. The behavior of the eigenvalues and eigenvectors are unchanged.

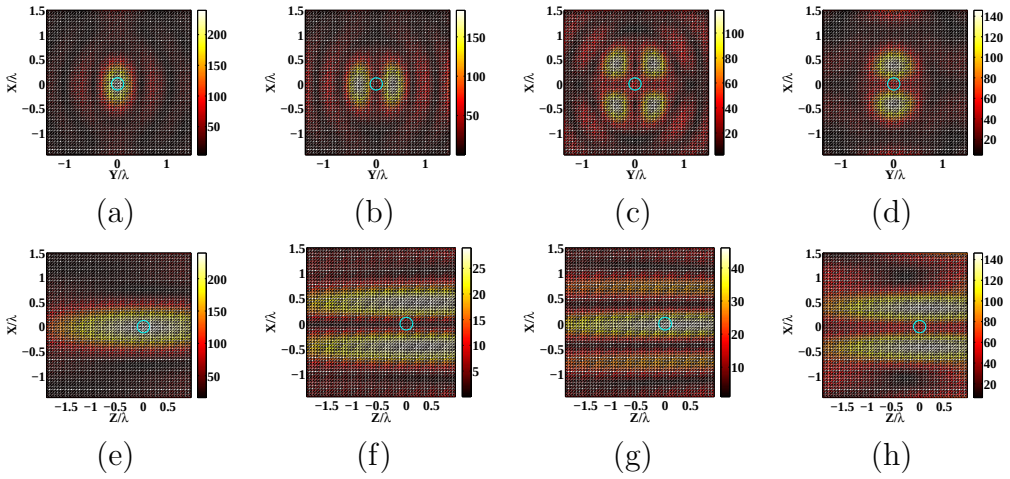


**Figure 3.11 :** *Intensity map in $W$ of the electric field deduced from four eigenvectors related to the four largest eigenvalues using illuminations at the wavelength $\lambda = 0.6$ $m$, when one single scatterer is embedded in the soil and the antennas located in the air are oriented along $x$-direction. (a)-(d): in the $(x, y)$ plane for $z = 0$. (e)-(h): in the $(x, z)$ plane for $y = 0$. Each column corresponds to the first, the second, the third and the fourth eigenvalue. The circle represent the actual profile of the target.*

### 3.4.2.2 Vectorial illumination

In case of the antennas taking three different orthogonal orientations ($x$-axis, $y$-axis and $z$-axis), the focalization map is given in Fig. 3.12. Note that due to the limited numerical aperture of the half-space configuration, the number of eigenvalues associated to each scatterer is smaller than that of the homogeneous background configuration (two instead of three).

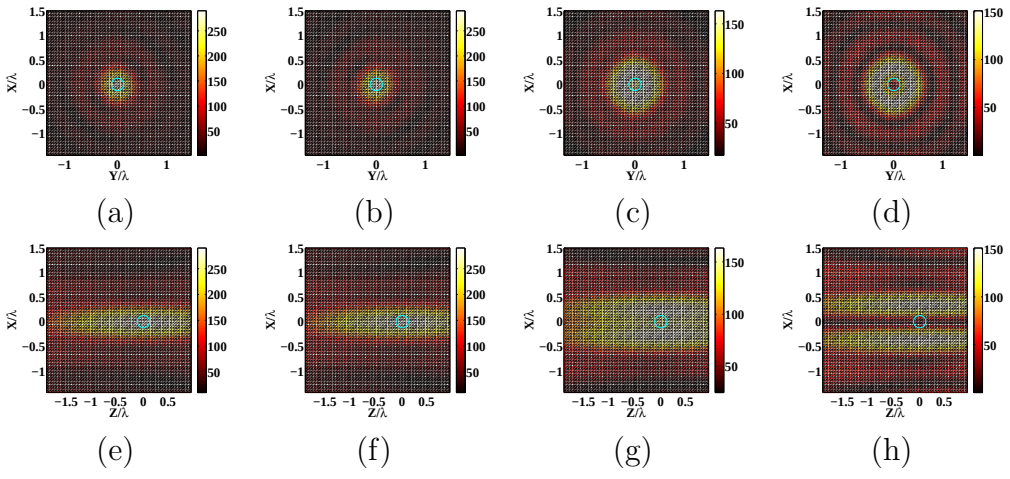


**Figure 3.12 :** *Same as Fig. 3.11, while the antennas take three orthogonal directions.*

## 3.5 Conclusions

In this chapter, we present one of the time reversal technique in the time-harmonic regime, the DORT method. It permits to localize and enumerate echogeneous scatterers in cluttered medium. We have analyzed the effect of the polarization and reported some simple examples on the focalization of one single scatterer in homogeneous space or in half-space configuration. The behavior of the invariance parameters of the time reversal operator has been analyzed, with respect to different levels of noise and with respect to the backgrounds (homogeneous and half-space). Owing to the DORT method, the investigating domain can be restricted to the 'brightest' region provided by the focusing wave which is much smaller than the scattering domain. We can summarize all the results above concerning the behavior of the eigenvalues in Table. 3.1, with one single dielectric scatterer present in noiseless medium. The limited-aspect data case will be further studied in Chap. 4, both for homogeneous space and for half-space configuration.

| | Complete | Limit-homogeneous | Limit-half |
|---|---|---|---|
| Scalar illumination | 1 | 1 | 1 |
| Vectorial illumination | 3 | 3 | 2 |

**Table 3.1 :** *Number of dominant eigenvalues with respect to different configurations. Complete configuration: sources and receivers are regularly placed along all possible directions within* $4\pi$ *steradians. Limit-homogeneous: homogeneous background configuration with the limited-aspect data. Limit-half: half-space configuration with the limited-aspect data.*

In addition to the focalization ability of the DORT method, we also propose to include these focusing fields into the HM for reducing the computation time and augmenting the signal-to-clutter ratio of characterization in case of cluttered medium. This is reported in detail in the next chapter.

Chapter 4

# Numerical synthetic results of focalization and characterization for scatterers in highly cluttered environment

This chapter is related to two publications:
1. T. Zhang, P. C. Chaumet, E. Mudry, K. Belkebir and A. Sentenac, *Electromagnetic wave imaging of targets buried in a cluttered medium using an hybrid Inversion-DORT method*, Inverse Problems, **28**, 125008 (2012);
2. T. Zhang, P. C. Chaumet, A. Sentenac and K. Belkebir, *Three-dimensional imaging of targets buried in a cluttered semi-infinite medium* , Journal of Applied Physics, **114**, 143101 (2013).

## Contents

# 4.1 Introduction

We have reported the principle of the DORT method, which permits to localize scatterers in cluttered environment, and we have given preliminary results of focalization using the DORT method in the presence of one single scatterer. Moreover, we presented the clutter model where the permittivity of the medium fluctuated is of the form of Gaussian function. Generally, we take a large scattering domain for generating the synthetic data. Thanks to the DORT method, the investigating domain used for reconstructing targets can be restricted to the 'brightest' region much smaller than the scattering domain. The inversion techniques which reconstruct the permittivity map of a given investigating domain have been explained in Chap. 2. The accuracy of the non-linear reconstructions is strongly dependent on the signal to noise ratio and on the size of the investigating domain[13]. When targets are buried in an inhomogeneous medium, the investigating domain should be large enough to account properly for the perturbation induced by the clutter. In this case, the inversion requires important computational resources, especially in the three-dimensional vectorial configuration, and often fails because of the large number of unknowns compared to the number of data.

In this chapter, we propose to combine the advantages of the non-linear inversion methods to that of the DORT method. We show that this hybrid technique can be used to detect, localize and characterize targets buried in highly contrasted clutter supporting multiple scattering in a much better way than the classical inversion methods alone. Hereafter the combined DORT-inversion method will be called HM-DORT, and the classical inversion method will be called HM. Our analysis is supported by three-dimensional vectorial simulations of an imaging experiment in which two spheres buried in a random inhomogeneous medium are illuminated and observed by an array of monochromatic micro-wave antennas. We will study this problem in two different configurations, for the homogeneous space configuration, and for the half-space configuration.

# 4.2 Derivation of the HM-DORT

It has been shown that the DORT method provides a means for generating incident fields focusing onto a given scatterer. We propose here to introduce this information in the inversion procedure. This idea was first presented in Ref. 5 in the simplified 2D scalar configuration and yielded a marked improvement of the targets reconstruction, while the definition of the cost functional is different, which will be explained at the end of this section. Another main difference between the scalar and vectorial configuration, apart from the increased computational complexity, is that the DORT analysis provides three eigenvectors focusing on each target in the 3D vectorial homogeneous case (two eigenvector for the 3D vectorial half-space configuration) whereas it provides only one eigenvector in the scalar case. Hence, we expect the HM-DORT to be even more interesting in the 3D vectorial configuration than in the scalar configuration.

To introduce the DORT fields in the inversion procedure, we note $\boldsymbol{E}_{\zeta}^{\mathrm{inc;DORT}}$, $\zeta = 1, \cdots, N_{\mathrm{ev}}$, the DORT incident fields that focus onto the targets. Here, $N_{\mathrm{ev}}$ is the number of the eigenvalues

associated with the targets. The number of $N_{\text{ev}}$ can be determined from Tab. 3.1, while for several cases in presence of strong noise, the eigenvalues belonging to the targets would be blurred by the noise. The scattered field $\boldsymbol{f}_{\zeta}^{\text{DORT}}$ associated to the incident field $\boldsymbol{E}_{\zeta}^{\text{inc;DORT}}$ is easily calculated through, Eq. (3.12), and reads

$$\boldsymbol{f}_{\zeta}^{\text{DORT}}(\boldsymbol{r}) = \sum_{l=1}^{N} \sum_{\alpha}^{x,y,z} V_{l,\alpha}(\zeta) \boldsymbol{f}_{l,\alpha}^{\text{mes}}(\boldsymbol{r}). \tag{4.1}$$

As described in Sec. 2.2.4, we suggest here to use $N_{\text{ev}}$ incident field $\boldsymbol{E}_{\zeta}^{\text{inc;DORT}}$ and $N$ scattered field $\boldsymbol{f}_{\zeta}^{\text{DORT}}$ derived from DORT in the iterative scheme, instead of the incident field $\boldsymbol{E}_{l,\alpha}^{\text{inc}}$ and the scattered field $\boldsymbol{f}_{l,\alpha}^{\text{mes}}$. Therefore, the contrast and the total fields in the test domain $\Omega$ are determined iteratively by minimizing a cost functional of the form at the iteration $n$

$$\mathcal{F}_n^{\text{DORT}}(\chi_n, \boldsymbol{E}_{\zeta,n}^{\text{DORT}}) = W_{\Omega}^{\text{DORT}} \sum_{\zeta=1}^{N_{\text{ev}}} \|\boldsymbol{h}_{\zeta,n}^{(1;\text{DORT})}\|^2 + W_{\Gamma}^{\text{DORT}} \sum_{\zeta=1}^{N_{\text{ev}}} \|\boldsymbol{h}_{\zeta,n}^{(2;\text{DORT})}\|^2, \tag{4.2}$$

where the residual error $\boldsymbol{h}_{\zeta,n}^{(1;\text{DORT})}$ and $\boldsymbol{h}_{\zeta,n}^{(2;\text{DORT})}$ are defined similar to $\boldsymbol{h}_{l,n}^{(1)}$ and $\boldsymbol{h}_{l,n}^{(2)}$, respectively,

$$\boldsymbol{h}_{\zeta,n}^{(1;\text{DORT})} = \boldsymbol{E}_{\zeta,n}^{\text{DORT}} - \boldsymbol{E}_{\zeta}^{\text{inc;DORT}} - \overline{\overline{\boldsymbol{A}}} \chi_n \boldsymbol{E}_{\zeta,n}^{\text{DORT}}, \tag{4.3}$$

$$\boldsymbol{h}_{\zeta,n}^{(2;\text{DORT})} = \boldsymbol{f}_{\zeta}^{\text{DORT}} - \overline{\overline{\boldsymbol{B}}} \chi_n \boldsymbol{E}_{\zeta,n}^{\text{DORT}}. \tag{4.4}$$

The normalizing coefficients $W_{\Omega}^{\text{DORT}}$ and $W_{\Gamma}^{\text{DORT}}$ are given by

$$W_{\Omega}^{\text{DORT}} = \frac{1}{\sum_{\zeta=1}^{N_{\text{ev}}} \|\boldsymbol{E}_{\zeta}^{\text{inc;DORT}}\|_{\Omega}^2} \quad \text{and} \quad W_{\Gamma}^{\text{DORT}} = \frac{1}{\sum_{\zeta=1}^{N_{\text{ev}}} \|\boldsymbol{f}_{\zeta}^{\text{DORT}}\|_{\Gamma}^2}. \tag{4.5}$$

The updating directions are taken to be of the same form as the ones described in subsection 2.2.4, where the gradients are involved with the cost functional $\mathcal{F}_n^{\text{DORT}}$. Notice that the definition of the cost function is different from the two-dimensional case that was done by Dubois. In Ref. 5, the DORT field was introduced into the cost function as $\mathcal{F}_n^{\text{DORT}} \times \mathcal{F}_n$ or $\mathcal{F}_n + \gamma^2 \mathcal{F}_n^{\text{DORT}}$. Here, we use only the DORT incident fields $\mathcal{F}_n^{\text{DORT}}$ in the cost functional, which permits to reduce significantly the number of unknowns of the inverse problem. Indeed, for 3D vectorial configuration in homogeneous space, the cost function $\mathcal{F}_n$ is a non-linear expression with respect to $6N$ complex unknown $(\kappa_{l,\alpha,n;\boldsymbol{\nu}}, \kappa_{l,\alpha,n;\boldsymbol{\omega}})$ and two real unknown $(\beta_{n;\xi}, \beta_{n;\eta})$, while the cost function $\mathcal{F}_n^{\text{DORT}}$ depends only on $2N_{\text{ev}}$ complex unknown $(\kappa_{\zeta,n;\boldsymbol{\nu}}, \kappa_{\zeta,n;\boldsymbol{\omega}})$ and two real unknown $(\beta_{n;\xi}, \beta_{n;\eta})$. On the contrary, if we use $\mathcal{F}_n^{\text{DORT}} \times \mathcal{F}_n$ as the new cost functional, it is related to $6N + 2N_{\text{ev}}$ complex unknown $(\kappa_{l,\alpha,n;\boldsymbol{\nu}}, \kappa_{l,\alpha,n;\boldsymbol{\omega}})$ and two real unknown $(\beta_{n;\xi}, \beta_{n;\eta})$. Hence, in three-dimension, we suggest to use $\mathcal{F}_n^{\text{DORT}}$ as the cost functional as expecting to reduce drastically the computational time with this procedure.

## 4.3 Homogeneous space configuration

Similar as the discussions in Chap. 3, we perform some simulation work in the homogeneous space configuration with DORT and HM as a first step. The three-dimensional imaging configuration simulated in this section is depicted in Fig. 4.1. We consider an infinite homogeneous lossless medium of permittivity $\varepsilon_b$. Targets under study are defined by their relative permittivity $\varepsilon$ and are confined in a domain $W$. They are surrounded by an inhomogeneous medium with relative permittivity $\varepsilon_c(\boldsymbol{r}) = \varepsilon_b + \varepsilon_f(\boldsymbol{r})$ where $\varepsilon_f(\boldsymbol{r})$ is a random function which is null outside $W$ and whose average is null over $W$. A two-dimensional array of $N$ crossed-dipole monochromatic antennas lying in a plane above $W$ is used to illuminate and observe the scene. This configuration resembles that

which is encountered in the detection of buried objects, except that the antennas lying in the same homogeneous medium as the targets, and we do not consider the interface effect here. Note that, in practice this configuration can be obtained with a proper impendance matching of the antennas or an appropriate time windowing. The finite size of the clutter expansion, which is necessary for computation purpose, is chosen wide enough for representing an 'infinite' clutter perturbation.

In this section, we first compare, on a given configuration, the performances of the HM-DORT to that of the DORT or HM alone. Then, we study the robustness of the HM-DORT with respect to the structural noise surrounding the scatterers. Last, we point out the interest of using a non-linear inversion scheme and the full-polarized data for retrieving the targets.

### 4.3.1 Computational setup

In most cases, the scattering domain $W$ of the imaging configuration depicted in Fig. 4.1 is a box with size $(5\lambda \times 5\lambda \times 4\lambda)$ box, centered at $(0, 0, -\lambda)$ where $\lambda$ is the illumination wavelength in the homogeneous lossless medium. The antenna array is described by a lattice of $N = 81$ antennas regularly distributed on a square of side of $8\lambda$, which is located at $z = 2\lambda$, *i. e.* $\lambda$ above the cluttered environment. In most of our reported cases, the antennas take three different orientations, with $\alpha = x, y, z$.

The scattering domain includes two dielectric spheres embedded in a highly cluttered environment. The smallest sphere, centered at the origin, has a radius of $\lambda/6$, with relative permittivity $\varepsilon = 3\varepsilon_b$. The largest sphere is located at $(0.5\lambda, 0, -0.7\lambda)$ and has a radius of $\lambda/4$ with the same relative permittivity. The random permittivity of the clutter, $\varepsilon_f(\boldsymbol{r})$, is defined as a Gaussian variable with zero mean and standard deviation $\sigma_f$ and Gaussian correlation function $C(\boldsymbol{r})$ with correlation length $l_c$, modeled as Eq. (3.1).

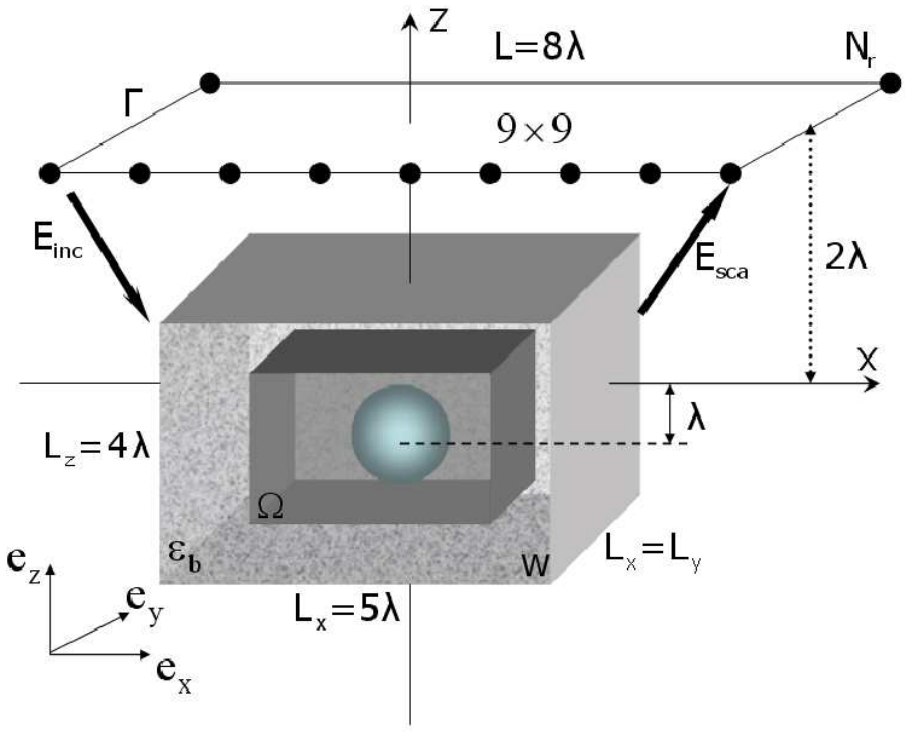


**Figure 4.1 :** *Geometry of the problem. The transmitters and receivers are regularly distributed on a plane, located on one side of the objects. The objects are confined in a disordered medium $W$.*

To indicate the presence of multiple scattering within $W$, we introduce $\mathrm{Err}_{\mathrm{born}}$ as

$$\mathrm{Err}_{\mathrm{born}} = \frac{\sum_{l=1}^{N}\sum_{\alpha}^{x,y,z} \|\boldsymbol{E}_{l,\alpha}^{\mathrm{sca}} - \boldsymbol{E}_{l,\alpha}^{\mathrm{sca;born}}\|_{\Gamma}^{2}}{\sum_{l=1}^{N}\sum_{\alpha}^{x,y,z} \|\boldsymbol{E}_{l,\alpha}^{\mathrm{sca}}\|_{\Gamma}^{2}}, \tag{4.6}$$

where $\boldsymbol{E}_{l,\alpha}^{\mathrm{sca;born}}$ is the scattered field computed under the classical Born approximation[76], stated as in Sec. 1.4.4.4, *i.e.* the total field inside the clutter and targets $\boldsymbol{E}_{l,\alpha}$ is assumed to be equal to the incident field $\boldsymbol{E}_{l,\alpha}^{\mathrm{inc}}$. Eq. (2.2) can be rewritten as

$$\boldsymbol{E}_{l,\alpha}^{\mathrm{sca;born}}(\boldsymbol{r}) = \int_{\Omega} \boldsymbol{G}(\boldsymbol{r},\boldsymbol{r}')\chi(\boldsymbol{r}')\boldsymbol{E}_{l,\alpha}^{\mathrm{inc}}(\boldsymbol{r}')\mathrm{d}\boldsymbol{r}'. \tag{4.7}$$

The Born approximation is usually valid if the target is weakly scattering (with small permittivity contrast or small size).

### 4.3.2 Comparison of the HM-DORT with the DORT and inversion techniques

In this first study, we consider an uncorrelated clutter (the correlation length $l_c = \lambda/10$ being equal to the mesh size) with a realization-dependent standard deviation of $\varepsilon_f$ is $\sigma_f$=0.068$\varepsilon_b$ yielding to $\mathrm{Err}_s = 174\%$, $\mathrm{Err}_d = 2\%$ and $\mathrm{Err}_{\mathrm{born}} = 48\%$ respectively. The values of $\mathrm{Err}_{\mathrm{born}}$ and $\mathrm{Err}_d$ indicate that the configuration supports moderate multiple scattering (within the targets and within the clutter) but that the interaction between targets and the clutter is weak. We first perform the DORT analysis of the scattered field data. The evolution of the eigenvalue in presence of clutter is given in Fig. 4.2. There exist six significant eigenvalues with respect to other tiny ones. To determine the correspondence between the eigenvalues and the scatterers, we provide the intensity map generated by the corresponding eigenvectors, shown in Figs. 4.3 and 4.4.

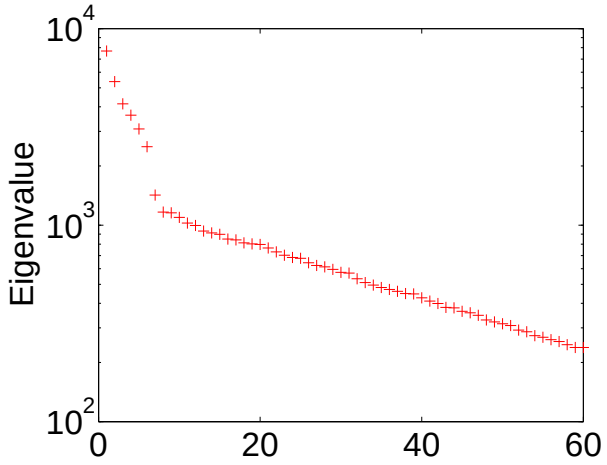


**Figure 4.2 :** *Eigenvalue of the time reversal operator in homogeneous space with vectorial illumination, with the clutter* $l_c = \lambda/10$ *and* $\sigma_f$=0.068$\varepsilon_b$.

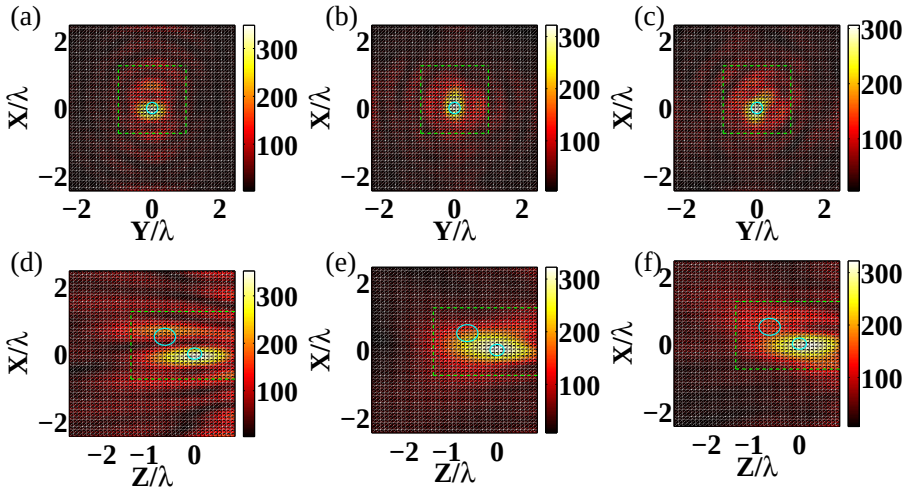


**Figure 4.3 :** *Intensity map in $W$ of the electric field formed by the three eigenvectors of the TRO related to the three largest eigenvalues. These three eigenvectors focus on the sphere which is the closest to the antennas. The clutter is described by $l_c = \lambda/10$, $\sigma_f = 0.068\varepsilon_b$ with $\mathrm{Err}_s = 174\%$ $\mathrm{Err}_d = 2\%$ and $\mathrm{Err}_{\mathrm{born}} = 48\%$ . (a)-(c) maps in $(x, y)$ plane at $z = 0$. (d)-(f) maps in $(x, z)$ plane at $y = 0$. Each column corresponds to the first, the second and the third eigenvalue. The dash box indicates the investigating domain $\Omega$ used in the inversion procedure.*

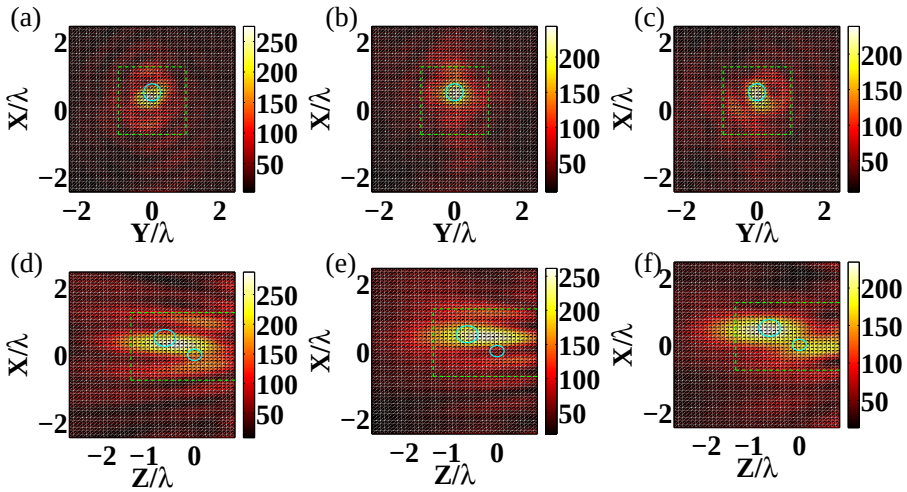


**Figure 4.4 :** *Same as Fig. 4.3, but the eigenvectors correspond to the fourth, fifth and sixth eigenvalues. They focus on the sphere which is the furthest from the antennas. (a)-(c) maps in $(x, y)$ plane at $z = -0.7\lambda$. (d)-(f) maps in $(x, z)$ plane at $y = 0$. Each column corresponds to the fourth, the fifth and the sixth eigenvalue.*

Figures 4.3 and 4.4 show the intensity of the electric field radiated by the antennas in the homogeneous medium with permittivity $\varepsilon_b$, with the currents given by the eigenvectors of the TRO. As expected, the first three eigenvalues correspond to the scatterer whose signature on the

antennas is dominant. In our configuration, it corresponds to the smallest sphere which is closer to the antennas than the largest one. The fourth to the sixth eigenvalues correspond to the second most important signature, which is that of the largest sphere. There are three eigenvalues focusing on each scatterer, depending on the polarization of the antennas. In section 3.4, we have checked that if only one component of polarization is used in the scattered field data, there is only one eigenvalue related to the scatterer. This is in agreement with the conclusion of Ref. 3. In this incomplete imaging configuration, it is seen that the DORT eigenvectors allows the localization of the two scatterers with, however, an anisotropic spots, particularly elongated along the illumination direction ($z$-axis).

In a second step, we apply the HM-DORT to the scattered field data in order to reconstruct quantitatively the permittivity map of the investigating domain. The investigating domain $\Omega$ is limited to the 'brightest' region given by the DORT field intensity map, *i.e.* a box placed at $[-0.75\lambda, 1.25\lambda] \times [-\lambda, \lambda] \times [-1.5\lambda, \lambda]$, which is indicated by the dashed squares plotted in Figs. 4.3 and 4.4. The inversion procedure is stopped when the cost functions reach a plateau.

To quantify the quality of the image we also define a contrast reconstruction error as

$$\mathrm{Err}_\chi = \frac{\|\chi_{\mathrm{actual}} - \chi_{\mathrm{rec}}\|_\Omega^2}{\|\chi_{\mathrm{actual}}\|_\Omega^2}, \tag{4.8}$$

where $\chi_{\mathrm{actual}}$ is the permittivity contrast of the actual objects while $\chi_{\mathrm{rec}}$ is the reconstructed permittivity contrast.

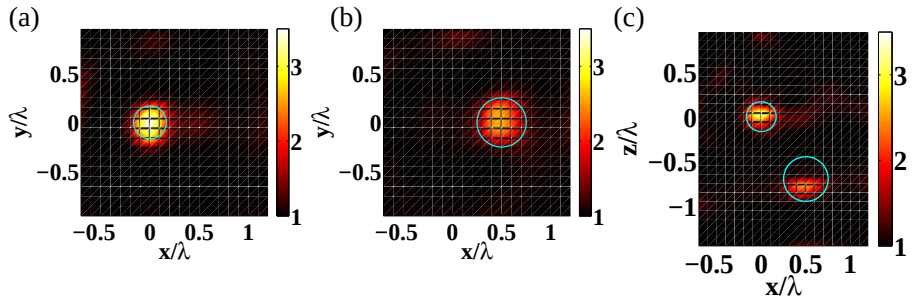


**Figure 4.5 :** *HM-DORT reconstructed permittivity obtained for the same configuration as that described in Fig. 4.3 (a) and (d) maps in the $(x, y)$ plane at $z = 0$ and $z = -0.7\lambda$ respectively. (c) map in the $(x, z)$ plane for $y = 0$.*

In Fig. 4.6, we compare the HM-DORT reconstruction to that obtained with the HM scheme without using focusing waves.

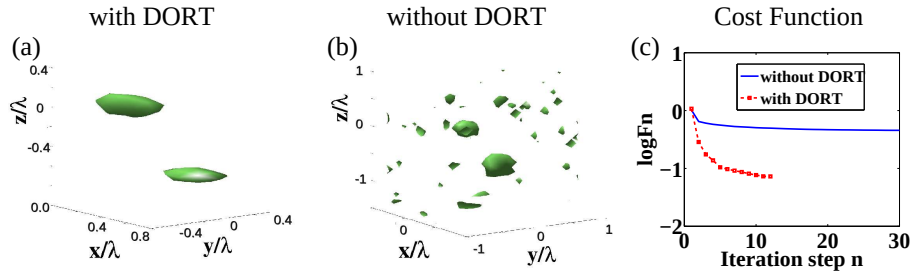


**Figure 4.6 :** *The configuration is the same as that described in Fig. 4.3. (a) Iso-surface of the reconstructed permittivity profile at $\varepsilon = 2$ using the HM-DORT procedure. (b) same as (a) using the HM inversion procedure. (c) Evolution of the cost function (log-scale representation) versus the iteration step using the HM-DORT (dashed curve) and HM (solid curve). All these plots correspond to the reconstruction shown in Fig. 4.5.*

We observe a better localization using the HM-DORT procedure than the DORT method, especially in the $z$-direction. Moreover, a better characterization is obtained with the HM-DORT than with the HM alone. The HM-DORT procedure permits to avoid the ghosts that are present around the targets in the HM reconstruction. This is confirmed by the contrast error criterion $\mathrm{Err}_\chi$ which is equal to 63% for the HM-DORT and to 153% for the HM. Moreover, the cost function converges more quickly with the HM-DORT than with the HM, the converged value being one order of magnitude, lower in the former case than in the latter. The HM-DORT computational time, (206 s), is about 200 times shorter than that of the HM scheme. This discrepancy is explained by the number of incidences and the convergence rate, see Fig. 4.6 (c). Indeed, the HM-DORT uses only 6 incidences (which correspond to the significant eigenvectors of the TRO) whereas the HM scheme uses 243 different incidences.

The HM-DORT technique can also be used to reconstruct the targets sequentially. In Fig. 4.7, we have restricted the investigating domain to a smaller domain $\Omega_1$ ($\Omega_2$) that surrounds the first (second) target. In this case, sole the incident fields focusing on the chosen target are kept in the inversion process. We observe in Fig. 4.7 that this sequential reconstruction yields a better estimation of the targets while diminishing the computational time. With the HM using non-optimized incident fields, the selective reconstruction on $\Omega_1$ and $\Omega_2$ is worse than that obtained with the initial larger investigating domain $\Omega$, as shown in Fig. 4.8.

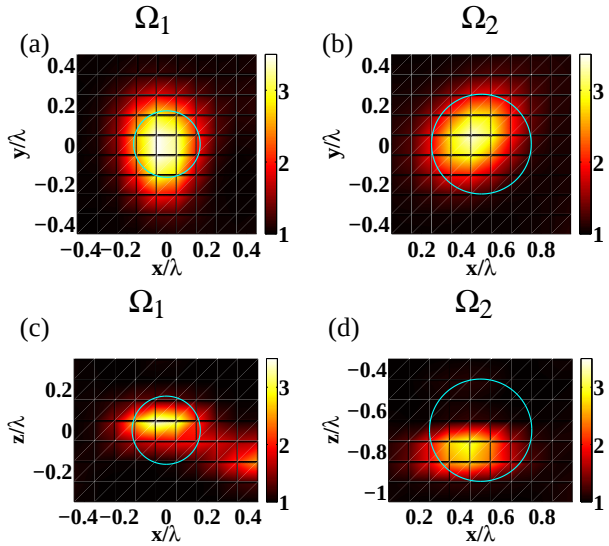


**Figure 4.7 :** *HM-DORT reconstructions for the same configuration as that of Fig. 4.5, but with investigating boxes that are restricted, successively, to domains surrounding each target, $\Omega_1$ and $\Omega_2$. $\Omega_1$ is centered at the origin with size $\lambda \times \lambda \times 0.8\lambda$, while $\Omega_2$ is centered at $(0.5\lambda, 0, -0.7\lambda)$ with same size. (a) map in the $(x, y)$ plane at $z = 0$ in $\Omega_1$. (b) map in the $(x, y)$ plane at $z = -0.7\lambda$ in $\Omega_2$. (c) map in the $(x, z)$ plane at $y = 0$ in $\Omega_1$. (d) map in the $(x, z)$ plane at $y = 0$ in $\Omega_2$.*

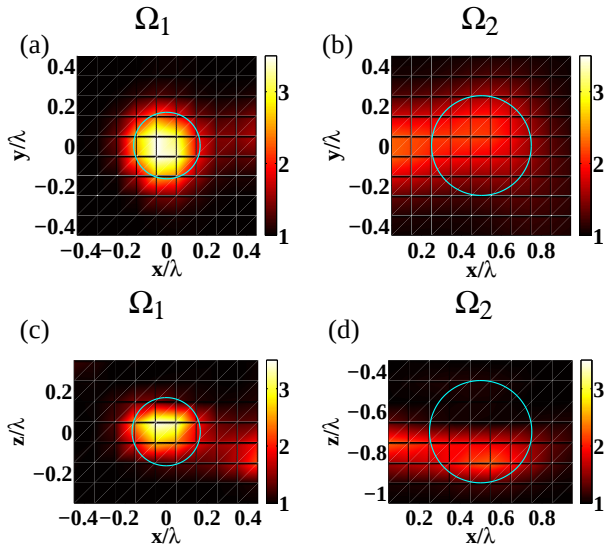


**Figure 4.8 :** *Same as Fig. 4.7, but with the HM procedure.*

### 4.3.3 Influence of the size of the clutter and of its specific permittivity distribution

The size of the scattering domain chosen for these simulations may be thought too small to mimic accurately a realistic experiment where the targets are buried in an infinite inhomogeneous soil.

Indeed, as it stands the width of $W$ is smaller than the antennas lattice width. We have thus performed other experiments with twice bigger scattering domains to check that the reconstructions provided by the HM-DORT procedure were not changed. More precisely, we considered a scattering domain $W$ of size $(10\lambda \times 10\lambda \times 10\lambda)$ that is enlarged by a factor of two in $x$, $y$ directions and of two and a half in $z$ direction as compared to the one chosen in the previous simulation. For a meaningful comparison, we kept exactly the same clutter around the objects as that used in Fig. 4.5.

We observe in Fig. 4.9 that the six dominant eigenvectors of the TRO for the large scattering domain $W$ yield intensity maps that are very similar to that obtained for the small $W$, Figs. 4.3 and 4.4. Hence, even if the noise level ratio $\mathrm{Err}_s$ is changed from 171% (small $W$) to 541% (large $W$), the DORT method still enables to generate incident fields that focus on targets.

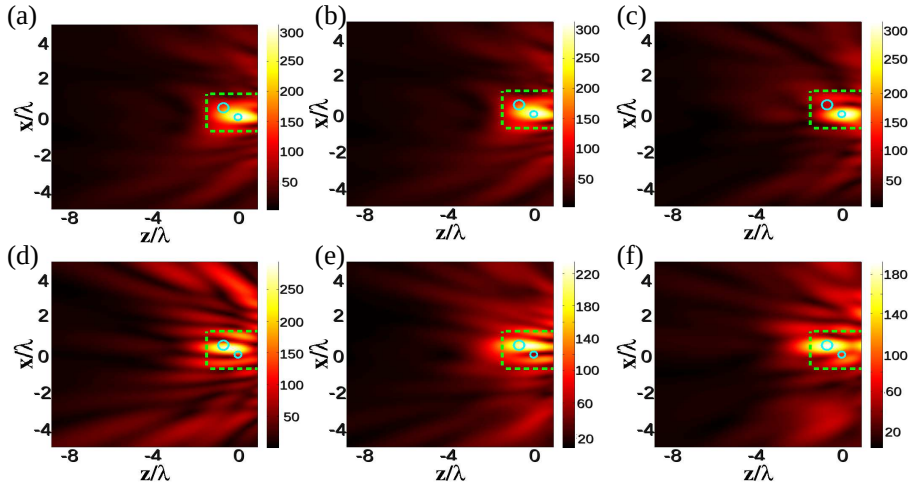


**Figure 4.9 :** *Intensity map of the electric field formed by the eigenvectors of the TRO related to the six largest eigenvalues in $(x, z)$ plane for $y = 0$, for a configuration similar to that used for Figs. 4.3 and 4.4, except that the scattering domain $W$ is ten times larger.*

Comparing Fig. 4.5 with Fig. 4.10, we observe that the reconstruction obtained with the HM-DORT procedure for large $W$, is very close to that obtained with small $W$, with similar contrast errors, $\mathrm{Err}_\chi = 68\%$ and 62% respectively.

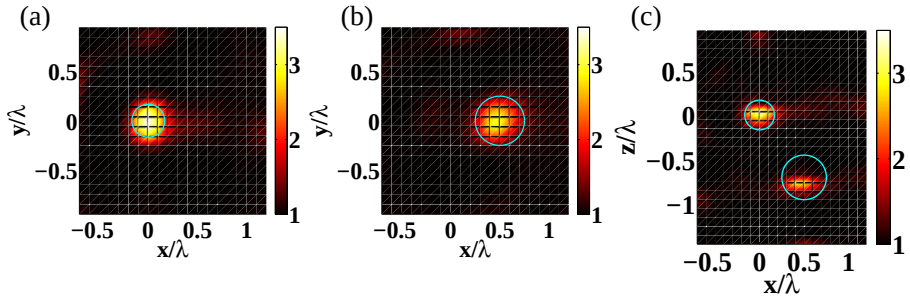


**Figure 4.10 :** *HM-DORT reconstructed permittivity for a configuration similar to that used in Fig. 4.5 except that the scattering domain $W$ is ten times larger, (the investigating domain $\Omega$ is kept the same). (a) and (b) maps in the $(x, y)$ plane at $z = 0$ and $z = -0.7\lambda$, respectively. (c) map in the $(x, z)$ plane at $y = 0$.*

This result is not surprising as, with the DORT focusing fields, sole the inhomogeneities close to the targets participate to the scattered field data that are used in the inversion procedure. Note that this property may also be considered a drawback, as it confers an increased importance to the specific clutter distribution surrounding the targets. Thus, to check the generality of our results, we have also verified that the reconstructions obtained for different clutter realizations with the same statistics, were similar.

The analysis presented in this section was repeated for different clutter types and always led to the same conclusion: The HM-DORT is always superior to the HM scheme without optimized incident fields for characterizing the targets and for limiting the computational cost and it ameliorates significantly the information brought by the DORT approach alone, in particular for localizing the target along the $z$-axis. Moreover, thanks to the studies conducted on large scattering domain and many clutter realizations, we believe that our simulations give a good estimate of the imaging achievements of the HM-DORT for realistic geometries in which the targets are buried in an infinite clutter with given statistics. We now describe more precisely the performances of the HM-DORT for different clutter types.

### 4.3.4 Robustness of the HM-DORT with respect to the clutter statistics.

In this section, we apply the HM-DORT to data stemming from targets buried in different clutter types. We study the robustness of the reconstructions versus increasing clutter standard deviation $\sigma_f$ and versus the clutter correlation length $l_c$.

#### 4.3.4.1 Influence of the clutter standard deviation.

In this paragraph, the correlation length is kept fixed at $l_c = \lambda/10$, while the standard deviation is increased. In the first example, the realization-dependent standard deviation of $\varepsilon_f$, $\sigma_f$=$0.096\varepsilon_b$, which yields $\mathrm{Err}_s \approx 400\%$ and $\mathrm{Err}_d = 2\%$. The evolution of eigenvalues versus different levels of noise is presented in Fig. 4.11. In case of $\sigma_f = 0.068\varepsilon_b$ (green circle line), the eigenvalues corresponding to the targets can be easily distinguished from those belonging to the noise. As the standard deviation increases, the ones corresponding to the noise space raise so much that there is no significant discrepancy between the echogeneous scatterers and the noise. Fig. 4.12 present the intensity map concerned with the eigenvectors and one can observe that the two scatterers are still well localized.

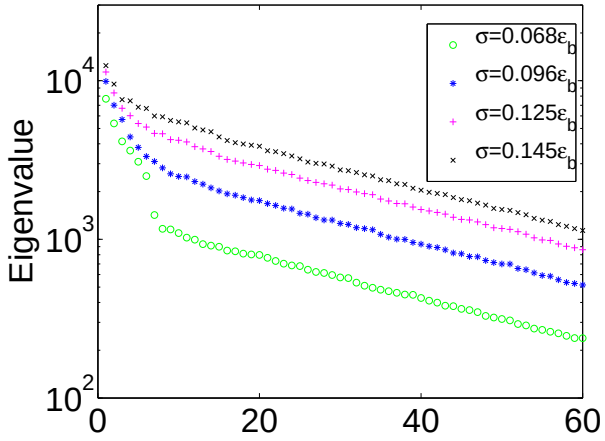


**Figure 4.11 :** *Eigenvalue of the time reversal operator in homogeneous space with vectorial illumination, in presence of two scatterers. The correlation length of the clutter keeps at* $l_c = \lambda/10$*, but the standard deviation is varied:* $\sigma_f = 0.068\varepsilon_b$ *(green-circle line),* $\sigma_f = 0.096\varepsilon_b$ *(blue-star line),* $\sigma_f = 0.125\varepsilon_b$ *(magenta-add line),* $\sigma_f = 0.145\varepsilon_b$ *(black-cross line).*

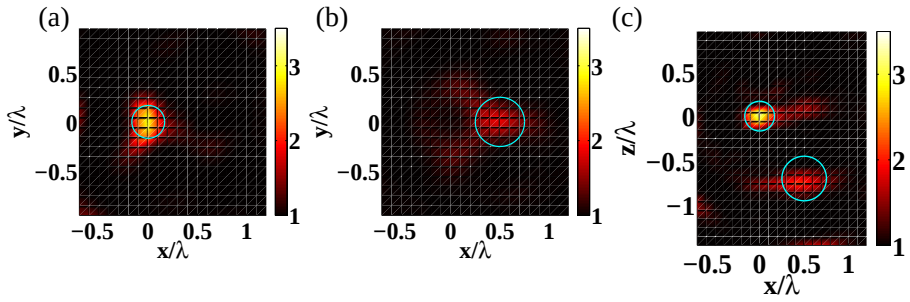


**Figure 4.12 :** *Same as Fig. 4.5 but the clutter is defined by* $l_c = \lambda/10$*,* $\sigma_f$*=0.096*$\varepsilon_b$ *yielding* $\mathrm{Err}_s = 400\%$ *and* $\mathrm{Err}_d = 2\%$*.*

In the second example, the standard deviation reaches $\sigma_f$=0.125$\varepsilon_b$, leading to $\mathrm{Err}_s$=682% and $\mathrm{Err}_d = 2\%$. In this case, there is only two eigenvectors that focus on the deepest scatterer (the least echogeneous one), as showed in Fig 4.13 but the selective reconstruction of the targets provided by the HM-DORT is still satisfactory, see Figs 4.14. Note that, in this case, the reconstruction of the least echogeneous target has been obtained using the only two focusing incident DORT fields.

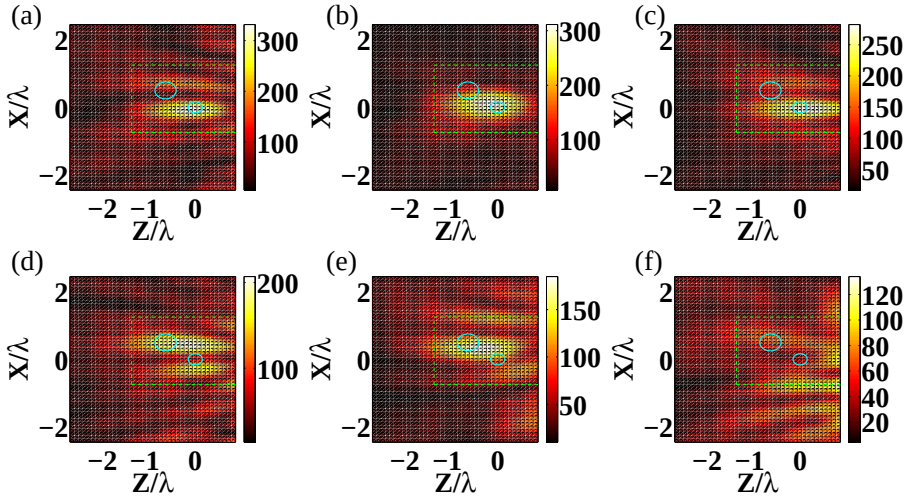


**Figure 4.13 :** *Intensity in the $(x, z)$ plane at $y = 0$, of the electric field given by the six eigenvectors corresponding to the six highest eigenvalues. The structural noise,* $\mathrm{Err}_s = 682\%$ *and* $\mathrm{Err}_d = 2\%$ *is obtained with $l_c = \lambda/10$ and $\sigma_f$=0.125$\varepsilon_b$. Top: the intensity corresponding to the first, the second, the third eigenvalue. Bottom: the intensity corresponding to the fourth, the fifth, the sixth eigenvalue.*

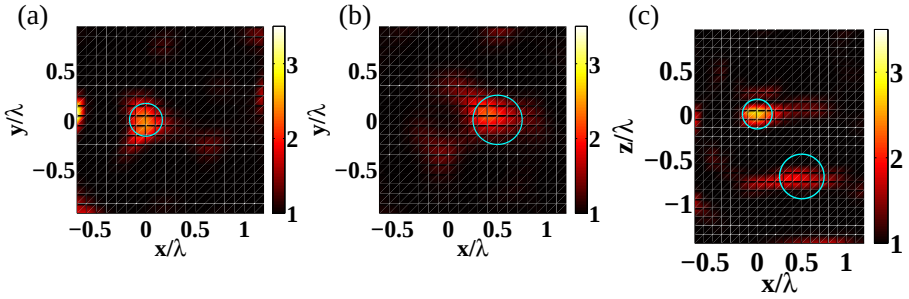


**Figure 4.14 :** *Same as Fig. 4.5 but the clutter is defined by $l_c = \lambda/10$, $\sigma_f$=0.125$\varepsilon_b$ yielding* $\mathrm{Err}_s = 682\%$ *and* $\mathrm{Err}_d = 2\%$.

If the noise is further amplified to reach $\sigma_f$=0.145$\varepsilon_b$, corresponding to $\mathrm{Err}_s = 900\%$ and $\mathrm{Err}_d = 2\%$, the DORT method does not provide any eigenvectors focusing on the deepest scatterer and the related reconstruction is deceiving.

#### 4.3.4.2 Influence of the correlation length.

In this paragraph, we analyze the influence of the clutter correlation length on the reconstruction. We first consider clutters with standard variations $\sigma_f \approx 0.06\varepsilon_b$ and noise levels $\mathrm{Err}_s \approx 200\%$, that are similar to the one taken for Figs. 4.5 and increase the correlation lengths $l_c$ from $\lambda/10$ to $\lambda$. At this moderate noise level, we observe that the DORT focusing properties weakly depend on the correlation lengths. Whatever the correlation lengths, the six dominant eigenvectors yield incident fields that focus on each scatterer. The HM-DORT reconstructions are quite accurate and resembles that obtained for the uncorrelated clutter, Fig. 4.5.

On the contrary, at higher standard deviations, $\sigma_f \approx 0.1\varepsilon_b$ and higher noise levels $\mathrm{Err}_s \approx 400\%$, the DORT focusing properties depend strongly on the correlation lengths. At $l_c = \lambda/10$, one obtains

three eigenvectors focusing on each target and the reconstructions are good and similar to that displayed in Fig. 4.12. For $l_c = \lambda/2$, it becomes difficult to localize the deepest scatterer with the first six dominant eigenvectors intensity maps, as seen in Figure 4.15. However, the HM-DORT permits to retrieve accurately both targets, Fig. 4.16. When $l_c = \lambda$, the focusing properties of the DORT fields are further deteriorated. Moreover, the eigenvectors that are roughly focusing on the least echogeneous target do not correspond to the third, fourth and fifth highest eigenvalues. In this case, it is required to conduct a careful study of the intensity maps of the eigenvectors in order to determine the most significant eigenvectors. This analysis implies that we have some *a priori* information on the sought targets. With this additional procedure, the HM-DORT reconstruction obtained with the six most significant eigenvectors yields a good estimate of the targets. Note that, similarly to the $l_c = \lambda/2$ case, the localization of the targets given by HM-DORT is much better than that obtained with DORT alone.

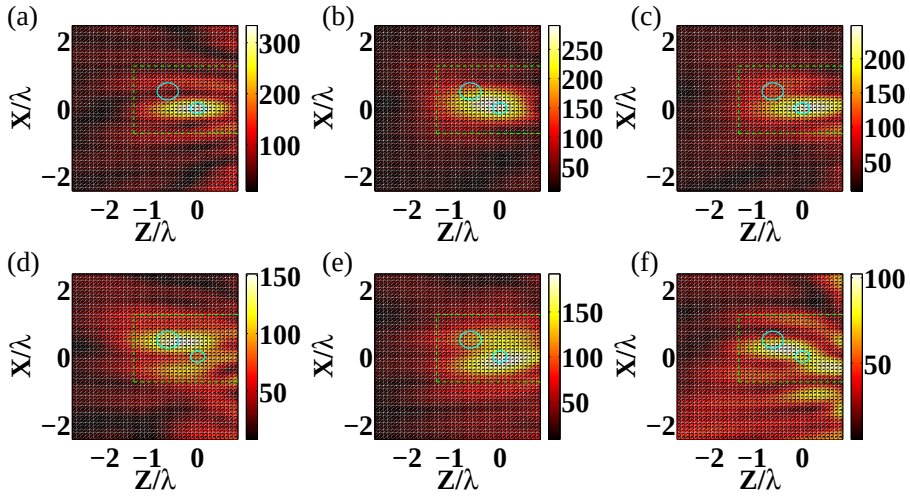


**Figure 4.15 :** *Same as Fig. 4.13, but the clutter with the correlation length $l_c = \lambda/2$, $\sigma_f = 0.1\varepsilon_b$, where the clutter environment corresponds to 400% noise.*

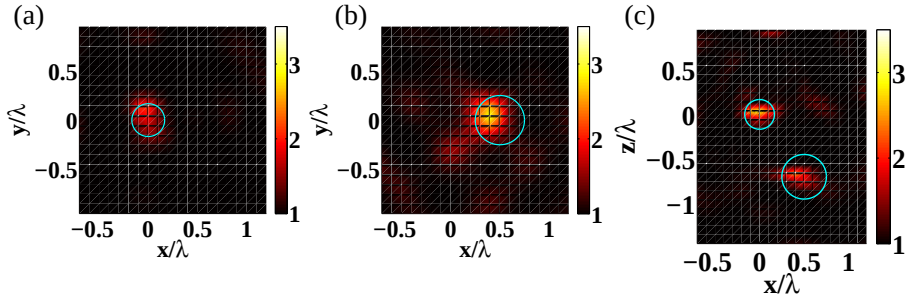


**Figure 4.16 :** *Same as Fig. 4.5, except that the clutter environment corresponds to 400% noise, with the correlation length $l_c = \lambda/2$, $\sigma_f = 0.1\varepsilon_b$.*

#### 4.3.4.3 Influence of the coupling between the targets and the clutter

Up to now, we have considered configurations in which targets and the clutter are weakly coupled, $\mathrm{Err}_d < 5\%$. In other terms, the field detected by the antennas can be modeled by the coherent sum of the field radiated by the spheres in the homogeneous background medium with the field

radiated by the clutter alone. In this paragraph we investigate the performance of the HM-DORT algorithm when there is multiple scattering between the targets and the clutter. Keeping almost the same $\mathrm{Err}_s$ as Fig. 4.5, we chose a configuration with $l_c = \lambda$ and $\sigma(\varepsilon_f) = 0.055\varepsilon_b$, that yielded $\mathrm{Err}_d = 54\%$, $\mathrm{Err}_{\mathrm{born}} = 123\%$. The coupling between the targets and the clutter is caused by the presence of highly contrasted inhomogeneities close to the targets. The HM-DORT reconstruction displayed in Figs. 4.17 (a)-(c) shows that this configuration can be handled without difficulty with our algorithm.

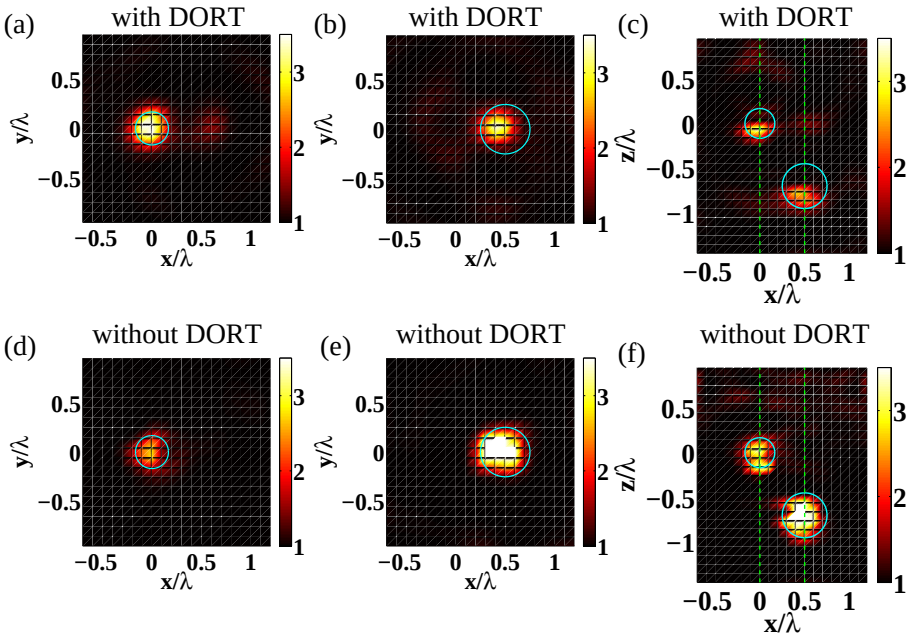


**Figure 4.17 :** *Reconstructed permittivity distribution, (a)-(c): using the HM-DORT. (d)-(f) using the HM procedure. The clutter is defined by* $l_c = \lambda$, $\sigma_f = 0.055\varepsilon_b$ *but one has chosen a specific realization where* $\mathrm{Err}_s = 182\%$ *and* $\mathrm{Err}_d = 54\%$, *implying a significant coupling between the spheres and the clutter.*

Figure 4.18 show that without DORT, the reconstructed relative permittivity of the deepest scatterer is overestimated while that obtained with DORT is accurately retrieved.

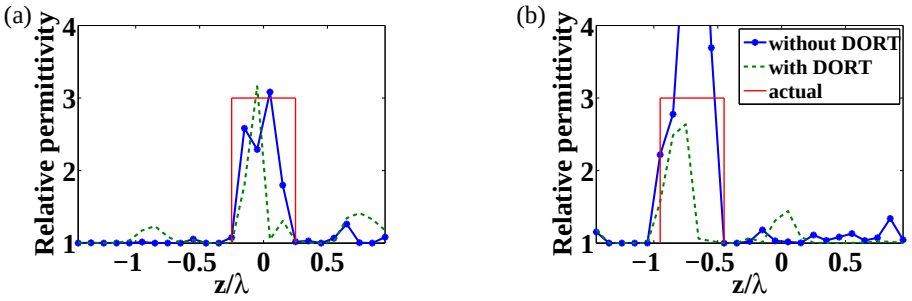


**Figure 4.18 :** *Relative permittivity versus $z/\lambda$ along the vertical line in Fig. 4.17 (c) and (f). (a) $y = 0$ and $x = 0$ (smallest scatterer). (b) $y = 0$ and $x = 0.5\lambda$ (largest scatterer). Solid line presents the actual profile, dashed line reconstruction with DORT and solid line with crosses reconstruction without DORT.*

To summarize this part, we have shown that the HM-DORT algorithm provides satisfactory images of the targets even when they are buried in clutters with high standard deviations (up to $0.125\varepsilon_b$) or large correlation lengths in which the focusing properties of the DORT fields are deteriorated. In the following section, we stress the importance of using a non-linear inversion scheme and the full-polarized data to obtain this performance.

#### 4.3.4.4 Evolution of the reconstruction versus different clutter with the same statistical characteristics

In order to test the stability of our HM-DORT, we choose 20 different noise realizations with the same statistical characteristics as that used in Sec. 4.3.2, *i.e.* the same standard deviation and the same correlation length. Figure 4.19 shows the evolution of the error on the contrast $\mathrm{Err}_\chi$ of the brightest scatterer versus 20 random seeds. The mean value of $\mathrm{Err}_\chi$ is 54%, and the standard deviation is 9%, assuring again that the case presented in Sec. 4.3.2 corresponds to a typical case. We report in Fig. 4.20 the reconstruction for the worst case, *i.e.* $\mathrm{Err}_\chi = 75\%$. The scatterer is still well reconstructed, except that at the edge of the investigating domain, it is deteriorated by the strong noise. Notice that this study has been done for the case of small and large correlation lengths, either in presence of multiple scattering, or using different size of the clutter yielded always the same results: the reconstruction does not depend noticeably of the clutter realizations of the random process but only of the standard deviation and correlation length of the noise.

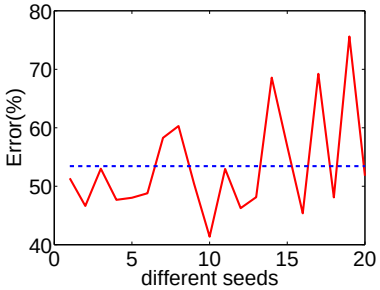


**Figure 4.19 :** $\mathrm{Err}_\chi$ *for the selective reconstruction on the brightest scatterer versus different noise seedings, where $l_c = \lambda/10$, and $\sigma_f = 0.068\varepsilon_b$.*

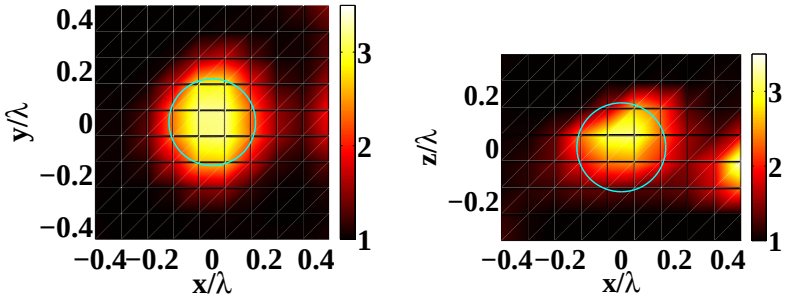


**Figure 4.20 :** *Selective reconstruction results for the brightest scatterer, corresponding to the case of the largest reconstruction error,* $\mathrm{Err}_\chi = 75\%$.

### 4.3.5 Interest of using a non-linear inversion scheme and full polarized data

The HM-DORT used in this work is based on a non-linear inversion scheme. In other terms, both the permittivity and the total field inside the investigating domain $\Omega$ are unknown and sought by the algorithm. In this section, we consider a simpler linear-inversion-DORT technique in which the total field inside $\Omega$ is assumed to be the incident field (Born's approximation). The linear-inversion-DORT scheme is implemented easily from the HM-DORT algorithm by setting the search directions for the total field to zero and enforcing the total field to be equal to the incident field. The interest of the linear-inversion technique is that it is much faster than the non-linear-inversion version. Unfortunately, it is seen in Fig. 4.21 that the linear-HM-DORT scheme fails to retrieve the targets even in the least noisy configuration, $\mathrm{Err}_s = 174\%$, corresponding to Fig. 4.5. In this configuration, the coupling between the targets and the clutter is weak but there is some multiple scattering within the clutter and within the targets as indicated by $\mathrm{Err}_{\mathrm{born}} = 48\%$. The latter is sufficient to deteriorate significantly the performances of the linear inversion scheme. This example stresses the importance of using non-linear inversion techniques even for moderately contrasted clutter ($\sigma_f \approx 0.06\varepsilon_b$) and even if there is no coupling between the targets and the clutter ($\mathrm{Err}_d < 5\%$).

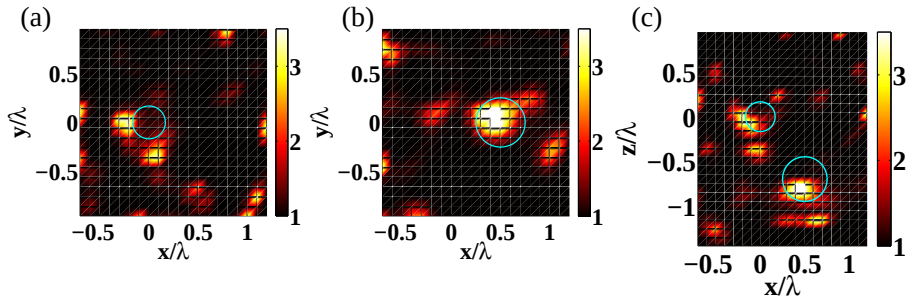


**Figure 4.21 :** *Same as Fig. 4.5 but a linear-HM-DORT procedure assuming single scattering is used for getting the reconstructions.*

Another reason for the performance of our imaging scheme in highly noisy environment is that we use the three orientations of the antennas for illuminating and observing the scene. We are thus able to generate several DORT fields focusing on each targets. We now consider a simpler

imaging configuration where the emitting and receiving antennas are oriented only along the $x$ or $y$-axis so that only scalar data are collected as in an acoustical problem. In this case, only one DORT field focusing on each target can be found. In Fig. 4.22 we plot the reconstructions obtained with these truncated data for the same geometry as that used in Fig. 4.6. We observe a significant deterioration of the results as compared to Fig. 4.6 (a), the reconstruction error on the contrast reaching $\mathrm{Err}_\chi = 191\%$ and $\mathrm{Err}_\chi = 177\%$ for the $x$ and $y$ orientations, to be compared to $\mathrm{Err}_\chi = 62\%$ for the full-polarized data. Hence, even for the least noisy experiment ($\mathrm{Err}_s = 171\%$), the use of the full-polarized data appears to ameliorate significantly the reconstruction.

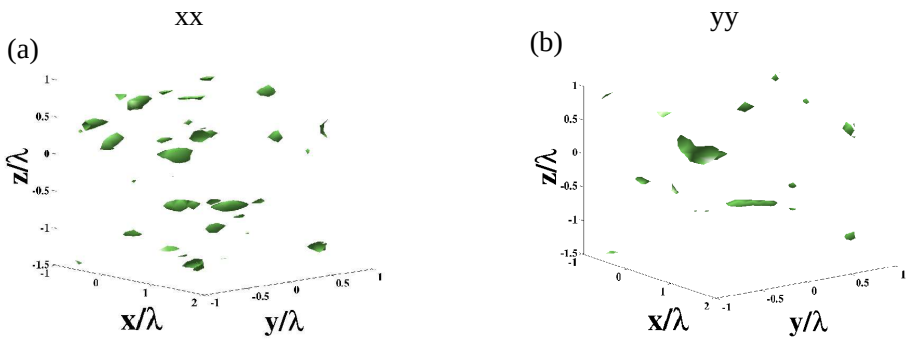


**Figure 4.22 :** *Iso-surface of the reconstructed permittivity profile at $\varepsilon = 2$ using the HM-DORT procedure for the same configuration as that used in Fig. 4.6. (a) The antennas are oriented along the $x$ direction and the scattered field is detected along the $x$ direction only. (b) The antennas are oriented along the $y$ direction and the scattered field is detected along the $y$ direction only.*

### 4.3.6 Conclusion

In this section, we have numerically studied the imaging issue of targets buried in a random inhomogeneous medium, with the antennas lying in the same homogeneous medium. We have shown that using the three-dimensional vectorial Time Reversal Operator (DORT method), one can generate different incident fields that focus selectively on each target. We have proposed an hybrid method, named HM-DORT, that uses the answer of the medium to these DORT fields for reconstructing the permittivity of a region of interest with a non-linear optimization scheme. The HM-DORT procedure appears localizes better the targets than the DORT procedure alone, especially in the $z$ direction, and is more efficient than a HM scheme for characterizing the targets, with significantly less computational burden. It permits to handle very noisy configurations, with clutter standard deviation up to 12%, that support multiple scattering. Last, we have stressed the importance of using non-linear inversion algorithms and full-polarized data for achieving this performance.

## 4.4 Half-space configuration

In the last section, we deal with detecting and characterizing three-dimensional scatterers in a disordered medium with no interface. In general, sources and objects to be detected are always located in two different mediums, which has more significance especially in medical imaging, mineral exploration and through-wall imaging. The rules of detection and localization also hold, similar as the homogeneous configuration in Sec. 4.3. Herein, we focus to 'limited-aspect' data configurations, where a flat interface separates the homogeneous medium (the air) containing the full-polarized antennas, from another semi-infinite medium embedding the objects under test. Different from the homogeneous case, the response in presence of the interface in Green's function is taken into account

for both forward and inverse scattering problem, given in Sec. 1.4.3.2. It has been proved that accounting for the interface is mandatory in Ref. 82, especially for the scattered field calculations.

### 4.4.1 Computational setup

In this section are reported performances of our approach to localize and characterize buried targets in a highly cluttered environment. All data are obtained with the CDM forward solver for which the mesh size of the scattering domain $a = \lambda_{\text{ref}}/18$ where $\lambda_{\text{ref}} = 0.6$ m is the wavelength in vacuum of an impinging wave at the reference frequency $f_{\text{ref}} = 500$ MHz. The flat interface separating the measurement medium (air) and the host medium (drive soil of relative permittivity $\varepsilon_b = 3$) where targets are buried in is at $z = \lambda_{\text{ref}}$. The measurement surface $\Gamma$ is at $z = 2\lambda_{\text{ref}}$ and therefore at $\lambda_{\text{ref}}$ above the interface as shown in Fig. 4.23. The measurement surface $\Gamma$ is made of a lattice of $L = 81$ antennas regularly distributed on a square of side size $8\lambda_{\text{ref}}$. Each antenna may play either the role of an emitter or the role of a receiver. Scattering objects to be characterized are confined entirely in a large box $W$ beneath the interface and of volume $(3\lambda_{\text{ref}} \times 3\lambda_{\text{ref}} \times 3\lambda_{\text{ref}})$. The scattering domain $W$ is centered at $(0, 0, -0.5\lambda_{\text{ref}})$. For the inversion, the investigating domain $\Omega \subset W$ is discretized with a mesh size of $a = \lambda_{\text{ref}}/10$ which is almost twice larger than the mesh size $a = \lambda_{\text{ref}}/18$ used to generate the synthetic data. All reconstructed imaginary parts of relative permittivities vanish. Hence, only the real part of the reconstructed permittivities are presented.

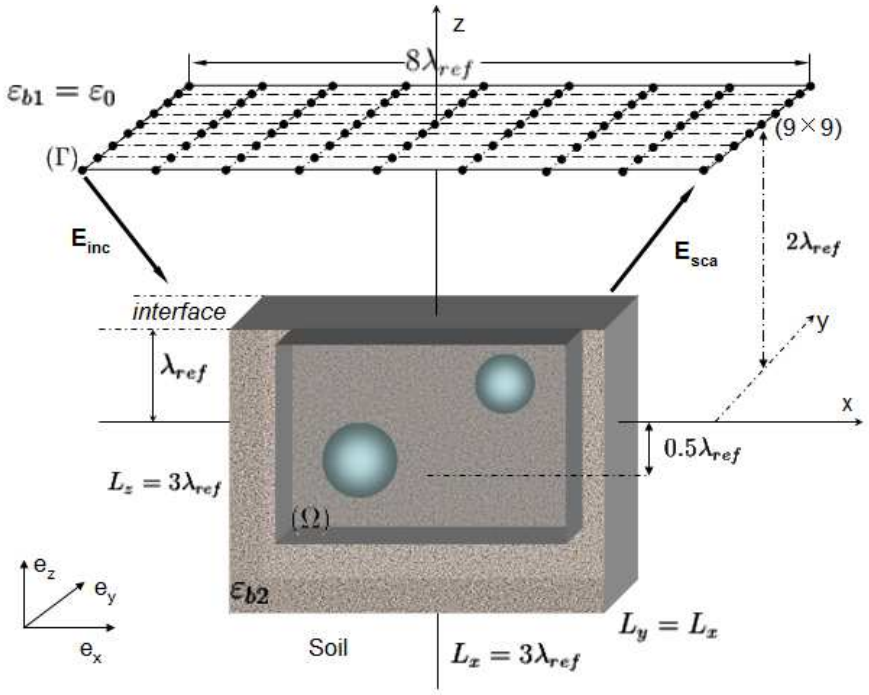


**Figure 4.23 :** *Geometry of the studied problem. Targets are embedded in the lower medium and probed from the upper medium. The probing surface is constituted of transmitters and receivers regularly distributed on a plane. Geometrical dimensions of targets being about the order of the wavelength of the incident field thus the scattering is within resonant regime.*

We can obtain better imaging resolution working at higher excitation frequencies, but the initial guess deduced from the backpropagation procedure[8,56] or set as a tiny constant is not efficient any more in presence of interfaces. When the contrast of the scatterer is large with respect to the surrounding medium, or the diameter becomes large compared to the wavelength in the medium, there exists non-uniqueness of the solution, which has been explored in Ref. 5. An acceptable

reconstruction can be obtained by using the frequency-hopping approach[5,19,55,99]. The initial guess of an unknown object at the lowest frequency is assumed to be a small constant $\varepsilon^{ini} = C$, in which $\xi_0 = \eta_0 = 0$ must be rejected since it involves vanishing gradients. By gradually increasing the operating frequency, the initial guess of the higher frequency is obtained at the final reconstruction result of the lower frequency, we are then able to determine the required detail of distribution of permittivity. The *a priori* information should be included in the inversion procedure, stating that the contrast $\chi$ is positive in the medium[100]. This is achieved by changing Eq. (2.20) to

$$\chi_n = \xi_n^2 + i\eta_n^2, \tag{4.9}$$

the reconstructed relative permittivity of the target is in the form of

$$\varepsilon(\boldsymbol{r}) = \varepsilon_b + \xi_n^2(\boldsymbol{r}) + i\eta_n^2(\boldsymbol{r}). \tag{4.10}$$

### 4.4.2 Reconstruction of a target without clutter

We start the analysis of the performance of the reconstruction with ideal data, *i.e.* two spheres of relative permittivity $\varepsilon = 5$ buried below the interface. The smallest scatterer located at $(0.5\lambda_{\text{ref}}, 0.4\lambda_{\text{ref}}, 0.5\lambda_{\text{ref}})$, with radius $r_1 = \lambda_{\text{ref}}/8$ is closer to the interface, while the larger sphere of radius $r_2 = \lambda_{\text{ref}}/6$ and centered at $(-0.5\lambda_{\text{ref}}, 0.4\lambda_{\text{ref}}, -0.5\lambda_{\text{ref}})$ is embedded deeper.

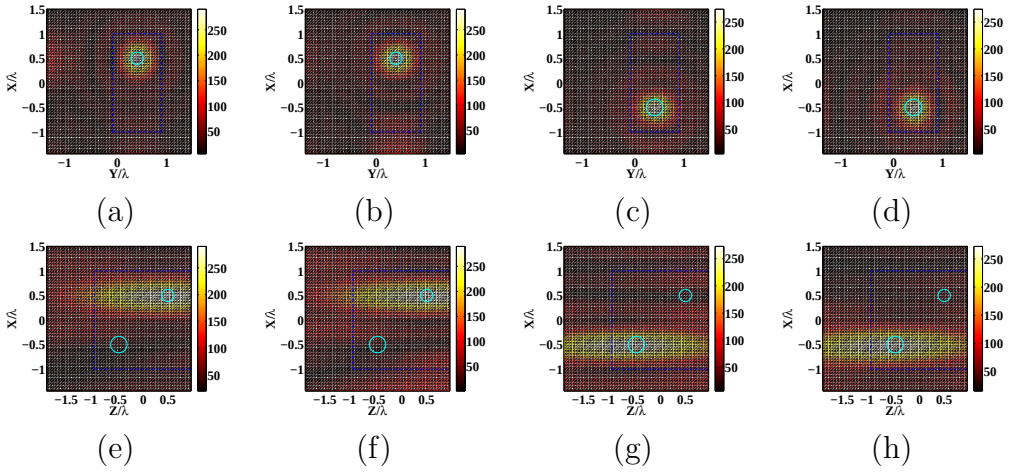


**Figure 4.24 :** *Intensity map in $W$ of the electric field deduced from four eigenvectors related to the four largest eigenvalues using illuminations at fixed wavelength $\lambda_{\text{ref}}$, when two scatterers are embedded in background medium without clutter. (a)-(d): in the $(x, y)$ plane, (a) and (b) for $z = 0.5\lambda_{\text{ref}}$, (c) and (d) for $z = -0.5\lambda_{\text{ref}}$. (e)-(h): in the $(x, z)$ plane for $y = 0.4\lambda_{\text{ref}}$. Each column corresponds to the first, the second, the third and the fourth eigenvalue. The circles represent the actual profiles of the targets, while the dashed box represents the investigating domain $\Omega$ to be used in the inversion procedure.*

Intensities of fields within $W$ domain derived from eigenvectors of the TRO are presented in Fig. 4.24 for the first four largest eigenvalues. Clearly, eigenvectors corresponding to the first and the second eigenvalue synthesize a wave focusing onto the scatterer near to the interface while eigenvectors corresponding to the third and the fourth eigenvalue focus on the deeper sphere far away from the interface. Notice that in the absence of the interface each scatterer is associated to three eigenvalues[46], hence the first effect of the presence of the interface is to decrease the number

of pertaining eigenvalues per scatterer. In the $(x, z)$ plane, the elongated shape of the field intensity along the $z$-axis results from positions of antennas which are placed only on one side of targets. From these intensities maps, the investigating domain $\Omega$ to be used in the inversion can fairly be restricted to a volume of $(2\lambda_{\text{ref}} \times \lambda_{\text{ref}} \times 2\lambda_{\text{ref}})$, centered at $(0, 0.4\lambda_{\text{ref}}, 0)$. The volume of this box is $4\lambda_{\text{ref}}^3$, about seven times smaller than the scattering domain $W$ used in the forward scattering problem to generate the data.

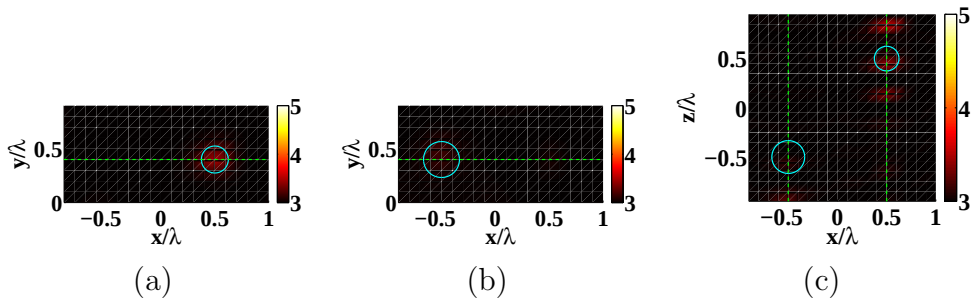


**Figure 4.25 :** *Map of reconstructed permittivity distribution using the DORT focusing fields shown in Figs. 4.24 at fixed wavelength $\lambda_{\text{ref}}$, when no noise is added. (a) in the $(x, y)$ plane for $z = 0.5\lambda_{\text{ref}}$. (b) in the $(x, y)$ plane for $z = -0.5\lambda_{\text{ref}}$. (c) in the $(x, z)$ plane for $y = 0.4\lambda_{\text{ref}}$.*

Figure 4.25 shows the reconstruction results at $\lambda_{\text{ref}}$ using focusing waves deduced from the DORT method shown in Fig. 4.24. The reconstruction exhibits ghost objects along the $z$-direction which are particularly visible on the axial cut of the reconstructed profile plotted in Figs. 4.28 (a) and (b). The low value of the cost function shows that these repica located along the $z$-axis with a periodicity about $\frac{\lambda_{\text{ref}}}{2\sqrt{\varepsilon_b}}$ provide the same scattered field than that of the actual scatterer. This oscillating behavior is a direct consequence of the limited numerical aperture of the imaging system and has been largely studied in the two-dimensional configuration[5]. Indeed, in our configuration, the objects under study are localized more or less at the center of the array antennas. The incident field at the object domain radiated by transmitters located around the edge of the measurement array is weak as compared to the one generated by a transmitter located just above the object. This is due to the strong Fresnel reflection on the interface for large angle of incidence. This is the same for the measured field, the scattered field by the targets on the antennas close to the edge of the array is weak. It means that the antennas on the edge participate weakly to the construction of the DORT focalizing incident field. We have checked that reducing by a factor two the width of the domain where the antennas are located leads to similar reconstructions (not shown) than those of Fig. 4.25. It means that the numerical aperture of the illumination and reception are dramatically reduced by the presence of the interface. Therefore the number of admissible solutions for the inverse scattering problem increases, in others terms, false alarms are unfortunately expected in the axial direction of illumination. We have checked that this oscillating behavior of the reconstructed profile also occurs in homogeneous configuration when the numerical aperture is drastically reduced.

To compensate for the lack of information due to the small numerical aperture of the imaging system, we used polychromatic data and applied the frequency-hopping approach as described in Ref. 5. It consists in reconstructing the targets with a low frequency data and using the result as an initial guess for performing the inversion at higher frequency. We simulated the data for three different incident wavelengths $\lambda_1 = 3\lambda_{\text{ref}}$, $\lambda_2 = 1.5\lambda_{\text{ref}}$ and $\lambda_{\text{ref}}$. Note that these supplementary illuminations do not provide higher numerical aperture of the imager and do not provide higher spatial frequencies information.

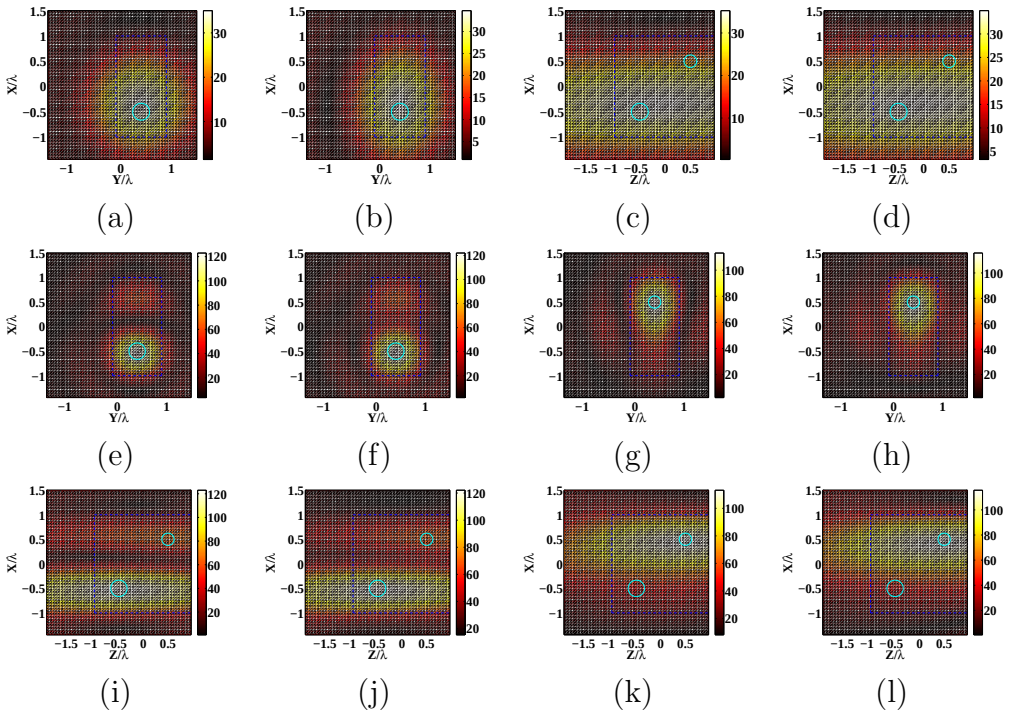


**Figure 4.26 :** *Same configuration as Fig. 4.24, but with the antennas working at two larger wavelengths. (a)-(d): map of modulus of the focusing wave associated with the first and the second eigenvalue at the wavelength* $\lambda_1 = 3\lambda_{\text{ref}}$*, (a) and (b) in* $(x, y)$ *plane for* $z = -0.5\lambda_{\text{ref}}$*, (c) and (d) in* $(x, z)$ *plane for* $y = 0.4\lambda_{\text{ref}}$*. (e)-(l) intensity map deduced from the eigenvectors for the wavelength* $\lambda_2 = 1.5\lambda_{\text{ref}}$ *, each column corresponds to the first, the second, the third eigenvalue and the fourth eigenvalue, (e) and (f) [(g) and (h)] in* $(x, y)$ *plane for* $z = -0.5\lambda_{\text{ref}}$ *[*$z = 0.5\lambda_{\text{ref}}$*]. (i)-(l): in* $(x, z)$ *plane for* $y = 0.4\lambda_{\text{ref}}$*.*

The detection and localization of scatterers are always determined by the highest operating frequency when the frequency-hopping approach is used. Comparing Fig. 4.26 with Fig. 4.24, the focusing spot slims down when the frequency increases, proving that the best resolution of focalization can be reached at the highest frequency. As regards illuminations at the wavelength $\lambda_1 = 3\lambda_{\text{ref}}$, the two scatterers are not resolved any more, there exist yet two eigenvectors focusing on the area of interest, Figs. 4.26 (a)-(d). With a shorter wavelength $\lambda_2 = 1.5\lambda_{\text{ref}}$, as shown in Figs. 4.26 (e)-(l), the scatterers are separated despite of slight coupling.

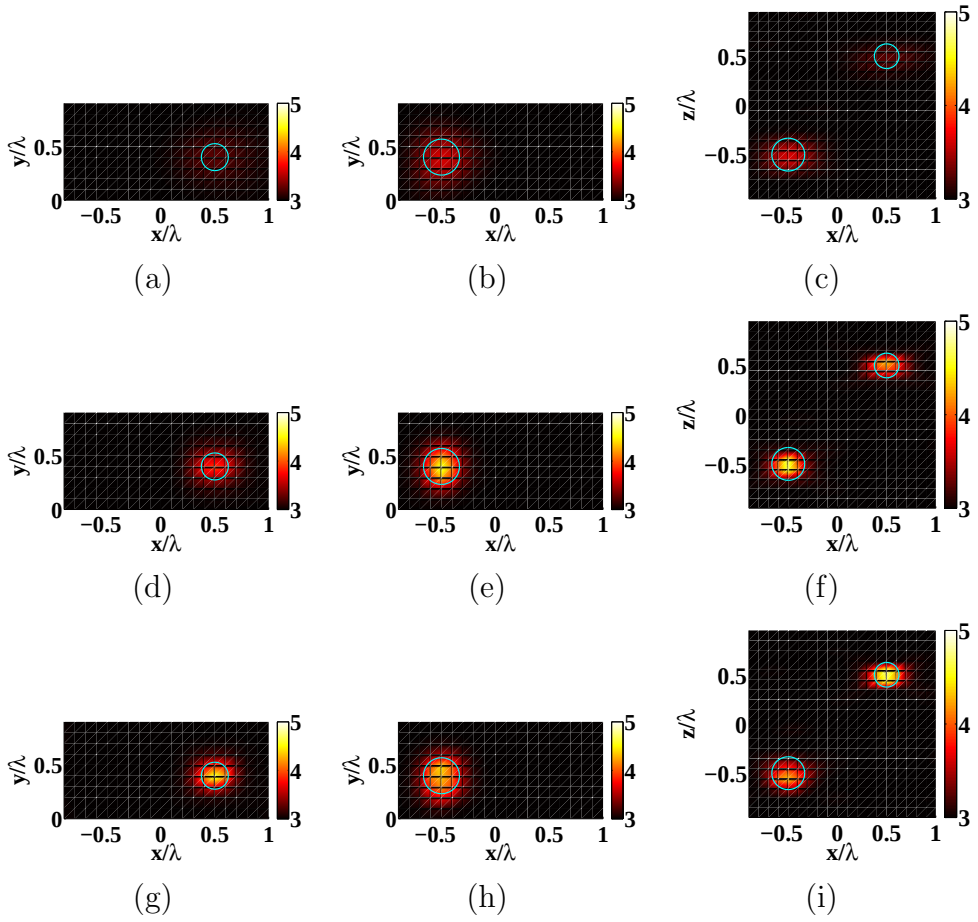


**Figure 4.27 :** *Reconstructed permittivity distribution for two scatterers using the frequency-hopping approach and the DORT method, when no noise is added. (a)-(c): results obtained at the wavelength* $\lambda_1 = 3\lambda_{\text{ref}}$ *using a tiny constant as the initial guess. (d)-(f): results obtained at the wavelength* $\lambda_2 = 1.5\lambda_{\text{ref}}$ *with the final reconstruction result obtained at* $\lambda_1 = 3\lambda_{\text{ref}}$ *as the initial guess. (g)-(i): results obtained at the wavelength* $\lambda_{\text{ref}}$ *with the final reconstruction result obtained at* $\lambda_2 = 1.5\lambda_{\text{ref}}$ *as the initial guess. Left: in* $(x, y)$ *plane for* $z = 0.5\lambda_{\text{ref}}$*. Middle: in* $(x, y)$ *plane for* $z = -0.5\lambda_{\text{ref}}$*. Right: in* $(x, z)$ *plane for* $y = 0.4\lambda_{\text{ref}}$*.*

The result of the frequency-hopping approach is shown in Fig. 4.27. The inversion started at $\lambda_1$ and the final result was used as initial guess for the inversion at $\lambda_2$ and repeated the process for $\lambda_{\text{ref}}$. For the illuminations at the largest wavelength $\lambda_1 = 3\lambda_{\text{ref}}$, ratios of radii of two spheres to the wavelength are about $r_1 = \lambda_1/24$ and $r_2 = \lambda_1/18$, respectively. Due to the small size of the sphere compared to the wavelength, it is difficult to retrieve such small details. Hence, the reconstructed relative permittivity is much smaller than the actual one at the lowest frequency. As the frequency increases, the reconstruction resolution is ameliorated. The two scatterers are now satisfactorily reconstructed at $\lambda_{\text{ref}}$ both in shape and permittivity estimation and the oscillating behavior of the estimated permittivity has disappeared. Quantitative comparison between reconstructed profiles and the actual one along the axial direction is shown in Figs. 4.28 (a) and (b). The best result, plotted with red solid lines, is obtained when the frequency-hopping approach is applied.

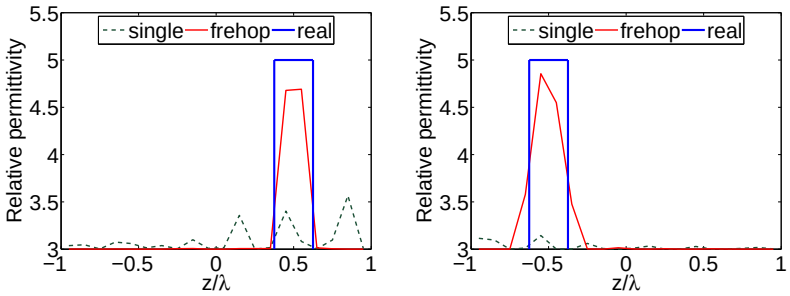


**Figure 4.28 :** *Map of reconstructed permittivity distribution using the DORT focusing fields shown in Figs. 4.24 without a clutter. The relative permittivity is plotted versus (a) $z$ for $x = 0.5\lambda_{\text{ref}}$ and $y = 0.4\lambda_{\text{ref}}$; (b) $z$ for $x = -0.5\lambda_{\text{ref}}$ and $y = 0.4\lambda_{\text{ref}}$. The solid curves denote the actual profiles of the scatterers, the profile of the permittivity obtained in use of frequency hopping is in red solid line, while the profile obtained at fixed wavelength is in dark green dashed line.*

### 4.4.3 Reconstruction in a cluttered medium

We now investigate the influence of clutter on the imaging performance. We consider the same configuration as previously but the targets are now buried in a cluttered medium, described as Sec. 3.2. The ratio of clutter-to-signal (CSR) is defined as Eq. (3.2). In the next reported examples the multiple scattering between the clutter and the targets is negligible. Yet, the computation of the scattered fields is carried out rigorously.

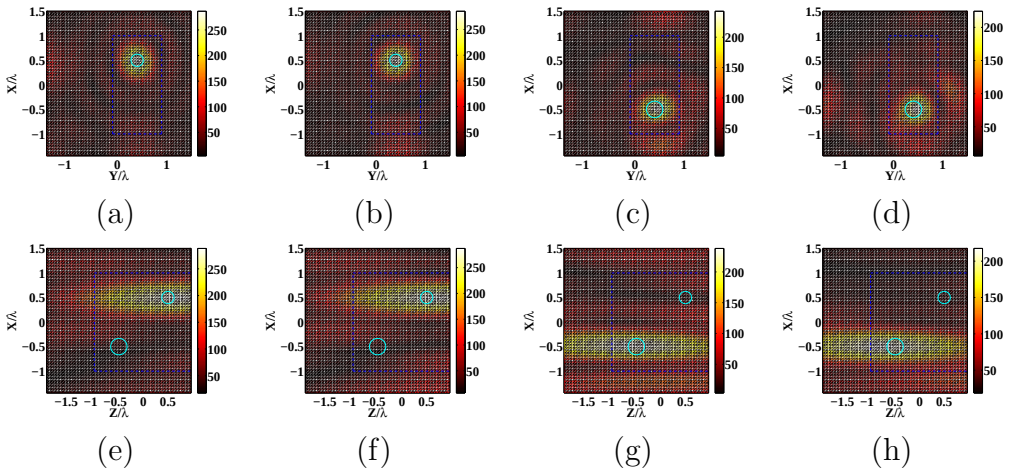


**Figure 4.29 :** *Intensity map of the electric field deduced from eigenvectors working at the shortest wavelength $\lambda_{\text{ref}}$, when 101.9% noise is added, corresponding to $l_c = \lambda_{\text{ref}}/18$ and $\sigma_f = 0.058$. (a) and (b) [(c) and (d)] in the $(x, y)$ plane for $z = 0.5\lambda_{\text{ref}}$ [$z = -0.5\lambda_{\text{ref}}$]. (e)-(h): in the $(x, z)$ plane for $y = 0.4\lambda_{\text{ref}}$. Each column corresponds to the first, the second, the third eigenvalue and the fourth eigenvalue.*

In the first example, we consider an quasi-uncorrelated clutter with standard deviation $\sigma_f = 0.058$ and correlation length $l_c = \lambda_{\text{ref}}/18$, the corresponding CSR is 6.5%, 16.0%, 102% at $\lambda_1 = 3\lambda_{\text{ref}}$, $\lambda_2 = 1.5\lambda_{\text{ref}}$, $\lambda_{\text{ref}}$, respectively. For all wavelengths and even when the clutter-to-signal CSR is as high as 102%, the DORT method permits to localize the targets, seeing Fig. 4.29.

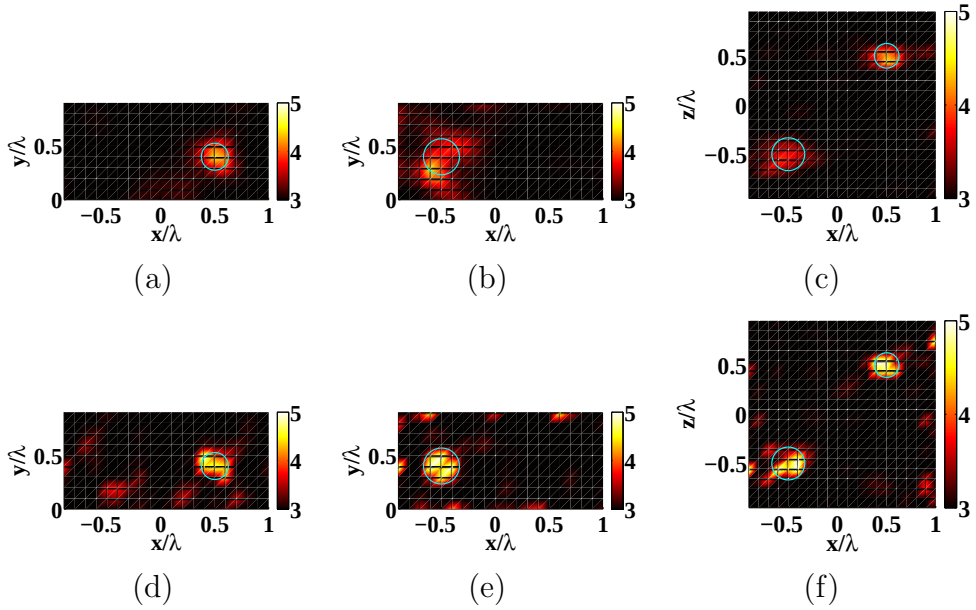


**Figure 4.30 :** *Reconstructed permittivity distribution at the wavelength $\lambda_{\text{ref}}$ using the frequency-hopping approach, when 102% noise is added, corresponding to $l_c = \lambda_{\text{ref}}/18$ and $\sigma_f = 0.058$. (a)-(c): using the HM-DORT. (a) in $(x, y)$ plane for $z = 0.5\lambda_{\text{ref}}$. (b) in $(x, y)$ plane for $z = -0.5\lambda_{\text{ref}}$. (c) in $(x, z)$ plane for $y = 0.4\lambda_{\text{ref}}$. (d)-(f): same as (a)-(c) while using the HM algorithm.*

The reconstruction obtained using the HM-DORT and with the HM alone are reported in Fig. 4.30. In both cases, the frequency hopping procedure is applied. The superiority of HM-DORT is clearly seen. Using HM, bright scatterers are reconstructed in the entire volume of the investigating domain, blurring the targets signal and increasing the level of false alarms, Figs. 4.30 (d)-(f).

The improvement of the HM-DORT is particularly obvious in the view of iso-surfaces where with the HM false alarms appear in the entire investigating domain, blurring thus the reconstructed targets, Fig. 4.31 (b). With the HM-DORT [Fig. 4.31 (a)] effects related to the presence of the clutter is remarkably diminished and only the two echogeneous targets are retrieved. The quality of the reconstruction is quantitatively estimated by the reconstruction error of $\chi$. Using HM-DORT this error is about 66% and raises up to 282% when HM is used. The value of the cost function is one order of magnitude lower with the HM-DORT than the one obtained with the HM, Fig. 4.31 (d). Moreover, the computational time of HM-DORT (which uses only 4 incident fields at each inversion) at the wavelength $\lambda_{\text{ref}}$ is 287 s, about 80 times smaller than that of the HM (22201 s) (which uses 81 incident fields).

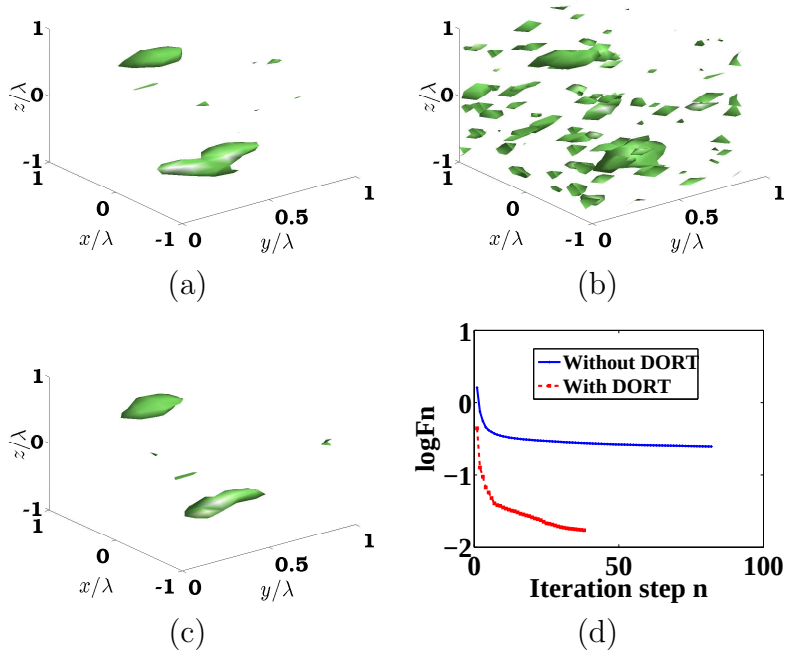


**Figure 4.31 :** *The configuration is the same as that described in Fig. 4.29. (a) Iso-surface of the reconstructed permittivity profile at* $\varepsilon = 3.5$ *using the HM-DORT procedure. (b) same as (a) using the HM procedure. (c) same as (a) in case that clutter is generated in a larger domain* $W$ *with the size of* $(6\lambda_{\text{ref}} \times 6\lambda_{\text{ref}} \times 3\lambda_{\text{ref}})$*. (d) Evolution of the cost function (log-scale representation) versus the iteration step using the HM-DORT (dashed curve) and the HM (solid curve). All these plots correspond to the reconstruction results shown in Fig. 4.30.*

It is worth noting that, although the clutter is accounted for only in the domain $W$, our numerical experiment can be used to infer the behavior of the imaging system in a realistic situation where the clutter is present everywhere in the host medium. Indeed, results do not change when the size of $W$ increased. We display in Fig. 4.31 (c) the reconstruction obtained by HM-DORT when $W$ is multiplied by a factor of four to reach $(6\lambda_{\text{ref}} \times 6\lambda_{\text{ref}} \times 3\lambda_{\text{ref}})$ (keeping the same clutter distribution in the initial $W$ and the same statistics). In this case, the clutter-to-signal ratio is increased to 29%, 65%, 325% at wavelengths $\lambda_1 = 3\lambda_{\text{ref}}$, $\lambda_2 = 1.5\lambda_{\text{ref}}$, $\lambda_{\text{ref}}$, respectively. Yet, the two scatterers are still well localized by DORT and the reconstructions are similar to those obtained with the small $W$ with the same error $\text{Err}_\chi = 66\%$. The focusing property of DORT permits to diminish drastically the influence of the clutter far from the targets.

To evaluate the reproducibility of HM-DORT, different distributions of clutter with the same statistical characteristics have been generated. We used the same correlation length and standard deviation of fluctuation as those used in Fig. 4.30. Twenty different random seedings are used for generating correlated noise. For each realization the HM-DORT is run.

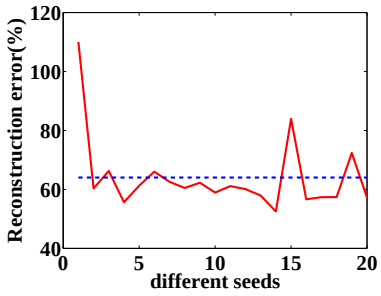


**Figure 4.32 :** *Evolution of error of reconstruction on the contrast of scatterers at the wavelength* $\lambda_{\text{ref}}$ *versus* 20 *different noise seedings, with the same configuration as Sec. 4.4.3, where* $l_c = \lambda_{\text{ref}}/18$*, and* $\sigma_f = 0.058$*.*

Figure. 4.32 reports the evolution of the reconstructed contrast error $\text{Err}_\chi$ versus 20 different noise seedings. In the case of $l_c = \lambda_{\text{ref}}/18$, despite of different noise contributions, the mean value of reconstruction error is 64%, the confidence interval is 3%, ensuring that for most clutter distributions, the reconstruction error $Err_\chi$ is inside the interval of confidence. This means that our HM-DORT succeeds in characterizing scatterers in the presence of different kinds of noise. We present here the reconstruction result corresponding to the worst case for which $\text{Err}_\chi$ is the highest (seed 1), see Fig. 4.33. Comparing with Figs. 4.30 (a)-(c), the two scatterers are well characterized with however some minor artefacts.

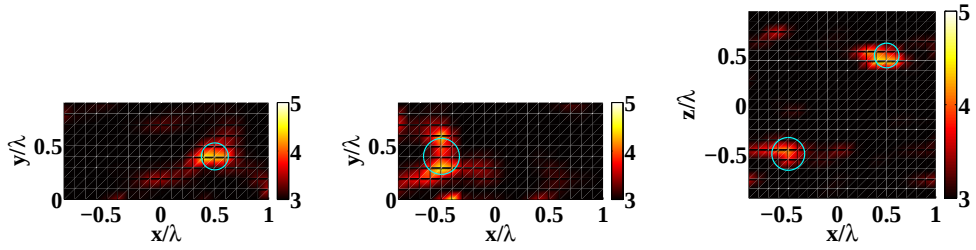


**Figure 4.33 :** *Same as Figs. 4.30 (a)-(c), while the clutter distribution is different, corresponding to the worst case in which the reconstruction error is greatest (*$Err_\chi = 110\%$*). (a) in* $(x, y)$ *plane for* $z = 0.5\lambda_{\text{ref}}$*. (b) in* $(x, y)$ *plane for* $z = -0.5\lambda_{\text{ref}}$*. (c) in* $(x, z)$ *plane for* $y = 0.4\lambda_{\text{ref}}$*.*

### 4.4.4 Influence of the polarization of the incident field

In our configuration, emitting and receiving antennas are oriented along three orientations, $x$-axis, $y$-axis and $z$-axis, respectively. In order to illustrate the necessity of using the vectorial case we consider a simple configuration where the antennas are oriented along one single direction, $x$-axis or $y$-axis.

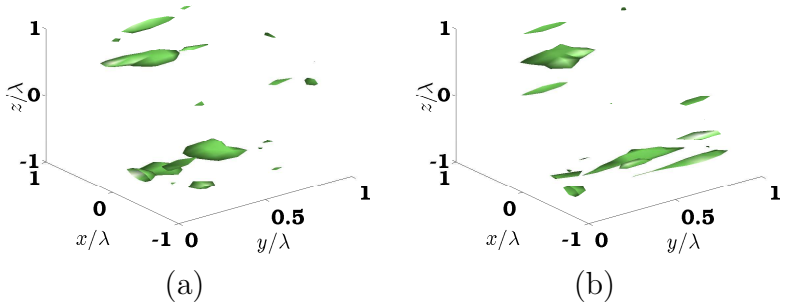


**Figure 4.35 :** *Iso-surface of the reconstructed permittivity profile at $\varepsilon = 3.5$ using the HM-DORT procedure for the same configuration as that used in Fig. 4.31 (a). (a) The antennas are oriented along the $x$-direction and the scattered field is detected along the $x$-direction only. (b) The antennas are oriented along the $y$-direction and the scattered field is detected along the $y$-direction only.*

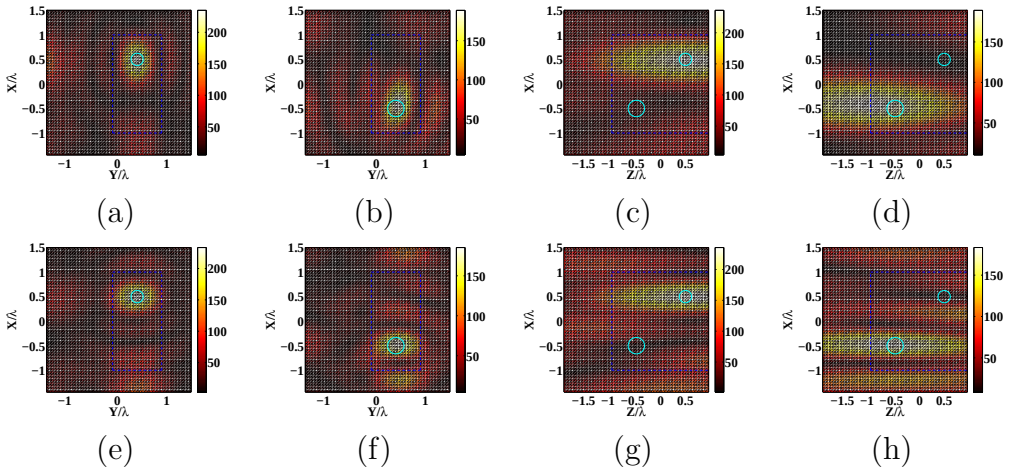


**Figure 4.34 :** *Intensity map of the electric field deduced from eigenvectors working at the shortest wavelength $\lambda_{\text{ref}}$, when 102% noise is added, corresponding to $l_c = \lambda_{\text{ref}}/18$ and $\sigma_f = 0.058$, in the case of antennas taking only one orientation. (a)-(d): The antennas are oriented along the $x$-direction and the scattered field is detected along the $x$-direction only. (e)-(h): The antennas are oriented along the $y$-direction and the scattered field is detected along the $y$-direction only. (a) and (e) [(b) and (f)] in the $(x, y)$ plane for $z = 0.5\lambda_{\text{ref}}$ [$z = -0.5\lambda_{\text{ref}}$], corresponding to the first [the second] eigenvalue. (c) and (g) [(d) and (h)]: in the $(x, z)$ plane for $y = 0.4\lambda_{\text{ref}}$, corresponding to the first [the second] eigenvalue.*

Figs. 4.34 shows the intensity map of the focusing field when emitting and receiving antennas are oriented along only $x$-direction or $y$ direction. Comparing with Figs. 4.29, only one eigenvalue is associated to each echogeneous scatterer. The reconstruction obtained from the scalar data with HM-DORT is displayed as iso-surface in Fig. 4.35. We observe a clear deterioration of the image as compared to that obtained with the vectorial data, Fig. 4.31 (a). The reconstruction is deteriorated

qualitatively. The reconstruction error in the scalar case is $\mathrm{Err}_\chi = 101\%$ and $\mathrm{Err}_\chi = 96\%$ for the $x$ and $y$ orientations respectively, to be compared to $\mathrm{Err}_\chi = 66\%$ for the full-polarized data.

### 4.4.5 Influence of the structural noise

In this section, we study the robustness of HM-DORT and the frequency-hopping approach[55,85].

#### 4.4.5.1 Influence of the standard deviation

The correlation length $l_c$ is kept fixed at $\lambda_{\mathrm{ref}}/18$, while the standard deviation is augmented to $\sigma_f = 0.07$, leading to CSR $= 9\%, 23\%, 148\%$ for the wavelength $\lambda_1 = 3\lambda_{\mathrm{ref}}$, $\lambda_2 = 1.5\lambda_{\mathrm{ref}}$, $\lambda_{\mathrm{ref}}$, respectively. Unsurprisingly, with such level of noise at $\lambda_{\mathrm{ref}}$, the ability of DORT for focusing on the scatterers is deteriorated. In particular, the eigenvector corresponding to the fourth eigenvalue generates a wave that focuses both on the scatterer and on the clutter with the same intensity level, shown in Fig. 4.36. On the other hand, the data at $\lambda_2 = 1.5\lambda_{\mathrm{ref}}$ are less noisy and yield DORT fields that focus exclusively on the scatterer. Thus we use the DORT intensity maps at $\lambda_2 = 1.5\lambda_{\mathrm{ref}}$ for defining the investigating domain used for the inversion procedure.

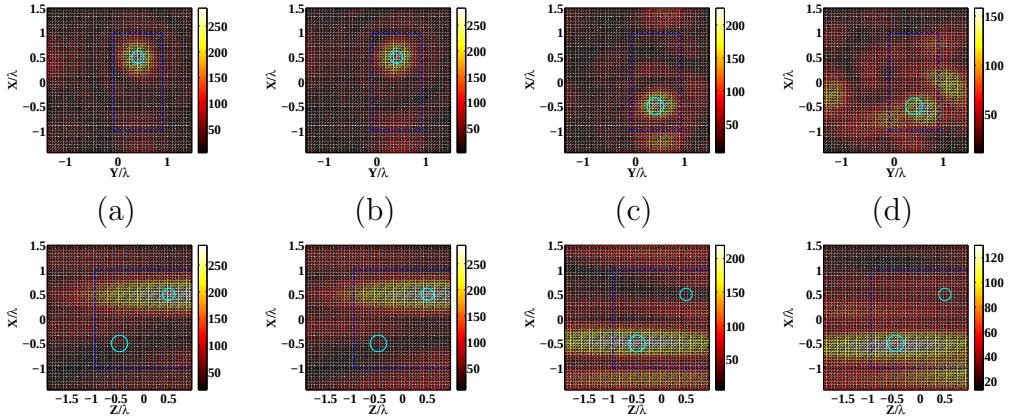


**Figure 4.36 :** *Intensity map of the electric field deduced from the eigenvectors at the wavelength* $\lambda_{\mathrm{ref}}$*, when 148% noise is added, in which* $l_c = \lambda_{\mathrm{ref}}/18$ *and* $\sigma_f = 0.07$*. Each column corresponds to the first, the second, the third and the fourth eigenvalue. (a) and (b) [(c) and (d)] in* $(x, y)$ *plane for* $z = 0.5\lambda_{\mathrm{ref}}$ *[*$z = -0.5\lambda_{\mathrm{ref}}$*]. (e)-(h) in* $(x, z)$ *plane for* $y = 0.4\lambda_{\mathrm{ref}}$*.*

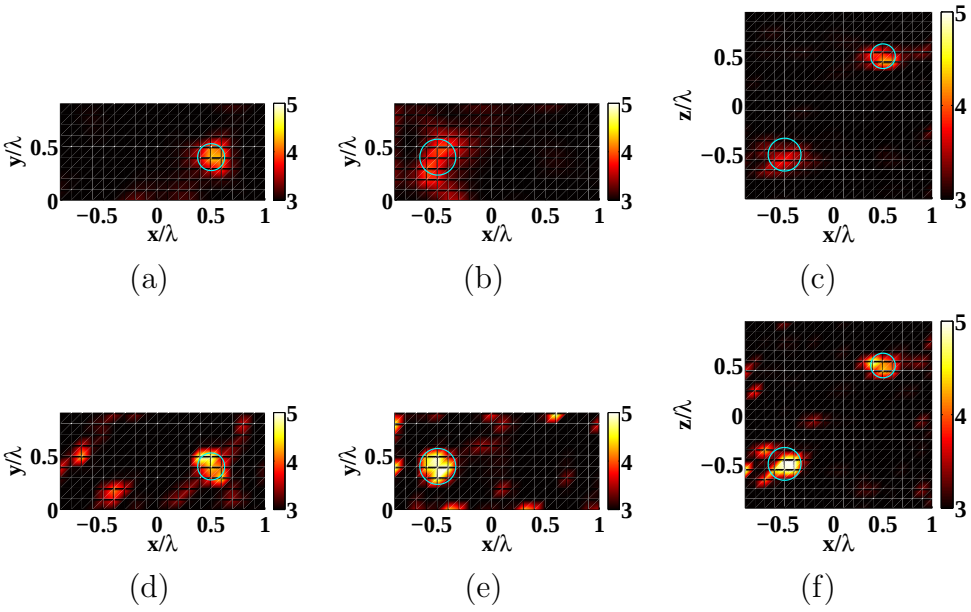


**Figure 4.37 :** *Same as Fig. 4.30, while 148.4% noise is added, corresponding to* $l_c = \lambda_{\text{ref}}/18$ *and* $\sigma_f = 0.07$*, using the incident focusing waves as shown in Fig. 4.36.*

In Fig. 4.37, we plot the reconstructed relative permittivity in $(x, z)$ plane obtained at the wavelength $\lambda_{\text{ref}}$ with the frequency-hopping procedure. Due to the bad focalization of the fourth eigenvalue, sole the three incident fields associated to the three largest eigenvalues are used in the inversion procedure. The reconstruction of the two scatterers is similar to that displayed in Figs. 4.30 (a)-(c). On the other hand, the reconstruction given by the HM is totally blurred by the noise stemming from the clutter, Figs. 4.30 (d)-(f).

### 4.4.5.2 Influence of the correlation length

In this section, the influence of the correlation length $l_c$ on the reconstruction is analyzed. Hereafter, the standard deviation of the clutter $\sigma_f = 0.058$ is kept equal to the one used for Fig. 4.30 while the correlation length $l_c$ is increased. We quantify the strength of the clutter (SC) with a single number as

$$\text{SC} = \sum_{l=1}^{N} \sum_{\alpha}^{x,y,z} \|\boldsymbol{f}_{l,\alpha}^{\text{clutter}}\|_{\Gamma}^2. \tag{4.11}$$

Figure 4.38 (a) shows the evolution of *SC* with respect to the correlation length for the half-space configuration (solid line) and for the homogeneous background configuration (dashed line) (corresponding to $\varepsilon_b = 1$)[46]. When $l_c \ll \lambda$ the clutter can be homogenized which leads to a low scattered field, and when $l_c \gg \lambda$ the large-scale spatial variation of the clutter does not perturb the signal radiated by the targets as it is locally homogeneous. The most disturbing effect of the clutter is expected for correlation lengths corresponding to the maximum of SC. Notice that the behavior of SC with respect to the correlation length differs strongly depending on the configuration under study. In the half-space configuration, the SC curve exhibits a sharp peak centered about $l_c = 0.1\lambda$, while in the homogeneous configuration, the SC curve exhibits a smooth behavior with a maximum at $l_c \approx 0.3\lambda$. When $l_c = \lambda_{\text{ref}}/10$ and $\sigma_f = 0.058$, one obtains a CSR equal to 34%, 66% and 282% for $\lambda_3 = 3\lambda_{\text{ref}}$, $\lambda_2 = 1.5\lambda_{\text{ref}}$ and $\lambda_{\text{ref}}$, respectively. In this case, due to the high level of noise, the DORT fields at $\lambda_{\text{ref}}$ are not able to focus on the target far from the interface. One obtains only

two fields focusing on the target close to the interface. On the other hand, at $\lambda_2 = 1.5\lambda_{\text{ref}}$ and $\lambda_3 = 3\lambda_{\text{ref}}$, the DORT method yields four focusing fields aiming at both targets.

The reconstruction obtained with HM-DORT and the frequency-hopping procedure for $\lambda_2 = 1.5\lambda_{\text{ref}}$ and $\lambda_3 = 3\lambda_{\text{ref}}$ using the four focusing incident fields is displayed in Fig. 4.38. The two scatterers are well localized but the smallest target close to the interface is under evaluated. Adding the third wavelength $\lambda_{\text{ref}}$ in the frequency-hopping procedure with the four incident fields deteriorates the reconstruction (not shown) because the additional data obtained with the third and fourth DORT eigenvectors at $\lambda_{\text{ref}}$ correspond essentially to the clutter signature. Yet, by restricting at $\lambda_{\text{ref}}$ the incident DORT fields to the first two eigenvectors and running the inversion with an initial guess corresponding to the reconstruction obtained at $1.5\lambda_{\text{ref}}$, one ameliorates the reconstruction of the target close to the interface while leaving unchanged the reconstruction of the target far from the interface, Fig. 4.38.

In the last example, we consider a clutter with $l_c$ equal to $0.3\lambda_{\text{ref}}$. As expected in this case, the CSR decreases with the wavelength. It is equal 339%, 64% and 41% for $\lambda_1 = 3\lambda_{\text{ref}} = 10l_c$, $\lambda_2 = 1.5\lambda_{\text{ref}}$ and $\lambda_{\text{ref}}$, respectively. The reconstruction obtained with the frequency-hopping procedure using the three wavelengths is shown in Fig. 4.39 (a) and Figs. 4.39 (c) and (d) in dashed line. One observes that the scatterer far from the interface is under evaluated and that it is accompanied by ghost objects regularly placed along the $z$-axis. These oscillations indicate that the frequency-hopping procedure is not optimal. Indeed, the reconstruction obtained at $3\lambda_{\text{ref}}$ is strongly perturbed by the clutter signature and this noisy initial guess compromises the following inversions. Now, choosing another wavelength for starting the frequency-hopping procedure is not easy. Taking a much larger $\lambda$, which ensures that the clutter signature is low, yields a poor reconstruction, due to the lack of high spatial frequency information, which is basically useless in the frequency-hopping procedure. Similarly, the smaller wavelengths which permit the diminution of SC, are too close to $1.5\lambda_{\text{ref}}$ and do not bring additional information. Thus, we decided to keep the same wavelength range $[\lambda_{\text{ref}}, 3\lambda_{\text{ref}}]$ but used a finer discretization step. When six operating wavelengths, $3\lambda_{\text{ref}}$, $2.5\lambda_{\text{ref}}$, $2\lambda_{\text{ref}}$, $1.5\lambda_{\text{ref}}$, $1.25\lambda_{\text{ref}}$, $\lambda_{\text{ref}}$, are considered in the frequency-hopping procedure, the reconstruction is ameliorated, as seen in Fig. 4.39 (b) and Figs. 4.39 (c) and (d) in solid line. This example points out the limitation of the frequency-hopping procedure. Depending on the clutter characteristics, its implementation (choice of the wavelengths, choice of the kept incident fields in the inversion) must be adapted.

### 4.4.6 Influence of the Born approximation on focalization and reconstruction

The HM-DORT discussed above is based on a non-linear algorithm. The synthetic data is generated rigorously, the total field is calculated by considering the polarization interaction inside the scattering domain. In the inversion procedure, both the permittivity and the total field inside the investigating domain are unknown and sought by the algorithm. While it is time-consuming for calculating rigorously the total field, especially for a large number of subunits. Hence it is meaningful to check the validity of the Born approximation in use of the DORT focusing fields in the inversion procedure, similarly as the homogeneous case that we have discussed in Sec. 4.3.

#### 4.4.6.1 Forward and inverse problem with Born's approximation

In this subsection, we propose to test the DORT method under the Born approximation. Bearing in mind that the scattered field equation is calculated with the Green's function that accounts for the interface, Eq. (1.21). While one does not need to resolve the self-consistent Eq. (1.33), the total field is assumed to be equal to the incident field. For the inverse problem, we consider a simpler linear inversion algorithm, using the same approximation as the forward problem, and the search direction for the total field is set to zero.

We keep the same realization of the correlated noise as above. Referred to Eq. (4.6), the computation error on Born's approximation $\text{Err}_{\text{Born}}$ is 150%, 134% and 204% at the wavelength $\lambda_1 = 3\lambda_{\text{ref}}$, $\lambda_2 = 1.5\lambda_{\text{ref}}$ and $\lambda_{\text{ref}}$, respectively. In this configuration, the coupling effect between

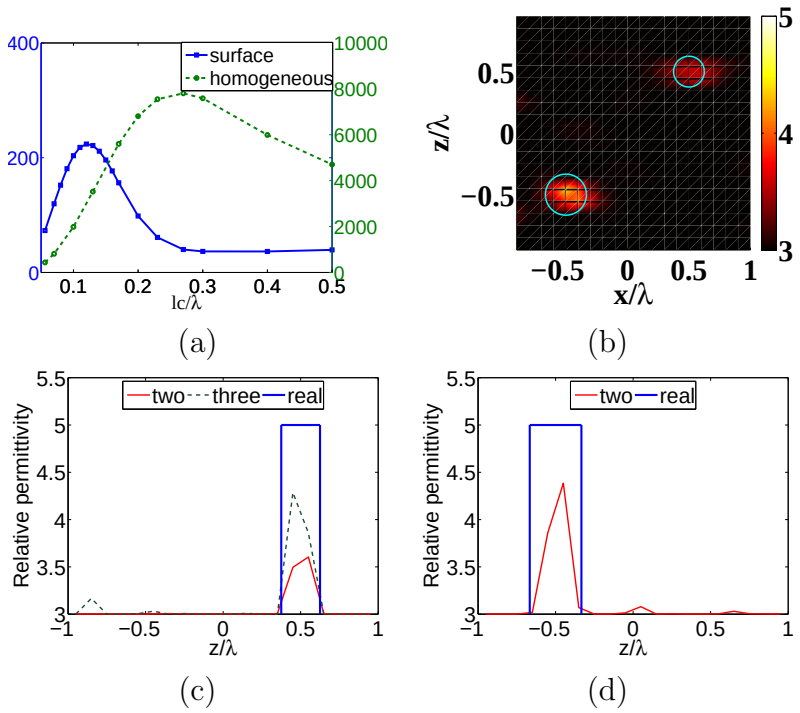


**Figure 4.38 :** *(a) Strength of the clutter scattered intensity, SC, versus $l_c/\lambda$ for the half-space configuration (solid line) and for the homogeneous configuration (dashed line). (b)-(d) Reconstructed permittivity obtained with HM-DORT and a frequency-hopping procedure using only $\lambda_3 = 3\lambda_{\text{ref}}$ and $\lambda_2 = 1.5\lambda_{\text{ref}}$. The clutter is defined by a correlation length $l_c = 0.1\lambda_{\text{ref}}$ and a standard deviation $\sigma_f = 0.058$ (b) Cut in the $(x, z)$ plane for $y = 0.4\lambda_{\text{ref}}$. (c) Reconstructed permittivity with respect to $z$ at $x = 0.5\lambda_{\text{ref}}$ and $y = 0.4\lambda_{\text{ref}}$. The blue solid curve denotes the actual permittivity of the targets, the red dashed line corresponds to the reconstructed profile obtained with HM-DORT and a frequency-hopping procedure restricted to $\lambda_3 = 3\lambda_{\text{ref}}$ and $\lambda_2 = 1.5\lambda_{\text{ref}}$. The black line indicates the reconstruction obtained when the data obtained at $\lambda_{\text{ref}}$ for the two incident DORT fields focusing on the target close to the interface are included in the frequency-hopping procedure. (d) same as (c) but $x = -0.5\lambda_{\text{ref}}$ and $y = 0.4\lambda_{\text{ref}}$. Note that the black line (not shown) is superposed to the red one.*

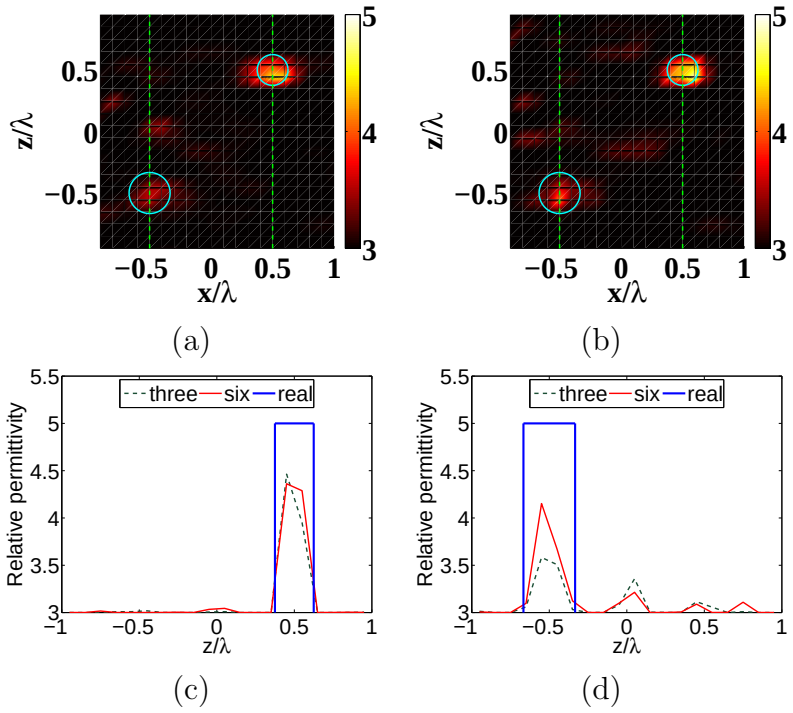


**Figure 4.39 :** *Reconstructed relative permittivity with* $l_c = 0.3\lambda_{\text{ref}}$ *and* $\sigma_f = 0.058$*, using the HM-DORT Only the results obtained at the wavelength* $\lambda_{\text{ref}}$ *are given here. (a) using three wavelengths, in the* $(x, z)$ *plane for* $y = 0.4\lambda_{\text{ref}}$*. (b) same as (a) but using six wavelengths for the frequency hopping. (c) and (d) the relative permittivity is plotted versus (c)* $z$ *for* $x = 0.5\lambda_{\text{ref}}$ *and* $y = 0.4\lambda_{\text{ref}}$*. (d)* $z$ *for* $x = -0.5\lambda$ *and* $y = 0.4\lambda_{\text{ref}}$*. The plain solid curves denote the actual profiles of the scatterers. The green dashed lines denote the result obtained using three wavelengths, and the red solid lines correspond to the results given using six wavelengths.*

clutter and scatterers is negligible. While the notable value of $\mathrm{Err}_{\mathrm{Born}}$ indicates that the multiple scattering effects within the clutter and within the scatterers are dominant.

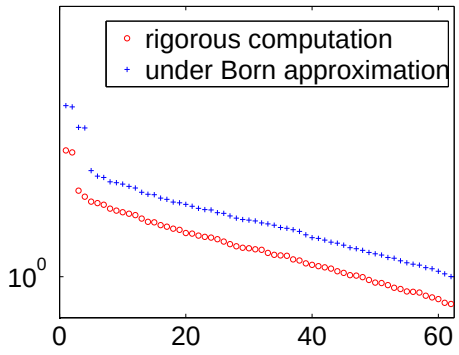


**Figure 4.40 :** *Evolutions of the eigenvalues corresponding to the rigorous computation and the computation under the Born approximation, with the same configuration as Fig. 4.29 (circle curve, rigorous computation; cross curve, computation under the Born approximation).*

We observe from Fig. 4.40 the evolution of the eigenvalues. Under the Born approximation, the plot of the eigenvalues on Fig. 4.40 (cross curve) exhibits four dominant eigenvalues. According to the analysis above, the first two eigenvalues focus on the most echogeneous scatterer. The third and the fourth eigenvalue correspond to the second echogeneous scatter. On the contrary, in the case of the simulated date generated rigorously, only two eigenvalues are clearly separated from other ones (circle curve). The following two eigenvalues corresponding to the second scatterer are roughly of the same order as those belonging to the noise space. One can conclude that the scatterers are easily recognizable under the Born approximation, because the multiple scattering effects within the scatterers and within the clutter are not taken into account.

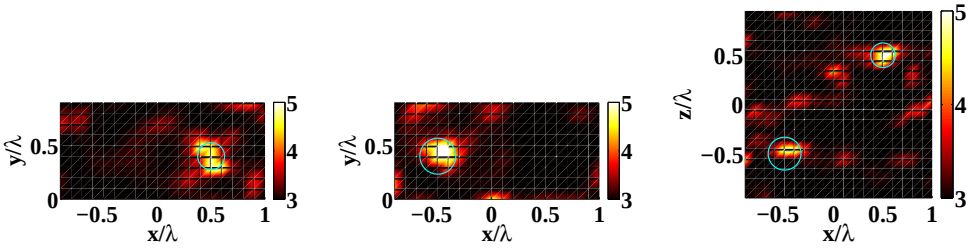


**Figure 4.41 :** *Same as Figs. 4.30 (a)-(c), while the synthetic data are generated under the Born approximation, and a linear Inversion-DORT method is used in the inversion procedure. (a) in $(x, y)$ plane for $z = 0.5\lambda_{\mathrm{ref}}$. (b) in $(x, y)$ plane for $z = -0.5\lambda_{\mathrm{ref}}$. (c) in $(x, z)$ plane for $y = 0.4\lambda_{\mathrm{ref}}$.*

In Fig. 4.41, we plot the map of relative permittivity obtained with a linear inversion procedure scheme, where the Born approximation is used for both the forward and inverse problem. We can yet observe the profile of each scatterer in the imaging plane, while comparing with Fig. 4.30 (a)-(c), the two scatterers are surrounded by enormous small ghosts, especially at the edge of the investigating domain. The imaging resolution is greatly deteriorated using the linear algorithm, confirmed quantitatively by $\mathrm{Err}_\chi$ equal to 468% (only 66% for the HM algorithm).

#### 4.4.6.2 Forward problem computed rigorously and the Born approximation for the inverse problem

Now, for the forward problem, the scattered field is calculated rigorously, the same manner as mentioned in Sec. 4.4.3. The difference is that we consider a simpler linear inversion algorithm, assuming that the total field equal to the incident field, and the search direction for the total field is set to zero.

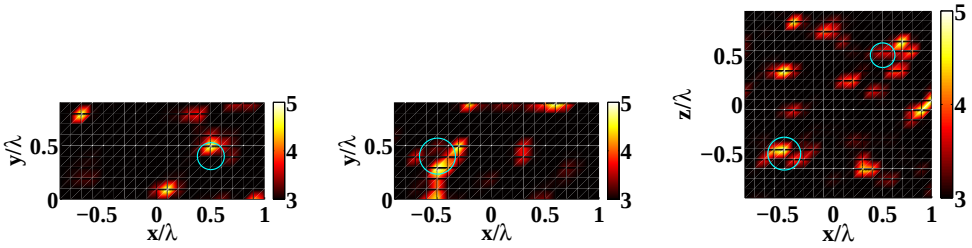


**Figure 4.42 :** *Same as Figs. 4.41 (a)-(c), except that the synthetic data are generated rigorously.*

Unfortunately, the linear HM-DORT fails to retrieve the two scatterers at the wavelength $\lambda_{\text{ref}}$, in the case of the synthetic diffracted field generated rigorously, Figs. 4.42. $\text{Err}_\chi = 851\%$, meaning that the reconstruction is no longer accurate using the inversion technique under the classical Born approximation. Up to now, we have checked the validity of Born's approximation in the process of using DORT method. In our configuration, it is required to calculate rigorously the scattered field and use a non-linear algorithm for reconstructing scatterers, regardless of the computation time.

### 4.4.7 Conclusion

In this section, we have analyzed the performance of the HM-DORT for localizing and characterizing scatterers buried under a flat interface in a highly cluttered semi-infinite medium. This realistic imaging configuration is plagued by a low numerical aperture due to the impedance matching between the antennas and the host medium. We have shown that the HM-DORT approach, which uses only data obtained with the DORT incident fields that focus on the strongest scatterers, is always more efficient than the classical inversion technique, where the entire of data are used, for extracting and imaging the targets.

To diminish the reconstruction artifacts stemming from the small effective numerical aperture of the imager, we have considered multi-frequency data and implemented a frequency-hopping procedure. We have pointed out that the clutter effect depends strongly on the ratio between the clutter correlation length and the wavelength. The frequency-hopping performance depending strongly on the initial reconstruction at low frequency, its strategy (choice of the wavelengths, choice of the DORT incident fields in the inversion procedure) must be adapted to the clutter characteristics.

To avoid the wavelength adjustment of this sequential inversion procedure and to ameliorate the reconstruction, a global multi-frequency reconstruction approach using the DORT incident fields may be an interesting alternative.

## 4.5 Conclusions

In this chapter, we investigated the focalization ability of the DORT method on simulated data under two different configurations in the time-harmonic regime, firstly, antennas lying in the same

medium as the scatterers, and secondly, antennas and scatterers are separated by an interface. For both of these two configurations, we have verified that using the HM-DORT inversion procedure, we can obtain a better characterization of targets under test than with the HM. While in the presence of the interface, we have to use the frequency-hopping approach to eliminate the oscillations due to the fact the numerical aperture is greatly reduced. The focusing waves and subsequently the reconstruction are dependent of the correlation length and of the standard deviation. We should adapt the frequency-hopping strategy following the correlation length. We have also emphasized the importance of using non-linear inversion algorithms and full-polarized data for achieving better reconstructions.

# Part III

# Three-dimensional experimental results in Tomographic Diffractive Microscopy

# Introduction of PART III

## Three-dimensional experimental results in Tomographic Diffractive Microscopy

In the last chapters, we have presented the forward model and the inversion scattering algorithm. We have provided that using a nonlinear iterative inversion method (HM), combined with the DORT focusing technique, a quantitative characterization and ameliorate the signal-to-clutter ratio in the case of scatterers buried in cluttered medium was achieved.

In this part, we propose to study the characterization ability of this combined method using experimental data. The DORT method has been applied in RADAR with microwave data[101] and also in optical imaging domain[48]. In our team (SEMOX, Insitut Fresnel), a quite recent optical imaging technique, Tomographic Diffractive Microscopy (TDM) has been developed experimentally in three-dimension, while in scalar configuration, meaning that the illuminations are polarized along one single direction and the scattered field are collected in the same projection. In this thesis work, we propose to apply the DORT method in TDM technology. Thanks to DORT, scatterers are focalized selectively in the case of a multi-target medium. The extra information around each scatterer can be eliminated thanks to DORT. In particular, in the presence of disordered medium, the signal-to-noise ratio can be ameliorated using DORT. Using the time-reversal concept, it has been shown that an isotropic reconstruction can be realized by placing a mirror after the focal point[102]. This concept could be applied in DORT for obtaining an isotropic focalization.

As we have presented in Chap. 4, combining with DORT, it is important to use full-polarized data for improving the imaging performance. In this part, firstly,a full-polarization TDM technology will be provided in Chap. 5 and it will be combined with the DORT method in Chap. 6.

Chapter 5

# Full-polarization technology in tomographic diffractive microscopy

This chapter is related to one publication:

1. T. Zhang, Y. Ruan, G. Maire, D. Sentenac, A. Talneau, K. Belkebir, P. C. Chaumet and A. Sentenac, *Full-polarized tomographic diffraction microscopy achieves a resolution about one fourth of the wavelength*, Physical Review Letters, **111**, 243904 (2013).

## Contents



## 5.1 Introduction

Tomographic Diffractive Microscopy (TDM) is a promising digital imaging technique. It consists in recording (via an interferometric setup[103–105] or using a wavefront sensor[13], or an off-axis holography technique[106]), the amplitude and phase of the scattered field for many successive different illuminations. In the single scattering regime, the merging of the scattered data over different incidences enables the TDM theoretically to reconstruct the sample permittivity with a transverse resolution about one-fourth of the wavelength[103,105], see Appendix F. Notice that in conventional optical microscope[107–109], the resolution is limited to half of the wavelength (Abbe's limit).

Remarkably, in two-dimension, a transverse resolution about $\lambda/4$ has been experimentally observed on elongated objects[110] with TDM. Yet, this achievement has never been evidenced on a three-dimensional specimen. The most likely reason is that TDM does not account for the light polarization effect in the image formation process. The holograms are obtained for one given polarization state and the reconstruction procedures are based on scalar approximate models[50,51,104]. In

three dimension, with only 20 different illumination angles, a transverse reconstruction resolution of 400 nm can be provided experimentally[49]. This resolution corresponds exactly to the Rayleigh limit of our microscope ($0.6\lambda/\text{NA} \approx 400$ nm) with $\lambda = 633$ nm and NA=0.95, and is far from the theoretical resolution limit achieved by TDM.

In this chapter, we sought to exploit the full potential of TDM by taking advantage of the light polarization[111,112]. We will present the first experimental implementation of a TDM that records and processes the vectorial field scattered by a sample (both amplitude and phase) for any incident polarization state to yield the sample permittivity map.

## 5.2 Polarization resolved methods for TDM

In this section, we will present the retrieval of the measured full vectorial scattered field of the sample, for any polarization state of the illumination (full-polarized TDM), with the help of the Jones operator. The TDM setup is a modified reflection microscope in which an off-axis holography technique has been introduced to recover the phase and amplitude of the field at the microscope image plane, see Fig. 5.1. We chose the reflection configuration because it has been shown to allow a significant improvement of the axial resolution[98,102,113]. A collimated laser beam (He-Ne wavelength $\lambda = 633$ nm), controlled by a mirror mounted on step motors (Newport NSA12), illuminates the sample through an air objective with $NA = 0.95$ (Zeiss Epiplan-Apochromat $\times 50$) under various angles of incidence.

For the experimental realization, two half wave plates $HW_1$ and $HW_2$ have been inserted in the setup to adjust the polarization state for both the illumination beam and the reference beam, where the reference beam is used to control the polarization state of the measured scattered field. The experimental work has been done by Yi RUAN, and more precise experimental descriptions have been given in his thesis work[106]. I will explain in detail how one links to the theoretical vectorial fields calculated by the forward model.

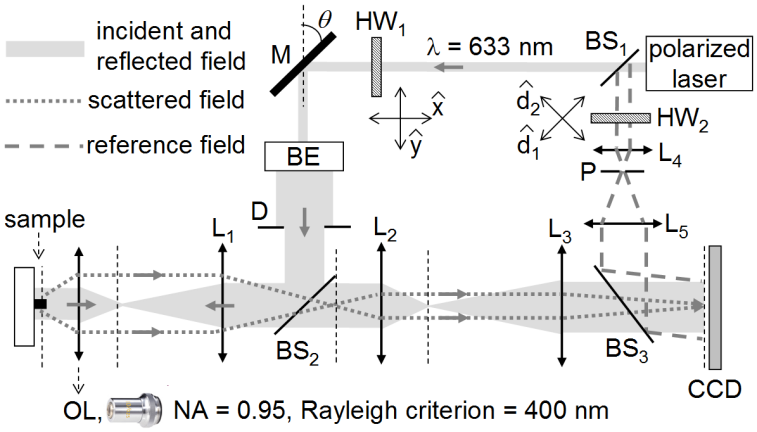


**Figure 5.1 :** *Schematic of the full-polarized TDM setup. M the rotative mirror. BE the beam expander. D the diaphragm. BS the beam splitter. OL the objective lens. P the pinhole. $L_1$ the tube lens. $L_2$ and $L_3$ are the relay lenses ($f' = 3.5$ and 20 cm, respectively). $HW_1$ and $HW_2$ the half-wave plate on the incident field and reference field, respectively.*

### 5.2.1 Measurement of the full vectorial scattered field

At the image plane of the microscope, overlooking the magnification factor, the field scattered by the sample $\boldsymbol{E}^{\mathrm{sca}}$, for a given illumination, reads as

$$\boldsymbol{E}^{\mathrm{sca}}(\boldsymbol{r}_{\parallel}) = \int_{k_{\parallel}<k_0\mathrm{NA}} \frac{1}{\gamma}(e_s\hat{\boldsymbol{s}} + e_p\hat{\boldsymbol{p}})\ \exp(i\boldsymbol{k}_{\parallel}\cdot\boldsymbol{r}_{\parallel})\mathrm{d}\boldsymbol{k}_{\parallel}, \tag{5.1}$$

where $\boldsymbol{e}_z$ denotes the optical axis of the microscope, $k_0 = 2\pi/\lambda$, $\gamma = \sqrt{(2\pi/\lambda)^2 - k_{\parallel}^2}$, $\hat{\boldsymbol{s}} = \boldsymbol{e}_z \times \hat{\boldsymbol{k}}$, $\hat{\boldsymbol{p}} = \hat{\boldsymbol{s}} \times \hat{\boldsymbol{k}}$ with $\boldsymbol{k} = \boldsymbol{k}_{\parallel} + \gamma\boldsymbol{e}_z$, and $(e_s, e_p)$ are the complex amplitudes of the scattered plane wave propagating along $\boldsymbol{k}$, corresponding to $\hat{\boldsymbol{s}}$ and $\hat{\boldsymbol{p}}$ components, respectively.

Generally, the polarization states in the illumination and the detection bases are fixed by the vertical and horizontal directions of polarizer, denoted by $\hat{\boldsymbol{y}}$ and $\hat{\boldsymbol{x}}$, respectively. In most of the previous work of our group on 3D TDM technology[13,25], all the measurements were conducted with both the illumination and the detection bases polarized along $\hat{\boldsymbol{y}}$ direction (called $\hat{\boldsymbol{y}}\hat{\boldsymbol{y}}$ configuration, first letter indicating the direction of the illumination, and second one for the detection). Now for realizing full-polarization and measuring the Jones operator, this procedure has to be repeated for two independent incident polarization states $(\hat{\boldsymbol{x}}, \hat{\boldsymbol{y}})$ and measured along two orthogonal directions $(\hat{\boldsymbol{x}}, \hat{\boldsymbol{y}})$. Hence, the full-polarized TDM mode requires four intensity measurements for each incident angle (and possibly only two using Ref. 112), for example, $\hat{\boldsymbol{y}}\hat{\boldsymbol{y}}$, $\hat{\boldsymbol{y}}\hat{\boldsymbol{x}}$, $\hat{\boldsymbol{x}}\hat{\boldsymbol{y}}$ and $\hat{\boldsymbol{x}}\hat{\boldsymbol{x}}$, respectively, to match the rigorously calculated theoretical scattered field. The amplitude and the phase of the measured scattered field have to be calibrated, by using the specular reflected field[49]. It has to be noted that there is no specular reflection for the measurements $\hat{\boldsymbol{y}}\hat{\boldsymbol{x}}$ and $\hat{\boldsymbol{x}}\hat{\boldsymbol{y}}$. Thus, to avoid turning off the specular reflection, one records with a CCD camera (Kappa DX4-1020FW), the interference patterns between $\boldsymbol{E}^{\mathrm{sca}}$ and an off-axis reference wave which is successively polarized along two different directions $\hat{\boldsymbol{d}}_1$ and $\hat{\boldsymbol{d}}_2$, as shown in Fig. 5.2, here, $\alpha = 45$ degree. Processing the holograms yield $\boldsymbol{E}\cdot\hat{\boldsymbol{d}}_1$ and $\boldsymbol{E}\cdot\hat{\boldsymbol{d}}_2$ from which $(e_s, e_p)$ for all $\boldsymbol{k}_{\parallel}$ such that $\boldsymbol{k}_{\parallel} < k_0\mathrm{NA}$ are easily extracted. Then for each incident angle, the new four groups of measured scalar data are defined as: $E^{\hat{\boldsymbol{y}}\hat{\boldsymbol{d}}_1}_{\mathrm{s;exp}}$, $E^{\hat{\boldsymbol{y}}\hat{\boldsymbol{d}}_2}_{\mathrm{s;exp}}$, $E^{\hat{\boldsymbol{x}}\hat{\boldsymbol{d}}_1}_{\mathrm{s;exp}}$ and $E^{\hat{\boldsymbol{x}}\hat{\boldsymbol{d}}_2}_{\mathrm{s;exp}}$, where the superscript, for example, $\hat{\boldsymbol{y}}\hat{\boldsymbol{d}}_1$ means that the incident wave is oriented along the $\hat{\boldsymbol{y}}$ direction and the reference wave is polarized along the $\hat{\boldsymbol{d}}_1$ direction.

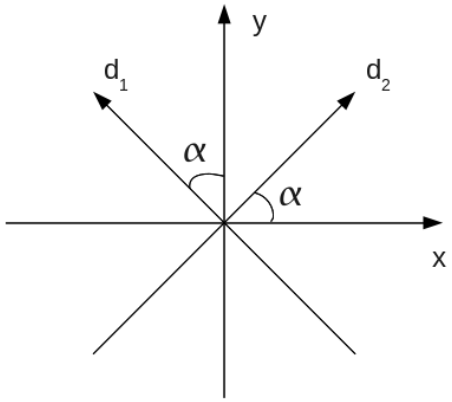


**Figure 5.2 :** *The detection and the illumination state for full-polarization configuration.*

Once we get the scattered electric field with the incident field in the base $\hat{\boldsymbol{y}}$ or $\hat{\boldsymbol{x}}$, of any polarization state (TM and TE mixed), we need to first perform the normalization procedure

to match with the theoretical calculated field. Then we will decompose the normalized fields corresponding to pure TM or TE illumination.

## 5.2.2 The normalization procedure

*Note that this part is explained very technically. You can skip it for the first reading and move directly to the reconstruction results.*

The fluctuations of the laser source change the amplitude of the illuminations for different incidences. The phase of the illumination beam is different when reaching the sample for different illumination angles because the optical path of the illumination and reference beams varies for each illumination. It is necessary to normalize the measured scattered fields $\boldsymbol{f}_l$, prior to performing the non-linear inversion. The matching of the different scattered fields is based on a normalization ensuring that each specularly reflected field matches (both in amplitude and phase) with that theoretically calculated by the forward scattering model, at each illumination. This normalization procedure implies that the permittivity of the substrate is known (note that ellipsometric measurements can be performed at a known incidence angle by rotating polarizer to determine the unknown complex reflection and transmission coefficients of the optical components present between the source and the camera) and that the specular reflection has to be far stronger than the field scattered in the same direction by the sample.

### 5.2.2.1 Amplitude normalization

The amplitude normalization procedure is done in the part of experimental processing procedure[49,106], which will be recalled briefly here. Note that the total field measured in the image space for illumination number $l$ is called $\tilde{\boldsymbol{f}}_l$, to distinguish it from $\boldsymbol{f}_l$, the field transferred in the Fourier space and used by the inversion algorithm.

The inversion assumes that the object is illuminated for each angle of incidence by a plane wave with unit amplitude. The measured amplitudes $\|\tilde{\boldsymbol{f}}_l\|$ have therefore to be normalized according to this hypothesis so that a correct estimation of the permittivity can be retrieved. The amplitude normalization is moreover useful to correct the intensity fluctuations of the illuminating beam that can occur from one illumination angle to another. It is performed for each illumination $l$ by multiplying $\tilde{\boldsymbol{f}}_l$ by the factor $M_l$ :

$$M_l = \frac{|\gamma_l| S}{2\pi \langle \|\tilde{\boldsymbol{f}}_l\| \rangle_S}, \tag{5.2}$$

where $\gamma_l = -k_0 \cos\theta_l$ is the projection of the illumination wave vector on the optical axis of the microscope (the minus sign is due to the reflection configuration), and $S$ the surface of the field of view that can be imaged on the CCD sensor. $\langle \|\tilde{\boldsymbol{f}}_l\| \rangle_S$ is the mean field modulus averaged over the field of view: as the object is small on the CCD image, it can be considered as the mean field modulus reflected by the substrate. The multiplication by $M_l$ ensures that the maximal value of $\|\boldsymbol{f}_l\|$ in far field, which corresponds to the specular reflection, is equal to that scattered by a portion of substrate of surface $S$ when illuminated by a plane wave with unity amplitude, as calculated by the forward scattering model. The Fresnel amplitude reflection coefficient on the substrate $r_l$ for each illumination $l$ is extracted from Eq. (5.2) and will be introduced in the following phase normalization procedure.

### 5.2.2.2 Phase normalization

In the forward scattering model, the phase origin is placed on the substrate and in the middle of the transverse dimensions of the investigating domain $\Omega$, shown as Fig. 5.3. It means that for any illumination angle, the phase of this incident beam is equal to zero at this position. Experimentally, the phase origin is drifted and different for each illumination beam. This mismatch of phase caused by the varied optical path must be corrected[106]. Here, we need firstly to normalize the amplitudes and the phases of measured specular reflected fields. Then we add the term of the theoretical

specular reflected fields (projected along two detected polarizers), obtained by the theoretical incident field with amplitude $|A_{\text{inc}}^{\text{theo}}| = 1$ and $\varphi_{\text{inc}}^{\text{theo}} = 0$.

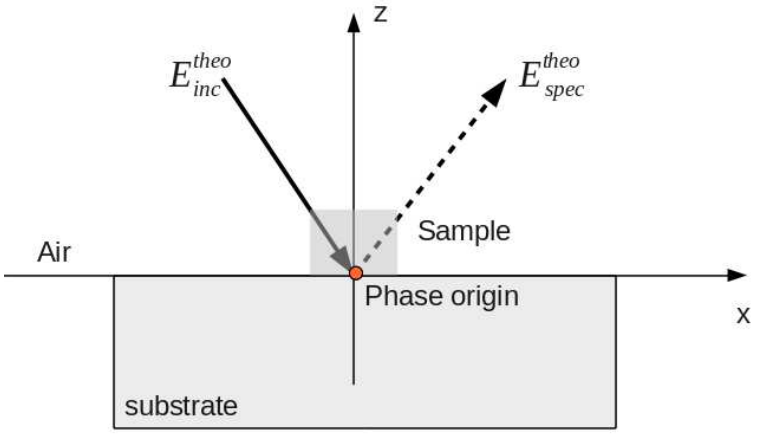


**Figure 5.3 :** *Position of the theoretical phase origin with respect to the substrate and the object.*

The theoretical incident plane waves polarized along TM and TE polarization, for each illumination, are represented respectively as

$$\boldsymbol{E}_{\text{inc;theo}}^{\hat{\boldsymbol{s}}} = \hat{\boldsymbol{s}} \ \exp(i\boldsymbol{k}_{\text{inc}} \cdot \boldsymbol{r}), \tag{5.3}$$

$$\boldsymbol{E}_{\text{inc;theo}}^{\hat{\boldsymbol{p}}} = \hat{\boldsymbol{p}}_{\boldsymbol{i}} \ \exp(i\boldsymbol{k}_{\text{inc}} \cdot \boldsymbol{r}), \tag{5.4}$$

where the amplitude is equal to 1 and the phase origin $\varphi_{\text{inc}}^{\text{theo}}$ is taken to be equal to zero. Then the reflected fields propagating along $\boldsymbol{k}_{\text{ref}}$ are represented as

$$\boldsymbol{E}_{\text{ref;theo}}^{\hat{\boldsymbol{s}}} = r_s \ \hat{\boldsymbol{s}} \ \exp(i\boldsymbol{k}_{\text{ref}} \cdot \boldsymbol{r}), \tag{5.5}$$

$$\boldsymbol{E}_{\text{ref;theo}}^{\hat{\boldsymbol{p}}} = r_p \ \hat{\boldsymbol{p}}_{\boldsymbol{r}} \ \exp(i\boldsymbol{k}_{\text{ref}} \cdot \boldsymbol{r}), \tag{5.6}$$

where $r_p$ and $r_s$ are the Fresnel amplitude reflection coefficients corresponding to TM and TE polarization, respectively.

An incident plane wave polarized along $x$-direction can be decomposed along TM and TE polarization as

$$\boldsymbol{E}_{\text{inc;theo}} = -\sin\phi_{\text{inc}} \boldsymbol{E}_{\text{inc;theo}}^{\hat{\boldsymbol{s}}} + \cos\phi_{\text{inc}} \boldsymbol{E}_{\text{inc;theo}}^{\hat{\boldsymbol{p}}}, \tag{5.7}$$

where $\phi_{\text{inc}}$ is the angle between $\boldsymbol{E}_{\text{inc;theo}}$ and $\hat{\boldsymbol{p}}$ direction, and the reflected field is represented as

$$\boldsymbol{E}_{\text{ref;theo}} = -\sin\phi_{\text{inc}} \boldsymbol{E}_{\text{ref;theo}}^{\hat{\boldsymbol{s}}} + \cos\phi_{\text{inc}} \boldsymbol{E}_{\text{ref;theo}}^{\hat{\boldsymbol{p}}}, \tag{5.8}$$

$$= (-\sin\phi_{\text{inc}} r_s \ \hat{\boldsymbol{s}} + \cos\phi_{\text{inc}} r_p \ \hat{\boldsymbol{p}}_{\boldsymbol{r}}) \ \exp(i\boldsymbol{k}_{\text{ref}} \cdot \boldsymbol{r}). \tag{5.9}$$

Hence the phase of $\boldsymbol{E}_{\text{ref;theo}}$ depends both of $r_s$ and $r_p$ and this phase should match the phase of the experimental specular reflected field.

To normalize the phase, the procedure to follow is

Step 1:

Firstly, we define several parameters here. The simplified system is shown as Fig. 5.4 (a). In

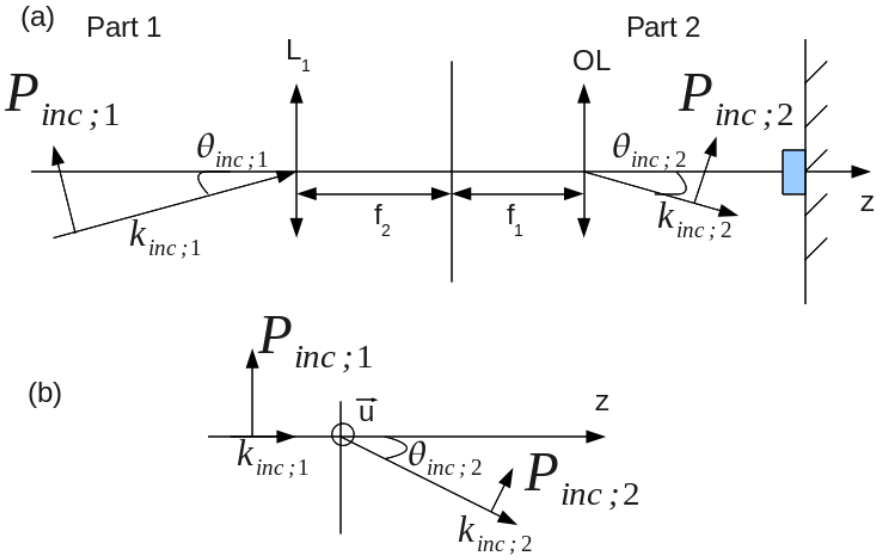


**Figure 5.4 :** *Simplified geometry of the problem. (a) The whole experiment is divided into two parts, part-1 and part-2. OL: microscope objective; $L_1$: associated tube lens. (b) Rotation around axis* $\mathbf{u} = \boldsymbol{k}_{\mathrm{inc};1} \wedge \boldsymbol{k}_{\mathrm{inc};2}$.

part-1, after the deflection of the mirror and before the transmission through the objectives and lens, $\theta_{\mathrm{inc};1} \approx 0$, the illumination beam is supposed to be propagating along the optical axis. The incident wave vector $\boldsymbol{k}_{\mathrm{inc};1}(\theta_{\mathrm{inc};1}, \phi_{\mathrm{inc};1}) \approx \boldsymbol{e}_z$. The incident fields can be polarized along vertical direction or horizontal direction

$$\boldsymbol{P}_{\mathrm{inc};1}^{\mathrm{theo}} \approx \begin{cases} \hat{\boldsymbol{y}} & \text{vertical direction,} \\ \hat{\boldsymbol{x}} & \text{horizontal direction.} \end{cases} \tag{5.10}$$

Step 2:

After passing through objectives and tubes lens, we illuminate the sample with a parallel beam over a wide range of incidence angles $\theta_{\mathrm{inc};2}$. The wave vector $\boldsymbol{k}_{\mathrm{inc};2}(\theta_{\mathrm{inc};2}, \phi_{\mathrm{inc}})$ in part-2 of the plane wave illuminating the samples

$$\boldsymbol{k}_{\mathrm{inc};2} = \begin{bmatrix} \sin\theta_{\mathrm{inc};2}\cos\phi_{\mathrm{inc}} \\ \sin\theta_{\mathrm{inc};2}\sin\phi_{\mathrm{inc}} \\ \cos\phi_{\mathrm{inc}} \end{bmatrix} = \begin{bmatrix} k_{\mathrm{inc};2}^{\mathrm{x}} \\ k_{\mathrm{inc};2}^{\mathrm{y}} \\ k_{\mathrm{inc};2}^{\mathrm{z}} \end{bmatrix}, \tag{5.11}$$

where $\theta_{\mathrm{inc};2}$ is the illumination angle in the sample plane. We note that the objective conserves the modulus of the plane wave and rotates the electric field vector direction around $\mathbf{u}$, see Fig. 5.4.

For calculating the incident field vector $\boldsymbol{P}_{\mathrm{inc};2}^{\mathrm{theo}}$ in part-2 with any polar angle, we use the rotation matrix. In three-dimensional space, every rotation can be interpreted as a rotation by a given angle about a single fixed axis of rotation, seeing Fig. 5.4 (b). The direction $\mathbf{u}$ that is left fixed by the rotation is defined as here

$$\mathbf{u} = \begin{bmatrix} u_x \\ u_y \\ u_z \end{bmatrix} = \frac{\boldsymbol{k}_{\mathrm{inc};1} \wedge \boldsymbol{k}_{\mathrm{inc};2}}{\|\boldsymbol{k}_{\mathrm{inc};1} \wedge \boldsymbol{k}_{\mathrm{inc};2}\|}. \tag{5.12}$$

The matrix for a rotation by $\theta_{\mathrm{inc};2}$ about $\mathbf{u}$ is

$$\boldsymbol{R} = \begin{bmatrix} u_x^2+(1-u_x^2)\cos\theta_{\mathrm{inc};2} & u_xu_y(1-\cos\theta_{\mathrm{inc};2})-u_z\sin\theta_{\mathrm{inc};2} & u_xu_z(1-\cos\theta_{\mathrm{inc};2})+u_y\sin\theta_{\mathrm{inc};2} \\ u_xu_y(1-\cos\theta_{\mathrm{inc};2})+u_z\sin\theta_{\mathrm{inc};2} & u_y^2+(1-u_y^2)\cos\theta_{\mathrm{inc};2} & u_yu_z(1-\cos\theta_{\mathrm{inc};2})-u_x\sin\theta_{\mathrm{inc};2} \\ u_xu_z(1-\cos\theta_{\mathrm{inc};2})-u_y\sin\theta_{\mathrm{inc};2} & u_yu_z(1-\cos\theta_{\mathrm{inc};2})+u_x\sin\theta_{\mathrm{inc};2} & u_z^2+(1-u_z^2)\cos\theta_{\mathrm{inc};2} \end{bmatrix}, \tag{5.13}$$

where $\det(\boldsymbol{R}) = 1$ and $\boldsymbol{R}^{-1} = \boldsymbol{R}^t$, the inverse of this matrix is its own transpose.

Now, the incident field in part-2 can be calculated by applying the rotation matrix, written as below

$$\boldsymbol{P}^{\text{theo}}_{\text{inc;2}} = \boldsymbol{R}\ \ \boldsymbol{P}^{\text{theo}}_{\text{inc;1}}. \tag{5.14}$$

Step 3:

The incident field $\boldsymbol{P}^{\text{theo}}_{\text{inc;2}}$ in part-2 can be transferred from the base $\mathbb{R}(\hat{\boldsymbol{x}}, \hat{\boldsymbol{y}}, \hat{\boldsymbol{z}})$ to the base $\mathbb{S}(\hat{\boldsymbol{s}}, \hat{\boldsymbol{p}})$, by applying a transfer matrix as

$${}_{\mathbb{S}}\boldsymbol{P}^{\text{theo}}_{\text{inc;2}} = \boldsymbol{M}\ \ {}_{\mathbb{R}}\boldsymbol{P}^{\text{theo}}_{\text{inc;2}}, \tag{5.15}$$

where $\boldsymbol{M}$ is a $2 \times 3$ matrix, defined as

$$\boldsymbol{M} = \begin{bmatrix} \cos\theta_{\text{inc;2}}\cos\phi_{\text{inc}} & \cos\theta_{\text{inc;2}}\sin\phi_{\text{inc}} & -\sin\theta_{\text{inc;2}} \\ -\sin\phi_{\text{inc}} & \cos\phi_{\text{inc}} & 0 \end{bmatrix}, \tag{5.16}$$

Then, the reflected field ${}_{\mathbb{S}}\boldsymbol{P}^{\text{theo}}_{\text{ref;2}}$ in part-2 is calculated as

$${}_{\mathbb{S}}\boldsymbol{P}^{\text{theo}}_{\text{ref;2}} = \mathbf{f}({}_{\mathbb{S}}\boldsymbol{P}^{\text{theo}}_{\text{inc;2}}, r_s, r_p), \tag{5.17}$$

where $\mathbf{f}({}_{\mathbb{S}}\boldsymbol{P}^{\text{theo}}_{\text{inc;2}}, r_s, r_p)$ is the Fresnel reflectivity depending on ${}_{\mathbb{S}}\boldsymbol{P}^{\text{theo}}_{\text{inc;2}}$ and the polarization state, as shown in Eqs. (5.5) and (5.6).

Then we go back to the base $\mathbb{R}(\hat{\boldsymbol{x}}, \hat{\boldsymbol{y}}, \hat{\boldsymbol{z}})$, by performing

$${}_{\mathbb{R}}\boldsymbol{P}^{\text{theo}}_{\text{ref;2}} = \boldsymbol{M}'\ \ {}_{\mathbb{S}}\boldsymbol{P}^{\text{theo}}_{\text{ref;2}}, \tag{5.18}$$

where $\boldsymbol{M}'$ is defined as

$$\boldsymbol{M}' = \begin{bmatrix} \cos\theta_{\text{inc;2}}\cos\phi_{\text{inc}} & -\sin\phi_{\text{inc}} \\ \cos\theta_{\text{inc;2}}\sin\phi_{\text{inc}} & \cos\phi_{\text{inc}} \\ -\sin\theta_{\text{inc;2}} & 0 \end{bmatrix}. \tag{5.19}$$

Step 4:

The reflected field is finally received on CCD camera. After the lens in Fig. 5.1, the polar angle $\theta_{\text{inc;1}}$ is closed to zero. We can perform a similar projection as

$$\boldsymbol{P}^{\text{theo}}_{\text{ref;1}} = \boldsymbol{R}^{-1}\boldsymbol{P}^{\text{theo}}_{\text{ref;2}}. \tag{5.20}$$

Seeing Fig. 5.2, the two polarizers for detection $\hat{\boldsymbol{d}}_1$ and $\hat{\boldsymbol{d}}_2$ are represented as

$$\hat{\boldsymbol{d}}_1 = -\sin\alpha\ \ \hat{\boldsymbol{x}} + \cos\alpha\ \ \hat{\boldsymbol{y}}, \tag{5.21}$$

$$\hat{\boldsymbol{d}}_2 = \ \ \cos\alpha\ \ \hat{\boldsymbol{x}} + \sin\alpha\ \ \hat{\boldsymbol{y}}. \tag{5.22}$$

The experimental specular reflected field measured on CCD camera, *i.e.* for illumination polarized along $\hat{\boldsymbol{x}}$ direction and detection polarized along $\hat{\boldsymbol{d}}_1$, can be expressed as

$$E^{\hat{\boldsymbol{x}}\hat{\boldsymbol{d}}_1}_{\text{spec;mes}} = \boldsymbol{E}^{\hat{\boldsymbol{x}}}_{\text{ref;exp}} \cdot \hat{\boldsymbol{d}}_1 = |A^{\text{exp}}_{\text{spec}}|\exp(i\varphi^{\text{exp}}_{\text{spec}}), \tag{5.23}$$

where $|A^{\text{exp}}_{\text{spec}}|$ and $\varphi^{\text{exp}}_{\text{spec}}$ are modulus and phase of the specular field $E^{\hat{\boldsymbol{x}}\hat{\boldsymbol{d}}_1}_{\text{spec;mes}}$ measured on CCD camera.

In order to match the measured scattered field with the theoretical scattered field, using the measured specular field as reference, we perform a normalization procedure as

$$E^{\hat{\boldsymbol{x}}\hat{\boldsymbol{d}}_1}_{\text{sca;cor}} = E^{\hat{\boldsymbol{x}}\hat{\boldsymbol{d}}_1}_{\text{sca;mes}} \times \frac{\boldsymbol{P}^{\text{theo};\hat{\boldsymbol{x}}}_{\text{ref;1}} \cdot \hat{\boldsymbol{d}}_1}{E^{\hat{\boldsymbol{x}}\hat{\boldsymbol{d}}_1}_{\text{spec;mes}}}. \tag{5.24}$$

Similarly, all of other measured scattered fields $E^{\hat{\boldsymbol{x}}\hat{\boldsymbol{d}}_2}_{\text{sca;mes}}$, $E^{\hat{\boldsymbol{y}}\hat{\boldsymbol{d}}_1}_{\text{sca;mes}}$ and $E^{\hat{\boldsymbol{y}}\hat{\boldsymbol{d}}_2}_{\text{sca;mes}}$ can be corrected as Eq. (5.24), denoted by $E^{\hat{\boldsymbol{y}}\hat{\boldsymbol{d}}_1}_{\text{sca;cor}}$, $E^{\hat{\boldsymbol{y}}\hat{\boldsymbol{d}}_2}_{\text{sca;cor}}$, $E^{\hat{\boldsymbol{x}}\hat{\boldsymbol{d}}_1}_{\text{sca;cor}}$ and $E^{\hat{\boldsymbol{x}}\hat{\boldsymbol{d}}_2}_{\text{sca;cor}}$.

For $\hat{\boldsymbol{x}}$-orientation incident field, the corrected scattered fields projected along horizontal and vertical direction are written as (where $\alpha$ denotes the angle between $\hat{\boldsymbol{x}}$ and $\hat{\boldsymbol{d}}_2$ for detections)

$$E^{\hat{\boldsymbol{x}}\hat{\boldsymbol{x}}}_{\text{sca;cor}} = -\sin\alpha \;\; E^{\hat{\boldsymbol{x}}\hat{\boldsymbol{d}}_1}_{\text{sca;cor}} + \cos\alpha \;\; E^{\hat{\boldsymbol{x}}\hat{\boldsymbol{d}}_2}_{\text{sca;cor}}, \tag{5.25}$$

$$E^{\hat{\boldsymbol{x}}\hat{\boldsymbol{y}}}_{\text{sca;cor}} = \;\; \cos\alpha \;\; E^{\hat{\boldsymbol{x}}\hat{\boldsymbol{d}}_1}_{\text{sca;cor}} + \sin\alpha \;\; E^{\hat{\boldsymbol{x}}\hat{\boldsymbol{d}}_2}_{\text{sca;cor}}. \tag{5.26}$$

Similar as above, for $\hat{\boldsymbol{y}}$-orientation incident field, the corrected scattered fields projected along horizontal and vertical direction are written as

$$E^{\hat{\boldsymbol{y}}\hat{\boldsymbol{x}}}_{\text{sca;cor}} = -\sin\alpha \;\; E^{\hat{\boldsymbol{y}}\hat{\boldsymbol{d}}_1}_{\text{sca;cor}} + \cos\alpha \;\; E^{\hat{\boldsymbol{y}}\hat{\boldsymbol{d}}_2}_{\text{sca;cor}}, \tag{5.27}$$

$$E^{\hat{\boldsymbol{y}}\hat{\boldsymbol{y}}}_{\text{sca;cor}} = \;\; \cos\alpha \;\; E^{\hat{\boldsymbol{y}}\hat{\boldsymbol{d}}_1}_{\text{sca;cor}} + \sin\alpha \;\; E^{\hat{\boldsymbol{y}}\hat{\boldsymbol{d}}_2}_{\text{sca;cor}}. \tag{5.28}$$

Notice that if the incident field is in pure TM or TE polarization, then the reflectivity $\mathbf{f}(_{\mathbb{S}}\boldsymbol{P}^{\text{theo}}_{\text{inc;2}}, r_s, r_p)$ in Eq. (5.17) is simplified into a scalar coefficient. The reflected field in part-2 can be written as

$$\begin{aligned} {}_{\mathbb{R}}\boldsymbol{P}^{\text{theo}}_{\text{ref;2}} &= \boldsymbol{M}' \;\; {}_{\mathbb{S}}\boldsymbol{P}^{\text{theo}}_{\text{ref;2}}, \\ &= \boldsymbol{M}'\mathbf{f}({}_{\mathbb{S}}\boldsymbol{P}^{\text{theo}}_{\text{inc;2}}, r_s, r_p) \;\; {}_{\mathbb{S}}\boldsymbol{P}^{\text{theo}}_{\text{inc;2}}, \\ &= \boldsymbol{M}'\mathbf{f}({}_{\mathbb{S}}\boldsymbol{P}^{\text{theo}}_{\text{inc;2}}, r_s, r_p) \;\; \boldsymbol{M} \;\; {}_{\mathbb{R}}\boldsymbol{P}^{\text{theo}}_{\text{inc;2}}, \\ &= \mathbf{f}({}_{\mathbb{S}}\boldsymbol{P}^{\text{theo}}_{\text{inc;2}}, r_s, r_p) {}_{\mathbb{R}}\boldsymbol{P}^{\text{theo}}_{\text{inc;2}}. \end{aligned} \tag{5.29}$$

Finally, we get the same representation as Eqs. (5.5) and (5.6). In scalar case, we calculate the specular reflected field as Eqs. (5.5) and (5.6) in Ref. 13. Otherwise, we have to perform the complicated projection procedure involved with full-polarized data, using the rotation matrix $\boldsymbol{R}$.

#### 5.2.2.3 Decomposition in TM and TE polarizations

Once we get the scattered fields by illuminations in the base $(\hat{\boldsymbol{x}}, \hat{\boldsymbol{y}})$, one can easily obtain the scattered field for the illuminations along TM and TE polarizations. The incident fields after passing

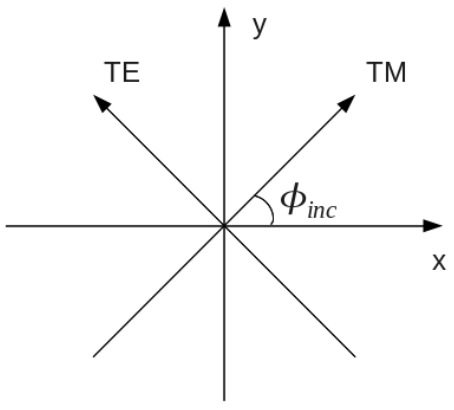


**Figure 5.5 :** *Orientation of the TM and TE polarizations compared to the vertical* $\hat{\boldsymbol{y}}$ *and horizontal* $\hat{\boldsymbol{x}}$ *directions.* $\phi_{\text{inc}}$ *is azimuthal angle in spherical coordinate system.*

through objective and tube lens, seeing Fig. 5.5, are decomposed for TM and TE polarizations as

$$\begin{pmatrix} \boldsymbol{E}^{\hat{p}}_{\text{inc}} \\ \boldsymbol{E}^{\hat{s}}_{\text{inc}} \end{pmatrix} = \begin{pmatrix} \cos\phi_{\text{inc};2} & \sin\phi_{\text{inc};2} \\ -\sin\phi_{\text{inc};2} & \cos\phi_{\text{inc};2} \end{pmatrix} \begin{pmatrix} \boldsymbol{E}^{\hat{\boldsymbol{x}}}_{\text{inc}} \\ \boldsymbol{E}^{\hat{\boldsymbol{y}}}_{\text{inc}} \end{pmatrix}, \tag{5.30}$$

where $\boldsymbol{E}^{\hat{p}}_{\text{inc}}$ and $\boldsymbol{E}^{\hat{s}}_{\text{inc}}$ are normalized incident fields polarized along TM and TE polarization, respectively.

The vectorial scattered fields $\boldsymbol{E}^{\hat{\boldsymbol{y}}}_{\text{cor}}$ and $\boldsymbol{E}^{\hat{\boldsymbol{x}}}_{\text{cor}}$ can be deduced from the corrected scattered fields measured on CCD camera $E^{\hat{\boldsymbol{y}}\hat{\boldsymbol{x}}}_{\text{sca;cor}}$, $E^{\hat{\boldsymbol{y}}\hat{\boldsymbol{y}}}_{\text{sca;cor}}$, $E^{\hat{\boldsymbol{x}}\hat{\boldsymbol{x}}}_{\text{sca;cor}}$ and $E^{\hat{\boldsymbol{x}}\hat{\boldsymbol{y}}}_{\text{sca;cor}}$.

The linear combination relationship between the incident field in the base $(\hat{\boldsymbol{x}}, \hat{\boldsymbol{y}})$ and $(\hat{\boldsymbol{p}}, \hat{\boldsymbol{s}})$ is same for each component of the scattered field. Now, for each illumination angle, we can write as

$$\begin{pmatrix} \boldsymbol{E}^{\hat{p}}_{\text{cor}} \\ \boldsymbol{E}^{\hat{s}}_{\text{cor}} \end{pmatrix} = \begin{pmatrix} \cos\phi_{\text{inc};2} & \sin\phi_{\text{inc};2} \\ -\sin\phi_{\text{inc};2} & \cos\phi_{\text{inc};2} \end{pmatrix} \begin{pmatrix} \boldsymbol{E}^{\hat{\boldsymbol{x}}}_{\text{cor}} \\ \boldsymbol{E}^{\hat{\boldsymbol{y}}}_{\text{cor}} \end{pmatrix}. \tag{5.31}$$

$\boldsymbol{E}^{\hat{p}}_{\text{cor}}$ and $\boldsymbol{E}^{\hat{s}}_{\text{cor}}$ is the scattered field corresponding to pure TM and TE incident polarization, respectively.

With this normalization procedure, for any illumination angle polarized along $\hat{\boldsymbol{x}}$ or $\hat{\boldsymbol{y}}$ [even if it is not in $(x, z)$ plane or $(y, z)$ plane] and for two measurements on CCD camera in the base $(\hat{\boldsymbol{d}}_1, \hat{\boldsymbol{d}}_2)$, we can decompose the measured scattered fields into two parts, corresponding to TM and TE polarization, respectively. The vectorial scattered fields are obtained for both TM and TE polarizations, with unit incident amplitude and phase angle fixed at the substrate surface.

### 5.2.3 Influence of polarization measurements

For comparison purposes, we also consider the classical implementation of TDM in which the incident and reference polarization directions are the same, either $\hat{\boldsymbol{x}}$ or $\hat{\boldsymbol{y}}$. In these configurations (hereafter indicated by $\hat{\boldsymbol{x}}\hat{\boldsymbol{x}}$ or $\hat{\boldsymbol{y}}\hat{\boldsymbol{y}}$), the data consists of the scalar projection of the scattered field on the incident polarization state. Thus, there is four times less data in the $\hat{\boldsymbol{x}}\hat{\boldsymbol{x}}$ or $\hat{\boldsymbol{y}}\hat{\boldsymbol{y}}$ modes than in the full-polarization mode. In this section, we present new reconstructions for the objects using different polarization configurations for the measurements:

1. $\hat{\boldsymbol{y}}\hat{\boldsymbol{y}}$
2. $\hat{\boldsymbol{x}}\hat{\boldsymbol{x}}$
3. combining $\hat{\boldsymbol{y}}\hat{\boldsymbol{y}}$ and $\hat{\boldsymbol{x}}\hat{\boldsymbol{x}}$
4. combining $\hat{\boldsymbol{y}}\hat{\boldsymbol{d}}_1$, $\hat{\boldsymbol{y}}\hat{\boldsymbol{d}}_2$, $\hat{\boldsymbol{x}}\hat{\boldsymbol{d}}_1$ and $\hat{\boldsymbol{x}}\hat{\boldsymbol{d}}_2$ to retrieve the full vectorial field for both TE and TM illuminations
5. combining $\hat{\boldsymbol{y}}\hat{\boldsymbol{d}}_1$, $\hat{\boldsymbol{y}}\hat{\boldsymbol{d}}_2$, $\hat{\boldsymbol{x}}\hat{\boldsymbol{d}}_1$ and $\hat{\boldsymbol{x}}\hat{\boldsymbol{d}}_2$ to retrieve the full vectorial field for TE illuminations only
6. combining $\hat{\boldsymbol{y}}\hat{\boldsymbol{d}}_1$, $\hat{\boldsymbol{y}}\hat{\boldsymbol{d}}_2$, $\hat{\boldsymbol{x}}\hat{\boldsymbol{d}}_1$ and $\hat{\boldsymbol{x}}\hat{\boldsymbol{d}}_2$ to retrieve the full vectorial field for TM illuminations only

The experimental setup is shown in Fig. 5.1. All of the samples that we used were fabricated by Anne Talneau at the Laboratoire de Photonique et Nanostructures de Marcousssis.

In this study, the samples to be imaged are deposited on a silicon substrate and are described by a relative permittivity contrast $\chi(\boldsymbol{r})$ with respect to the planar geometry [13,98]. The unknown sample permittivity contrast is reconstructed from the TDM data using the HM based on a rigorous vectorial electromagnetic model of the scattered far field $(e_s, e_p)$, which, in particular, accounts for the substrate [82], described in Sec. 1.4.3 and 2.2.4. To improve the reconstruction, the unknown permittivity contrast in the investigating domain $\Omega$ is assumed to be real and positive. Note that the method is adapted to any TDM data. In the full-polarization mode, the cost function involves the full vectorial field scattered by the sample whereas in the $\hat{\boldsymbol{x}}\hat{\boldsymbol{x}}$ or $\hat{\boldsymbol{y}}\hat{\boldsymbol{y}}$ mode, it involves only the projection of the scattered field.

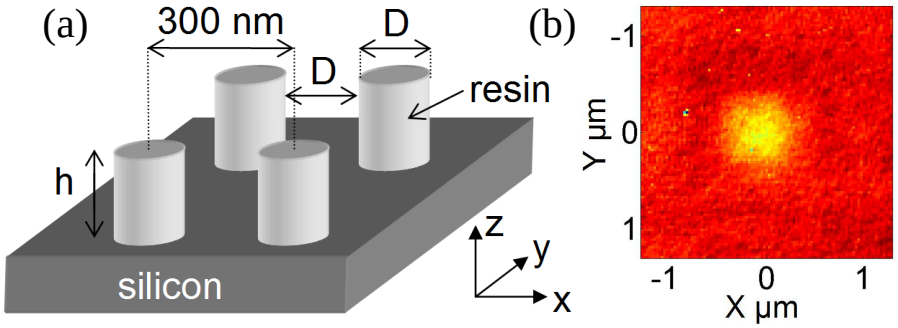


**Figure 5.6 :** *(a) Sample geometry. $D$ =150 nm and $h$ =150 nm. (b) Wide-field image of the sample obtained using spatially incoherent illumination: details of the object are not resolved.*

#### 5.2.3.1 Resin cylinders with diameter 150 nm and height 150 nm

For investigating the performance of our setup, we consider a sample made of four $h = 150$ nm high resin cylinders with diameter $D = 150$ nm and relative permittivity $\varepsilon = 2$ deposited on a planar Si substrate of relative permittivity $15 + i0.15$, and centered at the summits of a square with sides 300 nm along $\hat{\boldsymbol{x}}$ and $\hat{\boldsymbol{y}}$ as depicted in Fig. 5.6 (a). The scattered far field was measured in both the full-polarized and scalar ($\hat{\boldsymbol{x}}\hat{\boldsymbol{x}}$, $\hat{\boldsymbol{y}}\hat{\boldsymbol{y}}$) modes for 10 incident directions in the $(x, z)$ plane and 10 in the $(y, z)$ plane with inclined angles varying from $-50°$ to $50°$. With this angular configuration, the Rayleigh limit of the microscope is about $0.6\lambda/NA \approx 400$ nm, *i.e.* well above the cylinders interdistance. It is observed in Fig. 5.6 (b) that, unsurprisingly, the four cylinders can not be distinguished on a classical wide-field microscope image (here obtained by summing the sample field intensities for all the illuminations).

We first analyze the achievement of a classical TDM implementation by processing the scalar $\hat{\boldsymbol{y}}\hat{\boldsymbol{y}}$ data with the usual inverse Fourier transform algorithm[103]. The latter relies on a scalar, free-space (no substrate) single scattering model which states that the far field scattered in the $\boldsymbol{k}$ direction by a sample illuminated by a plane wave with wave vector $\boldsymbol{k}_{\text{inc}}$ is proportional to the three-dimensional Fourier transform of $\chi(\boldsymbol{r})$ taken at $\boldsymbol{k} - \boldsymbol{k}_{\text{inc}}$. Theoretically, in a noise-free configuration, the transverse image resolution should be about $0.25\lambda/\text{NA} \approx 170$ nm with our angle configuration, *i.e.* below the rods center interdistance[105]. Yet, it is seen in Fig. 5.7 (a) that the simple inversion scheme fails in retrieving the sample. Its noise sensitivity (due to the weak number of incidences) and its model errors are prohibitive for imaging such small objects. On the other hand, applying the iterative inversion method to the same scalar data provides a much better sample estimate, by processing the scalar $\hat{\boldsymbol{x}}\hat{\boldsymbol{x}}$ or $\hat{\boldsymbol{y}}\hat{\boldsymbol{y}}$ data, shown in Figs. 5.7 (b) and (c). The cylinders height is now accurately retrieved. However, their shapes are strongly elongated along the $\hat{\boldsymbol{y}}$ axis for $\hat{\boldsymbol{x}}\hat{\boldsymbol{x}}$ data, Fig. 5.7 (b), and similarly, they are elongated along the $\hat{\boldsymbol{x}}$ axis for $\hat{\boldsymbol{y}}\hat{\boldsymbol{y}}$ data, see Fig. 5.7 (c). This resolution anisotropy is a direct consequence of the incident and reference polarization choice, as observed in Ref. 114, and will be explained below. Here, we also $\text{Err}_\chi$ to assess quantitatively the quality of reconstruction, defined as Eq. (4.8). For the only measured scalar data $\hat{\boldsymbol{x}}\hat{\boldsymbol{x}}$ and $\hat{\boldsymbol{y}}\hat{\boldsymbol{y}}$, the reconstruction error $\text{Err}_\chi$ is 76% and 72%, respectively.

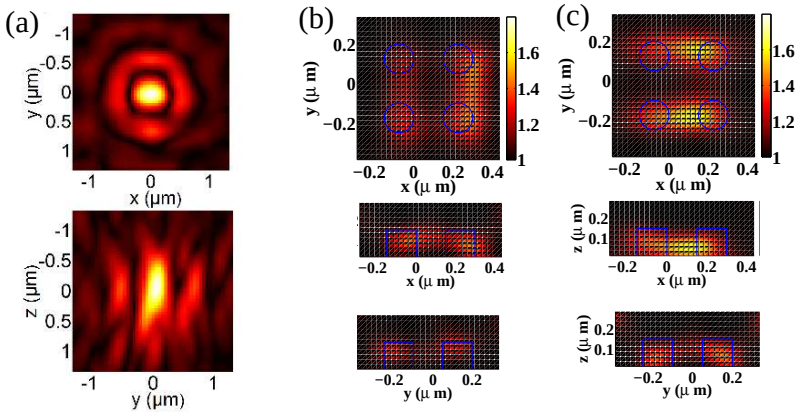


**Figure 5.7 :** *Sample reconstructions obtained from the scalar* $\hat{\boldsymbol{y}}\hat{\boldsymbol{y}}$ *and* $\hat{\boldsymbol{x}}\hat{\boldsymbol{x}}$ *data. (a) Longitudinal and transverse cuts of the three dimensional image given by a direct inversion method based on a free-space scalar model, using the scalar* $\hat{\boldsymbol{y}}\hat{\boldsymbol{y}}$ *data. (b) Longitudinal and transverse cuts of the relative permittivity estimation given by the HM algorithm using the scalar* $\hat{\boldsymbol{y}}\hat{\boldsymbol{y}}$ *data. (c) Same as (b) while using the scalar* $\hat{\boldsymbol{x}}\hat{\boldsymbol{x}}$ *data.*

We now turn to the reconstructions obtained with vectorial data stemming either from the combined scalar $\hat{\boldsymbol{x}}\hat{\boldsymbol{x}}$ and $\hat{\boldsymbol{y}}\hat{\boldsymbol{y}}$ data, Figs. 5.8 (a)-(c), or the full-polarized vectorial mode, Figs. 5.8 (d)-(f). In both cases, the four cylinders are accurately retrieved with isotropic resolution. The full-polarized vectorial data yielding a slightly better quantitative estimation of the permittivity level with $\mathrm{Err}_\chi = 56\%$ than the combined $\hat{\boldsymbol{x}}\hat{\boldsymbol{x}}$ and $\hat{\boldsymbol{y}}\hat{\boldsymbol{y}}$ data ($\mathrm{Err}_\chi = 63\%$). Note that the resolution, defined as the full width at half maximum of the reconstructed permittivity peaks, Figs. 5.8 (c) and 5.8 (f), is about one fourth of the wavelength.

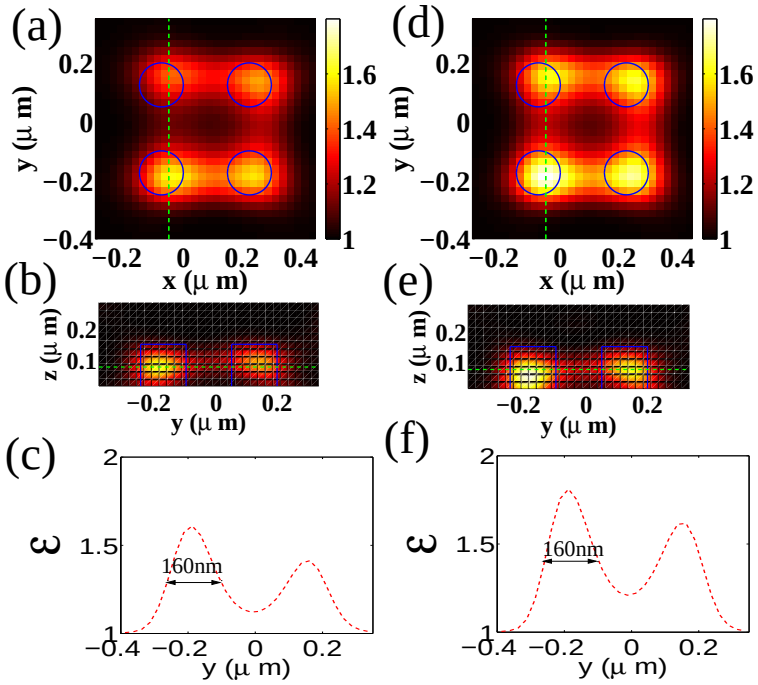


**Figure 5.8 :** *Sample reconstructions obtained by the iterative inversion method based on a rigorous vectorial model of the field, (a)-(c) from the combined $\hat{\boldsymbol{x}}\hat{\boldsymbol{x}}$ and $\hat{\boldsymbol{y}}\hat{\boldsymbol{y}}$ data. (d)-(f) from the full-polarized vectorial data. (a) and (d) $(x, y)$ section. (b) and (e) $(y, z)$ section taken along the dashed line in (a) and (d). (c) and (f) reconstructed permittivity along the dashed line in (b) and (e). The full width at half maximum of the reconstructed permittivity averaged over the four dots is slightly below half the classical Rayleigh criterion.*

The role of the incident and reference polarization states on the image resolution requires a careful analysis. Indeed, when single scattering is dominant (which is the case for this sample), the scalar $\hat{\boldsymbol{x}}\hat{\boldsymbol{x}}$ or $\hat{\boldsymbol{y}}\hat{\boldsymbol{y}}$ data give access to the sample permittivity Fourier coefficients within the same Fourier domain as the vectorial full-polarized data[98]. Hence, the resolution of the image depends only on the ability to extract, from noisy data, the permittivity Fourier coefficients at the highest accessible spatial frequencies. The latter are conveyed by the far field scattered at high angles, namely for large $\boldsymbol{k} - \boldsymbol{k}_{\text{inc}}$. Now, in presence of a substrate, the far field behavior in these directions significantly differs depending on the incident polarization state. In Fig. 5.9, we plot the scattered far field modulus in the $\boldsymbol{k}_{\|}$ plane obtained experimentally and theoretically when the sample is illuminated under 50° in the $(x, z)$ plane with a TM-polarized (corresponding to the $\hat{\boldsymbol{x}}$-direction for the incident half-wave plate) and TE-polarized (corresponding to the $\hat{\boldsymbol{y}}$-direction) plane waves. In both cases, we have verified that with a larger illumination angle, we can detect a diffraction lobe at higher spatial frequencies, which guarantees the imaging resolution. We observe that the back scattered field is about twice bigger with the TM-polarized incident wave than with the TE-polarized incident wave. The better signal to noise ratio at high angles obtained with TM-polarized incident waves explains the better resolution along the $\hat{\boldsymbol{y}}$ direction that is observed in Fig. 5.7 (d).

To confirm this interpretation, we plot, in Fig. 5.10, the relative permittivity map reconstructed by the iterative inversion method from the scattered vectorial field obtained using only TE-polarized incident waves, Figs. 5.10 (a) and (b), or only TM-polarized incident waves, Figs. 5.10 (c) and (d). As expected, the TM-polarized mode yields an accurate sample reconstruction ($\text{Err}_{\chi} = 69\%$), with the profile similar to that of the full-polarized mode, while the TE-polarized mode provides

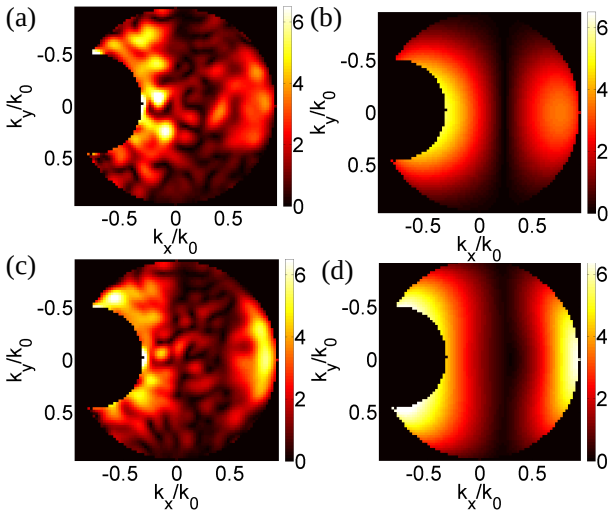


**Figure 5.9 :** *Experimental (a)-(c) and theoretical (b)-(d) modulus of the far field scattered by the sample illuminated in the* $(x, z)$ *plane under* $50°$ *of incidence. The scattered field is normalized by the incident magnitude times* $10^8$*. The black disk on the left indicates the non-exploitable angular domain about the specular reflection. (a)-(b) the incident wave is TE-polarized. (c)-(d) the incident wave is TM-polarized. One observes on the right of the plots that the back scattered field amplitudes, which convey the highest spatial frequency sample information, are twice bigger in TM-polarization than in TE-polarization.*

a totally blurred image($\mathrm{Err}_\chi = 75\%$). Note that, with our specific illumination configuration, the combined $\hat{\boldsymbol{x}}\hat{\boldsymbol{x}}$ and $\hat{\boldsymbol{y}}\hat{\boldsymbol{y}}$ data include that corresponding to TM-polarized illumination, which explains the accuracy of its related reconstruction, Figs. 5.8 (a)-(c).

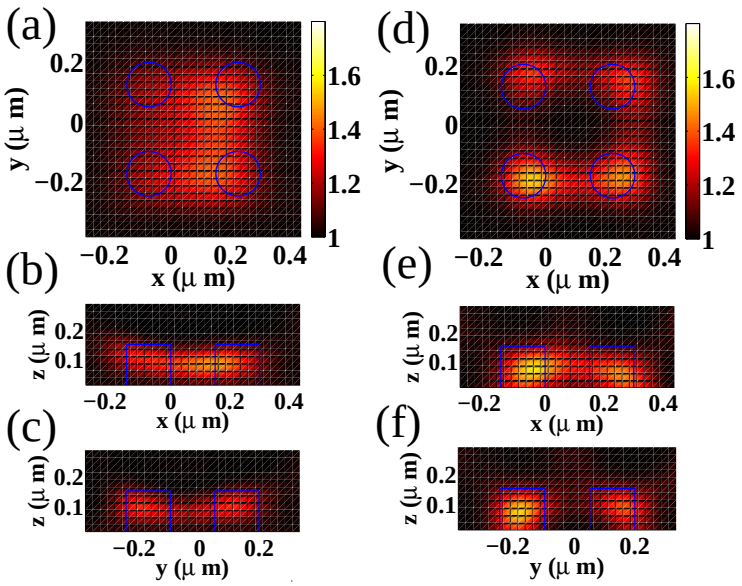


**Figure 5.10 :** *$(x, y)$ (a) and (d), $(x, z)$ (b) and (e) and $(y, z)$ (c) and (f) sections of the reconstructed permittivity given by the iterative 'rigorous' inversion method from the measured far field. (a)-(c) with TE-polarized incident waves. (d)-(f) with TM-polarized incident waves. The superiority of TM illumination for imaging the sample is evidenced.*

#### 5.2.3.2 Dielectric dodecagon structure made of 12 resin rods

Now, in order to confirm the potential of the full-polarized TDM technology, we consider a more complex sample made of twelve resin rods of width 100 nm, length 300 nm and height 140 nm radially placed at the summit of a dodecagon (Fig. 5.11 gray map). We consider eight directions of incidence, defined by a fixed polar angle $\theta_{\text{inc}} = 60°$ and an azimuthal angle $\phi_{\text{inc}}$ regularly spaced within $2\pi$. This illumination scheme corresponds typically to that encountered in a dark-field microscope. The synthesized dark-field microscope image, obtained by summing the scattered intensities recorded at the image plane for all the illuminations, displays a simple ring with appropriate inner and outer radius without any hint of the rods presence (Fig. 5.11 hot map). On the other hand, the full-polarized TDM recovers the twelve rods, Fig. 5.12 (a), demonstrating a resolution about 160 nm (about $\lambda/4$), similar to that obtained with the cylinder. The reconstructed permittivity taken along a circle passing trough the middle of the rods demonstrate that the technique is able to distinguish the rods whatever their orientation and even when their interdistance is smaller than one-fourth of the wavelength. On the contrary, when sole the combined $\hat{\boldsymbol{x}}\hat{\boldsymbol{x}}$ and $\hat{\boldsymbol{y}}\hat{\boldsymbol{y}}$ data are used, one observes a significant deterioration of the reconstruction as compared to that obtained with the full-polarized data.

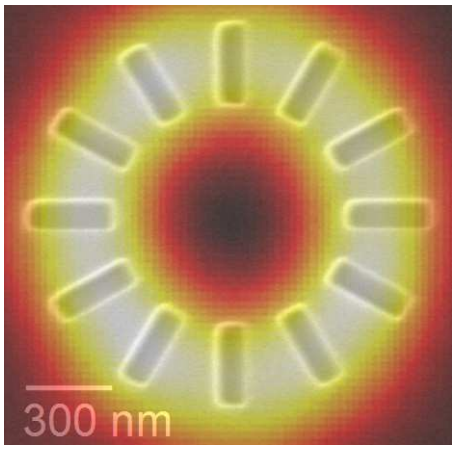


**Figure 5.11 :** *Transmission electronic microscope image (gray map) and dark-field optical microscope image (hot map).*

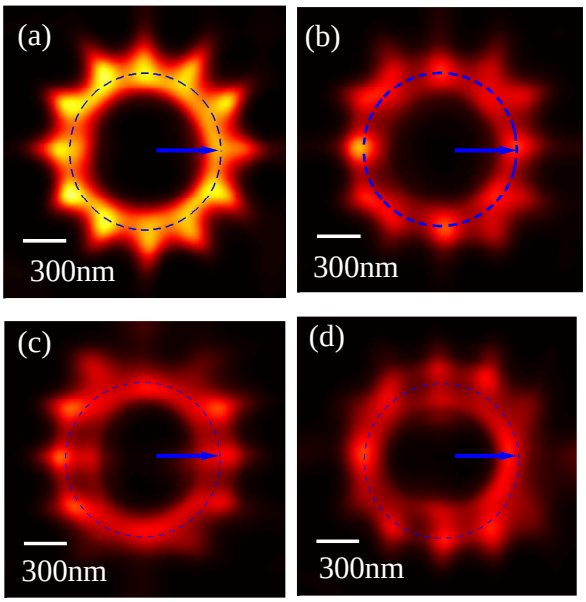


**Figure 5.12 :** *(a) Reconstructed permittivity averaged over the sample's height using full-polarized TDM data. (b) Reconstructed permittivity averaged over the sample's height using combined $\hat{\boldsymbol{x}}\hat{\boldsymbol{x}}$ and $\hat{\boldsymbol{y}}\hat{\boldsymbol{y}}$ data. (c) Reconstructed permittivity averaged over the sample's height using scalar $\hat{\boldsymbol{y}}\hat{\boldsymbol{y}}$ data. (d) Reconstructed permittivity averaged over the sample's height using scalar $\hat{\boldsymbol{x}}\hat{\boldsymbol{x}}$ data.*

To further illustrate the importance of getting the full-polarized data, we plot in Fig. 5.13 (a), the reconstruction obtained with the combined $\hat{\boldsymbol{x}}\hat{\boldsymbol{x}}$ and $\hat{\boldsymbol{y}}\hat{\boldsymbol{y}}$ data and that obtained with the full-polarized data, along the dashed circle of Fig. 5.12. This observed anisotropy of resolution is due

to the absence of the cross polarization in the $\hat{\boldsymbol{x}}\hat{\boldsymbol{x}}$ and $\hat{\boldsymbol{y}}\hat{\boldsymbol{y}}$ data, and in agreement with the analysis conducted for four cylinders of diameter 150 nm.

The reconstruction of the dodecagon sample using only the scalar $\hat{\boldsymbol{x}}\hat{\boldsymbol{x}}$ or $\hat{\boldsymbol{y}}\hat{\boldsymbol{y}}$ data is illustrated in Figs. 5.12 (c) and (d) and Fig. 5.13 (b). We observe that the $\hat{\boldsymbol{x}}\hat{\boldsymbol{x}}$ and $\hat{\boldsymbol{y}}\hat{\boldsymbol{y}}$ data fail to reconstruct the rods oriented parallel to the other polarization, and is worse than that obtained with the combined $\hat{\boldsymbol{x}}\hat{\boldsymbol{x}}$ and $\hat{\boldsymbol{y}}\hat{\boldsymbol{y}}$ data.

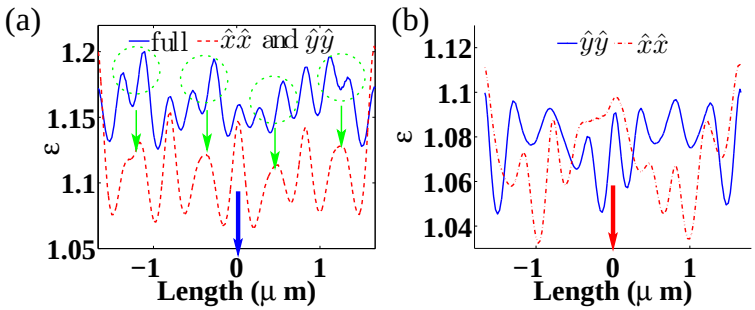


**Figure 5.13 :** *Permittivity along the blue dashed circle in Fig. 5.12. (a) Blue plain line the full-polarized data and red dashed line the combined* $\hat{\boldsymbol{x}}\hat{\boldsymbol{x}}$ *and* $\hat{\boldsymbol{y}}\hat{\boldsymbol{y}}$ *data. (b) Blue plain line the scalar* $\hat{\boldsymbol{y}}\hat{\boldsymbol{y}}$ *data and red dashed line the scalar* $\hat{\boldsymbol{x}}\hat{\boldsymbol{x}}$ *data.*

## 5.3 Conclusions

In conclusion, we have developed a three-dimensional TDM microscope that exploits all the information accessible via the diffraction process (intensity, phase and polarization state of the scattered field for any possible illumination within the numerical aperture of the objective). The full-polarized information is obtained with four intensity measurements per incident angle and special care must be taken to calibrate properly the measured scattered fields. In the single scattering regime, this ultimate full-polarization microscope is able to reconstruct permittivity maps with a resolution about one-fourth of the wavelength. The illuminations with TM-polarization can give a better reconstruction resolution than TE-polarization, one reason is that the intensity of the scattered field is larger with TM-polarization than with TE-polarization when the sample is deposited on a substrate, for large incident angles. The better resolution stems from in TM-polarization than in TE. We have shown that characterizing a sample with a complex structure (dodecagon structure), the full polarized data was necessary to obtain a resolution about one-fourth of the wavelength.

Chapter 6

# Application of DORT in tomographic diffractive microscopy

## Contents



## 6.1 Introduction

In chapter 4, we have tested the focalization ability of the DORT method in three-dimensional cluttered medium. The information on 'bright' scatterers can be extracted from the surrounding medium owing to DORT. Each significant eigenvalue is associated to one scatterer in single scattering regime, depending on the polarization state of illuminations. Selective focalization can be realized by numerically backpropagating the corresponding eigenvector. Then, the investigating domain for each scatterer can be determined by observing the intensity map generated by the eigenvector. Using the combined HM-DORT procedure, we can get a better characterization of targets than HM only, and the calculation time can be drastically reduced due to the reduction of illumination numbers. All of these results were based on simulated data.

In chapter 5, we presented a full-polarization TDM able to measure the vectorial field scattered by a sample for any incident polarization state. The full-polarized microscope enables to reconstruct the sample permittivity map with a resolution about one-fourth of the wavelength whatever the direction in the transverse plane. This achievement is superior to all previous TDM realizations[13,49]. In this chapter, we propose to use the vectorial experimental data provided by TDM to test the DORT method presented in chapter 4. Note that we have shown that HM-DORT procedure yielded a better reconstruction when using vectorial data than when using scalar data only .

With the classical TDM reconstruction procedure (HM), the investigating domain is taken large enough to include the whole sample. If the latter is made of a few small scatterers that are

far from one another this choice leads to an important useless time-consuming inversion procedure. Therefore, it is important to detect and localize the scatterers forming the sample prior to apply any inverse scattering algorithm. To solve this computation burden, we propose to use the DORT method to localize a specific scatterer. Then we define a 'bright' region around it to form a investigating domain dedicated to this target. Last, we apply the HM-DORT procedure in the investigating domain to retrieve more precisely the permittivity map of the target

## 6.2 Selective imaging and characterizing problem in TDM

Three steps are required[1] to apply the DORT method in the experimental setup of TDM. First, we need to calculate the scattering matrix $\boldsymbol{K}$ from the scattered field measured by the TDM, see Chap. 5. After processing, one obtains the vectorial field scattered by the sample for $l = 1, 2, \cdots, N$ different incident angles and two incident polarization states TE ($s$) and TM ($p$), for $N$ observation directions (corresponding to $N$ pixels of the camera). The measured scattered fields can be decomposed into two parts, $\boldsymbol{E}_{\mathrm{s}}^{\mathrm{sca}}$ and $\boldsymbol{E}_{\mathrm{p}}^{\mathrm{sca}}$, corresponding to the incident field in pure TE ($s$) and TM ($p$) polarization. Then, the measured vectorial scattered fields can be further projected along TM and TE polarization. The scattering matrix $\boldsymbol{K}$ is reconstructed in a different way from Chap. 4, where the antennas take three different orientations ($x$, $y$ and $z$). In TDM, the scattered field is approximately a transverse plane wave in far field region. So for each incident angle $i$, at the receiving position $j$, four different groups of data are measured, as $K_{ij}^{pp}$, $K_{ij}^{ps}$, $K_{ij}^{sp}$ and $K_{ij}^{ss}$. The first letter of the superscript indicates the polarization state of the illumination (TM or TE), and the second letter indicates the projection of the vectorial scattered field on the polarization state TM or TE. Then we can construct a scattering matrix $\boldsymbol{K}$ of dimension $2N \times 2N$.

$$\boldsymbol{K} = \begin{pmatrix} K_{11}^{pp} & K_{12}^{pp} & \dots & K_{1N}^{pp} & K_{11}^{ps} & K_{12}^{ps} & \dots & K_{1N}^{ps} \\ K_{21}^{pp} & K_{22}^{pp} & \dots & K_{2N}^{pp} & K_{21}^{ps} & K_{22}^{ps} & \dots & K_{2N}^{ps} \\ \vdots & \vdots & \ddots & \vdots & \vdots & \vdots & \ddots & \vdots \\ K_{N1}^{pp} & K_{N2}^{pp} & \dots & K_{NN}^{pp} & K_{N1}^{ps} & K_{N2}^{ps} & \dots & K_{NN}^{ps} \\ K_{11}^{sp} & K_{12}^{sp} & \dots & K_{1N}^{sp} & K_{11}^{ss} & K_{12}^{ss} & \dots & K_{1N}^{ss} \\ K_{21}^{sp} & K_{22}^{sp} & \dots & K_{2N}^{sp} & K_{21}^{ss} & K_{22}^{ss} & \dots & K_{2N}^{ss} \\ \vdots & \vdots & \ddots & \vdots & \vdots & \vdots & \ddots & \vdots \\ K_{N1}^{sp} & K_{N2}^{sp} & \dots & K_{NN}^{sp} & K_{N1}^{ss} & K_{N2}^{ss} & \dots & K_{NN}^{ss} \end{pmatrix}. \tag{6.1}$$

The second step is the eigenvalue decomposition of the time reversal operator $\boldsymbol{L} = \boldsymbol{K}^{\dagger}\boldsymbol{K}$. In theory, the scattering matrix $\boldsymbol{K}$ is strictly symmetrical (due to the reciprocity theorem), see Chap. 3. In the experimental configuration however, this is not the case. The non-symmetrical behavior can be corrected by replacing each element $\boldsymbol{K}_{ij}$, by $\frac{1}{2}(\boldsymbol{K}_{ij} + \boldsymbol{K}_{ji})$[95]. If one performs the singular value decomposition on the matrix $K$, there is no need to care about this non-symmetric character[115]. Here, we did not modify the data and kept the non-symmetric $\boldsymbol{K}$ matrix for building the time reversal operator and calculating the eigenvalues of the TRO. It is known that in scalar configuration, for one single point-like scatterer, there exists one significant eigenvalue of the time-reversal operator. According to the analysis in Chap. 3, with TM and TE illumination together, it is likely that each independent point-like scatterer yields two dominant eigenvalues. However, when complex configurations are considered, the number of eigenvalues will depend on the size of the scatterer, the polarization state of the illumination and the property of the background medium, etc. Thus, one must give a specific attention to the determination of the significant eigenvalues.

The third step is the backpropagation of each eigenvector. This procedure can be accomplished either numerically or experimentally. The experimental backpropagation can be realized by generating a new incident pulse with spatial light modulator, with the phase modulated by the

eigenvector[48], and we can observe the localization map on the CCD camera at the image plane. The numerical backpropagation can also be simulated if the propagating medium is known.

In this chapter, we used the simulation of the backpropagated eigenvectors of the time reversal operator to localize the different scatterers forming the sample and applied the HM-DORT to characterize more quantitatively their shape and permittivity.

### 6.2.1 Four identical resin cylinders in a symmetrical geometry

We first consider a symmetrical structure, where the sample is made of four $h = 150$ nm high resin rods with diameter $D = 500$ nm and relative permittivity $\varepsilon = 2$ deposited on a planar silicon substrate of relative permittivity $15 + i0.15$. The four cylinders are centered at the summits of a square with sides 1 $\mu$m. The structure of sample is similar as Fig. 5.6 (a). The sample is imaged with the TDM setup described in Chap. 5. This first experiment will help us to understand what happens if the different targets have the same ability of diffraction. For this experiment, we consider 88 different plane wave illuminations. The polar angle (angle between the incident vector and the $z$-axis) $\theta_{\text{inc}}^{\max} = 57°$, and the azimuthal angle $\phi_{\text{inc}}$ is evenly distributed between 0 and 360°. The size of the scatterer is of the same order as the wavelength of illumination, so we are in the resonance domain. The investigating domain is set as 2 $\mu$m $\times$ 2 $\mu$m $\times$ 0.4 $\mu$m. The scattered fields are measured for both TM and TE incident polarizations. In this experiment, the scattered field along the directions that are close to the specular reflection direction is masked by the huge specular reflection due to the silicon substrate and must be discarded, see Fig. 6.1 (a). Thus, the components of matrix $\boldsymbol{K}$ whose receiving position is inside the specular reflection region are set to zero, shown as Fig. 6.1 (b). Then the time reversal operator $L$ is constructed and diagonalized. The eigenvalues distribution is shown in Fig. 6.2.

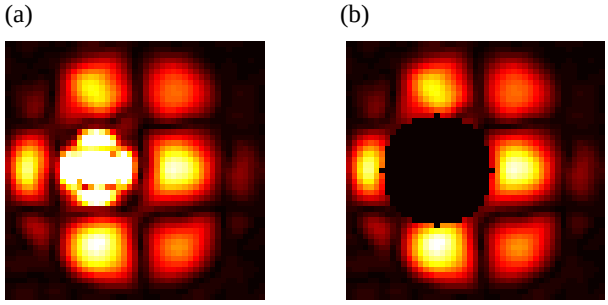


**Figure 6.1 :** *Experimental modulus of the far field scattered by the sample illuminated in the $(x, z)$ plane under 17° of incidence, (a) with the specular reflection, (b) without the specular reflection.*

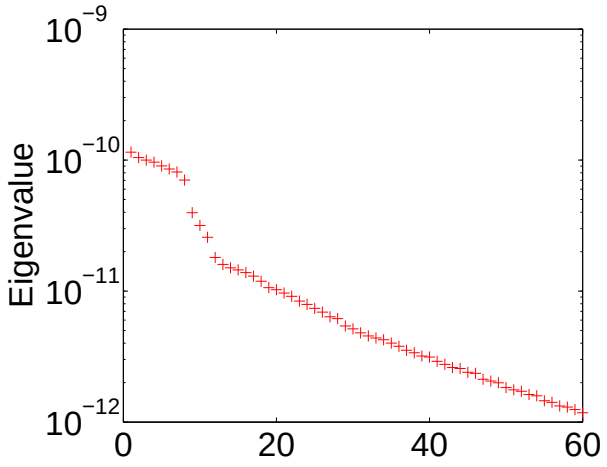


**Figure 6.2 :** *Eigenvalue of the time reversal operator in presence of four equal resin cylinders, using both TM and TE illuminations.*

From Fig. 6.2, one observes that the largest eight eigenvalues are of the same order and significantly greater than the other eigenvalues. We expect that these eight eigenvalues correspond to the four targets. The following eigenvalues correspond either to that of the antisymmetric eigenvectors linked to the targets, or to the noise space.

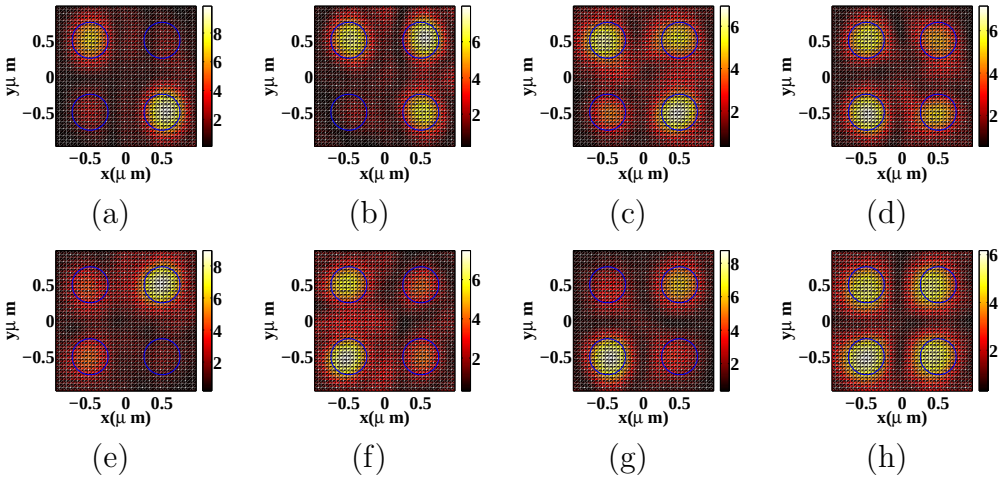


**Figure 6.3 :** *Intensity map in the investigating domain formed by the eight eigenvectors of the TRO related to the eight largest eigenvalues, in* $(x, y)$ *plane for* $z = 200$ *nm, with four identical cylinders deposited on the substrate.*

Figure 6.3 shows the intensity map in the $(x, y)$ plane for $z = 200$ nm, generated by the eight eigenvectors corresponding to the largest eight eigenvalues. In an ideal experiment without noise, each eigenvector should generate a field focusing simultaneously on the four targets[95]. Experimentally, however, this degenerate situation is disturbed by the measured noise. For some eigenvectors, the modulus of the backpropagated field is maximum on several cylinders *i.e. corresponding to an incomplete degenerate case*. For some other eigenvectors, the modulus of the backpropagated incident fields is maximum exclusively on one scatterer, *i.e. a complete non-degenerate case*, see

Fig. 6.3 (e). Thus, as it stands, the backpropagation of the eigenvectors does not permit a selective focalization on each scatterer. Yet, the scatterers being sufficiently well resolved, a selective focalization can be obtained by forming an appropriate linear combination of the different eigenvectors[95], as described in Appendix D. By forming a linear combination of the eight eigenvectors we were able to generate four incident fields that focused selectively on each of the four bright spots that were observed in Fig. 6.3. The selective focusing field on each scatterer is presented in Fig. 6.4. In the $(x, y)$ plane, the intensity of the incident focusing field presents a 'maximum' in the region where the scatterer is. In the $(x, z)$ plane, the focusing spot is elongated along $z$-direction, as shown in Figs. 6.4 (e)-(h). The transverse focusing width is about $\lambda/2$, centered at $z = 200$ nm.

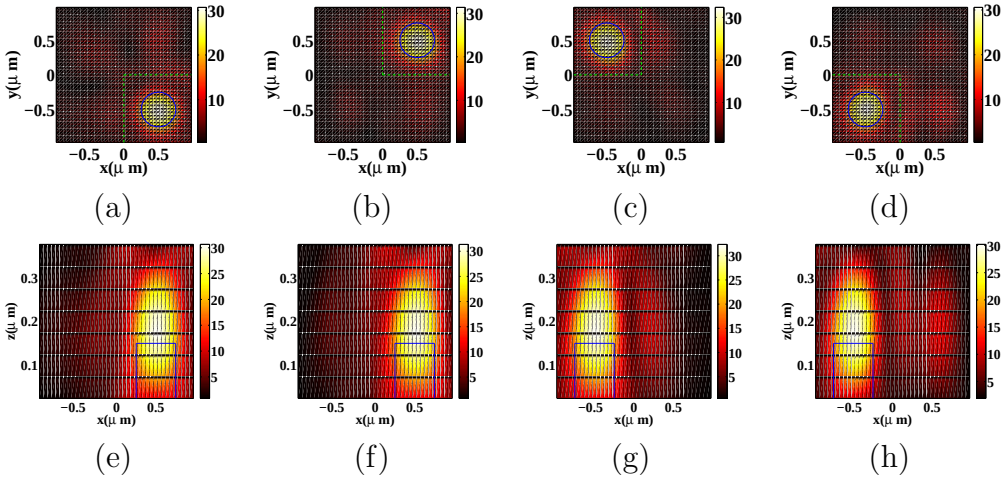


**Figure 6.4 :** *Intensity map in the investigating domain formed by the four linear combined eigenvectors. (a)-(d) in $(x, y)$ plane for $z = 200$ nm. (e)-(h) in $(x, z)$ plane for $y = 500$ nm [(e) and (h)] or $y = -500$ nm [(f) and (g)]. The four identical cylinders are focused selectively.*

To ameliorate the characterization of a given target, we then apply the HM-DORT inversion procedure with the only one incident field that focuses on that target. The investigating domain is defined from the intensity level of the focusing incident field. It is restricted to a small domain about the scatterer and plotted as a green line in Fig. 6.4. The height of the investigating domain in the $z$-direction is 0.4 $\mu$m. This procedure is repeated for the four scatterers.

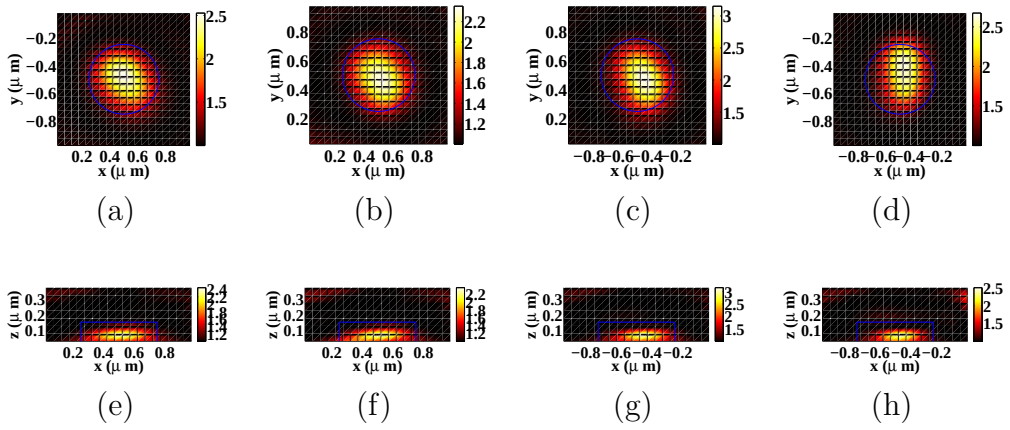


**Figure 6.5 :** *Reconstructed permittivity distribution, (a)-(d) in* $(x, y)$ *plane for* $z = 100$ *nm. (e) and (h) in* $(x, z)$ *plane for* $y = -500$ *nm. (f) and (g) in* $(x, z)$ *plane for* $y = 500$ *nm.*

The reconstruction result with the HM-DORT procedure is shown in Fig. 6.5. We observe that owing to the HM-DORT procedure, the targets are better localized in especially in the $z$-direction. The real height of the scatterers can be now be inferred from the reconstructed permittivity map with a good accuracy. On the contrary, the DORT method is totally unable to estimate the dimension of the target along $z$-direction.

### 6.2.2 Four resin cylinders of different sizes distributed in a large domain

The first example that we have considered was a symmetrical structure made of four identical scatterers which required to form a linear combination of eigenvectors to focus on each scatterer selectively. Now, consider a configuration in which the scatterers have different scattering cross section so that each eigenvector is associated to sole one scatterer.

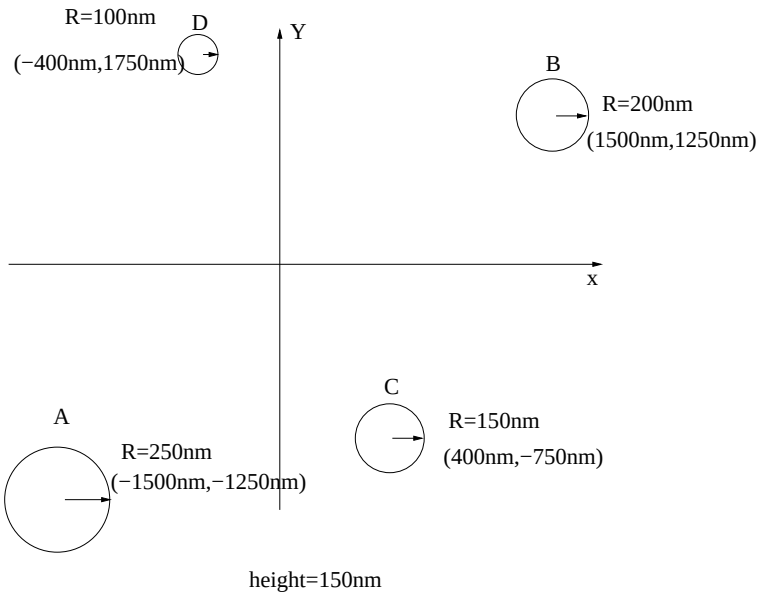


**Figure 6.6 :** *Sample geometry in the transverse cut plane, composed of four different resin cylinders.*

The sample is described in Fig. 6.6. It is composed of four different resin cylinders, with same permittivity and same height $h = 150$ nm deposited on a Si substrate. The radius of these cylinders are 100 nm, 150 nm, 200 nm and 250 nm respectively. The largest scatterer has the strongest scattering cross section. The experiment is conducted with 88 illuminations, with $\theta_{\text{inc}}^{\max} = 61°$, and $\phi_{\text{inc}}$ is evenly distributed between 0 and 360°. To avoid setting the components of $\boldsymbol{K}$ which are close to the specular region to zero, as in Sec. 6.2.1, we conducted two measurements, one with the sample and one without the sample (sole the silicon substrate). By subtracting these two fields we were able to restitute the scattered field in the specular region.

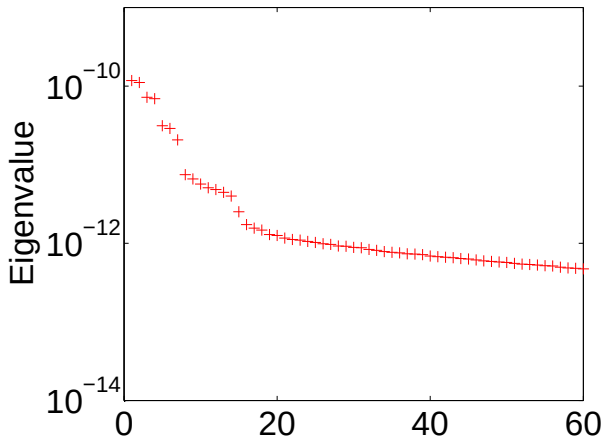


**Figure 6.7 :** *Eigenvalue of the time reversal operator in presence of four different resin cylinders, with both TM and TE illuminations.*

The distribution of the eigenvalues of the time reversal operator is presented in Fig. 6.7. We observe six eigenvalues that are of the same order and significantly larger than the others. The following eigenvalues decay smoothly down to the 15-th eigenvalue. The remaining eigenvalues

are much smaller and are clearly attributed to the noise space. In the following, we consider only the first 16-th eigenvalues. In Fig. 6.8 we plot the intensity map formed by the corresponding 16 eigenvectors.

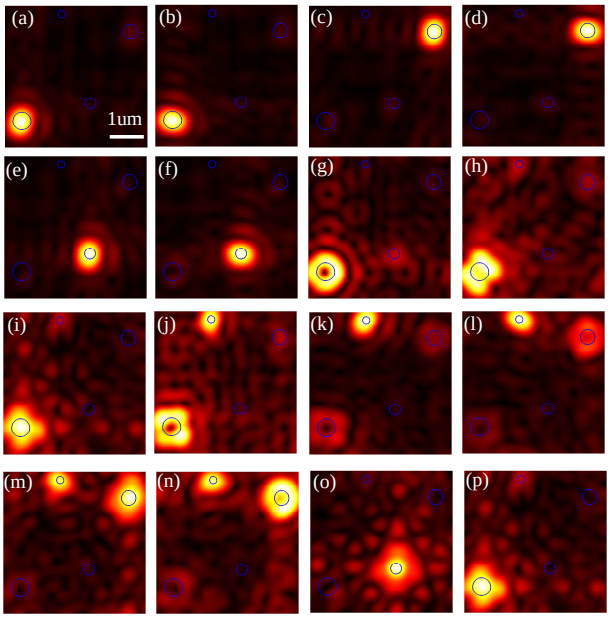


**Figure 6.8 :** *Intensity map in $(x, y)$ plane for $z = 100$ nm, generated by sixteen eigenvectors corresponding to the sixteen largest eigenvalues, with both TM and TE polarizations.*

From Fig. 6.8, we can determine the number and the location of scatterers. The first and the second eigenvectors form focusing waves associated to the strongest scatterer A [Figs. 6.8 (a) and (b)], of the radius 250 nm. The second strongest scatterer B (with $r = 200$ nm) is localized with the focusing waves generated by the third and the fourth eigenvectors, seeing Figs. 6.8 (c) and (d). The scatterer C, of radius 150 nm, is localized by the waves formed by the fifth and sixth eigenvalues, as shown in Figs. 6.8 (e) and (f). Then, the analysis of the field of the eigenvector corresponding to the seventh eigenvalue to the 16-th must be done with caution because of the noise influence.

Basically, we interpret the seventh, the eighth, the ninth and the tenth eigenvectors as antisymmetric eigenvectors related to scatter A [Figs. 6.8 (g)-(j)]. Yet, it seems that the tenth eigenvector is coupled with the weakest scatterer D (of the radius 100 nm). Indeed, the scatterers being not point-like, the electromagnetic scattered field is no longer isotropic, so that the symmetric and antisymmetric eigenvectors can couple to each other[4]. Fortunately, the scatterer D is not totally blurred by its surrounding stronger scatterers and by the experimental noise. The eigenvectors corresponding to the eleventh and the twelfth eigenvalues allow synthesizing a backpropagated waves that focuses on it [Figs. 6.8 (k) and (l)]. The thirteenth and fourteenth eigenvectors present an antisymmetric property on scatterer B and at the same time are coupled to scatterer D [Figs. 6.8 (m) and (n)]. Similarly, the fifteenth eigenvector corresponds to the antisymmetric eigenvector of scatterer C [Fig. 6.8 (o)], while the sixteenth eigenvector correspond to a higher order eigenvector linked to scatterer A [Fig. 6.8 (p)]. To summarize, in this configuration, with both TM and TE incident polarizations, we found at least two eigenvalues corresponding to eigenvectors focusing on each scatterer.

The reconstruction obtained with only HM procedure is shown in Fig. 6.9. The investigating domain used in the HM inversion procedure had a dimension of 5 $\mu$m $\times$ 5 $\mu$m $\times$ 200 nm. There

were 88 known illuminations (with both TM and TE polarizations) and 88 measured vectorial scattered fields to be used.

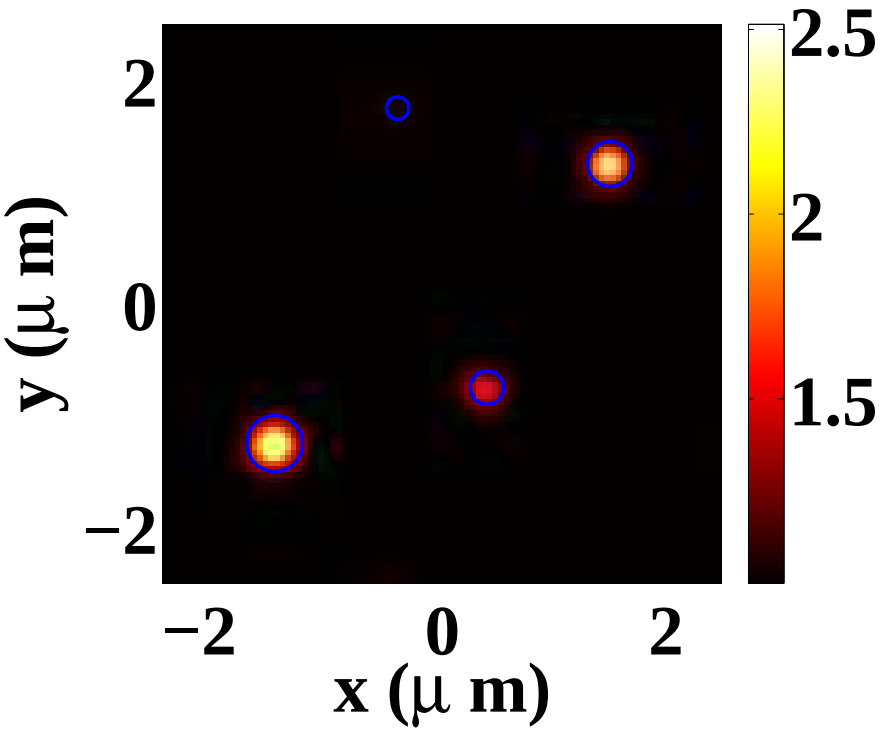


**Figure 6.9 :** *Reconstruction permittivity distribution of four different resin cylinders, in* $(x, y)$ *plane for* $z = 100$ *nm, with only HM procedure. The investigating domain is chosen as* $5\ \mu m \times 5\ \mu m \times 200$ *nm, containing all scatterers inside it.*

One observe that the three strongest scatterers are accurately reconstructed. The retrieved value of permittivity is closed to the real one for scatterer A and B. While the permittivity is underestimated for scatterer C, and unfortunately the information about the scatterer D is totally lost. Its size is so small compared to the other three scatterers that it is hidden in the reconstruction procedure. This remark points out the interest of the DORT technique which was able to localize scatterer D and the interest of the HM-DORT approach.

As the four scatterers can be localized with DORT, we can define four investigating domains surrounding each scatterer. We thus perform an HM-DORT for each target by using only the incident backpropagated eigenvector fields that focus on that target.

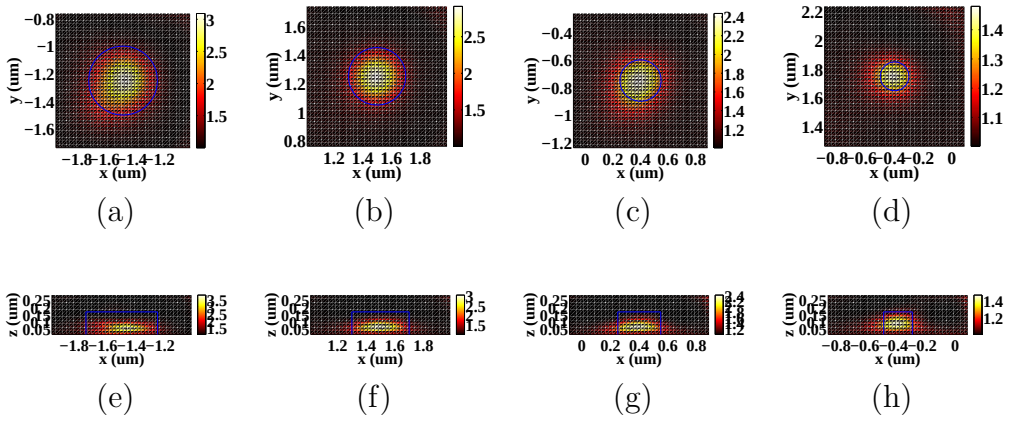


**Figure 6.10 :** *Selective HM-DORT reconstruction for four different cylinders, with the investigating domains restricted surround each scatterer, refereed to Fig. 6.8, of the dimension* 1 $\mu m \times 1\ \mu m \times 300\ nm$.

From Fig. 6.10, we observe that permittivity profiles of all the scatterers are satisfactorily reconstructed. The different sizes of these scatterers can be easily distinguished from the largest to the smallest. We admit that the reconstructed permittivity of scatterer D is weaker than the actual permittivity of itself, while this imperfection is not the consequent of the inversion procedure. The eigenvectors which synthesize the incident focusing fields on this scatterer are unfortunately also coupled to the antisymmetric eigenvectors of other scatterers, this can be perceived from Figs. 6.8 (k) and (l). So the corresponding scattered fields include not only the contribution of scatterer D, but also that stemming from its neighboring scatterers. However, the HM-DORT procedure appears are significantly superior to the HM procedure alone: first, we can obtain an initial estimation of location information of scatterers, thanks to the focalization ability of the DORT method. Second, once the location for each scatterer is determined, the investigating domain can be limited to a small region, and only the incident focusing fields are included in the inversion procedure, instead of all illuminations (HM procedure). Thus, the number of unknowns in the inverse problem is significantly reduced, and the computation time is also greatly reduced. In fact, with the HM procedure, it takes about 1380 s per iteration. While with the HM-DORT procedure, we only need 3 s per iteration. The superiority of HM-DORT over HM is all the more important than the scatterers are far from each other. Third and most important, the smallest scatterer is satisfactorily reconstructed using the HM-DORT whereas it is not seen with the HM.

## 6.3 Conclusions

In conclusion, we have applied the HM-DORT reconstruction technique to experimental data obtained with the TDM setup. Scatterers of different scattering cross section are detected and characterized in a much better way with the HM-DORT procedure than with the HM alone.

# Part IV

# Imaging and characterizing problem in time domain

# Introduction of PART IV

## Imaging and characterizing problem in time domain

In the last chapters, we have presented some reconstruction examples using time-harmonic electromagnetic fields. We have studied the DORT method in order to tackle the problem of the characterization of buried targets in cluttered media. We have proposed to combine the DORT method with an iterative algorithm and reported results of its application to the problem of characterizing targets surrounded by cluttered environment. Moreover, this new approach has been tested against experimental data in the framework of the TDM. With full-polarization data, we were able to reconstruct scatterers with a resolution about one-fourth of the wavelength. In the presence of several 'isolated' scatterers, we realized a selective reconstruction.
In Chap. 4, we showed that to diminish the reconstruction artifacts stemming from the small effective numerical aperture of the imager, we need to consider multi-frequency data. This can be achieved by using a sequential inversion procedure (frequency-hopping approach) or by using a global multi-frequency procedure (multiple-frequency approach). In this part, we propose to investigate the non-linear inversion algorithm using experimental frequency-diversity data[116]. The scattering domain is now assumed to be illuminated by a short-time pulse, which is equivalent to illuminate by a field with large bandwidth spectrum. In this case, both lower and higher frequencies components are considered. We will firstly test the transient inversion method using synthetic data, generated by the CDM. Then, we perform this inversion procedure using experimental data.

Chapter 7

# Inversion problem using frequency-diversity data

## Contents



## 7.1 Introduction

In the last chapters, we have studied the non-linear inversion algorithm (HM) for monochromatic configuration. This algorithm was combined with one of the time reversal technique (DORT) to detect and characterize scatterers in noisy environments, using synthetic data. The combined method (HM-DORT) has also been applied in the TDM, with full-polarized measured data in order to realize selective focalizations and characterizations. These configurations require a large number of exciting sources, and scattered fields need to be measured by large number of receiving points. As we have stated in Chap. 4, when targets are separated from the upper medium (where sources and receivers are) by an interface, the mono-frequency data is not sufficient anymore. The effective numerical aperture is reduced because, for antennas far away from targets, the reflection of the radiated field increases as the incident angles increase. To circumvent this, we proposed to apply the frequency-hopping procedure in order to improve the quality of the reconstruction. The drawback is in some cases, analyzed in Chap. 4, the clutter is very strong at one frequency, and consequently, the reconstruction at higher frequencies, as is suggested with frequency-hopping approach, fails. To avoid the bottleneck brought by this sequential inversion procedure, we propose to use a multiple-frequency inversion approach, where scattered data at all frequencies are inverted together.

In this chapter, we will test the reconstruction ability of these inversion algorithms on stepped-frequency experimental data. This full-polarization data was measured in an anechoic chamber of Institut Fresnel, France[116].

## 7.2 Reconstruction of targets using frequency - diversity experimental data

In this section, we report the performance of the multiple-frequency inversion approach and compare the reconstruction results with the ones obtained using the frequency-hopping approach. Data used for inversion are these carried out in the anechoic chamber of Institut Fresnel[116].

### 7.2.1 Multiple-frequency inversion procedure

When applying the frequency-hopping approach, the minimized cost function is at each frequency step defined as in Eq. (2.18). We minimize this function sequentially for each operating frequency. The initial estimate at the lowest operating frequency is obtained by the back-propagation procedure.

On the contrary, using the multiple-frequency method, the measured data at all operating frequencies are minimized together. In this case, the minimized cost function takes the form

$$\begin{aligned}\mathcal{F}_n(\chi_n, \boldsymbol{E}_{1,1,n}, \cdots, \boldsymbol{E}_{1,P,n}, \cdots, \boldsymbol{E}_{N,1,n}, \cdots, \boldsymbol{E}_{N,P,n}) &= \mathcal{F}_n(\chi_n, \boldsymbol{E}_{\bullet,\bullet,n}) \\ &= W_\Gamma \sum_{l=1}^{N}\sum_{p=1}^{P} \|\boldsymbol{h}_{l,p,n}^{(2)}\|_\Gamma^2 + W_\Omega \sum_{l=1}^{N}\sum_{p=1}^{P} \|\boldsymbol{h}_{l,p,n}^{(1)}\|_\Omega^2,\end{aligned} \tag{7.1}$$

where $N$ is the number of incidences, $P$ is the number of frequencies. This minimization procedure is described in detail in Sec. 2.3. The initial estimate is also obtained by the back-propagation procedure, with however data being the scattered fields for all frequencies.

In order to improve the efficiency of the inversion procedure, and for both of these two minimization procedures, we exploit *a priori* information stating that the real and imaginary part of the desired complex electrical permittivity must be greater than unity and non-negative, respectively.

### 7.2.2 Experimental setup

All experimental data were obtained in an anechoic chamber of dimensions $(14 \times 6.5 \times 6.5)$ m$^3$. The experimental setup is described in detail in Ref. 117. The incident field is changed with two polarizations, while the total field is measured for only one direction of the receiving antenna. By virtue of the reciprocity theorem, *i.e.*, switching the role of the emitter and the receiver, we can obtain the vectorial total field for one incident polarization. The experimental data consists measuring the co-polarized and cross-polarized scattered fields. The co-polarized scattered field is noisier at high frequencies than at low frequencies. The cross polarization error due to the experimental setup is larger than co-polarization error. Since targets are relatively small compared to the wavelength of the incident field, the cross-polarized field component is much weaker than its co-polarized counterpart and consequently much noisier. More precisely, we found that the magnitude of the cross-polarized term is at least ten times smaller than that of the co-polarized term and the residue $\boldsymbol{h}_{l,p,n}^{(2)}$ between the experimental data and the field computed for the actual targets, is always below 0.1 for the co-polarized term, while it reaches 4000, 57, and 17 for the cross-polarized component at 3, 5, and 7 GHz, and is about 1 for the total vectorial field (combined co-polarized term and cross-polarized term) at all frequencies[118]. Nevertheless, we will consider both co-polarized and cross-polarized components in the inversion procedure.

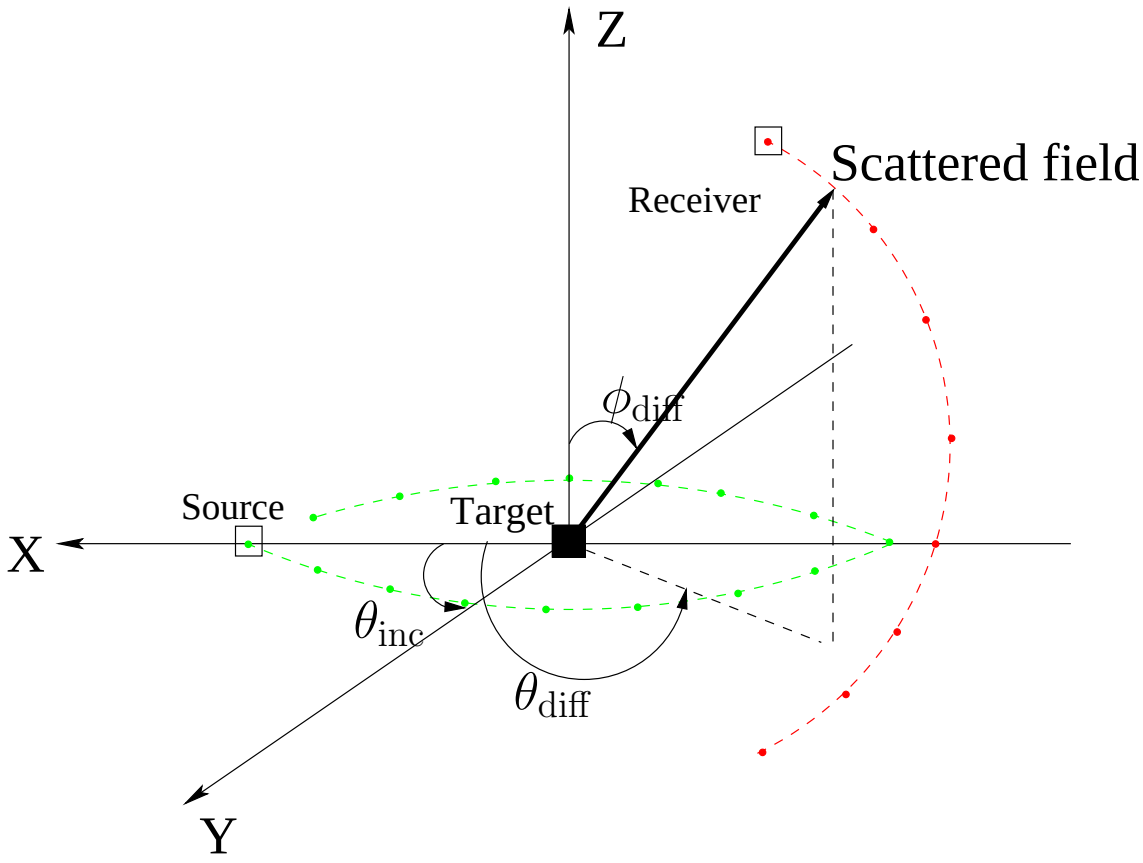


**Figure 7.1 :** *Sketch of the experimental setup. The illumination is done on the* $(x, y)$ *plane with* $\theta_{\text{inc}}$ *ranging from* $0°$ *to* $350°$ *with a step* $10°$ *(green line). The receiver position* $\theta_{\text{diff}}$ *ranges from* $0°$ *to* $320°$ *with the angular step* $40°$ *and* $\phi_{\text{diff}}$ *ranges from* $30°$ *to* $150°$ *with the step* $15°$ *(red line).*

Figure 7.1 shows the sketch of the experimental setup. The incident wave is assumed to be a plane wave propagating in the $(x, y)$ plane with $\theta_{\text{inc}}$ ranging from $0°$ to $350°$ with a step $10°$ (green line). The receiver position $\theta_{\text{diff}}$ ranges from $0°$ to $320°$ with the angular step $40°$ and $\phi_{\text{diff}}$ ranges from $30°$ to $150°$ with the angular step $15°$ (red line), therefore the total field are measured in 81 different positions. The distance from the emitter or receiver to the center of the setup is 1.795 m and 1.796 m, respectively. Two different fields are measured for each receiver, the total field (*i.e.*, the field measured in the presence of targets) and the incident field (*i.e.*, the field measured without targets). Therefore, the scattered field is obtained by subtracting the incident field from the total one. The drift errors caused by this long delay are corrected according to the procedure described in Ref. 119. The scattered field is recorded for 21 different frequencies, ranging from 3 GHz up to 8 GHz with a step 0.25 GHz, respectively. Targets are placed in the vacuum.

Several previous work have been carried out with the same three-dimensional (3D) Fresnel experimental data, using all emitters and receivers (complete configuration). In Ref. 57, different three-dimensional targets were reconstructed using the CGM method at fixed frequency. The multiple scattering effect was considered in Ref. 118, where *a priori* information on the lower and upper permittivity of the targets was also included for improving the resolution. Performances of CGM, CSI, and HM methods have been analyzed in Ref. 12. It has been verified that the HM was more efficient than other iterative methods and more robust against the presence of the noise in data. The frequency-hopping procedure was also applied using HM.

All reconstructions using Fresnel experimental data mentioned above are based on iterative inversion method at fixed frequency or processed with the frequency-hopping approach. In Ref. 120, these data are inverted using a multiplicative-regularized contrast inversion method, for different frequencies either simultaneously or sequentially. In this thesis work, we will also use a multiple-frequency method with HM inversion procedure. However a regularization procedure is not plagued in the inversion. The multiple-frequency inversion procedure has been described in Sec. 2.3. First, we will check the effectiveness of these methods using complete data. Then, we will consider a more difficult case, by using only one emitter, located at ($x = 1.795$ m, $y = 0$ m, $z = 0$ m) and the receivers in the angular direction with $\theta_{\text{diff}} = 120°, 160°, 200°, 240°$, as shown in Fig. 7.1. Only the transmitted scattered field is considered in the inversion procedure. Henceforth, this configuration is refereed from now on as incomplete configuration. For the inversion procedure, we assume that targets are confined in a bounded box $\Omega$ sized $(12.5 \times 12.5 \times 12.5)$ cm$^3$. The discretization size of $\Omega$ is taken equal to $d = 0.5$ cm whatever the operating frequency. At the central frequency $f_0 = 5.5$ GHz, the lattice size is about $\lambda_0/10$. In all reported results, we present only the real part of the reconstructed permittivity. The reconstructed imaginary part vanished in all cases.

### 7.2.3 Multiple-frequency and frequency-hopping approach

The multiple-frequency method and the frequency-hopping approach will be compared. Four different targets will be considered (Fig. 7.2).

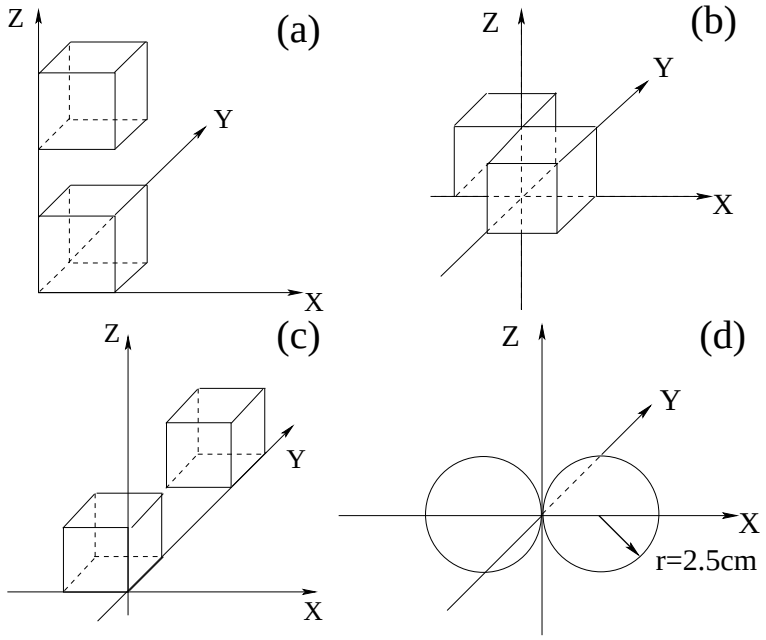


**Figure 7.2 :** *(a) Two dielectric cubes of relative permittivity $\varepsilon = 2.4$ and of the side $a = 2.5$ cm located at $(a/2, a/2, a/2)$ and $(a/2, a/2, 5a/2)$. (b) Same cubes as (a) located at $(-a/2, a/2, a/2)$ and $(a/2, -a/2, a/2)$. (c) same cubes as (a) located at $(a/2, -a/2, 3a/2)$ and $(a/2, 3a/2, 3a/2)$. (d) Two dielectric spheres in contact of relative permittivity $\varepsilon = 2.6$ and of radius $r = 2.5$ cm located at $(-r, 0, 0)$ and $(r, 0, 0)$.*

#### 7.2.3.1 Two cubes along the $z$-direction

The first considered target [Fig. 7.2 (a)] is made of two cubes placed along $z$-axis of relative permittivity $\varepsilon = 2.4$ and of side size $a = 2.5$ cm, and they are separated along the $z$- axis by 5 cm. Under the complete configuration, we obtain an accurate reconstruction result using the frequency-hopping approach, Figs. 7.3 (a)-(c). Switching to the incomplete configuration, the reconstruction result obtained with the frequency-hopping approach is deteriorated, Figs. 7.3 (g)-(i), where artefacts appear outside the targets. Whereas with the multiple-frequency method, successful reconstruction is obtained for both configurations. The reconstructed background is perfectly equal to one and the reconstructed permittivity is close to the actual value, Figs. 7.3 (d)-(f) and (j)-(l). This is emphasized through the contrast error. With the multiple-frequency method, $\text{Err}_\chi = 29\%$ for the complete configuration and $\text{Err}_\chi = 48\%$ for the incomplete configuration, whereas with the frequency-hopping approach, $\text{Err}_\chi = 53\%$ for the complete configuration and $\text{Err}_\chi = 354\%$ for the incomplete configuration. One can conclude that the multiple-frequency method is more robust to the presence of the noise in data than the frequency-hopping approach, particularly under the incomplete configuration.

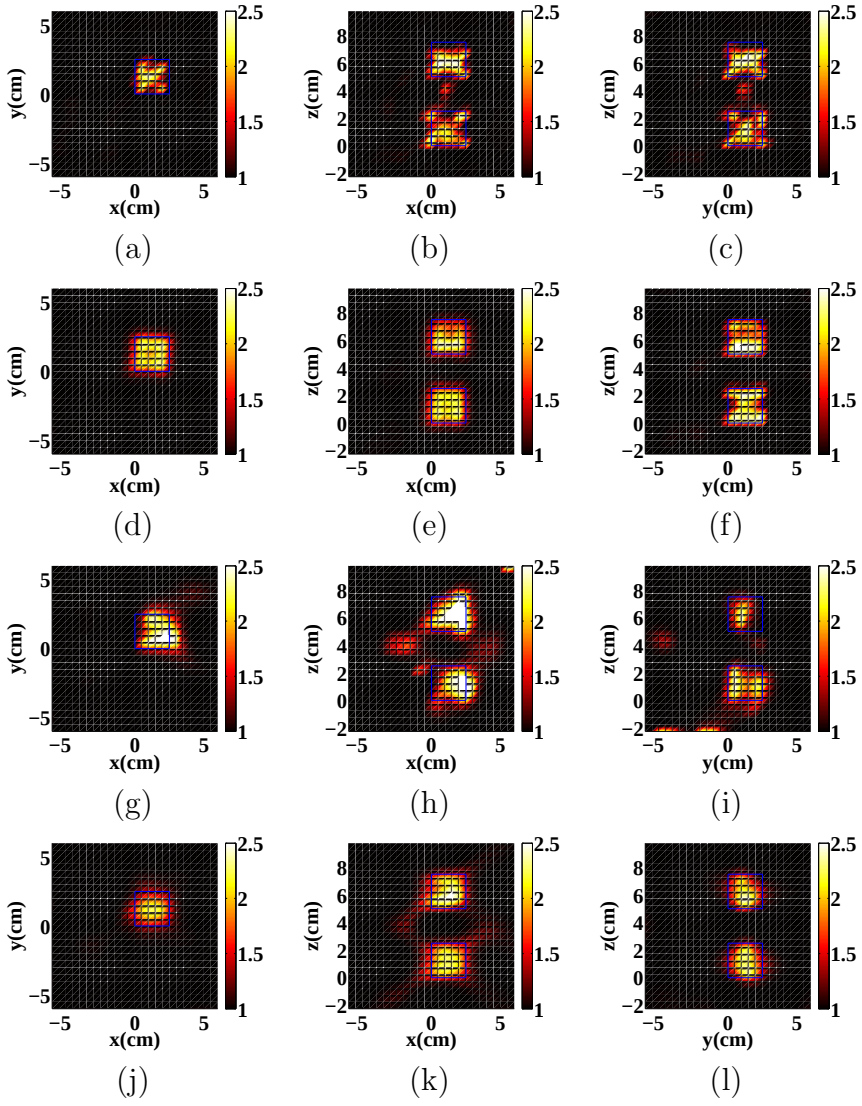


**Figure 7.3 :** *Reconstructed permittivity of the first target (two cubes along the z-axis) presented in Fig. 7.2 (a), in use of (a)-(c): frequency-hopping method (complete configuration). (d)-(f): multiple-frequency method (complete configuration). (g)-(i): frequency-hopping method (incomplete configuration). (j)-(l): multiple-frequency method (incomplete configuration). (a), (d), (g) and (j): in the* $(x, y)$ *plane at* $z = 1.25$ *cm. (b), (e), (h), and (k): in the* $(x, z)$ *plane at* $y = 1.25$ *cm. (c), (f), (i), and (l): in the* $(y, z)$ *plane at* $x = 1.25$ *cm.*

#### 7.2.3.2 Two cubes in contact by one edge

In this section, we consider two cubes placed in the $(x, y)$ plane that are in contact through one edge as depicted in Fig. 7.2 (b). Figure. 7.4 compares the reconstruction results using the multiple-frequency method and the frequency-hopping approach, under the complete and the incomplete configuration. Under the complete configuration, the reconstruction result obtained by the multiple-frequency approach is satisfactory, except that the permittivity is underestimated, Figs. 7.4 (d)-(f) with $\mathrm{Err}_\chi = 54\%$. The reconstruction result is better than that obtained by the frequency-hopping approach, [Figs. 7.4 (a)-(c)]. The contrast error for the latter approach

reaches $\text{Err}_\chi = 98\%$. When dealing with the incomplete configuration, the reconstruction with the frequency-hopping is deteriorated, Figs. 7.4 (g)-(i) with $\text{Err}_\chi = 141\%$. The two cubes are stuck together and seem to constitute a single object. In this case, using the multiple-frequency approach, the reconstruction result is not so good as the previous case (for the two cubes along the $z$ direction), Figs. 7.4 (j)-(l) with $\text{Err}_\chi = 105\%$. Nevertheless, the contrast error is still better than that of the frequency-hopping approach.

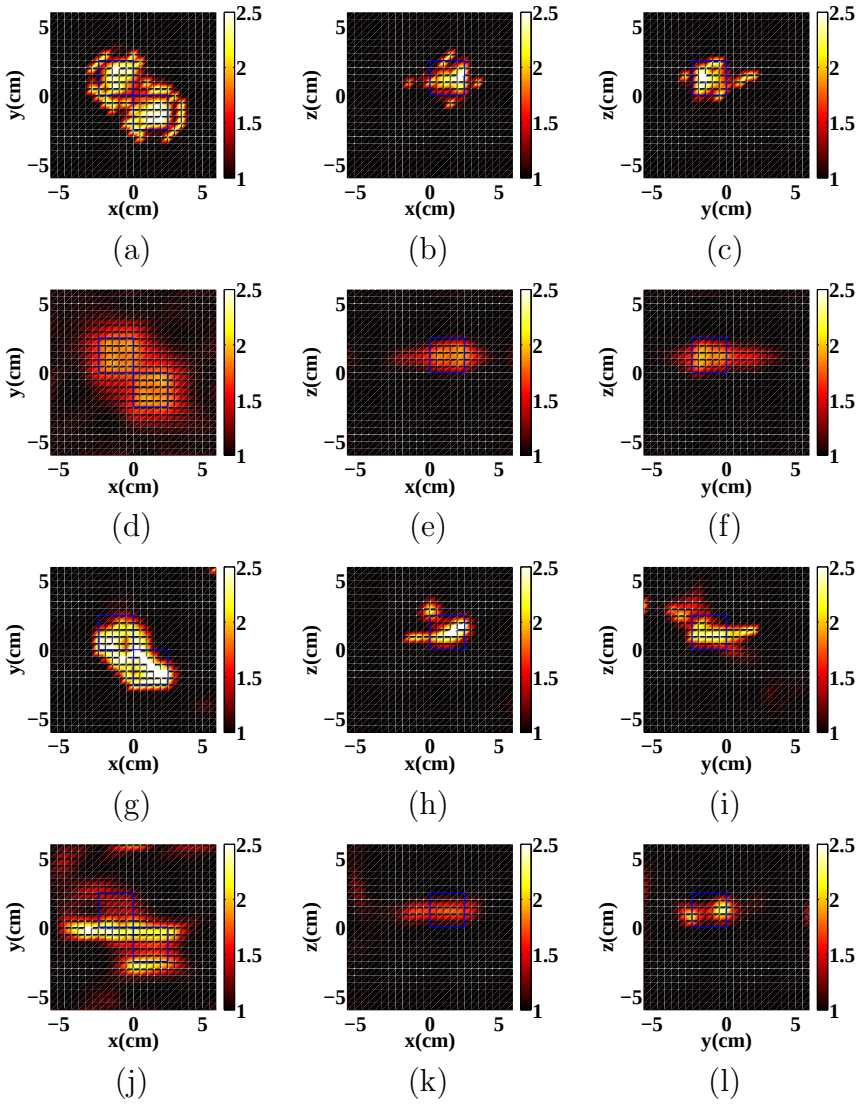


**Figure 7.4 :** *Reconstructed permittivity of the second target (two cubes with one edge in contact) presented in Fig. 7.2 (b) using (a)-(c): frequency-hopping method (complete configuration). (d)-(f): multiple-frequency method (complete configuration). (g)-(i): frequency-hopping method (incomplete configuration). (j)-(l): multiple-frequency method (incomplete configuration). (a), (d), (g) and (j): in the $(x, y)$ plane at $z = 1.25$ cm. (b), (e), (h) and (k): in the $(x, z)$ plane at $y = -1.25$ cm. (c), (f), (i) and (l): in the $(y, z)$ plane at $x = 1.25$ cm.*

This failure of the multiple-frequency method is surprising and unexpected. Since the frequency-hopping approach provided a reasonable reconstruction [Fig. 7.4 (g)-(i)]. One would expect to

arrive at worst to a similar reconstruction with the multiple-frequency algorithm. This is clearly not the case [Fig. 7.4 (j)-(l)].

One possible interpretation of the non-satisfactory reconstruction could be due to the fact that the measured scattered field of high frequencies contribute too much in the minimized cost function, Eq. (7.1). Hence, the iterative processus might be trapped into a local minimum. It is well-known that iterative technique convergences at low frequency with a poor resolution, while at high frequency the convergence is not guaranteed[58]. Notice that both techniques, the multiple-frequency approach and the frequency-hopping approach provide reconstructions of quality far away from the ones obtained with the complete configuration.

In the following, we investigate the possibility to restore the resolution. One option would be to modify the minimized cost function to a frequency-weighted cost function.

In order to quantify the contributions for both high frequencies and low frequencies, we propose to analyze the behavior of the weighting coefficient at each operating frequency in Eq. (7.2). We define a new frequency-dependent function $W(p)$:

$$W(p) = \sum_{l=1}^{N} \|\boldsymbol{f}_{l,p}^{\text{mes}}\|_{\Gamma}^{2}. \tag{7.2}$$

Figure 7.5 shows the evolution of $W(p)/(f_p)^{\alpha}$ versus the frequency $f_p$ with different weighting coefficient $\alpha$. The behavior of $W(p)$ without the weighting coefficient ($\alpha = 0$) is represented with the blue-solid line. As the frequency increases, the amplitude of the measured fields at higher frequencies become more significant as compared to those of lower frequencies. We propose to weight the measured scattered fields by a factor of $1/(f_p)^{\alpha}$. We present here evolutions with three different weighting coefficients, $\alpha = 1$, 2 and 3. Fig. 7.5 shows that for $\alpha = 0$, high frequencies are dominant while for $\alpha = 3$, low frequencies are dominant.

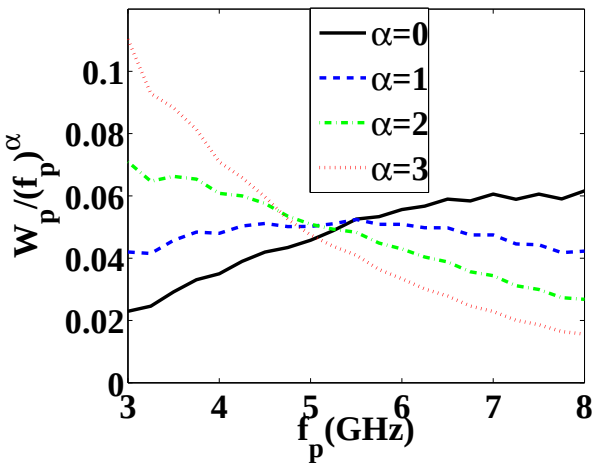


**Figure 7.5 :** *Evolution of $W(p)/(f_p)^{\alpha}$ of the second target (two cubes with one edge in contact) versus the frequency (GHz) with the weighting coefficient $\alpha$ equal to 0 for black-solid line, 1 for blue-dashed line, 2 for green-dash-dot line, 3 for red-dotted line.*

The idea is now to take profit, in the inversion algorithm, of this weighting function in order to balance high and low frequency contributions. We let one parameter $\alpha$ free that we will vary. Other choices of a weighting function were not investigated.

We introduce the frequency weighting in the inversion by defining a new cost function $\tilde{F}_n(\chi_n, \boldsymbol{E}_{\cdot,\cdot,n})$ as

$$\tilde{F}_n(\chi_n, \boldsymbol{E}_{\cdot,\cdot,n}) = \frac{\sum_{l=1}^{N}\sum_{p=1}^{P}(1/f_p)^{\alpha}\|\boldsymbol{h}_{l,p,n}^{(2)}\|_{\Gamma}^2}{\sum_{l=1}^{N}\sum_{p=1}^{P}(1/f_p)^{\alpha}\|\boldsymbol{f}_{l,p}^{\mathrm{mes}}\|_{\Gamma}^2} + \frac{\sum_{l=1}^{N}\sum_{p=1}^{P}(1/f_p)^{\alpha}\|\boldsymbol{h}_{l,p,n}^{(1)}\|_{\Omega}^2}{\sum_{l=1}^{N}\sum_{p=1}^{P}(1/f_p)^{\alpha}\|\boldsymbol{E}_{l,p}^{\mathrm{inc}}\|_{\Omega}^2}, \tag{7.3}$$

here the two normalizing coefficients are defined as

$$\tilde{W}_{\Omega} = \frac{1}{\sum_{l=1}^{N}\sum_{p=1}^{P}(1/f_p)^{\alpha}\|\boldsymbol{E}_{l,p}^{\mathrm{inc}}\|_{\Omega}^2}, \qquad \text{and} \qquad \tilde{W}_{\Gamma} = \frac{1}{\sum_{l=1}^{N}\sum_{p=1}^{P}(1/f_p)^{\alpha}\|\boldsymbol{f}_{l,p}^{\mathrm{mes}}\|_{\Gamma}^2}. \tag{7.4}$$

Eq. (7.3) can be represented as

$$\tilde{F}_n(\chi_n, \boldsymbol{E}_{\cdot,\cdot,n}) = \tilde{W}_{\Gamma}\sum_{l=1}^{N}\sum_{p=1}^{P}(1/f_p)^{\alpha}\|\boldsymbol{h}_{l,p,n}^{(2)}\|_{\Gamma}^2 + \tilde{W}_{\Omega}\sum_{l=1}^{N}\sum_{p=1}^{P}(1/f_p)^{\alpha}\|\boldsymbol{h}_{l,p,n}^{(1)}\|_{\Omega}^2, \tag{7.5}$$

with the residue errors $\boldsymbol{h}_{l,p,n}^{(1)}$ and $\boldsymbol{h}_{l,p,n}^{(2)}$ defined as

$$\boldsymbol{h}_{l,p,n}^{(1)} = \boldsymbol{E}_{l,p}^{\mathrm{inc}} + \chi\overline{\overline{\boldsymbol{A}}}_p\boldsymbol{E}_{l,p,n} - \boldsymbol{E}_{l,p,n}, \qquad \text{and} \qquad \boldsymbol{h}_{l,p,n}^{(2)} = \boldsymbol{f}_{l,p}^{\mathrm{mes}} - \overline{\overline{\boldsymbol{B}}}_p\chi\boldsymbol{E}_{l,p,n}. \tag{7.6}$$

We need to pay attention to the calculation of the gradient with respect to the contrast and the total field, presented in Appendix. C.3. A part of this, the inversion scheme is unchanged.

We try the multiple-frequency method weighted by different coefficients, and we compare the reconstruction results in Fig. 7.6.

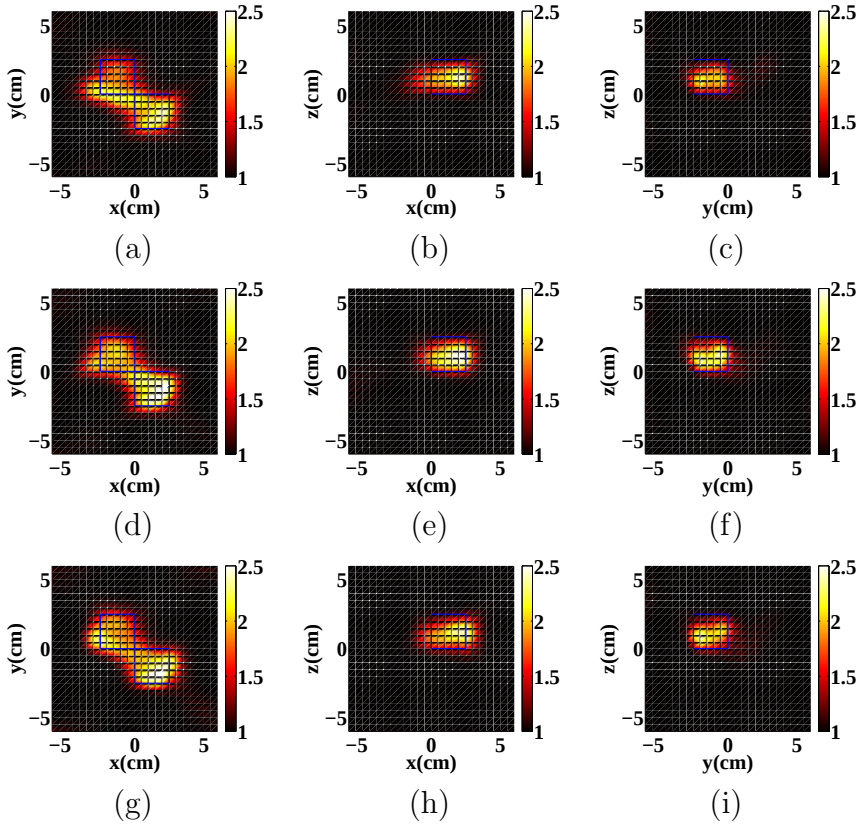


**Figure 7.6 :** *Reconstructed permittivity of the second target (two cubes with one edge in contact) presented in Fig. 7.2 (b) in incomplete configuration in use of multiple-frequency method with the weighting coefficient (a)-(c) :* $\alpha = 1$*, with* $\mathrm{Err}_\chi = 61.5\%$*. (d)-(f):* $\alpha = 2$*, with* $\mathrm{Err}_\chi = 47.4\%$*. (g)-(i):* $\alpha = 3$*, with* $\mathrm{Err}_\chi = 46.9\%$*. (a), (d) and (g) in the* $(x, y)$ *plane at* $z = 1.25$ *cm. (b), (e) and (h) in the* $(x, z)$ *plane at* $y = -1.25$ *cm. (c), (f) and (i) in the* $(y, z)$ *plane at* $x = 1.25$ *cm.*

From Fig. 7.6, we can conclude that weighting the measured field contribution at all frequencies can ameliorate the reconstruction, compared to the same incomplete configuration while without any weightings, as shown in Figs. 7.4 (j)-(l). With $\alpha = 2$ or $\alpha = 3$, the reconstructed two cubes are more homogeneous and clearly better than the reconstruction result without the weighting processing under complete configuration, Figs. 7.4 (d)-(f). To further numerically evaluate the amelioration of this weighting coefficient, we define a parameter as

$$\mathrm{Err}_p = \frac{\sum_{l=1}^{N} \|\boldsymbol{f}_{l,p}^{\mathrm{mes}} - \boldsymbol{E}_{l,p}^{\mathrm{cal}}\|_\Gamma^2}{\sum_{l=1}^{N} \|\boldsymbol{f}_{l,p}^{\mathrm{mes}}\|_\Gamma^2}. \tag{7.7}$$

The residual error versus the frequency between the measured scattered field and the calculated field obtained with the best available estimated contrast $\chi$ is defined in Eq. (7.7). The behavior of this residual error versus different weighting coefficients is shown in Fig. 7.7 (b) for all targets of the database. The residual error is minimum with $\alpha = 2$ and $\alpha = 3$ at almost all frequencies, which corresponds to the satisfactory reconstruction results obtained in Fig. 7.6.

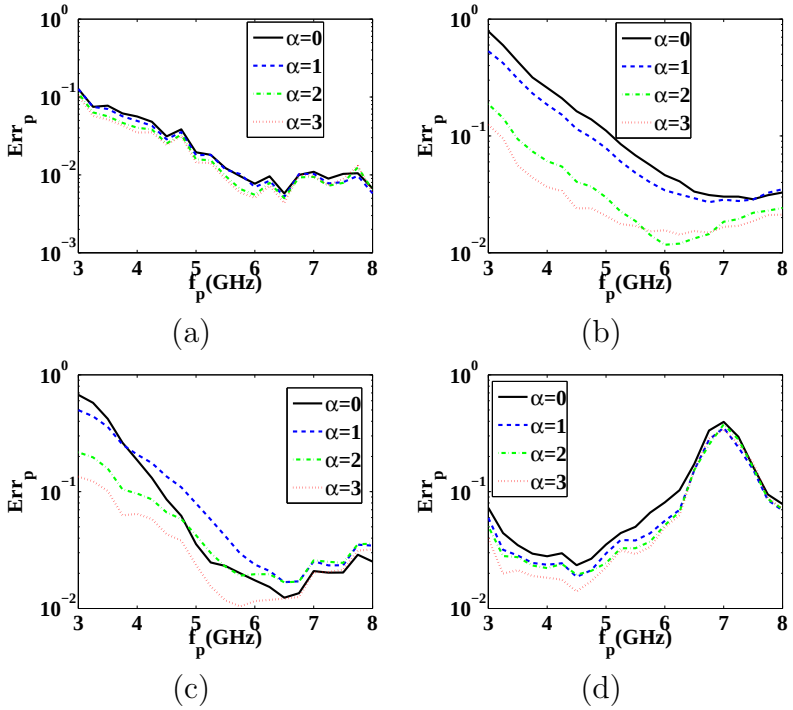


**Figure 7.7 :** *Evolution of* $\mathrm{Err}_p$ *versus the frequency (GHz) with the weighting coefficient* $\alpha$ *equal to* 0 *for black solid line,* 1 *for blue dashed line,* 2 *for green dash-dot line,* 3 *for red dotted line, under the incomplete configuration. (a) for the first target (two cubes along the z-axis). (b) for the second target (two cubes with one edge in contact). (c) for the third target (two cubes along the y-axis). (d) for the fourth target (two spheres in contact).*

Now, we explain the impact of the weighting factor on the first target (two cubes along the $z$-axis). The cost functional is weighted by these three different coefficients, the behavior of the residue error is shown in Fig. 7.7 (a). There is no much difference among the evolutions of the residual error for these three weighting coefficients. In order to make this more convincing, we have also tried other weighting coefficients $\alpha = 1 \sim 3$, with an interval 0.1, and we arrive at the same conclusion. Moreover, the reconstruction result is not influenced by the introduced weighting coefficients.

From the above analysis, we can conclude that for some targets, it is mandatory to perform the frequency weighting version of the inverse scheme. In most cases, with $\alpha = 3$, satisfactory reconstructions are achieved.

#### 7.2.3.3 Two cubes along the $y$-direction

Herein, we investigate the resolution along $y$-axis, Fig. 7.2 (d). Using the weighted multiple-frequency approach, we can see that the behavior of $\mathrm{Err}_p$ [Fig. 7.7 (c)] is similar to that of the previous case, Fig. 7.7 (b). With the weighting coefficient $\alpha = 3$, we can obtain a minimum residue error.

Under the complete configuration, using the multiple-frequency approach, the reconstruction result is correct. Similar to the previous case (two cubes in contact by one edge), the permittivity is underestimated and the two cubes are not distinctly separated along $y$-axis leading to $\mathrm{Err}_\chi = 60\%$, Figs. 7.8 (a)-(c). It is not surprising that with incomplete configuration the reconstruction result obtained by the frequency-hopping approach is clearly deteriorated ($\mathrm{Err}_\chi = 287\%$), Figs. 7.8 (d)-

(f). For the multiple-frequency approach without any weighting process, we can not obtain a satisfactory reconstruction result, Figs. 7.8 (g)-(i) ($\text{Err}_\chi = 187\%$). The best result is obtained by the multiple-frequency approach with the weighting coefficient $\alpha = 3$ ($\text{Err}_\chi = 62\%$), Figs. 7.8 (j)-(l). The two cubes are better separated along $y$-axis than in the complete configuration. Notice that in the $(x, y)$ plane, the two cubes are linked by a 'bridge' of weak permittivity distribution. To understand this undesirable result, we tried to invert the theoretical data generated by the CDM. The reconstruction is acceptable and the 'bridge' dispears. We can conclude that this is caused by the presence of noise in data.

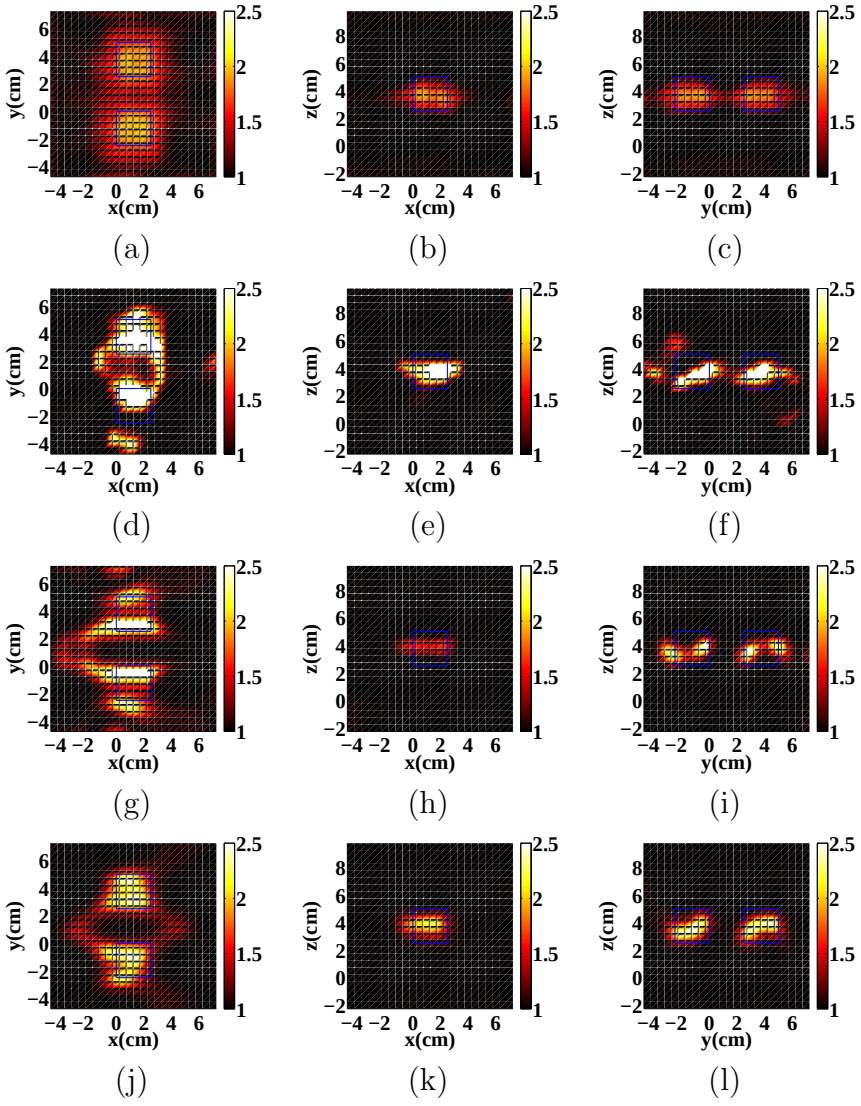


**Figure 7.8 :** *Reconstructed permittivity of the third target (two cubes along the y-axis) presented in Fig. 7.2 (c), in use of (a)-(c): multiple-frequency method (complete configuration). (d)-(f): frequency-hopping method (incomplete configuration). (g)-(i): multiple-frequency method (incomplete configuration) without weighting coefficient. (j)-(l): multiple-frequency method (incomplete configuration) with weighting coefficient* $\alpha = 3$*. (a), (d), (g) and (j) in the* $(x, y)$ *plane at* $z = 3.75$ *cm. (b), (e), (h) and (k) in the* $(x, z)$ *plane at* $y = 3.75$ *cm. (c), (f), (i) and (l) in the* $(y, z)$ *plane at* $x = 1.25$ *cm.*

#### 7.2.3.4 Two identical spheres in contact

For the fourth and the last example, we consider the target made of two dielectric spheres of relative permittivity $\varepsilon = 2.6$ and of radius $r = 2.5$ cm in contact, as shown in Fig. 7.2 (c). This case is more difficult than the previous cases because the two spheres are in contact and the dimension of the object is larger than the wavelength at the central illumination frequency $f_0 = 5.5$ GHz. We first attempted to reconstruction this structure with the incomplete configuration. Results are deceiving. Neither the multiple-frequency method nor the frequency-hopping approach succeeded

in retreiving the two spheres. With the complete configuration, results of inversions are presented in Fig. 7.9. We give here the reconstruction results using the multiple-frequency approach without and with the weighting coefficient, and we compare these results with the frequency-hopping approach.

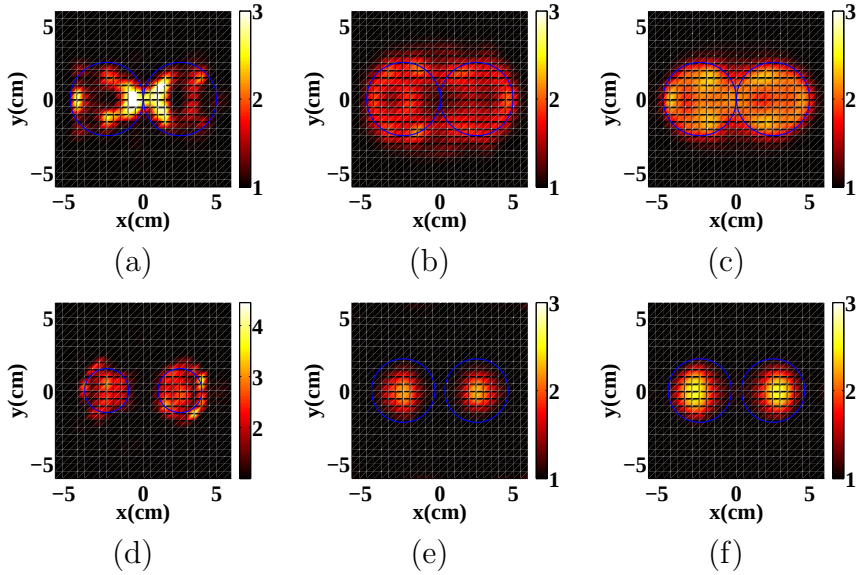


**Figure 7.9 :** *Reconstructed relative permittivity distribution for the fourth target (two spheres in contact) in the $(x, y)$ plane (a)-(c) for $z = 0$ cm, (d)-(f) for $z = -2$ cm. (a) and (d) using the frequency-hopping approach. (b) and (e) using the multiple-frequency approach with the weighting coefficient $\alpha = 0$. (c) and (f) same as (b) and (e), while with $\alpha = 3$.*

From Fig. 7.9, we can conclude that using the multiple-frequency approach with $\alpha = 3$, Figs. 7.9 (c) and (f), satisfactory reconstruction result is obtained leading to $\mathrm{Err}_\chi = 21\%$. The reconstructed permitivity distribution is almost homogeneous and the profile is well represented. On the contrary, without using the weighting coefficient ($\alpha = 0$), Figs. 7.9 (b) and (e), the reconstructed permittivity is poorer than with $\alpha = 3$, and the permittivity at the contact point is underestimated, leading to $\mathrm{Err}_\chi = 43.5\%$. For this case, the frequency-hopping approach [Figs. 7.9 (a) and (d)], fails to reconstruct this target, where the permittivity at the contact point is overestimated, leading to $\mathrm{Err}_\chi = 76.4\%$.

## 7.3 Conclusions

In this chapter, we have tested our non-linear inversion algorithm on experimental frequency-diversity data. Dealing with four different dielectric targets, we have shown that the reconstruction obtained with multiple-frequency method is always better than the one obtained with the frequency-hopping approach. For some targets and under the incomplete configuration, weighting the cost functional to ajust the balance of the fields for higher and lower frequencies is needed. Otherwise, if the components at high frequencies dominate too much in the cost functional, the stability of the minimization algortihm would not be guaranteed. Notice that with the weighting coefficient $\alpha = 3$, we always obtained satisfactory reconstruction result for the incomplete configuration. We have also tried $\alpha = 4$. The reconstruction is equivalent or slightly deteriorated compared to $\alpha = 3$. Moreover, the optimum $\alpha = 3$ is obtained for the incomplete configuration.

In fact, the choice of this parametre depends on the configuration, *i.e.*, $\alpha = 3$ is not always the optimum for the complete configuration at hand.

Chapter 8

# Inversion problem using transient data

## Contents



## 8.1 Introduction

In the last chapter, we validated our multiple-frequency inversion algorithm against experimental data. In this chapter, we will move on to the transient scattered data. The excitation is assumed to be a single transient pulse, and the inversion problem is formulated in the frequency domain rather than directly in the time domain[54], as mentioned previously in Sec. 1.5 and 2.3. The short time-duration incident pulse is transformed into the frequency domain by the Fourier transform. Both low and high frequency components are obtained. It has been shown that the dynamic range of iterative inversion techniques is large at lower frequencies than at higher frequencies[19]. At high frequencies, iterative techniques lead to better resolution but the convergence is not guaranteed.

In this chapter, we first apply the transient inversion method using synthetic data. Before to process the transient inversion, the scatterers are localized thanks to the time reversal approach. The performances of reconstruction using the frequency-hopping approach and the transient inversion method are analyzed and compared. We end this chapter with the validation of this transient inversion algorithm against experimental data described in Chap. 7.

## 8.2 Inversion problem for transient scattered fields using synthetic data

In this section, we test the characterization ability on synthetic transient data, under the configuration of homogeneous background medium. The scattering domain is illuminated by a single incident electromagnetic pulse with a Gaussian envelop,

$$\mathcal{F}(t) = A\ \exp\left[-16\left(\frac{t-t_{\text{trans}}}{\tau}\right)^2\right]\ \cos(2\pi f_0 t). \tag{8.1}$$

The scattering problem is formulated in the frequency domain by the Laplace transform. The number of sampling frequencies $P$ should be large enough such that the spectrum of the incident pulse is well represented. Then $P$ resulting harmonic scattering problems are solved by the CDM. The harmonic scattered fields are then transformed into the transient domain by the inverse Laplace transform. This procedure is described in detail in Sec. 1.5. The inverse problem is resolved in the frequency domain. The minimization procedure is the same as that of the multiple-frequency approach. The difference is that the incident field and the scattered fields in the frequency domain are weighted by $F(\omega_p)$, the spectrum of the incident Gaussian pulse. The principle of the inversion procedure in the time domain that we choose is similar as the multiple-frequency approach. The minimized cost function is defined as

$$\mathcal{F}_n(\chi_n, \boldsymbol{E}_{\cdot,\cdot,n}) = \frac{\sum_{l=1}^{N}\sum_{p=1}^{P}\|\boldsymbol{h}_{l,p,n}^{(2)}\|_\Gamma^2}{\sum_{l=1}^{N}\sum_{p=1}^{P}\|\boldsymbol{f}_{l,p}^{\text{mes}}\|_\Gamma^2} + \frac{\sum_{l=1}^{N}\sum_{p=1}^{P}\|\boldsymbol{h}_{l,p,n}^{(1)}\|_\Omega^2}{\sum_{l=1}^{N}\sum_{p=1}^{P}\|\boldsymbol{E}_{l,p}^{\text{inc}}\|_\Omega^2}, \tag{8.2}$$

where the residue errors $\boldsymbol{h}_{l,p,n}^{(1)}$ and $\boldsymbol{h}_{l,p,n}^{(2)}$ are defined as

$$\boldsymbol{h}_{l,p,n}^{(1)} = F(\omega_p)\boldsymbol{E}_{l,p}^{\text{inc}} + \chi\overline{\overline{\boldsymbol{A}}}_p\boldsymbol{E}_{l,p,n} - \boldsymbol{E}_{l,p,n}, \qquad \text{and} \qquad \boldsymbol{h}_{l,p,n}^{(2)} = F(\omega_p)\boldsymbol{f}_{l,p}^{\text{mes}} - \overline{\overline{\boldsymbol{B}}}_p\chi\boldsymbol{E}_{l,p,n}. \tag{8.3}$$

### 8.2.1 Statement of the problem

The geometry of the problem is illustrated in Fig. 8.1, where $W$ denotes the scattering domain and $\Omega$ denotes the investigating domain that is confined in $W$. The scattering domain $W$ is illuminated by a single source located at (0,0,1.2 m), fed by the current of the Gaussian envelop, modulated at the central frequency $f_0 = 2$ GHz, with the wavelength $\lambda_0 = 0.15$ m. The time duration of the Gaussian pulse $\tau = 4$ ns, and the observation time window is between 2 ns and 16 ns. The pulse is shifted at $t_{\text{trans}} = 6$ ns. The receivers array collecting the transient electromagnetic field is represented by a lattice of $N = 81$ dipole antennas regularly distributed on a square of side size of 4.8 m, and is located at $z = 1.2$ m. Three-dimensional targets are presented in a homogeneous medium whose electromagnetic constants are $\varepsilon_0$ and $\mu_0$. In this configuration, the single source is located at the centre of the receivers array. Targets are assumed to be non-magnetic ($\mu = \mu_0$) and homogeneous with the relative permittivity $\varepsilon$. The emitting dipole antenna is oriented along a single direction $x$, whereas the receiving dipole antennas are polarized along $x$, $y$ and $z$ directions. The vectorial scattered field can thus be obtained. Measurements are performed using the CDM with $P = 28$ frequencies uniformly distributed from 1 GHz up to 3 GHz, with a frequency step of 71 MHz. Compared to the analytical expression of the pulse, we have checked that the spectrum of the incident pulse can be well represented with this choice of sampling frequencies.

### 8.2.2 Issue of time reversal focusing in time domain

In the time-harmonic regime, we choose one of the time reversal technique, the DORT method to detect and localize buried objects, using monochromatic data. In the time domain, according to

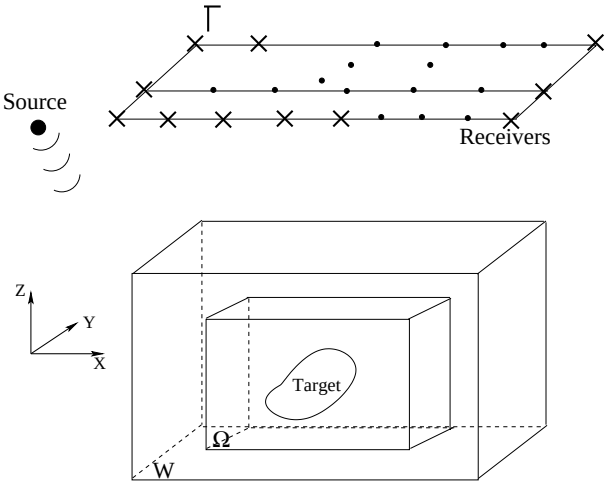


**Figure 8.1 :** *Geometry of the problem. The receivers are regularly distributed on a plane* $\Gamma$*, located on one side of the objects. The system is illuminated by a single source.*

the time invariance of the wave propagation Eq. (3.4), with $t$ changed to $-t$, the phase conjugation mirror becomes time reversal mirror with the same robustness and focusing properties. The back-propagated waves synthesize a wave focusing on each bright scatterer present in the scattering domain sequentially along the time[2,35,45].

The time reversal procedure is described as:

1. The scattering domain $W$ is illuminated by a single source, which radiates a Gaussian pulse $\mathcal{F}(t)$, shown as Fig. 8.2 (a).
2. The transient scattered fields are measured by all receivers, Fig. 8.2 (b).
3. The time reversal procedure is implemented numerically, Fig. 8.2 (c).

The transient scattered fields $\boldsymbol{\mathscr{E}}^{\mathrm{d}}(\boldsymbol{r}_m, t)$ are transformed into the frequency domain using the Laplace transform $\boldsymbol{E}^{\mathrm{d}}(\boldsymbol{r}_m, \omega_p) = \mathscr{L}_{\beta=0}[\boldsymbol{\mathscr{E}}^{\mathrm{d}}(\boldsymbol{r}_m, t)]$, where $\boldsymbol{r}_m (m = 1, 2, \cdots, M)$ denotes positions of receivers, $p = 1, 2, \cdots, P$ is the number of sampling frequency. For each receiver $m$, we have $P$ harmonic scattered fields $\boldsymbol{E}^{\mathrm{d}}(\boldsymbol{r}_m, \omega_p)$. The time reversal operation in the time domain is equivalent to the phase conjugation in the frequency domain. Thus, we can construct a focusing wave $\tilde{\boldsymbol{E}}(\boldsymbol{r}, \omega_p)$ in the frequency domain as

$$\tilde{\boldsymbol{E}}(\boldsymbol{r}, \omega_p) \ \ (\boldsymbol{r} \in W) = \sum_{m=1}^{M} \boldsymbol{G}(\boldsymbol{r}, \boldsymbol{r}_m, \omega_p) \boldsymbol{P}(\boldsymbol{r}_m, \omega_p), \tag{8.4}$$

where $\boldsymbol{P}(\boldsymbol{r}_m, \omega_p) \propto \left[\bar{\boldsymbol{E}}^{\mathrm{d}}(\boldsymbol{r}_m, \omega_p)\right]$. The overbar denotes the complex conjugation. $\boldsymbol{G}(\boldsymbol{r}, \boldsymbol{r}_m, \omega_p)$ denotes the Green function at each frequency $\omega_p$. The transient focusing field $\boldsymbol{\mathscr{E}}(\boldsymbol{r}, -t)$ is obtained through the inverse Laplace transform, $\boldsymbol{\mathscr{E}}(\boldsymbol{r}, -t) = \mathscr{L}^{-1}_{\beta=0}[\tilde{\boldsymbol{E}}(\boldsymbol{r}, \omega_p)]$. The intensity of this transient field at each point $\boldsymbol{r}$ inside the scattering domain $W$ along the time axis $t$ provides where the scatterers are.

### 8.2.3 Numerical results

In this section, we present some numerical results using synthetic data generated by the CDM. A single or two scatterers are studied. The investigating domain that is used in the inversion is determined by analyzing the time reversal waves. In the inversion procedure, two different inversion approaches are considered, the frequency-hopping approach and the transient inversion approach.

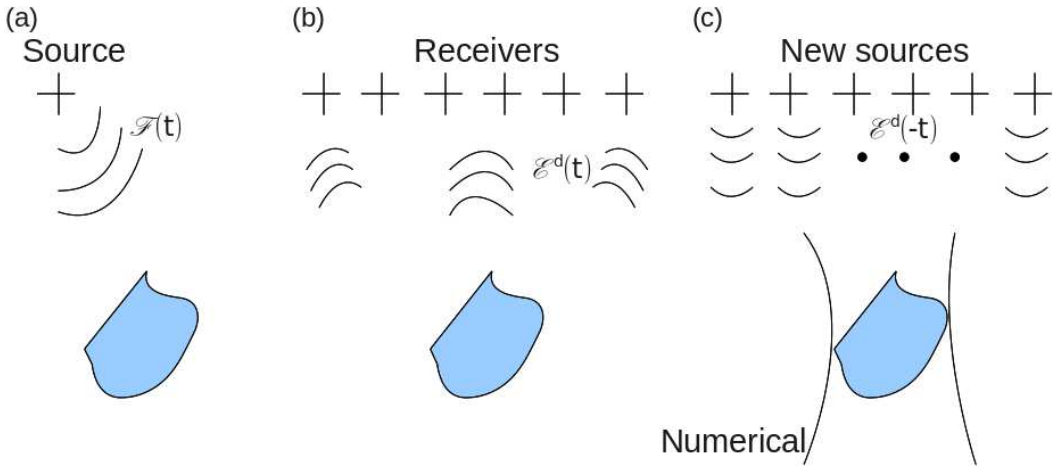


**Figure 8.2 :** *Schematic view of the time reversal procedure. (a) The scattering domain is illuminated by a transient source. (b) The transient scattered fields are detected by all receivers. (c) The time-reversed scattered fields are backpropagated by all receivers (new sources) for generating a focusing wave on the scatterer.*

#### 8.2.3.1 One single scatterer

Consider one single dielectric sphere of the radius $\lambda_0/6$ and of the relative permittivity $\varepsilon = 3$, located at the origin. The synthetic data are generated in a box of volume $(2\lambda_0 \times 2\lambda_0 \times 4\lambda_0)$, centered at the origin. The forward scattering problem is calculated with a mesh size $\lambda_0/10$, independent of the operating frequency. Fig. 8.3 presents one of the scattered fields received by the antenna at (−2.4 m,−2.4 m,1.2 m), at the edge of the receiver array.

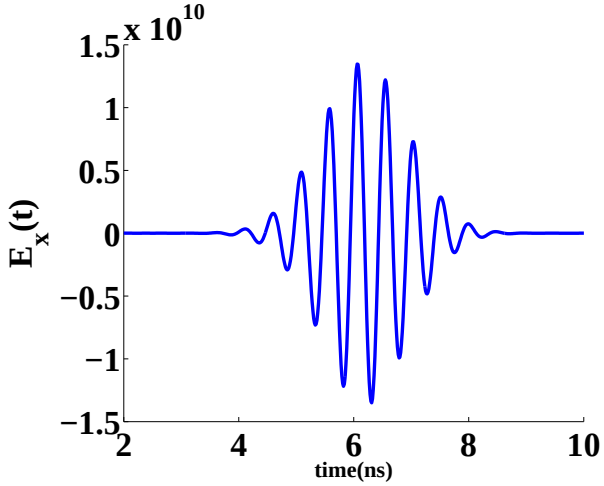


**Figure 8.3 :** *Form of the scattered field versus the time, that is received by the antenna located at (−2.4 m,−2.4 m,1.2 m).*

From Fig. 8.3, we can conclude that the time window is large enough to represent the scattered field in the time domain. We checked that if the time window $t_{\max} - t_{\min}$ is enlarged without changing the frequency range, by augmenting the number of sampling frequencies $P$, nothing

changes with the scattered field $\boldsymbol{\mathscr{E}}^{\mathrm{d}}(\boldsymbol{r}_m, t)$. There is no need to increase the number of sampling frequencies.

The investigating domain $\Omega$ is derived from the maximum position of the modulus of the time-reversed wave $\boldsymbol{\mathscr{E}}(\boldsymbol{r}, -t)$. Indeed, this maximum is related to the target under test and one can determine the scattering area, Fig. 8.4 (b).

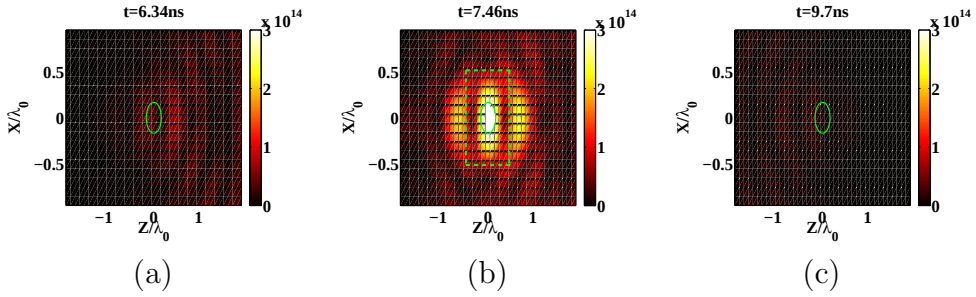


**Figure 8.4 :** *Modulus of the amplitude of the time-reversed wave in the scattering domain $W$ at three time points (a) $t = 6.34$ ns, generation of the wave. (b) $t = 7.46$ ns, focalization of the wave on the scatterer. The green dashed line represents the investigating domain $\Omega$ that we use to perform the inversion procedure. (c) $t = 9.7$ ns, disappearance of the wave.*

The time-reversed wave arrives at the edge of the scattering domain, Fig. 8.4 (a), and then, it focalizes on one echogeneous scatterer, Fig. 8.4 (b), and finally, it disappears, Fig. 8.4 (c). The instant of the focalization can be determined either by finding the maxima of the intensity of the time-reversed wave, or by determining the change in the convexity of the wavefront. In fact, before the focalization on the scatterer, the wave is concave, while after the focalization, this wave becomes convex.

Thus, thanks to the focalization ability of the time-reversed wave, we can limit the investigating domain in the inversion procedure to a box, of the size $(\lambda_0 \times \lambda_0 \times \lambda_0)$, centered at the origin. We use the same discretization size as the forward problem, $a_{\mathrm{inv}} = \lambda_0/10$.

In the following, we present the reconstruction results using two different strategies. The first one is the frequency-hopping approach. $P = 28$ inverse scattering problems are solved successively. For the lowest frequency, the initial estimate is obtained by the back-propagation procedure. For higher frequencies, the final inversion result obtained at the lower frequency is used as the initial estimate. The reconstruction result is shown in Figs. 8.5 (a)-(c).

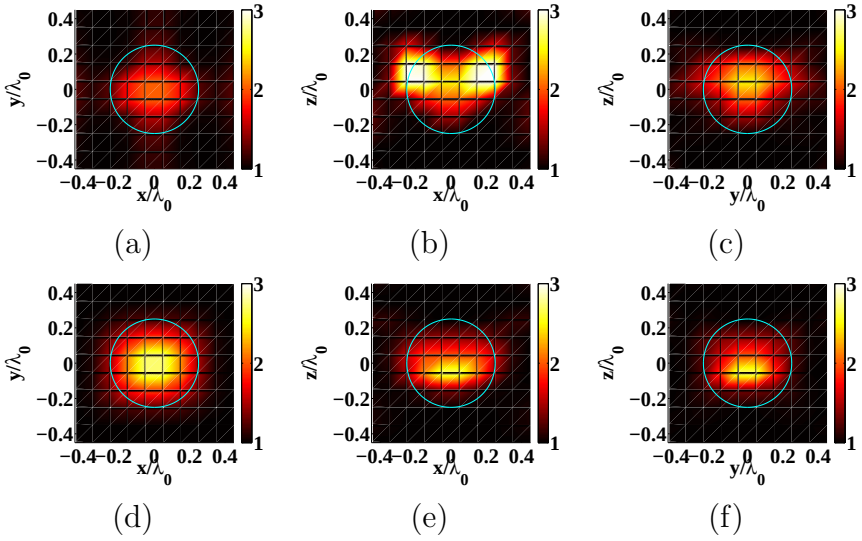


**Figure 8.5 :** *Reconstructed relative permittivity distribution for one single scatterer, with noiseless data. (a)-(c) using the frequency-hopping approach. (d)-(f) using the transient inversion method. (a) and (d) in $(x, y)$ plane for $z = 0$. (b) and (e) in $(x, z)$ plane for $y = 0$. (c) and (f) in $(y, z)$ plane for $x = 0$.*

The second strategy is the transient inversion method, as described in Sec. 2.3. The cost functional is defined in Eq. (8.2), with the incident source $N = 1$ and the number of frequency $P = 28$. Harmonic scattered fields at all frequencies are weighted by the spectrum of the incident pulse $F(\omega)$. The initial estimate is obtained for all frequencies by the back-propagation procedure. The reconstruction result is presented in Figs. 8.5 (d)-(f). This result is slightly better than that obtained with the frequency-hopping approach. This is particularly obvious in the $(x, z)$ plane where two spots appears on the single scatterer with the frequency-hopping approach.

Now, we propose to test the robustness of our inversion algorithms against noisy data. To simulate the measured noise, a random perturbation is added separately to the real and imaginary parts of each component of the harmonic scattered fields,

$$\mathrm{Re}[\boldsymbol{E}^b_{m,p}(\boldsymbol{r})] = \mathrm{Re}[\boldsymbol{E}_{m,p}(\boldsymbol{r})] + b\alpha_p(\boldsymbol{E}^{\max}_{r,p} - \boldsymbol{E}^{\min}_{r,p}), \tag{8.5}$$

$$\mathrm{Im}[\boldsymbol{E}^b_{m,p}(\boldsymbol{r})] = \mathrm{Im}[\boldsymbol{E}_{m,p}(\boldsymbol{r})] + b\beta_p(\boldsymbol{E}^{\max}_{i,p} - \boldsymbol{E}^{\min}_{i,p}), \tag{8.6}$$

where the coefficient $b$ denotes the level of noise that we want to add. $\alpha_p$ and $\beta_p$ are two random numbers with the uniform distribution between $-1$ and 1. $\boldsymbol{E}^{\max}_{r,p}$ and $\boldsymbol{E}^{\min}_{r,p}$ (resp. $\boldsymbol{E}^{\max}_{i,p}$ and $\boldsymbol{E}^{\min}_{i,p}$) correspond to the maximum and the minimum value of the real part (resp. imaginary part) of the scattered field at the frequency $f_p$ for all receivers.

The reconstruction results with $b = 40\%$ noisy data are reported in Fig. 8.6. Using the frequency-hopping approach, with one single source and in the presence of the noise, Figs. 8.6 (a)-(c), we can not obtain any reliable information from the permittivity map, neither the localization nor the geometric profile of the targets are accurately reconstructed. Several 'artefacts' appear. On the contrary, using the transient inversion method, we can obtain similar result as those obtained for noiseless data, Figs. 8.6 (d)-(f). It means that the inversion is more robust against the presence of noise in data when it is performed with all frequencies than when it is performed using the frequency-hopping approach.

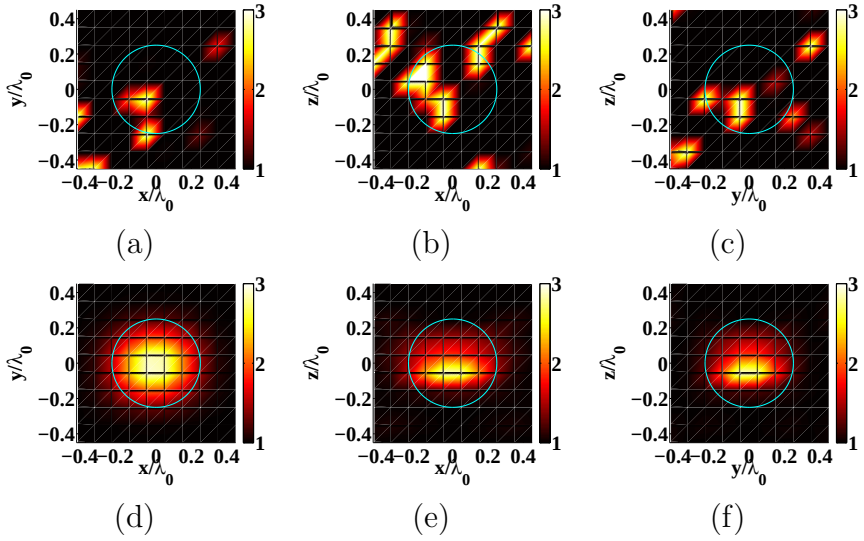


**Figure 8.6 :** *Same as Fig. 8.5, while $b = 40\%$ noise is added into the real part and the imaginary part of the harmonic scattered field.*

### 8.2.3.2 Discrimination of two scatterers

In this section, we apply the inversion to test the ability of our scheme to spatially separate the two scatterers.

We consider two dielectric spheres with the same radius ($\lambda_0/6$) and of the same permittivity ($\varepsilon = 3$), located at the origin (target B) and at $(0.5\lambda_0, 0, -0.7\lambda_0)$ (target A), respectively.

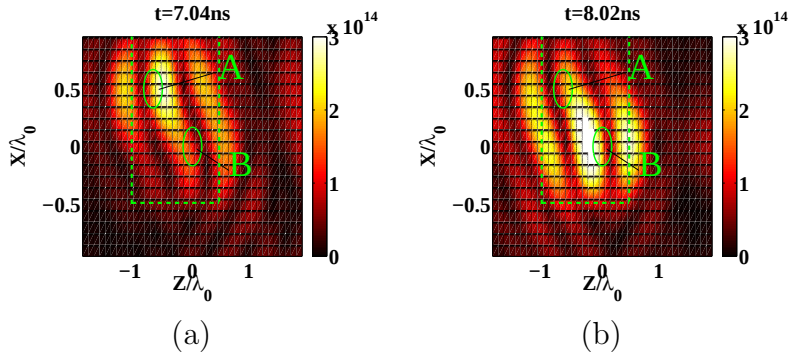


**Figure 8.7 :** *Modulus of the amplitude of the time-reversed wave in the scattering domain $W$ focusing on (a) target $A$ at $t = 7.04$ ns, generating of the wave. (b) target $B$ at $t = 8.02$ ns. The green dashed line denotes the investigating domain.*

Generally, the scattered fields by target B arrive firstly at the receivers, those of target A arrive later, because target B is closer to the receiver. From Fig. 8.7, the time-reversed wave focalizes on target A and then on target B. This can be understood as for the focusing wave, the time is reversed. The investigating domain can be limited into a smaller box of the size $(1.5\lambda_0 \times \lambda_0 \times 1.5\lambda_0)$, centered at $(0.25\lambda_0, 0, -0.35\lambda_0)$.

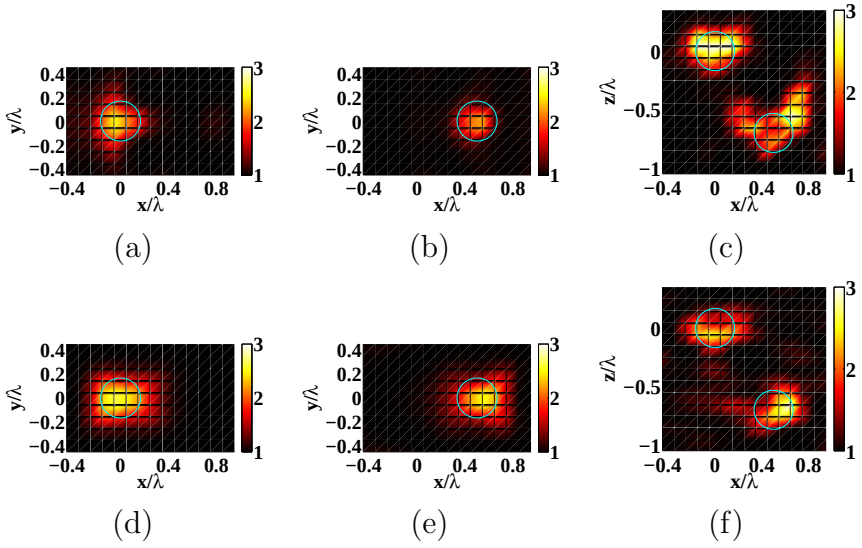


**Figure 8.8 :** *Reconstructed permittivity distribution for two scatterers, with the noiseless data. (a)-(c) using the frequency-hopping approach. (d)-(f) using the transient inversion method. (a) and (d) in* $(x, y)$ *plane for* $z = 0$*. (b) and (e) in* $(x, y)$ *plane for* $z = -0.7\lambda_0$*. (c) and (f) in* $(x, z)$ *plane for* $y = 0$*.*

The reconstruction results with noiseless data are reported in Fig. 8.8, using the two different algorithms. If we add $b = 40\%$ noise, the transient inversion method outperforms the frequency-hopping approach, Figs. 8.9 (d)-(f). When the frequency-hopping approach is used, the two scatterers are completely blurred by the noise, Figs. 8.9 (a)-(c).

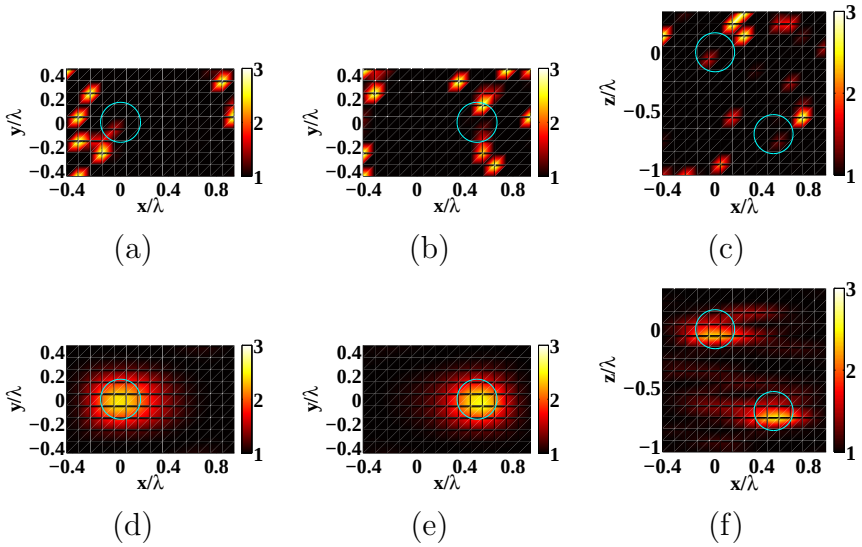


**Figure 8.9 :** *Same as Fig. 8.8, while* $b = 40\%$ *noise is added.*

From these numerical experiments, we conclude that the transient inversion method is efficient as compared to the frequency-hopping approach. This is particularly emphasized when data contain noise.

## 8.3 Inversion problem for transient scattered fields using experimental data

In order to perform the transient inversion procedure using experimental data, we synthesize a transient field from the multiple-frequency data measured in the anechoic chamber, mentioned in Chap. 7. These data have been processed with the multiple-frequency method in Chap. 7. We propose herein to apply the transient inversion scheme to these data.

The experimental data are synthesized from $P = 21$ harmonic fields measured at 3 GHz up to 8 GHz. The sampling frequency interval is therefore $\Delta f = 0.25$ GHz. We have the measured experimental data at hand, we need to furthermore synthesize a incident Gaussian wave. This wave should be generated in coincidence with the frequency-diversity data. According to the description in Sec. 1.5, the observation time span $\Delta t = 4$ ns is fixed to ensure that $\Delta f \Delta t = 1$. The incident Gaussian pulse [Fig. 1.4 (a)] is sampled in the time domain, with the time duration $\tau = 1.5$ ns, and the spectrum of the incident field is shown in Fig. 1.4 (b). In the time domain, the target is illuminated by the incident pulse, then the scattered field $\mathscr{E}^{\text{sca}}$ will be received some time later, depending on the distance among emitters, targets and receivers. But one does not need to increase the observation time window, it suffices to perform the inverse Fourier transform with $F(\omega)\mathrm{e}^{iwt_{\text{shift}}}$ instead of $F(\omega)$. According to the Fourier transform property, a time delay doesn't change the frequency content of $\mathcal{F}(\mathscr{E}^{\text{sca}})$ since the complex exponential always has a magnitude of 1, only the phase is altered.

### 8.3.1 Two cubes along the $z$-direction, two cubes in contact by one edge and two cubes along the $y$-direction

In order to verify if this time span is large enough, we augment four times the number of sampling frequency $P = 84$, keeping the frequency range unchanged, from 3 GHz to 8 GHz. The frequency step $\Delta f$ is reduced to 0.06 GHz, the time span $\Delta t$ is then increased to 16 ns. The theoretical transient scattered field in this configuration [Fig. 8.10 (a) blue line] is exactly the same as the one obtained with the sampling frequencies $P = 21$ ($t_{\text{shift}} = 6$ ns) [Fig. 8.10 (b) red line]. We can conclude that $\Delta f = 0.25$ GHz is enough to perform a transient inversion procedure.

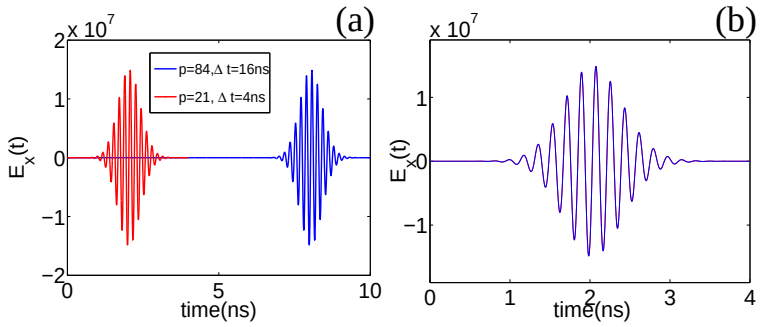


**Figure 8.10 :** *Shape of the theoretical scattered field in the time domain, for two cubes in contact by one edge. (a) blue line: $\Delta f = 0.06$ GHz, so the time span $\Delta t$=16 ns. red line: $\Delta f = 0.25$ GHz, $\Delta t$=4 ns. (b) The blue line in (a) is shifted into $0 - 4$ ns, and the red line in (a) keeps unchanged.*

#### 8.3.1.1 Localization of targets

In this section, we aim at localizing the targets before to reconstruct them. Assume that we have no knowledge about the target, we have to take a large box as the investigating domain. We

synthesize the time-reversed wave using Eq. (8.4). The localization of the target is determined by the maximum point of the intensity of time-reversed wave. The investigating domain used for the reconstruction procedure can be restricted to a small region.

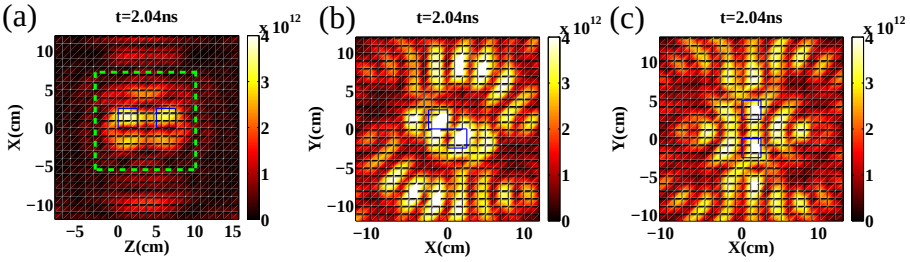


**Figure 8.11 :** *Modulus of the amplitude of the time-reversed wave in the scattering domain $W$. (a) For the two cubes along the $z$ direction. The dash box indicates the investigating domain used in the inversion procedure. (b) For the two cubes in contact by one edge. (c) For the two cubes along the $y$ direction. We present here only the moment at which the time-reversed wave focus on the target.*

As we can see the time-reversed wave in the case of the two cubes along the $z$-direction synthesizes a wave which focalizes on both cubes at the same time. Indeed, in this configuration, each cube can be considered as a small scatterer (compare to $\lambda_0$ the central frequency of the pulse) and due to the polarization of the incident field, there is no coupling between both scatterers (the two cubes are distributed along the $z$-direction and the incident polarization is also along the $z$-direction). If the two cubes are considered as two dipoles, the coupling is of order $1/r^2$ and $1/r^3$, where $r$ is the interdistance between the two cubes. The Green's function vanishes when $r \approx \lambda_0$, $\lambda_0$ is the central wavelength of the pulse. Hence we get two point of focalization on each cube, Fig. 8.11 (a). The investigating domain used for the inversion procedure can be limited to a smaller box indicated in Fig. 8.11 (a). This is no longer the case for the other configurations, *i.e.*, the two cubes along $y$-direction and the two cubes in contact by one edge. In fact, for these configurations there is a stronger coupling between the two cubes (the coupling is done through the term in $1/r$ in the Green's function which produces multiple scattering), which gives a focalization less punctual as the time-reversed wave feels the both scatterers as a large and single scatterer, as shown in Figs. 8.11 (b) and (c). But the investigating domain remains the same as that of the two cubes along the $z$ axis.

### 8.3.1.2 Reconstruction of targets

The reconstruction result obtained with the transient inversion procedure is shown in Fig. 8.12. For the first target, the reconstructed permittivity is underestimated while for the second target, the reconstructed permittivity distribution is acceptable but less homogeneous than that obtained by the weighted multiple-frequency approach, shown in Figs. 7.6. For the third target, the target is well retrieved except that the permittivity is overestimated.

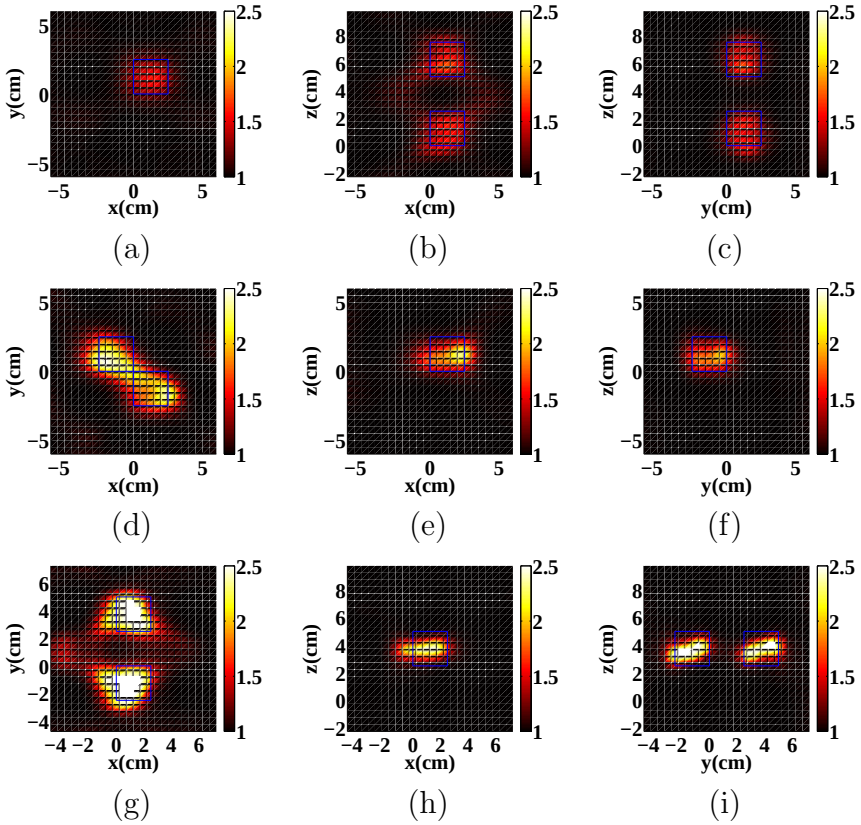


**Figure 8.12 :** *Reconstruction results obtained by the transient inversion data, under the incomplete configuration, where the scattered fields are weighted by a Gaussian incident pulse. (a)-(c): for the first target (two cubes along the z-axis). (d)-(f): for the second target (two cubes with one edge in contact). (g)-(i): for the third target (two cubes along the y-axis).*

All of reconstruction results obtained above are apparently better than that obtained by the frequency-hopping approach, under the incomplete configuration. This is emphasized with the contrast error $\mathrm{Err}_\chi$. Here, we summarize $\mathrm{Err}_\chi$ into the table 8.1, for these three targets and for different inversion methods. All reported results correspond to the incomplete configuration. Best

| $\mathrm{Err}_\chi$ | Along $z$-axis | In contact | Along $y$-axis |
|---|---|---|---|
| FH | 354% | 141% | 287% |
| MF | 48% | 105% | 187% |
| WMF ($\alpha = 3$) | 54% | 47% | 62% |
| TI | 66% | 57% | 200% |

**Table 8.1 :** *Summarization of the contrast error, for three different targets and for different inversion methods. All of results are obtained under the incomplete configuration. FH: frequency-hopping approach. MF: multiple-frequency approach. WMF: weighted multiple-frequency approach by $\alpha = 3$. TI: time inversion method.*

reconstruction results are obtained with the weighted multiple-frequency approach ($\alpha = 3$). The 'superiority' of the weighted multiple-frequency method is due to the fact that the components of lower frequencies are conserved while for the transient inversion, lower frequency component of the scattered fields are almost dumped by the Gaussian pulse shape.

### 8.3.2 Two identical spheres in contact

We propose to reconstruct the fourth target (two identical spheres in contact) using transient data, always under the incomplete configuration. We have checked that the sampling frequency $\Delta f$ is fine enough to well represent the transient scattered field. We begin with $\Delta f = 0.25$ GHz which leads to $\Delta t = 4$ ns. The theoretical and experimental scattered fields in the frequency domain are then transformed into the time domain, respectively. In Fig. 8.13, we present these fields computed for the receiver at (−0.449 m, 0.778 m, 1.555 m).

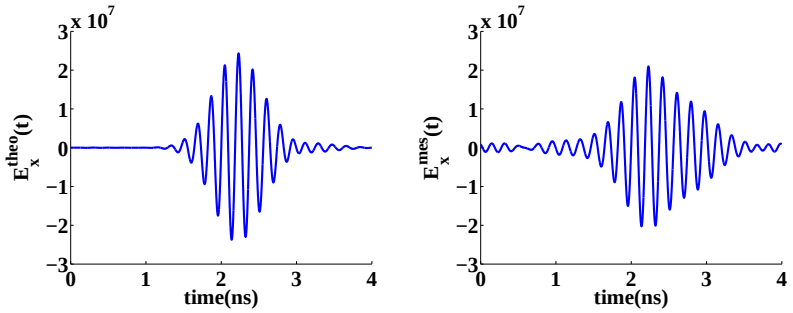


**Figure 8.13 :** *X component of the scattered field in the time domain for the receiver at (−0.449 m, 0.778 m, 1.555 m), for the two identical spheres in contact, with $\Delta t$=4 ns and $\Delta f$ = 0.25 GHz. (a) Theoretical calculated field. (b) Experimental field.*

We observe that components of experimental fields are different from the theoretical ones. It is not surprising that these two spheres can not be well reconstructed (not shown here). We compare these two fields in the frequency domain for each sampling frequency. The discrepancy between the theoretical and experimental fields is stronger at high frequencies than at low frequencies. In order to check that the unsatisfactory reconstruction are due, or not to the presence of the noise for high frequencies, we perform the inversion using synthetic data. The reconstruction result is not satisfactory. The size of spheres is relatively large with respect to the wavelengths at higher frequencies. This result is comprehensible as with the weighted multiple-frequency approach, under the incomplete configuration, the reconstruction is also disappointing. One possible solution to improve the result of the transient inversion for this specific target is to apply central-frequency-hopping approach[85,121]. The reconstruction procedure begins with a pulse centered at lower frequency, ranged for instance, from 3 GHz to 5.5 GHz. The final result is used as the initial estimate for the next reconstruction procedure, where the incident pulse is centered at higher frequency, ranged for instance, from 5.5 GHz to 8 GHz. Thus, we can take advantage of both lower frequencies and higher frequencies. Unfortunately, this approach could not be investigated using the available experimental data due to the rough frequency sampling.

## 8.4 Conclusions

In this chapter, we focused on the analysis of the performance of the transient inversion procedure, using synthetic data and experimental data. The transient data are transformed into the frequency

domain via a passage of Laplace transform. The time reversal focusing technique is studied for localizing one single scatterer and discriminating two independent scatterers. The transient inversion approach has been compared with the frequency-hopping procedure in presence of measured noise. We conclude that minimizing the measured data at all frequencies at the same time is more robust to the noise than minimizing them sequentially.

We have also tested the inversion methods using experimental data described in Chap. 7. The reconstruction results using the transient inversion method are not so good as that obtained by the weighted multiple-frequency approach, but clearly better than that obtained by the frequency-hopping approach.

# Conclusion

This thesis addresses the fundamental issue of imaging three-dimensional (3D) targets using electromagnetic waves. The imager principle consists in illuminating the target under various illuminations and processing the recorded scattered field with an appropriate inversion procedure (here the Hybrid Method, HM) in order to obtain the permittivity map of the object. The specificity of our approach is that all the possible information carried out by the scattered field by the target (phase, polarization and amplitude) are accounted for in the reconstruction procedure which is based on a rigorous modelling of the target-wave interaction.

We first studied, on simulated data, the localization and characterization of targets buried in a random inhomogeneous medium using an array of monochromatic micro-wave antennas. Taking advantage of the different polarizations directions of the emitting antenna and using the vectorial time reversal operator (DORT), we were able to synthesize several incident fields focusing selectively on each target. We developed a combined method, named HM-DORT, consisting in applying the inversion procedure (HM) to data obtained with the focusing DORT fields only. HM-DORT permitted to better localize and characterize the targets than the DORT technique alone. Moreover, it was shown to be significantly more efficient (both in terms of reconstruction quality and computation time) than applying the inversion method (HM) to the data obtained with the non-optimized fields radiated by the antennas. To improve the reconstruction in a half-space configuration (when the antenna array is placed above a half inhomogeneous space with an important dielectric contrast), we have implemented a HM-DORT frequency-hopping procedure taking advantage of multiple frequency data. Oscillations due to the fact that the numerical aperture is greatly reduced were eliminated. A resolution quasi-similar to that provided with the homogeneous background space configuration was obtained.

In a second part, we applied the vectorial inversion scheme (HM) and HM-DORT to experimental optical microscopy data provided by a specially built full-polarized tomographic diffractive microscope. The latter, which functioned in the reflection configuration, was able to record, within the numerical aperture of the objective, the intensity, the phase and the polarization state of the scattered field for any possible illumination. Targets to be observed consisted in sub-micronic resin cylinders deposited on a high reflective silicon substrate. We showed that for these weakly scattering objects, a transverse resolution about one-fourth of the wavelength is achieved. Note that this resolution is much better than that of all existing far field microscopes, and sets a landmark in the optical far field microscopy. We also stressed the interest of the HM-DORT for enhancing the signature of targets, and thus ameliorating the reconstruction of weak scatterers which may be otherwise blurred by that of more echogeneous objects.

In the last part of this thesis, we considered the imaging problem in the transient regime. This regime is mainly encountered in the microwave or radar domain in which the time response of a scene to an electromagnetic pulse can be recorded. We reformulated the inversion algorithm so

that all the frequency information contained in the time response are processed simultaneously. By adjusting the weighting coefficients in the multi-frequency cost function to be minimized, we were able to obtain a high resolution with a satisfactory stability. We showed on three-dimensional microwave experimental and simulated data that this technique is significantly more robust than the sequential frequency-hopping approach.

Perspectives of this work can be split in two parts, those concerning the use of the HM-DORT and those concerned with the transient regime.

We believe that the HM-DORT procedure is a very interesting tool for processing data of both the microwave and optical imaging domains especially when studying small localized objects. It diminishes the noise influence, ameliorates the reconstruction and significantly decreases the computational burden. In optical imaging, it could be used for improving the reconstruction of specific targets embedded in a distorting or noisy environment (such as the nucleus in a cell or inclusions in a dioptre with a rough interface). To check the performances of HM-DORT in presence of structural noise, we could start the study by inserting an aberrating layer between the target and the microscope objective[48]. Another challenge would be to apply HM-DORT to the mirror-imaging configuration developed previously by our team[98]. Indeed, it is expected that, in presence of a mirror, the DORT focusing fields will exhibit an isotropic intensity distribution (same width along the axial direction as in the transverse plane). One can thus consider to focus selectively on two targets distributed along the axial direction and to improve the axial resolution up to that in the transverse plane.

For imaging in the transient regime, the main perspective concerns the experimental validation and the applications. In this work we considered only multiple-frequency data obtained in a free-space configuration, in a controlled microwave experiment. We plan to extend the application of our transient reconstruction procedure to the optical domain. The data will be obtained at multiple frequencies with a super-continuum laser. The challenge will be to modify our inversion algorithm in order to account for the presence of an interface (targets being above or below the latter). Note that this development will be also required for addressing the important problem of detection and characterization of buried objects (such as water pipes) with a moving emitting/receiving microwave antenna. Last, and more fundamentally, we believe that studying the role of the dispersion in the transient imaging performance can be most interesting. This will require to introduce a model of the permittivity with respect to the frequency in the simulation of the data and to introduce additional parameters in the minimization of the cost function.

# Appendix

Appendix A

# Green's function

One approach to the solution of radiating problems is by means of vector potential $\boldsymbol{A}(\boldsymbol{r})$ and scalar potential $\phi(\boldsymbol{r})$ in an infinite vacuum space. The vector potential $\boldsymbol{A}(\boldsymbol{r})$ is defined as

$$\boldsymbol{B}(\boldsymbol{r}) = \mu_0 \boldsymbol{H}(\boldsymbol{r}) = \boldsymbol{\nabla} \times \boldsymbol{A}(\boldsymbol{r}). \tag{A.1}$$

$\boldsymbol{A}(\boldsymbol{r})$ is not uniquely determined, $\boldsymbol{A}'(\boldsymbol{r}) = \boldsymbol{A}(\boldsymbol{r}) + \boldsymbol{\nabla}\psi(\boldsymbol{r})$ (according to the gauge freedom),

$$\boldsymbol{\nabla} \times \boldsymbol{E}(\boldsymbol{r}) = i\omega\mu_0 \boldsymbol{H}(\boldsymbol{r}) = i\omega \boldsymbol{\nabla} \times \boldsymbol{A}(\boldsymbol{r}). \tag{A.2}$$

We have

$$\boldsymbol{E} = i\omega \boldsymbol{A}(\boldsymbol{r}) - \boldsymbol{\nabla}\phi(\boldsymbol{r}), \tag{A.3}$$

$$\boldsymbol{H}(\boldsymbol{r}) = \frac{1}{\mu_0} \boldsymbol{\nabla} \times \boldsymbol{A}(\boldsymbol{r}). \tag{A.4}$$

From the Maxwell equations (1.9), we can obtain a new equation associated to $\boldsymbol{A}(\boldsymbol{r})$ and $\boldsymbol{J}(\boldsymbol{r})$, where $\boldsymbol{J}(\boldsymbol{r})$ is the source distribution,

$$\boldsymbol{\nabla} \times \boldsymbol{\nabla} \times \boldsymbol{A}(\boldsymbol{r}) = -i\omega\mu_0\varepsilon_0 \boldsymbol{E}(\boldsymbol{r}) + \mu_0 \boldsymbol{J}(\boldsymbol{r}) = -i\omega\mu_0\varepsilon_0 \left[i\omega \boldsymbol{A}(\boldsymbol{r}) - \boldsymbol{\nabla}\phi(\boldsymbol{r})\right] + \mu_0 \boldsymbol{J}(\boldsymbol{r}). \tag{A.5}$$

The Lorenz gauge condition imposes

$$\boldsymbol{\nabla} \cdot \boldsymbol{A}(\boldsymbol{r}) = i\omega\mu_0\varepsilon_0 \phi(\boldsymbol{r}). \tag{A.6}$$

We also have the mathematical relationship equation as

$$\boldsymbol{\nabla} \times \boldsymbol{\nabla} \times \boldsymbol{A}(\boldsymbol{r}) = -\boldsymbol{\nabla}^2 \boldsymbol{A}(\boldsymbol{r}) + \boldsymbol{\nabla}[\boldsymbol{\nabla} \cdot \boldsymbol{A}(\boldsymbol{r})], \tag{A.7}$$

combining Eq. (A.7) together with the Lorenz gauge condition, we can rewrite Eq. (A.5) as

$$(\boldsymbol{\nabla}^2 + k_0^2)\boldsymbol{A}(\boldsymbol{r}) = -\mu_0 \boldsymbol{J}(\boldsymbol{r}). \tag{A.8}$$

## A.1 Scalar Green's function

We start with the deviation of the scalar Green's function $g(\boldsymbol{r}, \boldsymbol{r}')$, we replace the source $\mu_0 \boldsymbol{J}(\boldsymbol{r})$ in Eq. (A.8) by the point source $\delta(\boldsymbol{r} - \boldsymbol{r}')$

$$(\boldsymbol{\nabla}^2 + k_0^2) g(\boldsymbol{r}, \boldsymbol{r}') = -\delta(\boldsymbol{r} - \boldsymbol{r}'), \tag{A.9}$$

The scalar Green's function $g(\boldsymbol{r}, \boldsymbol{r}')$ is the response to point sources $\delta(\boldsymbol{r} - \boldsymbol{r}')$, and we can determine it in the spherical coordinate system. $g(\boldsymbol{r}, \boldsymbol{r}')$ depends on the relative position between observation point and source point, we can define a position vector $\boldsymbol{R} = \boldsymbol{r} - \boldsymbol{r}'$, with $R = |\boldsymbol{R}|$

$$(\boldsymbol{\nabla}^2 + k_0^2) g(\boldsymbol{R}) = -\delta(\boldsymbol{R}). \tag{A.10}$$

The solution of Eq. (A.10), $g(\boldsymbol{R})$ is spherically symmetric and independent of $\theta$ and $\phi$, it can be written as

$$\frac{1}{R}\frac{d^2}{dR^2}[Rg(\boldsymbol{R})] + k_0^2 g(\boldsymbol{R}) = -\delta(\boldsymbol{R}), \tag{A.11}$$

for $R \neq 0$, $\delta(\boldsymbol{R}) = 0$ and we have

$$\frac{d^2}{dR^2}[Rg(\boldsymbol{R})] + k_0^2 Rg(\boldsymbol{R}) = 0. \tag{A.12}$$

The solution of Eq. (A.12) must be an outgoing wave, and we have the scalar Green's function reads as

$$g(\boldsymbol{R}) = \frac{e^{ikR}}{4\pi R}. \tag{A.13}$$

## A.2 Dyadic Green's function

Beginning from the scalar Green's function, we deduce the dyadic Green function. A vectorial current source $\boldsymbol{J}$ leads to an electric field $\boldsymbol{E}$ with three components, $E_x$, $E_y$ and $E_z$. In this case, the Green's function must be a tensor that relates all components of the source with all components of the field, denoted as dyadic Green's function.

To determine the dyadic Green's function, we start with Eq. (1.16) given above. The first column of the tensor $\boldsymbol{G}$ corresponds to the field due to a point source in $x$-direction, the second column is the field due to a point source in $y$-direction, and the third column is the field due to a pint source in $z$-direction. Using the relation $\boldsymbol{\nabla} \cdot (\boldsymbol{\nabla} \times) = 0$, the divergence of Eq. (1.16) leads to

$$-k_0^2 \boldsymbol{\nabla} \boldsymbol{G}(\boldsymbol{r}, \boldsymbol{r}') = \boldsymbol{\nabla} \boldsymbol{I} \delta(\boldsymbol{r} - \boldsymbol{r}'). \tag{A.14}$$

According to $\boldsymbol{\nabla} \times \boldsymbol{\nabla} \times \boldsymbol{G}(\boldsymbol{r}, \boldsymbol{r}') = \boldsymbol{\nabla} [\boldsymbol{\nabla} \boldsymbol{G}(\boldsymbol{r}, \boldsymbol{r}')] - \boldsymbol{\nabla}^2 \boldsymbol{G}(\boldsymbol{r}, \boldsymbol{r}')$, combining Eqs. (1.16) and (A.14), we get

$$-\boldsymbol{\nabla}^2 \boldsymbol{G}(\boldsymbol{r}, \boldsymbol{r}') + \boldsymbol{\nabla} [\boldsymbol{\nabla} \boldsymbol{G}(\boldsymbol{r}, \boldsymbol{r}')] - k_0^2 \boldsymbol{G}(\boldsymbol{r}, \boldsymbol{r}') = \boldsymbol{I} \delta(\boldsymbol{r} - \boldsymbol{r}'), \tag{A.15}$$

$$(\boldsymbol{\nabla}^2 + k_0^2) \boldsymbol{G}(\boldsymbol{r}, \boldsymbol{r}') = -\left(\frac{1}{k_0^2} \boldsymbol{\nabla} \boldsymbol{\nabla} + \boldsymbol{I}\right) \delta(\boldsymbol{r} - \boldsymbol{r}'). \tag{A.16}$$

Using Eq. (A.9), we replace the $\delta$ function in Eq. (A.16),

$$\left(\boldsymbol{\nabla}^2 + k_0^2\right) \boldsymbol{G}(\boldsymbol{r}, \boldsymbol{r}') = \left(\frac{1}{k_0^2} \boldsymbol{\nabla} \boldsymbol{\nabla} + \boldsymbol{I}\right) (\boldsymbol{\nabla}^2 + k_0^2) g(\boldsymbol{r} - \boldsymbol{r}'), \tag{A.17}$$

$$(\boldsymbol{\nabla}^2 + k_0^2) \left[\boldsymbol{G}(\boldsymbol{r}, \boldsymbol{r}') - \left(\frac{1}{k_0^2} \boldsymbol{\nabla} \boldsymbol{\nabla} + \boldsymbol{I}\right) g(\boldsymbol{r}, \boldsymbol{r}')\right] = 0. \tag{A.18}$$

Hence a possible expression of the dyadic Green's function is

$$\boldsymbol{G}(\boldsymbol{r}, \boldsymbol{r}') = \left[\boldsymbol{I} + \frac{1}{k_0^2} \boldsymbol{\nabla} \boldsymbol{\nabla}\right] g(\boldsymbol{r}, \boldsymbol{r}'), \tag{A.19}$$

where the operator $\boldsymbol{\nabla} \boldsymbol{\nabla}$ is a dyadic operator

$$\boldsymbol{\nabla} \boldsymbol{\nabla} = \begin{vmatrix} \frac{\partial}{\partial x}\frac{\partial}{\partial x} & \frac{\partial}{\partial x}\frac{\partial}{\partial y} & \frac{\partial}{\partial x}\frac{\partial}{\partial z} \\ \frac{\partial}{\partial y}\frac{\partial}{\partial x} & \frac{\partial}{\partial y}\frac{\partial}{\partial y} & \frac{\partial}{\partial y}\frac{\partial}{\partial z} \\ \frac{\partial}{\partial z}\frac{\partial}{\partial x} & \frac{\partial}{\partial z}\frac{\partial}{\partial y} & \frac{\partial}{\partial z}\frac{\partial}{\partial z} \end{vmatrix}. \tag{A.20}$$

For the sake of computation simplicity, we replace $x$, $y$, $z$ components by two variables $\alpha$, $\beta$, where $\alpha$ and $\beta$ are either $x - x'$ or $y - y'$ or $z - z'$,

$$\frac{\partial R}{\partial \alpha} = \frac{\alpha}{R}, \tag{A.21}$$

$$\frac{\partial(\frac{\alpha}{R})}{\partial \beta} = -\frac{\alpha\beta}{R^3} + \frac{\delta_{\alpha\beta}}{R}. \tag{A.22}$$

Substituting Eqs. (A.21) and (A.22) into Eq. (A.19), we can get a final solution for the Green function in homogeneous space

$$\boldsymbol{G}(\boldsymbol{r},\boldsymbol{r}') = \frac{e^{ik_0R}}{4\pi k_0^2}\left[(3\widehat{\boldsymbol{R}}\otimes\widehat{\boldsymbol{R}}-\boldsymbol{I})\left(\frac{1}{R^3}-\frac{ik_0}{R^2}\right)+(\boldsymbol{I}-\widehat{\boldsymbol{R}}\otimes\widehat{\boldsymbol{R}})\frac{k_0^2}{R}\right]. \tag{A.23}$$

where $\widehat{\boldsymbol{R}} = \boldsymbol{R}/R$.

Appendix B

# Conjugate gradient method for solving the self-consistent equation

Equation (1.33) is a self-consistent equation, represented as

$$(\boldsymbol{I} - \boldsymbol{G}\alpha^0)\boldsymbol{E}^{\mathrm{loc}} = \boldsymbol{E}^{\mathrm{inc}}. \tag{B.1}$$

To get the solution of $\boldsymbol{E}^{\mathrm{loc}}$, this equation is simplified as

$$\boldsymbol{A}\boldsymbol{x} = \boldsymbol{b}, \tag{B.2}$$

where $\boldsymbol{x}$ is an unknown vector, $\boldsymbol{b}$ is a known vector, $\boldsymbol{A}$ is a known matrix. The solution of Eq. (B.2) is given by

$$\boldsymbol{x} = \boldsymbol{A}^{-1}\boldsymbol{b}, \tag{B.3}$$

Where $\boldsymbol{A}^{-1}$ represents the inverse of the matrix $\boldsymbol{A}$. In the case of a large scattering domain or a thin discretization, the number of the subunits $N$ becomes large and the computation of $\boldsymbol{A}^{-1}$ will be time-consuming. In order to accelerate our computation, we propose to use one of the most popular iterative methods, the conjugate gradient method[57,81,122] to get $\boldsymbol{x}$ nearest to the exact solution of Eq. (B.2). We minimize a function defined as

$$F_{\mathrm{cgm}} = \frac{\|\boldsymbol{A}\boldsymbol{x}_n - \boldsymbol{b}\|^2}{\|\boldsymbol{b}\|^2}, \tag{B.4}$$

Beginning from an initial guess $\boldsymbol{x}_i$, which can be equal to zero or a rough estimate of the value of $\boldsymbol{x}$. In our case the initial guess is often the incident field. The final solution can be obtained by series of iterative procedures $n$

$$\boldsymbol{x}_n = \boldsymbol{x}_{n-1} + \alpha_n \boldsymbol{d}_n, \tag{B.5}$$

where $\alpha_n$ is the scalar weight chosen at each iteration step $n$, by minimizing the function $F_{\mathrm{cgm}}$, with respect to $\boldsymbol{x}_n$. $\boldsymbol{d}_n$ is chosen as the conjugate gradient direction. $\boldsymbol{x}_n$ is updated iteratively until the value of $F_{\mathrm{cgm}}$ reaches the tolerance that we set.

Appendix C

# Gradient calculation for the cost functional

## C.1 Definition of the gradient of a functional

To define the gradient of a functional, we need to give the definition of the directional derivative of a functional $F$ of the variable $x$ in the space $\Omega$. The directional derivative of $F$ along the direction $u$ is defined as

$$D_x F(u) = \lim_{t \to 0} \frac{F(x+tu) - F(x)}{t}. \tag{C.1}$$

The gradient of $F$ with respect to $x$ is defined as

$$g_x = \arg\max_u (D_x F(u) | \|u\| = 1). \tag{C.2}$$

## C.2 Gradients for HM in the time-harmonic regime

First, we give the gradients used in the HM described in Sec. 2.2.4, derived from the cost functional

$$\begin{aligned} F(\chi, \boldsymbol{E}_1, \cdots, \boldsymbol{E}_N) &= F(\chi, \boldsymbol{E}_\bullet) \\ &= W_\Gamma \sum_{l=1}^{N} \|\boldsymbol{f}_l^{\mathrm{mes}} - \overline{\overline{\boldsymbol{B}}} \chi \boldsymbol{E}_l\|_\Gamma^2 + W_\Omega \sum_{l=1}^{N} \|\boldsymbol{E}_l^{\mathrm{inc}} + \overline{\overline{\boldsymbol{A}}} \chi \boldsymbol{E}_l - \boldsymbol{E}_l\|_\Omega^2, \end{aligned} \tag{C.3}$$

where $g_\chi$ is the gradient of $F(\chi, \boldsymbol{E}_l)$ with respect to $\chi$ assuming that $\boldsymbol{E}_l$ do not change,

$$g_\chi = \arg\max_u (D_\chi F(u) | \|u\| = 1) \qquad \text{for} \tag{C.4}$$

$$D_\chi F(u) = \lim_{t \to 0} \frac{F(\chi + tu, \boldsymbol{E}_l) - F(\chi, \boldsymbol{E}_l)}{t}. \tag{C.5}$$

$F(\chi + tu, \boldsymbol{E}_\bullet)$ can be expanded as

$$\begin{aligned} F(\chi + tu, \boldsymbol{E}_\bullet) = W_\Gamma \sum_{l=1}^{N} \|\boldsymbol{f}_l^{\mathrm{mes}} - \overline{\overline{\boldsymbol{B}}}(\chi + tu) \boldsymbol{E}_l\|_\Gamma^2 \\ + W_\Omega \sum_{l=1}^{N} \|\boldsymbol{E}_l^{\mathrm{inc}} + \overline{\overline{\boldsymbol{A}}}(\chi + tu) \boldsymbol{E}_l - \boldsymbol{E}_l\|_\Omega^2. \end{aligned} \tag{C.6}$$

For the sake of simplicity, we define here two residue errors for each illumination $l$

$$\boldsymbol{h}_l^{(1)} = \boldsymbol{E}_l^{\text{inc}} + \overline{\overline{\boldsymbol{A}}}\chi\boldsymbol{E}_l - \boldsymbol{E}_l, \tag{C.7}$$

$$\boldsymbol{h}_l^{(2)} = \boldsymbol{f}_l^{\text{mes}} - \overline{\overline{\boldsymbol{B}}}\chi\boldsymbol{E}_l, \tag{C.8}$$

$F(\chi + tu, \boldsymbol{E}_\cdot)$ can be rewritten as

$$\begin{aligned} F(\chi + tu, \boldsymbol{E}_\cdot) &= W_\Gamma \sum_{l=1}^{N} \|\boldsymbol{h}_l^{(2)} - t\overline{\overline{\boldsymbol{B}}}u\boldsymbol{E}_l\|_\Gamma^2 + W_\Omega \sum_{l=1}^{N} \|\boldsymbol{h}_l^{(1)} + t\overline{\overline{\boldsymbol{A}}}u\boldsymbol{E}_l\|_\Omega^2, \\ &= F(\chi, \boldsymbol{E}_l) - 2t\sum_{l=1}^{N} W_\Gamma \text{Re}\left\langle \boldsymbol{h}_l^{(2)}, \overline{\overline{\boldsymbol{B}}}u\boldsymbol{E}_l \right\rangle_\Gamma \\ &+ 2t\sum_{l=1}^{N} W_\Omega \text{Re}\left\langle \boldsymbol{h}_l^{(1)}, \overline{\overline{\boldsymbol{A}}}u\boldsymbol{E}_l \right\rangle_\Omega + O(t^2). \end{aligned}$$

Thus, the directional derivative $D_\chi F(u)$ is

$$\begin{aligned} D_\chi F(u) &= -2\sum_{l=1}^{N} W_\Gamma \text{Re}\left\langle \boldsymbol{h}_l^{(2)}, \overline{\overline{\boldsymbol{B}}}u\boldsymbol{E}_l \right\rangle_\Gamma + 2\sum_{l=1}^{N} W_\Omega \text{Re}\left\langle \boldsymbol{h}_l^{(1)}, \overline{\overline{\boldsymbol{A}}}u\boldsymbol{E}_l \right\rangle_\Omega, \\ &= -2\sum_{l=1}^{N} W_\Gamma \text{Re}\left\langle \overline{\overline{\boldsymbol{B}}}^{\dagger}\boldsymbol{h}_l^{(2)}, u\boldsymbol{E}_l \right\rangle_\Gamma + 2\sum_{l=1}^{N} W_\Omega \text{Re}\left\langle \overline{\overline{\boldsymbol{A}}}^{\dagger}\boldsymbol{h}_l^{(1)}, u\boldsymbol{E}_l \right\rangle_\Omega, \end{aligned}$$

with $\overline{\overline{\boldsymbol{A}}}^{\dagger}$ and $\overline{\overline{\boldsymbol{B}}}^{\dagger}$ are the adjoint operators of $\overline{\overline{\boldsymbol{A}}}$ and $\overline{\overline{\boldsymbol{B}}}$, respectively. $u$ is a scalar function while $\boldsymbol{E}_l$ is vectorial one.

Note that,

$$\begin{aligned} \left\langle \overline{\overline{\boldsymbol{B}}}^{\dagger}\boldsymbol{h}_l^{(2)}, u\boldsymbol{E}_l \right\rangle_\Gamma &= \int_\Gamma \overline{(\boldsymbol{B}^\dagger \boldsymbol{h}_l^{(2)})}(u\boldsymbol{E}_l)\mathrm{d}\boldsymbol{r}, \\ &= \int_\Gamma \overline{(\bar{\boldsymbol{E}}_l \overline{\overline{\boldsymbol{B}}}^{\dagger}\boldsymbol{h}_l^{(2)})}u\mathrm{d}\boldsymbol{r}, \\ &= \left\langle \bar{\boldsymbol{E}}_l \overline{\overline{\boldsymbol{B}}}^{\dagger}\boldsymbol{h}_l^{(2)}, u \right\rangle_\Gamma, \end{aligned}$$

where the overbar denotes the complex conjugation. Now,

$$\begin{aligned} D_\chi F(u) &= -2\sum_{l=1}^{N} W_\Gamma \text{Re}\left\langle \bar{\boldsymbol{E}}_l \overline{\overline{\boldsymbol{B}}}^{\dagger}\boldsymbol{h}_l^{(2)}, u \right\rangle_\Gamma + 2\sum_{l=1}^{N} W_\Omega \text{Re}\left\langle \bar{\boldsymbol{E}}_l \overline{\overline{\boldsymbol{A}}}^{\dagger}\boldsymbol{h}_l^{(1)}, u \right\rangle_\Omega, \\ &= -2\text{Re}\left\langle W_\Gamma \sum_{l=1}^{N} \bar{\boldsymbol{E}}_l \overline{\overline{\boldsymbol{B}}}^{\dagger}\boldsymbol{h}_l^{(2)} - W_\Omega \sum_{l=1}^{N} \bar{\boldsymbol{E}}_l \overline{\overline{\boldsymbol{A}}}^{\dagger}\boldsymbol{h}_l^{(1)}, u \right\rangle. \end{aligned}$$

Thus, we can finally get the gradient

$$g_\chi = -W_\Gamma \sum_{l=1}^{N} \bar{\boldsymbol{E}}_l \overline{\overline{\boldsymbol{B}}}^{\dagger}\boldsymbol{h}_l^{(2)} + W_\Omega \sum_{l=1}^{N} \bar{\boldsymbol{E}}_l \overline{\overline{\boldsymbol{A}}}^{\dagger}\boldsymbol{h}_l^{(1)}. \tag{C.9}$$

The positivity of $\chi$ is realized by retrieving two real auxiliary functions $\xi$ and $\eta$ instead of the complex valued $\chi$

$$\chi = \xi^2 + i\eta^2. \tag{C.10}$$

The gradients of these two real functions can be given as

$$g_\xi = g_\chi \frac{\partial \chi}{\partial \xi}, \tag{C.11}$$

$$g_\eta = g_\chi \frac{\partial \chi}{\partial \eta}, \tag{C.12}$$

we can get the gradient with respect to $\xi$ and $\eta$ as

$$g_\xi = -2\mathrm{Re}\left( W_\Gamma \sum_{l=1}^{N} \bar{\boldsymbol{E}}_l \bar{\overline{\boldsymbol{B}}}^{\dagger} \boldsymbol{h}_l^{(2)} - W_\Omega \sum_{l=1}^{N} \bar{\boldsymbol{E}}_l \bar{\overline{\boldsymbol{A}}}^{\dagger} \boldsymbol{h}_l^{(1)} \right), \tag{C.13}$$

$$g_\eta = -2\mathrm{Im}\left( W_\Gamma \sum_{l=1}^{N} \bar{\boldsymbol{E}}_l \bar{\overline{\boldsymbol{B}}}^{\dagger} \boldsymbol{h}_l^{(2)} - W_\Omega \sum_{l=1}^{N} \bar{\boldsymbol{E}}_l \bar{\overline{\boldsymbol{A}}}^{\dagger} \boldsymbol{h}_l^{(1)} \right). \tag{C.14}$$

Now, in order to get the gradient of $F(\chi, \boldsymbol{E}_l)$ with respect to the total field $\boldsymbol{E}_l$, we assume that $\chi$ and total fields $(\boldsymbol{E}_m)_{m=1,\cdots,N,m\neq l}$ do not change. We can write

$$g_{\boldsymbol{E}_l} = \arg\max_{\boldsymbol{u}} (D_{\boldsymbol{E}_l} F(\boldsymbol{u}) | \|\boldsymbol{u}\| = 1) \qquad \text{for} \tag{C.15}$$

$$D_{\boldsymbol{E}_l} F(\boldsymbol{u}) = \lim_{t\to 0} \frac{F\left(\chi, \boldsymbol{E}_l + t\boldsymbol{u}, (\boldsymbol{E}_m)_{m=1,\cdots,N,m\neq l}\right) - F\left(\chi, (\boldsymbol{E}_m)_{m=1,\cdots,N}\right)}{t}, \tag{C.16}$$

and $F\left[\chi, \boldsymbol{E}_l + t\boldsymbol{u}, (\boldsymbol{E}_m)_{m=1,\cdots,N,m\neq l}\right]$ can be expanded as

$$\begin{aligned}
F\left[\chi, \boldsymbol{E}_l + t\boldsymbol{u}, (\boldsymbol{E}_m)_{m=1,\cdots,N,m\neq l}\right] &= W_\Gamma \sum_{\substack{m=1\\m\neq l}}^{N} \|\boldsymbol{h}_m^{(2)}\|_\Gamma^2 + W_\Omega \sum_{\substack{m=1\\m\neq l}}^{N} \|\boldsymbol{h}_m^{(1)}\|_\Omega^2 \\
&+ W_\Gamma \|\boldsymbol{f}_l - \bar{\overline{\boldsymbol{B}}}\chi \boldsymbol{E}_l - t\bar{\overline{\boldsymbol{B}}}\boldsymbol{u}\chi\|_\Gamma^2 \\
&+ W_\Omega \|\boldsymbol{E}_l^{\mathrm{inc}} + \bar{\overline{\boldsymbol{A}}}\chi \boldsymbol{E}_l - \boldsymbol{E}_l - t\boldsymbol{u} + t\bar{\overline{\boldsymbol{A}}}\boldsymbol{u}\chi\|_\Omega^2, \\
&= W_\Gamma \sum_{\substack{m=1\\m\neq l}}^{N} \|\boldsymbol{h}_m^{(2)}\|_\Gamma^2 + W_\Omega \sum_{\substack{m=1\\m\neq l}}^{N} \|\boldsymbol{h}_m^{(1)}\|_\Omega^2 \\
&+ W_\Gamma \|\boldsymbol{h}_l^{(2)} - t\bar{\overline{\boldsymbol{B}}}\boldsymbol{u}\chi\|_\Gamma^2 + W_\Omega \|\boldsymbol{h}_l^{(1)} + t\bar{\overline{\boldsymbol{A}}}\boldsymbol{u}\chi - t\boldsymbol{u}\|_\Omega^2, \\
&= F(\chi, (\boldsymbol{E}_m)_{m=1,\cdots,N}) - 2tW_\Gamma \mathrm{Re}\left\langle \boldsymbol{h}_l^{(2)}, \bar{\overline{\boldsymbol{B}}}\boldsymbol{u}\chi\boldsymbol{u} \right\rangle_\Omega \\
&+ 2tW_\Omega \mathrm{Re}\left\langle \boldsymbol{h}_l^{(1)}, \bar{\overline{\boldsymbol{A}}}\chi\boldsymbol{u} - \boldsymbol{u} \right\rangle_\Gamma + O(t^2).
\end{aligned}$$

Thus, the directional derivative $D_{\boldsymbol{E}_l} F(\boldsymbol{u})$ is

$$\begin{aligned}
D_{\boldsymbol{E}_l} F(\boldsymbol{u}) &= -2W_\Gamma \mathrm{Re}\left\langle \boldsymbol{h}_l^{(2)}, \bar{\overline{\boldsymbol{B}}}\boldsymbol{u}\chi \right\rangle_\Omega + 2W_\Omega \mathrm{Re}\left\langle \boldsymbol{h}_l^{(1)}, \bar{\overline{\boldsymbol{A}}}\chi\boldsymbol{u} - \boldsymbol{u} \right\rangle_\Gamma, \\
&= -2W_\Gamma \mathrm{Re}\left\langle \bar{\chi}\bar{\overline{\boldsymbol{B}}}^{\dagger} \boldsymbol{h}_l^{(2)}, \boldsymbol{u} \right\rangle_\Omega + 2W_\Omega \mathrm{Re}\left\langle \bar{\chi}\bar{\overline{\boldsymbol{A}}}^{\dagger} \boldsymbol{h}_l^{(1)} - \boldsymbol{h}_l^{(1)}, \boldsymbol{u} \right\rangle_\Gamma, \\
&= 2\mathrm{Re}\left\langle -W_\Gamma \bar{\chi}\bar{\overline{\boldsymbol{B}}}^{\dagger} \boldsymbol{h}_l^{(2)} + W_\Omega \left( \bar{\chi}\bar{\overline{\boldsymbol{A}}}^{\dagger} \boldsymbol{h}_l^{(1)} - \boldsymbol{h}_l^{(1)} \right), \boldsymbol{u} \right\rangle.
\end{aligned}$$

We can finally have the descending direction with respect to $\boldsymbol{E}_l$ as

$$g_{\boldsymbol{E}_l} = -W_\Gamma \bar{\chi}\bar{\overline{\boldsymbol{B}}}^{\dagger} \boldsymbol{h}_l^{(2)} + W_\Omega \left( \bar{\chi}\bar{\overline{\boldsymbol{A}}}^{\dagger} \boldsymbol{h}_l^{(1)} - \boldsymbol{h}_l^{(1)} \right). \tag{C.17}$$

## C.3 Gradients for weighted multiple-frequency method

We rewrite the cost functional with the frequency-weighted coefficient

$$\tilde{F}(\chi, \boldsymbol{E}_{\cdot,\cdot}) = \tilde{W}_\Gamma \sum_{l=1}^{N}\sum_{p=1}^{P}(1/f_p)^\alpha \|\boldsymbol{h}_{l,p}^{(2)}\|_\Gamma^2 + \tilde{W}_\Omega \sum_{l=1}^{N}\sum_{p=1}^{P}(1/f_p)^\alpha \|\boldsymbol{h}_{l,p}^{(1)}\|_\Omega^2. \tag{C.18}$$

We first calculate the gradient $\tilde{g}_\chi$ with respect to the contrast, defined as

$$\tilde{g}_\chi = \arg\max_u (D_\chi \tilde{F}(u) | \|u\| = 1) \qquad \text{for} \tag{C.19}$$

$$D_\chi \tilde{F}(u) = \lim_{t\to 0} \frac{\tilde{F}(\chi + tu, \boldsymbol{E}_{l,p}) - \tilde{F}(\chi, \boldsymbol{E}_{l,p})}{t}, \tag{C.20}$$

where $\tilde{F}(\chi + tu, \boldsymbol{E}_\cdot)$ can be expanded as

$$\begin{aligned}\tilde{F}(\chi + tu, \boldsymbol{E}_\cdot) = {} & \tilde{W}_\Gamma \sum_{p=1}^{P}(1/f_p)^\alpha \sum_{l=1}^{N} \|\boldsymbol{f}_{l,p}^{\text{mes}} - \overline{\overline{\boldsymbol{B}}}(\chi + tu)\boldsymbol{E}_{l,p}\|_\Gamma^2 \\ & + \tilde{W}_\Omega \sum_{p=1}^{P}(1/f_p)^\alpha \sum_{l=1}^{N} \|\boldsymbol{E}_{l,p}^{\text{inc}} + \overline{\overline{\boldsymbol{A}}}(\chi + tu)\boldsymbol{E}_{l,p} - \boldsymbol{E}_{l,p}\|_\Omega^2.\end{aligned} \tag{C.21}$$

We substitute the residue error in Eq. (C.21) with $\boldsymbol{h}_{l,p}^{(1)}$ and $\boldsymbol{h}_{l,p}^{(2)}$ and we get

$$\begin{aligned}\tilde{F}(\chi + tu, \boldsymbol{E}_{\cdot,\cdot}) = {} & \tilde{W}_\Gamma \sum_{p=1}^{P}(1/f_p)^\alpha \sum_{l=1}^{N} \|\boldsymbol{h}_{l,p}^{(2)} - t\overline{\overline{\boldsymbol{B}}}u\boldsymbol{E}_{l,p}\|_\Gamma^2 \\ & + \tilde{W}_\Omega \sum_{p=1}^{P}(1/f_p)^\alpha \sum_{l=1}^{N} \|\boldsymbol{h}_{l,p}^{(1)} + t\overline{\overline{\boldsymbol{A}}}u\boldsymbol{E}_{l,p}\|_\Omega^2, \\ = {} & \tilde{F}(\chi, \boldsymbol{E}_{l,p}) - 2t\tilde{W}_\Gamma \sum_{p=1}^{P}(1/f_p)^\alpha \sum_{l=1}^{N} \text{Re}\left\langle \boldsymbol{h}_{l,p}^{(2)}, \overline{\overline{\boldsymbol{B}}}u\boldsymbol{E}_{l,p} \right\rangle_\Gamma \\ & + 2t\tilde{W}_\Omega \sum_{p=1}^{P}(1/f_p)^\alpha \sum_{l=1}^{N} \text{Re}\left\langle \boldsymbol{h}_{l,p}^{(1)}, \overline{\overline{\boldsymbol{A}}}u\boldsymbol{E}_{l,p} \right\rangle_\Omega + O(t^2).\end{aligned}$$

Similarly to the derivation procedure in Sec. C.2, we can finally get the gradient with respect to $\xi$ and $\eta$ with the frequency-weighted factor as

$$\tilde{g}_\xi = -2\text{Re}\left[\tilde{W}_\Gamma \sum_{p=1}^{P}(1/f_p)^\alpha \sum_{l=1}^{N} \bar{\boldsymbol{E}}_{l,p}\overline{\overline{\boldsymbol{B}}}^\dagger \boldsymbol{h}_{l,p}^{(2)} - \tilde{W}_\Omega \sum_{p=1}^{P}(1/f_p)^\alpha \sum_{l=1}^{N} \bar{\boldsymbol{E}}_{l,p}\overline{\overline{\boldsymbol{A}}}^\dagger \boldsymbol{h}_{l,p}^{(1)}\right], \tag{C.22}$$

$$\tilde{g}_\eta = -2\text{Im}\left[\tilde{W}_\Gamma \sum_{p=1}^{P}(1/f_p)^\alpha \sum_{l=1}^{N} \bar{\boldsymbol{E}}_{l,p}\overline{\overline{\boldsymbol{B}}}^\dagger \boldsymbol{h}_{l,p}^{(2)} - \tilde{W}_\Omega \sum_{p=1}^{P}(1/f_p)^\alpha \sum_{l=1}^{N} \bar{\boldsymbol{E}}_{l,p}\overline{\overline{\boldsymbol{A}}}^\dagger \boldsymbol{h}_{l,p}^{(1)}\right]. \tag{C.23}$$

Now, in order to get the gradient of $F(\chi, \boldsymbol{E}_{\cdot,\cdot})$ with respect to the total field $\boldsymbol{E}_{l,p}$, we assume that $\chi$ and total fields $(\boldsymbol{E}_{m,n})_{\binom{m=1,\cdots,N,m\neq l}{n=1,\cdots,P,n\neq p}}$ do not change. Then, we can write

$$g_{\boldsymbol{E}_{l,p}} = \arg\max_{\boldsymbol{u}} (D_{\boldsymbol{E}_{l,p}} F(\boldsymbol{u}) | \|\boldsymbol{u}\| = 1) \qquad \text{for} \tag{C.24}$$

$$D_{\boldsymbol{E}_{l,p}} F(\boldsymbol{u}) = \lim_{t\to 0} \frac{F\left[\chi, \boldsymbol{E}_{l,p} + t\boldsymbol{u}, (\boldsymbol{E}_{m,n})_{\binom{m=1,\cdots,N,m\neq l}{n=1,\cdots,P,n\neq p}}\right] - F\left[\chi, (\boldsymbol{E}_{m,n})_{\binom{m=1,\cdots,N}{n=1,\cdots,P}}\right]}{t}. \tag{C.25}$$

$F\left[\chi, \boldsymbol{E}_{l,p}+t\boldsymbol{u}, (\boldsymbol{E}_{m,n})_{\substack{m=1,\cdots,N,m\neq l\\ n=1,\cdots,P,n\neq p}}\right]$ can be expanded as

$$
\begin{aligned}
F\left[\chi, \boldsymbol{E}_{l,p}+t\boldsymbol{u}, (\boldsymbol{E}_{m,n})_{\substack{m=1,\cdots,N,m\neq l\\ n=1,\cdots,P,n\neq p}}\right] &= \tilde{W}_\Gamma \sum_{\substack{n=1\\ n\neq p}}^{P} (1/f_n)^\alpha \sum_{\substack{m=1\\ m\neq l}}^{N} \|\boldsymbol{h}_{m,n}^{(2)}\|_\Gamma^2 \\
&+ \tilde{W}_\Omega \sum_{\substack{n=1\\ n\neq p}}^{P} (1/f_n)^\alpha \sum_{\substack{m=1\\ m\neq l}}^{N} \|\boldsymbol{h}_{m,n}^{(1)}\|_\Omega^2 \\
&+ \tilde{W}_\Gamma (1/f_p)^\alpha \|\boldsymbol{f}_{l,p}^{\mathrm{mes}} - \chi \boldsymbol{E}_{l,p} - t\overline{\overline{\boldsymbol{B}}}\chi\boldsymbol{u}\|_\Gamma^2 \\
&+ \tilde{W}_\Omega (1/f_p)^\alpha \|\boldsymbol{E}_{l,p}^{\mathrm{inc}} + \overline{\overline{\boldsymbol{A}}}\chi\boldsymbol{E}_{l,p} - \boldsymbol{E}_{l,p} - t\boldsymbol{u} + t\overline{\overline{\boldsymbol{A}}}\chi\boldsymbol{u}\|_\Omega^2, \\
&= \tilde{W}_\Gamma \sum_{\substack{n=1\\ n\neq p}}^{P} (1/f_n)^\alpha \sum_{\substack{m=1\\ m\neq l}}^{N} \|\boldsymbol{h}_{m,n}^{(2)}\|_\Gamma^2 \\
&+ \tilde{W}_\Omega \sum_{\substack{n=1\\ n\neq p}}^{P} (1/f_n)^\alpha \sum_{\substack{m=1\\ m\neq l}}^{N} \|\boldsymbol{h}_{m,n}^{(1)}\|_\Omega^2 \\
&+ \tilde{W}_\Gamma (1/f_p)^\alpha \|\boldsymbol{h}_{l,p}^{(2)} - t\overline{\overline{\boldsymbol{B}}}\chi\boldsymbol{u}\|_\Gamma^2 \\
&+ \tilde{W}_\Omega (1/f_p)^\alpha \|\boldsymbol{h}_{l,p}^{(1)} + t\overline{\overline{\boldsymbol{A}}}\chi\boldsymbol{u} - t\boldsymbol{u}\|_\Omega^2, \\
&= F\left[\chi, (\boldsymbol{E}_{m,n})_{\substack{m=1,\cdots,N\\ n=1,\cdots,P}}\right] - 2t\tilde{W}_\Gamma (1/f_p)^\alpha \mathrm{Re}\left\langle \boldsymbol{h}_{l,p}^{(2)}, \overline{\overline{\boldsymbol{B}}}\chi\boldsymbol{u}\right\rangle_\Omega \\
&+ 2t\tilde{W}_\Omega (1/f_p)^\alpha \mathrm{Re}\left\langle \boldsymbol{h}_{l,p}^{(1)}, \overline{\overline{\boldsymbol{A}}}\chi\boldsymbol{u} - \boldsymbol{u}\right\rangle_\Gamma + O(t^2),
\end{aligned}
$$

we finally have the descending direction with respect to $\boldsymbol{E}_{l,p}$ as

$$
\tilde{g}_{\boldsymbol{E}_{l,p}} = -\tilde{W}_\Gamma (1/f_p)^\alpha \bar{\chi}\overline{\overline{\boldsymbol{B}}}^{\dagger}\boldsymbol{h}_{l,p}^{(2)} + \tilde{W}_\Omega (1/f_p)^\alpha \left(\bar{\chi}\overline{\overline{\boldsymbol{A}}}^{\dagger}\boldsymbol{h}_{l,p}^{(1)} - \boldsymbol{h}_{l,p}^{(1)}\right). \tag{C.26}
$$

Appendix D

# Linear combination of eigenvectors for selective focalization

Suppose that $\boldsymbol{V}_l(\zeta)$ is the $l$-th, component of TRO associated to the $\zeta$-th eigenvalue. We use $\boldsymbol{V}_l(\zeta)$ as the new complex currents of antennas, the corresponding backpropagated focusing field is noted as $\boldsymbol{E}_{\zeta}^{\text{inc;DORT}}(\boldsymbol{r})$, $\boldsymbol{r}$ is the position vector inside the scattering domain $W$. In degenerate cases, each eigenvector generates a wave focusing on $M$ scatterers at the same time, where $\boldsymbol{r}_j$ $(j = 1, 2, \cdots, M)$ denotes the center of each scatterer. The problem is to generate a new eigenvector focusing exclusively on one scatterer, through an appropriate linear combination of these eigenvectors. A new eigenvector $\boldsymbol{V}_l^{\text{new}}(\boldsymbol{r}_j)$ corresponding to scatterer $j$ can be generated by interpolating an additive phase $\phi_k^j$ onto each original eigenvector associated with the eigenvalue $k$, shown as

$$\boldsymbol{V}_l^{\text{new}}(j) = \boldsymbol{V}_l(N_{\text{diff}}) + \sum_{k=1}^{N_{\text{diff}}-1} \boldsymbol{V}_l(k)\exp(i\phi_k^j), \tag{D.1}$$

where $N_{\text{diff}}$ is the total number of eigenvalues focusing on these scatterers. In presence of a substrate, there exist two eigenvalues for each scatterer. According to Eq. (3.12), the new backpropagated field can be obtained with the same combination

$$\boldsymbol{E}_{\text{new}}^{\text{inc;DORT}}(\boldsymbol{r}) = \boldsymbol{E}_{N_{\text{diff}}}^{\text{inc;DORT}}(\boldsymbol{r}) + \sum_{k=1}^{N_{\text{diff}}-1} \boldsymbol{E}_k^{\text{inc;DORT}}(\boldsymbol{r})\exp(i\phi_k^j). \tag{D.2}$$

Starting from an initial guess $\phi_{k,0}^j = 0$ $(k = 1, 2, \cdots, N_{\text{diff}}-1)$, this adjusted phase can be iteratively obtained by minimizing a functional $F^{\text{mod}}(\phi_k^j)$ of the form

$$F_n^{\text{mod}}(\phi_{k,n}^j) = \sum_{p=1, p\neq j}^{M} \|\boldsymbol{E}_{\text{new}}^{\text{inc;DORT}}(\boldsymbol{r}_p)\| - \|\boldsymbol{E}_{\text{new}}^{\text{inc;DORT}}(\boldsymbol{r}_j)\|, \tag{D.3}$$

Eq. (D.3) can be interpreted as the discrepancy between the modulus of the incident field on the scatterer centred at $\boldsymbol{r}_j$ and the sum of the modulus of the incident fields on the other scatterers centred at $\boldsymbol{r}_p, (p = 1, 2, \cdots, M, p \neq j)$. When $F^{\text{mod}}(\phi_k^j)$ is minimized until

$$\frac{\|F_n^{\text{mod}}\left(\phi_{k,n}^j\right) - F_{n-1}^{\text{mod}}\left(\phi_{k,n-1}^j\right)\|}{\|F_{n-1}^{\text{mod}}(\phi_{k,n-1}^j)\|} < 10^{-6}. \tag{D.4}$$

The focusing field on scatterer $j$ is assumed to be much stronger than that of the others. It means that with this linear combination of the eigenvectors, we can generate a new backpropagated field focusing exclusively on one scatterer.

Appendix E

# Backpropagation method to generate an initial guess to the inverse algorithm

We present here the backpropagation method to generate an initial guess that is used in the inversion procedure described in Sec. 2.2.4.

First, for each illumination $l$, the initial estimate $\boldsymbol{\psi}_l^{\text{init}} = \chi^{\text{init}} \boldsymbol{E}_l^{\text{init}}$ inside the investigating domain $\Omega$ can be obtained by backpropagating the measured scattered field $\boldsymbol{f}_l^{\text{mes}}$ into $\Omega$, in the form of

$$\boldsymbol{\psi}_l^{\text{init}} = \gamma_l \boldsymbol{G}^\dagger \boldsymbol{f}_l^{\text{mes}}, \tag{E.1}$$

where $\boldsymbol{G}^\dagger$ is the adjoint operator of $\boldsymbol{G}$. The scalar weight $\gamma_l$ can be obtained by minimizing the cost function $\mathcal{F}(\gamma_l)$

$$\mathcal{F}(\gamma_l) = \|\boldsymbol{f}_l^{\text{mes}} - \boldsymbol{G}\psi_l^{\text{init}}\|_\Gamma^2 = \|\boldsymbol{f}_l^{\text{mes}} - \gamma_l \boldsymbol{G}\boldsymbol{G}^\dagger \boldsymbol{f}_l^{\text{mes}}\|_\Gamma^2. \tag{E.2}$$

$\mathcal{F}(\gamma_l)$ describes the discrepancy between the measured scattered field $\boldsymbol{f}_l^{\text{mes}}$ and that would be obtained by $\boldsymbol{\psi}_l^{\text{init}}$. $\gamma_l$ is derived under the necessary condition so that $\mathcal{F}(\gamma_l)$ is minimum, $\frac{\partial \mathcal{F}}{\partial \gamma_l} = 0$,

$$\gamma_l = \frac{\left\langle \boldsymbol{G}\boldsymbol{G}^\dagger \boldsymbol{f}_l^{\text{mes}}, \boldsymbol{f}_l^{\text{mes}} \right\rangle_\Gamma}{\|\boldsymbol{G}\boldsymbol{G}^\dagger \boldsymbol{f}_l^{\text{mes}}\|_\Gamma^2}. \tag{E.3}$$

Second, once the initial estimate $\boldsymbol{\psi}_l^{\text{init}}$ is obtained, an estimation of the total field $\boldsymbol{E}_l^{\text{init}}$ inside $\Omega$ can be deduced from Eq. (2.1),

$$\boldsymbol{E}_l^{\text{init}} = \boldsymbol{E}_l^{\text{inc}} + \boldsymbol{G}\psi_l^{\text{init}}. \tag{E.4}$$

At last, from the initial estimate $\boldsymbol{E}_l^{\text{init}}$ and $\boldsymbol{\psi}_l^{\text{init}}$ obtained above, we can derive the initial guess for $\xi_0$ and $\eta_0$ inside $\Omega$, respectively[8],

$$\xi_0^4(\boldsymbol{r}\in\Omega)=\frac{\displaystyle\sum_{l=1}^{N}\frac{\left\{\mathrm{Re}\left[\boldsymbol{\psi}_l(\boldsymbol{r})^{\text{init}}\bar{\boldsymbol{E}}_l^{\text{init}}(\boldsymbol{r})+\varepsilon_b\|\boldsymbol{E}_l^{\text{init}}(\boldsymbol{r})\|^2-\|\boldsymbol{E}_l^{\text{init}}(\boldsymbol{r})\|^2\right]\right\}^2}{\|\boldsymbol{E}_l^{\text{init}}(\boldsymbol{r})\|^2}}{\displaystyle\sum_{l=1}^{N}\|\boldsymbol{E}_l^{\text{init}}(\boldsymbol{r})\|^2}, \tag{E.5}$$

$$\eta_0^4(\boldsymbol{r}\in\Omega)=\frac{\displaystyle\sum_{l=1}^{N}\frac{\left\{\mathrm{Im}\left[\boldsymbol{\psi}_l(\boldsymbol{r})^{\text{init}}\bar{\boldsymbol{E}}_l^{\text{init}}(\boldsymbol{r})+\varepsilon_b\|\boldsymbol{E}_l^{\text{init}}(\boldsymbol{r})\|^2\right]\right\}^2}{\|\boldsymbol{E}_l^{\text{init}}(\boldsymbol{r})\|^2}}{\displaystyle\sum_{l=1}^{N}\|\boldsymbol{E}_l^{\text{init}}(\boldsymbol{r})\|^2}. \tag{E.6}$$

Where $\bar{\boldsymbol{E}}_l^{\text{init}}(\boldsymbol{r})$ denotes the complex conjugate matrix of $\boldsymbol{E}_l^{\text{init}}(\boldsymbol{r})$.

Appendix F

# Synthetic aperture and resolution in TDM

It has been proved that in far field and under the Born approximation, the field $\boldsymbol{E}^{\text{sca}}$ scattered along the wave vector $\boldsymbol{k}$ for an illuminating wave vector $\boldsymbol{k}_{\text{inc}}$ is directly proportional to the 3D Fourier transform of $\Delta\varepsilon$ taken at $\boldsymbol{k} - \boldsymbol{k}_{\text{inc}}$ [106],

$$\boldsymbol{E}^{\text{sca}}(\boldsymbol{k}, \boldsymbol{k}_{\text{inc}}) \propto \Delta\tilde{\varepsilon}(\boldsymbol{k} - \boldsymbol{k}_{\text{inc}}). \tag{F.1}$$

For a given angle of illumination with wave vector $\boldsymbol{k}_{\text{inc}}$, according to Eq. (F.1), TDM permits to detect the Fourier components of the object permittivity contrast on a cap of sphere of radius $k_0$, truncated by the numerical aperture (NA) of the objective used to collect the scattered field, and centered on the extremity of wave vector $-\boldsymbol{k}_{\text{inc}}$. This cap of sphere is represented on Fig. F.1 for the case of NA = 1. To increase the amount of Fourier components that can be detected, and therefore ameliorate the resolution of the object reconstruction, various angles of illumination are used successively on the sample. Each of them provides different Fourier components, and the merging of all the components is a process known as synthetic aperture generation. Indeed, a synthetic aperture is built through the measurement, and permits to access spatial frequencies of the object that are beyond those confined in sole the detection NA. This synthetic aperture is described in the three-dimensional Fourier space by an Optical Transfer Function (OTF) that is equal to one for a Fourier component that can be detected, and zero elsewhere. The permittivity contrast of the object that is reconstructed through an inverse Fourier transform ($\text{FT}^{-1}$) of the detected field can thus be written as

$$\Delta\varepsilon(\boldsymbol{r})_{\text{rec}} = \int_{-\infty}^{+\infty} (\Delta\tilde{\varepsilon}(\boldsymbol{K}) \times \text{OTF}) \text{e}^{\text{i}\boldsymbol{K}\cdot\boldsymbol{r}} \text{d}^3\boldsymbol{K} \tag{F.2}$$

$$= \Delta\varepsilon(\boldsymbol{r}) * \text{FT}^{-1}(\text{OTF}) = \Delta\varepsilon(\boldsymbol{r}) * \text{PSF}, \tag{F.3}$$

where * denotes the convolution product. The projections of $\boldsymbol{K}$ give the three-dimensional spatial frequencies of the object, and PSF is the point spread function which describes the response of the imaging system to a point source. The PSF is given by the inverse Fourier transform of the OTF. The reconstructed permittivity contrast of the object is therefore the actual one convoluted with the PSF. Depending on the configuration for illumination and detection, TDM has access to different Fourier components of the object, what modifies the OTF and the PSF. Hereafter are presented the main configurations that can be used and the associated OTF and PSF. Note that, for the sake of simplicity, an ideal numerical aperture equal to one is considered both for the illumination and the detection.

To obtain the biggest amount of Fourier components, the ideal case would consist in illuminating the object along all possible directions within $4\pi$ steradians, and performing the detection also for all these directions. Therefore for a given illumination direction, the accessible Fourier components lie on the surface of a sphere with radius $k_0$ (the smaller dotted sphere) in Fig. F.2.

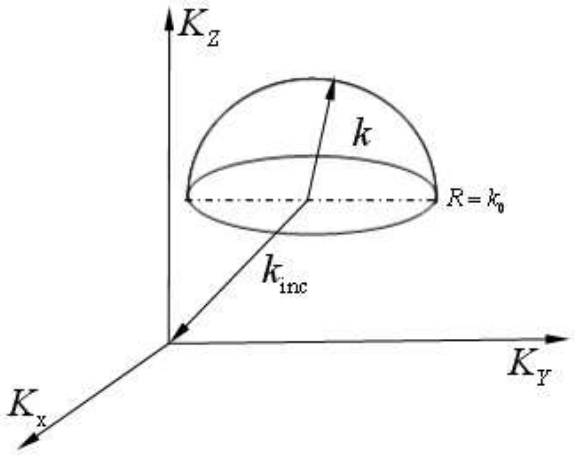


**Figure F.1 :** *Accessible 3D Fourier domain for one incidence.*

Then, varying the illumination angle permits to fill the volume of a sphere with radius $2k_0$, the larger solid sphere in Fig. F.2.

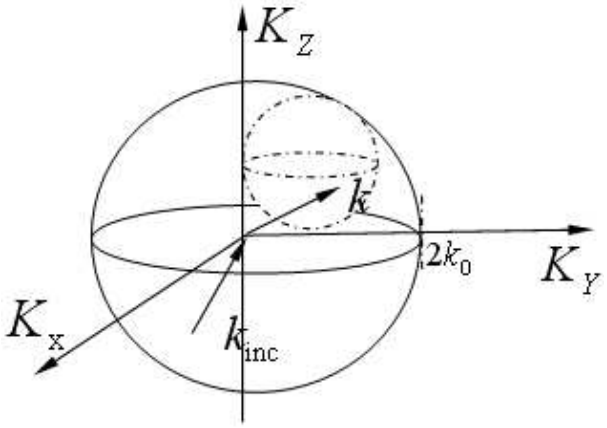


**Figure F.2 :** *OTF for the complete configuration.*

With this complete configuration, all the spatial frequencies given by $\boldsymbol{k} - \boldsymbol{k}_{\text{inc}}$ for any wave vectors $\boldsymbol{k}$ and $\boldsymbol{k}_{\text{inc}}$ are accessible. The Fourier coefficient of the permittivity can be measured within the entire sphere of radius $2k_0$ depicted in Fig. F.2. This sphere is known as the Ewald sphere.

In practice, the complete configuration is difficult to implement in a TDM setup, as most of the microscopes work in a transmission or in a reflection configuration. In the transmission case, the illumination is performed on one side of the sample along the optical axis, and the detection on the other side. The OTF is then only a portion of the sphere of radius $2k_0$ of the complete configuration. It is a torus with the $z$ axis as symmetrical axis, and its cross section in a longitudinal plane consists of two circles with radius $k_0$, as shown in Fig. F.3 (a).

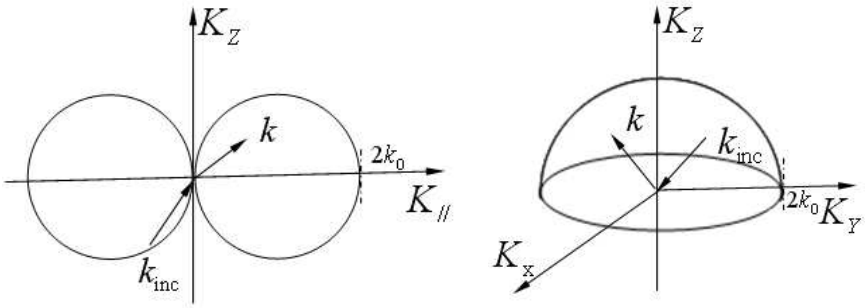


(a) (b)

**Figure F.3 :** *(a) OTF for the transmission configuration. (b) OTF for the reflection configuration.*

For the case of the reflection configuration, where the illumination and the detection are performed on the same side of the sample, the OTF becomes the half of the complete sphere of radius $2k_0$, on one side of the transverse plane $(x, y)$, as shown on Fig. F.3 (b).

Appendix G

# Publications included in this manuscript

## Contents

# Discrete dipole approximation in time domain with Laplace transform

Patrick C. Chaumet[1], Ting Zhang[1], Adel Rahmani[2], Boris Gralak[1], and Kamal Belkebir[1]
[1]*Aix Marseille Université, CNRS, Centrale Marseille, Institut Fresnel, UMR 7249, 13013 Marseille, France*
[2]*School of Mathematical Sciences, University of Technology Sydney, Broadway NSW 2007, Australia*

We present a new form of the discrete dipole approximation for electromagnetic scattering computations in time domain. We show that the introduction of complex frequencies, through the Laplace transform, significantly improves the computation time. We also show that the Laplace transform and its inverse can be combined to extract the field inside a scatterer at a real resonance frequency.

PACS numbers: PACS numbers: 02.60.Cb, 41.20.Jb, 42.25.Fx

## I. INTRODUCTION

Electromagnetic scattering by an arbitrary three-dimensional structure, in time domain, is usually modelled using the finite difference in time domain (FDTD) method [1–3]. In the FDTD, one solves numerically the differential form of Maxwell's equations on a grid. A constraint of the FDTD is that the entire computational domain needs to be discretized [4]. By contrast, the discrete dipole approximation (DDA), a scattering computation method, requires that only the scatterer (or its immediate neighbourhood) be discretized [5–8]. In the DDA the outgoing wave condition is automatically satisfied by using dyadic field susceptibility tensors to describe the linear-response of the fields. However, in its traditional formulation, the DDA is a frequency-domain method, restricted to time-harmonic fields.

Recently we generalized the DDA to handle arbitrary, non time-harmonic electromagnetic waves. The method, detailed in Ref. [9], consists in solving the electromagnetic scattering in frequency domain, and performing a Fourier transform to generate the time evolution of electromagnetic quantities. Of course, with this approach, one drawback of the DDA is that we must solve a large system of linear equations to find the fields inside the scatterer [4]. This can be prohibitive in terms of computer memory requirements. A common way to circumvent this problem is to use an iterative method. However, such an approach requires us to calculate many times a large matrix-vector product (MVP), and to do so for all the frequencies required to accurately describe the time evolution of the fields. Therefore, the main bottleneck for the computation time is the total number of MVP required in order to achieve the desired level of convergence of the iterative method. One can decrease the number of MVP by choosing an efficient iterative method, for instance we use a combination of the generalized product-type methods based on Biconjugate gradient (GPBICG) [10], a good initial value [9] and a preconditonner of Jacobi [11, 12], but nevertheless the convergence is still slow.

In this article we present a general strategy to reduce the number of MVP by introducing complex frequencies into the problem via the Laplace transform. The outcome is a reduction of the number of MVP, and hence a speed-up of the computation. However, this is not the only benefit. This new approach allows us to handle resonant scatterers, for instance a plasmon resonance, in time domain, something that the Fourier transform approach of Ref. [9] cannot do.

In Sect. II we briefly present the DDA method in both its time-harmonic and time domain versions, and then, in Sect. III we present the results. Finally in Sect. IV we present our conclusion.

## II. THEORY

In this section we describe the computation of the field scattered by an arbitrary object in frequency domain (electromagnetic fields written in upper case) and in time domain (electromagnetic fields written in lower case), using the DDA.

### A. DDA in time-harmonic case

As the DDA is a well known frequency domain method, we shall only describe it briefly here [6, 13]. Consider an object with dielectric permittivity $\varepsilon$ and arbitrary shape, in free space. For each frequency $\omega$ the object is discretized into $N$ polarizable elements. Each element $j$ located at $\mathbf{r}_j$ has an electric polarizability $\alpha(\mathbf{r}_j,\omega)$, given by:

$$\alpha(\mathbf{r}_j,\omega) = \frac{\alpha_0(\mathbf{r}_j,\omega)}{1-\frac{2}{3}ik^3\alpha_0(\mathbf{r}_j,\omega)}, \quad (1)$$

$$\alpha_0(\mathbf{r}_j,\omega) = \frac{3d^3}{4\pi}\frac{\varepsilon(\mathbf{r}_j,\omega)-1}{\varepsilon(\mathbf{r}_j,\omega)+2}, \quad (2)$$

where $d$ is the spacing of the DDA discretization lattice; $k=\omega/c$ is the wavenumber. Then, the local fields at subunit $i$ can be written as:

$$\mathbf{E}(\mathbf{r}_i,\omega)=\mathbf{E}_0(\mathbf{r}_i,\omega)+\sum_{j=1,i\neq j}^{N}\mathbf{T}(\mathbf{r}_i,\mathbf{r}_j,\omega)\alpha(\mathbf{r}_j,\omega)\mathbf{E}(\mathbf{r}_j,\omega). \quad (3)$$

$\mathbf{T}$ denotes the dyadic field-susceptibility tensor of free-space, *i.e.*,

$$\mathbf{T}(\mathbf{r}_i,\mathbf{r}_j,\omega) = e^{(ikr)}\left[\left(3\frac{\mathbf{r}\otimes\mathbf{r}}{r^2}-\mathbf{I}\right)\left(\frac{1}{r^3}-\frac{ik}{r^2}\right) - \left(\frac{\mathbf{r}\otimes\mathbf{r}}{r^2}-\mathbf{I}\right)\frac{k^2}{r}\right] \quad (4)$$

with $\mathbf{r} = \mathbf{r}_i - \mathbf{r}_j$ and $\mathbf{I}$ the unit tensor. $\mathbf{E}_0(\mathbf{r}_i,\omega)$ is the plane wave illuminating the object such that $\|\mathbf{E}_0(\mathbf{r},\omega)\| = E_0$. If we write Eq. (3) for all $N$ subunits forming the object, we get a linear system of size $3N \times 3N$ which can be written symbolically

$$\mathbf{AE} = \mathbf{E}_0, \quad (5)$$

where $\mathbf{A}$ is a matrix containing the dyadic field-susceptibility tensor and the polarizabilities. Notice as the sum in Eq. (3) is performed over $i \neq j$, $\mathbf{A}$ is a matrix with ones on the main diagonal. The main objective of the DDA is to solve as efficiently as possible the large linear system of Eq. (5).

The linear system can be solved iteratively using a number of methods similar to the conjugate gradient method [11, 14, 15]. Irrespective of which iterative method is used (not implying that the choice of the method is unimportant, see Ref. [16]), at each step of the iterative method, one needs to compute efficiently the matrix vector product (MVP) $\mathbf{AX}$ where $\mathbf{X}$ is an estimate of the local field given by the iterative method. The iterative process is stopped when

$$\frac{\|\mathbf{AX}_n - \mathbf{E}_0\|^2}{\|\mathbf{E}_0\|^2} < \epsilon, \quad (6)$$

where $\mathbf{X}_n$ is the $n$-th estimate of the local-field given by the iterative method, and $\epsilon$ the desired accuracy. Once the local field is obtained at each subunit position, the scattered field can be computed as

$$\mathbf{E}_{\mathrm{d}}(\mathbf{r},\omega) = \sum_{j=1}^{N} \mathbf{T}(\mathbf{r},\mathbf{r}_j,\omega)\alpha(\mathbf{r}_j,\omega)\mathbf{E}(\mathbf{r}_j,\omega). \quad (7)$$

To speed-up the computation of the MVP at each iteration, the product is calculated via Fast Fourier transform (FFT) as $\mathbf{A}$ can be written as a Toeplitz matrix [17, 18]. FFT notwithstanding, the solution of Eq. (5) is still the most time consuming part of the computation. Therefore, any step toward reducing the number of MVPs in the algorithm would be a major progress for this type of computation. This is particularly true for time-domain computations which requires that the corresponding time-harmonic problem be solved for several frequencies. We will get back to this problem in Sect. III.

### B. DDA in time domain

In this section we consider the case where the incident field is an electromagnetic pulse with a Gaussian envelop $f(t)$ and a spectrum centered on some frequency $\omega_0$:

$$f(t) = E_0 \exp\left[-16\left(\frac{t-t_0}{\tau}\right)^2\right]\cos(\omega_0 t), \quad (8)$$

where $\tau$ is related to the width of the envelop of the Gaussian pulse and $t_0$ is chosen large enough to assume that we have $f(t) = 0$, $\forall t \leq 0$. We define $F(s)$, the Laplace transform of $f(t)$ as [19]

$$F(s) = \mathscr{L}_\beta[f(t)] = \int_0^\infty f(t)e^{-st}\mathrm{d}t, \quad (9)$$

with $s = \beta + i\omega$. The inverse Laplace transform is defined along a Bromwich contour as:

$$f(t) = \mathscr{L}_\beta^{-1}[F(s)] = \frac{1}{2i\pi}\int_{\beta-i\infty}^{\beta+i\infty} F(s)e^{st}\mathrm{d}s \quad (10)$$

$$= \frac{e^{\beta t}}{2\pi}\int_{-\infty}^{\infty} F(\beta+i\omega)e^{i\omega t}\mathrm{d}\omega. \quad (11)$$

To get $\mathbf{e}_{\mathrm{d}}(\mathbf{r},t)$ the scattered field in time domain (or the local field inside the object), one needs to compute the inverse Laplace transform of $F(s)\mathbf{E}_{\mathrm{d}}(\mathbf{r},s)$ where $\mathbf{E}_{\mathrm{d}}(\mathbf{r},s)$ is obtained through Eqs. (3) and (7) with a complex frequency, *i.e.* in the expressions of the incident plane wave, field-susceptibility tensor (FST) and polarizability, $i\omega$ is replaced with $s$. As $\beta > 0$ the $e^{i\omega r/c}$ dependence of the FST becomes $e^{i\omega r/c}e^{-\beta r/c}$. In other words, the complex frequency introduces an evanescent decay in the FST.

Notice that Eq. (10) is the inverse Laplace transform which can be expressed in the form of a inverse Fourier transform, Eq. (11) [20]. At the cost of introducing of manageable truncation and discretization errors, $f(t)$ can now be computed efficiently *via* inverse fast Fourier transform (FFT). Let $\Delta\omega$ be the discretization step in the spectral domain, for an observation time span of $T_{\max}$ and with $N_s$ being the number of the sample (*i.e.* $\Delta t = T_{\max}/N_s$), we should choose our spectral step such that $\Delta\omega\Delta t = 2\pi/N_s$ or equivalently $\Delta\omega = 2\pi/T_{\max}$. Notice that due to the finite bandwidth of our pulse (Gaussian envelop), we suffer no truncation error in going from Eq (11) to a FFT. However, there remains the discretization error. The larger $\beta$, the stronger the damping in the FST, but due to the presence of the term $e^{\beta t}$ in the inverse Laplace transform which amplify the numerical error, parameter $\beta$ cannot exceed a maximum value $\beta_{\max}$ [21]. Finding this $\beta_{\max}$ is not easy and remains an empirical process. Wilcox [20, 21] proposed the following value

$$\beta_{\max} = 2\Delta\omega = \frac{4\pi}{T_{\max}}, \quad (12)$$

and Wedepohl [20, 21] proposed

$$\beta_{\max} = \frac{\log(N^2)}{T_{\max}}. \quad (13)$$

As we will show in Sect. III, to avoid any numerical error in the range of observation $[0,\ T_{\max}]$, the best value for our configuration is:

$$\beta_{\max} = \Delta\omega = \frac{2\pi}{T_{\max}}. \tag{14}$$

Notice that the expression of the polarizability in Eq. (1) introduces a set of triplets of poles given by the solutions to the following equation:

$$\omega^3 = -2i\pi\frac{c^3}{d^3}\frac{\varepsilon(\omega)+2}{\varepsilon(\omega)-1}. \tag{15}$$

If the scatterer has a frequency independent relative permittivity we get a single triplet of poles. If the relative permittivity is given by a single Drude-Lorentz resonance, one gets two triplets of poles, *i.e.* each new Drude-Lorentz resonance leads to an additional triplet of poles.

In each triplet, the poles can be deduced from each other by a $2\pi/3$ rotation in the complex plane. It follows that one or two poles within each triplet have a positive imaginary part. They can contribute to the Laplace transform if they are located inside the integration path, in the complex (frequencies) plane. In all the results presented in this article, it has been checked that all the poles are located outside the integration path, and therefore, the poles make no contribution the integrals. In the case where poles are located inside the integration path, their contribution can be determined using two methods. The first one is based on the use of Cauchy's integral theorem, and on the evaluation of the dyadic field-susceptibility at complex frequencies. The second method is to use a formulation of the DDA which uses the macroscopic field instead of the local field, thus avoiding the poles associated with the polarizability. While both formulations are strictly equivalent [13] it is usually more convenient to use the local field to compute the cross section [6] or optical forces for example [22–25].

Notice that if one is interested in the time evolution of the macroscopic field inside the object, one needs to store the electric field at all subunits for all the frequencies, hence the memory requirement would be the usual one for the DDA times the number of frequency. On the other hand, if one only needs the scattered field at one observation point, no extra cost in memory will be incurred.

## III. RESULTS

### A. Dielectric sphere with Mie resonances

In this section we consider a homogeneous sphere of radius $a$ with relative permittivity $\varepsilon$. Notice that for this geometry we use a modified prescription for the polarizability which accounts for local-field effects, and dramatically improves the accuracy of the DDA [26, 27]. The parameters of the incident pulse are $f_0 = 3.5$ GHz

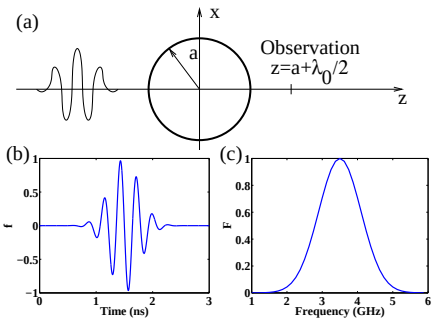


FIG. 1: (a) Sketch of the geometry of the problem. (b) Component $x$ of the incident field versus time. (c) Spectrum of the incident field, *i.e.* modulus of $F(s)$ with $\beta = 0$.

($\omega_0 = 2\pi f_0$ and $\lambda_0 \approx 85$ mm) and $\tau = 1.5$ ns and the total observation time is $T_{\max} = 8$ ns. We use 40 discrete frequencies across the spectrum of the pulse. The incident field is a plane wave propagating along $z$ and polarized along $x$, see Fig. 1(a). Figure 1(b) shows the incident field versus time and Fig. 1(c) its spectrum. The iterative method used is GPBICG with the criterion $\epsilon = 10^{-6}$ [10, 16]. Notice that as we need to compute the local field at each subunit position for each frequencies for a plane wave illumination, we can deduce from this intermediary result the scattering cross section of the sphere versus the frequency in the complex plane with:

$$C_{\text{ext}}(s) = \frac{4\pi k}{E_0^2}\sum_{j=1}^{N}\text{Im}\left[\mathbf{E}_0^*(\mathbf{r}_j,s)\alpha(\mathbf{r}_j,s)\mathbf{E}(\mathbf{r}_j,s)\right]. \tag{16}$$

Notice that when $\beta = 0$, $C_{\text{ext}}$ is computed along the real axis which can also be evaluated with Mie theory. We also point out that the solution of Eq. (5) is faster if one uses a good initial estimate of the local field. Usually, for single frequency problems one use the incident field, but as we are "frequency hopping", we use a linear combination of the local field obtained for the previous frequency as described in Ref. [9]. In the appendix we present some of the details of this procedure, and give the number of MVP for different iterative methods, for both dielectric spheres used in this section.

#### 1. *Dielectric sphere with weak resonances*

Consider a sphere of radius $a = \lambda_0/3$ with $\varepsilon = 4$. Figure 2(a) shows the extinction cross section, $C_{\text{ext}}$ versus frequency. In dotted line we have the prediction of Mie theory and in dashed line the DDA with $\beta = 0$, *i.e.* along the real axis. Notice that the convergence of the DDA is very good as the difference between the two results is very small. The dot dashed line is com-

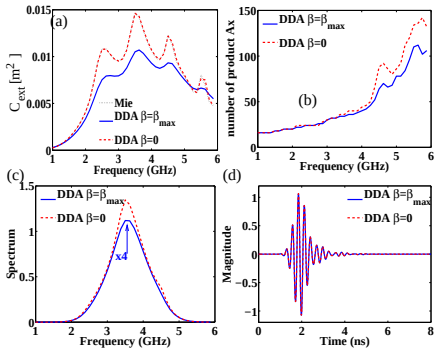


FIG. 2: (a) Extinction cross section with Mie calculation (dotted line), DDA with $\beta = 0$ (dashed line) and DDA with $\beta = \beta_{\max}$ (plain line). (b) Number of product $\mathbf{AX}$ for the iterative method to reach the convergence. (c) Spectrum of the scattered field. (d) Scattered field versus the time.

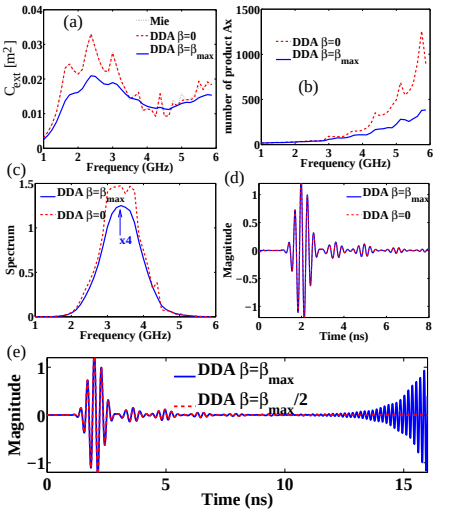


FIG. 3: Same legend for (a)-(d) as in Fig. 2(a)-(d) respectively. (e) Scattered field versus the time for $T'_{\max} = 2T_{\max} = 16$ ns with $\beta = 2\pi/T'_{\max} = \beta_{\max}/2$ in dashed line and $\beta = 2\pi/T_{\max} = \beta_{\max}$ in solid line.

puted with the value $\beta = \beta_{\max} = 2\pi/T_{\max}$. One can see that the scattering cross section computed with the damping term $\beta_{\max}$ presents weaker resonances, this is due to the fact that we compute $C_{\text{ext}}$ far from the real axis, hence far from the resonance localized on the real axis. In Fig. 2(b) the number MVP required by the iterative method to achieve convergence ($\epsilon = 10^{-6}$) is plotted versus frequency. When the DDA is used with $\beta = \beta_{\max}$ (solid line), the number of MVP is overall smaller than when $\beta = 0$. The effect is more pronounced around the weak resonances between 4 and 5 GHz.

Figure 2(d) shows the $x$ component of the scattered field, $\mathbf{e}_{\text{d}}(\mathbf{r}, t)$ estimated at $z = a + \lambda_0/2$ along the $z$ axis, see Fig. 1(a). Its spectrum is given in Fig. 2(c). In time domain, we obtain the same magnitude of the field irrespective of the value of $\beta$ as demonstrated by the fact that both curves in Fig. 2(d) are superimposed. Of course, the spectra on ($\beta = 0$) and off ($\beta = \beta_{\max}$) the real axis are different. When $\beta = \beta_{\max}$ the spectrum has the same spectral support but is damped (by a factor 4) and smoother. This is the very reason with this new formulation of the DDA allows us to compute the fields in time domain with fewer matrix-vector products. Obviously a lower value of $\beta$ yields a less smooth spectrum and increases the number of MVP required to achieve a given level of convergence.

Note that we checked that broadening the frequency domain does not change $\mathbf{e}_{\text{d}}(\mathbf{r}, t)$, meaning that we have no noticeable truncation error associated to the fact a true Gaussian envelop has an unbounded support.

### 2. *Dielectric sphere with large Mie resonances*

We now consider a sphere with radius $a = \lambda_0/2$ and $\varepsilon = 4$. In Fig. 3(a) the extinction cross section, $C_{\text{ext}}$, is plotted versus the frequency on the real axis and off the real axis. Compared to the example in the previous section, as the radius of the sphere has increased, the resonances on the real axis are sharper and more numerous (see the solid line in Fig. 3(a)). In dashed line we plot $C_{\text{ext}}$ computed with the DDA for $\beta = 0$. The comparison with Mie shows that the DDA calculation has a suitable level of convergence. With $\beta = \beta_{\max}$ the extinction cross section plot is strongly smoothed as no resonance appears at high frequencies, hence we can see the strong damping effect associated with the introduction of a complex frequency. The consequence, shown in Fig. 3(b), is a strong decrease of the number MVP needed by the iterative method to achieve the desired level of convergence when $\beta = \beta_{\max}$. The decrease factor for the higher frequencies is about 3 compared to the case $\beta = 0$ (no damping). Notice also that when $\beta = \beta_{\max}$ the number of MVP increases monotonically with the frequency, *i.e.* with the presence of slight resonances, contrary to $\beta = 0$. This can be understood from Fig. 3(c) where the spectrum of the scattered field is plotted for both values of $\beta$. When $\beta = \beta_{\max}$ (solid line) compared to $\beta = 0$ (dashed line) the spectrum is clearly smoothed and dampened by a factor 4. In Fig. 3(d) one can see that once again, in

the time domain, the computed scattered fields agree for both values of $\beta$.

If we look more closely at the time-domain plot, we notice that at the end of our observation time the scattered field still exhibits small oscillations. Therefore, if we want to study the fields over a longer period of time, for instance up to when these oscillations have died out, our time interval needs to be expanded by increasing $T_{\max}$ which was 8 ns. For example we can choose a new interval of observation $[0,\ T'_{\max}]$ where $T'_{\max} = 2T_{\max} = 16$ ns. As we use an inverse FFT we need to compute twice as many frequencies with $\beta'_{\max} = 2\pi/T'_{\max} = \beta_{\max}/2$ (dashed line in Fig. 3(e)) lest the numerical error be magnified by the factor $e^{\beta_{\max} t}$ at large times. This means that to get a longer observation timespan, one needs a dense sampling in the complex frequency domain. This is illustrated in Fig. 3(e) in solid line. Obviously, this means that the computation time will be larger for this configuration as there are more frequencies to consider as well as, for each frequency, more steps in the iterative solution of Eq. (5) as $\beta$ has a lower value. Notice that the numerical error with $\beta_{\max}$ (solid line) becomes noticeable around $t = 10$ ns hence just after $T_{\max} = 8$ ns. We have tested that the values used by Widepohl and Wilcox are too high and would introduce significant errors on the time evolution of the fields for times earlier than $T_{\max}$.

We emphasize that if the point of observation (where the fields are computed) is at a distance $r$ from the scatterer, one does not need to increase the observation time window, but should merely perform the inverse Laplace transform with the function $e^{sr/c}F(s)$ instead of $F(s)$ to perform a translation in time and keep the same time window.

### B. Sphere with a plasmon resonance

In this section we consider a particle supporting a plasmon resonance. We first present a model for the illumination configuration of in Fig. 1. Then we study a more realistic configuration with a gold particle illuminated by a pulse whose spectrum lies in the visible range and contains the plasmon resonance.

#### 1. *Sphere with a plasmon resonance weakly damped*

Consider a sphere smaller than the wavelength of illumination, with a relative permittivity given by a Drude model:

$$\varepsilon(\omega) = 1 - \frac{\omega_p^2}{\omega^2 + i\omega\Gamma}, \tag{17}$$

where $\omega_p$ denotes the plasmon frequency and $\Gamma$ the damping. The sphere has a radius $a = \lambda_0/10$ and supports a plasmon resonance at frequency $\omega_p = \sqrt{3}\omega_0$. Figure 4 shows the results obtained with $\Gamma = 0.1\omega_p$ (left column) and $\Gamma = 0.03\omega_p$ (right column). With strong damping

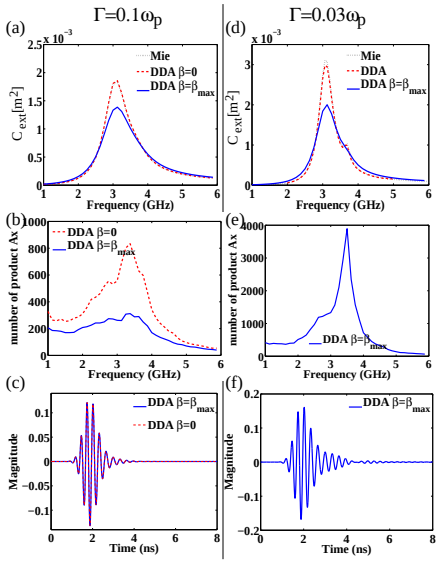


FIG. 4: (a)-(c) $\Gamma = 0.1\omega_p$: (a) Extinction cross section with Mie calculation (dotted line), DDA with $\beta = 0$ (dashed line) and DDA with $\beta = \beta_{\max}$ (plain line). (b) Number of MVP for the iterative method to reach the convergence. (c) Scattered field versus the time. (d)-(f) $\Gamma = 0.03\omega_p$: (d) Extinction cross section with Mie calculation (dotted line), DDA with $\beta = \beta_{\max}$ (plain line). The dashed line represents the extinction cross section obtained from the local field computed with Eq. (18). (e) Number of MVP for the iterative method to reach the convergence. (f) Scattered field versus the time.

*i.e.* $\Gamma = 0.1\omega_p$, Figs. 4(a)-(c), at the resonance the ratio of the number of MVP for $\beta = 0$ and $\beta = \beta_{\max}$ is at least 3. When $\Gamma = 0.03\omega_p$, Figs. 4(d)-(f), the resonance is particularly sharp (dotted line) and it is strongly dampened when $\beta = \beta_{\max}$ (solid line). Notice that the DDA with $\beta = 0$ fails to converge, however with $\beta = \beta_{\max}$ the number of iteration required to achieve convergence is still reasonable. The plot of the scattered field versus time shows that, due to the large resonance, an oscillation at wavelength $\lambda_0$ remains after the pulse has died out.

One of the problem of the DDA in the frequency domain is to handle resonances as the iterative method do not converge. We can use the method developed in this article to circumvent this problem. First we compute the local field $\mathbf{E}(\mathbf{r}_i, s)$ with $\beta = \beta_{\max}$ at each subunit position. Then, we get $\mathbf{e}(\mathbf{r}_i, t)$ through the inverse Laplace transform of $F(s)\mathbf{E}(\mathbf{r}_i, s)$. Now with a simple Fourier transform we can get $F(\omega)\mathbf{E}(\mathbf{r}_i, \omega)$. Then the local field

at each subunit position can be obtained with:

$$\mathbf{E}(\mathbf{r}_i,\omega) = \frac{1}{F(\omega)}\mathscr{L}_{\beta=0}\left\{\mathscr{L}^{-1}_{\beta=\beta_{\max}}\left[F(s)\mathbf{E}(\mathbf{r}_i,s)\right]\right\}. \quad (18)$$

Obviously when $F(\omega)$ is small, *i.e* the frequency is far from the central frequency of the spectrum, the numerical error is large. However, this a not really a problem because, in that case, we are far from the resonance and the conventional DDA method works well. In Fig. 4(d), in dashed line, we plot the extinction cross section calculated from the local field obtained with Eq. (18). Note that the curve is only plotted in the range [2, 5] GHz to avoid the numerical errors associated with small values of $F(\omega)$. As we can see, the extinction cross section computed using the DDA with Eq. (18) is in good agreement with Mie theory near the plasmon resonance.

### 2. *Gold particle*

We now consider the scattering of light by a gold particle illuminated by a pulse with $f_0 = 6.5\times10^{14}$ Hz and $\tau = 2.5\times10^{-14}$ (*i.e.* in the visible range). The relative permittivity of gold is represented by a Drude model, modified to account for the two interband transitions at $\lambda \approx 470$ nm and 330 nm:

$$\varepsilon(\omega) = \varepsilon_\infty - \frac{\omega_p^2}{\omega^2 + i\Gamma\omega} + G_1(\omega) + G_2(\omega) \quad (19)$$

where constants $\omega_p$, $\Gamma$, $\varepsilon_\infty$, and functions $G_1(\omega)$, $G_2(\omega)$ are given in Ref. [28].

*a. Spherical gold particle* We first study a gold sphere with radius $a = \lambda_0/10$, illuminated by a plane wave. In Figs. 5(a) and 5(b) we plot the incident field versus time and its spectrum. Due to the strong variations of the relative permittivity of the gold in the visible range, we use a finer discretization than in the previous case, *i.e.* 80 discrete frequencies across the spectrum of the pulse which leads to $T_{\max} = 26\times10^{-14}$ s. Figure 5(c) shows the scattered field versus time for $\beta = 0$ (solid line) and $\beta = 2\pi/T_{\max}$ (crosses). The two plots are in excellent agreement. To assess the accuracy of the Laplace method introduced in this article, we plot in Fig. 5(d) the relative error on the extinction cross section computed using Eq. (18) with $\beta = 0$ (plain line) and $\beta_m = 2\pi/T_{\max}$ (crosses), compared to Mie theory. We see that the two curves are perfectly superimposed. Indeed, the integrand is an analytic function in the considered domain of complex frequencies, and thus its integration, between two points in the complex plane, does not depend on the path between the points. Notice that given the spherical shape of the object, as we previously indicated, we use a modified prescription for the polarizability which accounts for local-field effects[27]. To illustrate the ability of our method to compute the field in time domain using the Laplace transform irrespective of the form of the polarizability, we plot in Figs. 5(c)

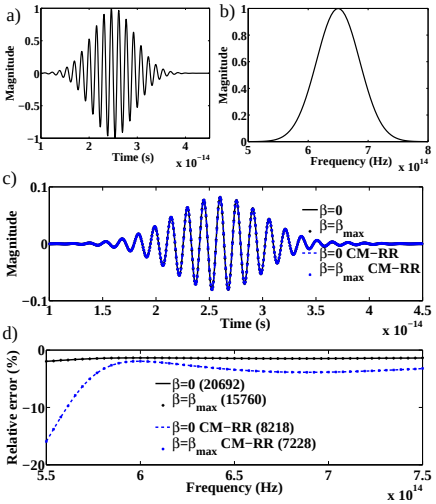


FIG. 5: (a) $x$ component of the incident field versus time. (b) Spectrum of the incident field, *i.e.* modulus of $F(s)$ with $\beta = 0$. (c) Scattered field at $z = a + \lambda_0/2$ versus time, for $\beta = 0$ and $\beta = \beta_{\max}$, for two prescriptions of the polarizability of the subunits: Clausius-Mossotti with radiative reaction term and local-field corrected formulation. (d) Relative error on the extinction cross section compared to Mie series of the Laplace transform technique with Eq. (18) for $\beta = 0$ and $\beta = \beta_{\max}$ for the two polarizability prescriptions. The number of MVP required to solve the linear system represented by Eq. (3) is given between brackets.

and 5(d) the same results (dashed line for $\beta = 0$ and $\times$ for $\beta = \beta_m$) for the Clausius-Mossotti model with radiative reaction term, *i.e.* Eqs. (1) and (2). As we can see, the accuracy of the extinction cross section computation is slightly lowered at low frequencies due to the large value of the relative permittivity. However, in the time domain, the field computation suffers no ill effect as the weight of the low frequency components of the field is weak in the overall spectrum. In Fig. 5(d) we also see that the number of MVP, given in brackets, increases with the modified prescription for polarizability which accounts for local-field effects.

*b. Cubic gold particle illuminated by a radiating dipole* In this section we study a cube with side $a = \lambda_0/2$, illuminated by a dipole located at $z = -2a - \lambda_0/2$, oriented along the $x$ axis, see Fig. 6(a). We use the Clausius Mossotti model with radiative reaction term for our polarizabilities [6]. The incident pulse is shown in Figs. 5(a) and 5(b), and is discretized using the same 80 frequencies as previously. In Fig. 6(b) we plot the scattered field at the observation point when the gold cube is illuminated by a dipole for different values of

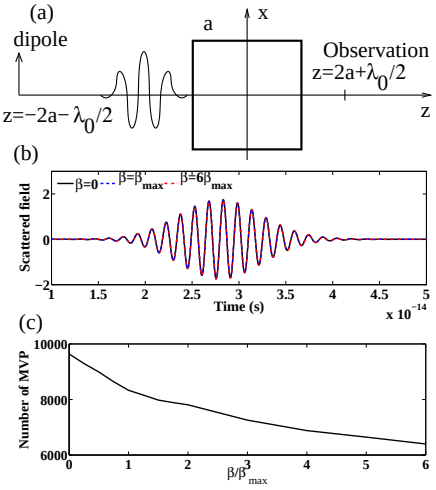


FIG. 6: (a) Geometry of the problem. A cubic gold target is illuminated by a radiating dipole oriented along the $x$ axis. (b) Scattered field at $z = 2a + \lambda_0/2$ versus time for $\beta = 0$ (plain line), $\beta = \beta_{\max}$ (dashed line) and $\beta = 6\beta_{\max}$ (dot-dashed line). (c) Number of MVP to compute all the 80 frequencies of the pulse versus the value of $\beta$.

$\beta$, with $\beta_{\max} = 2\pi/T_{\max}$. As the plasmon resonance of the particle is damped by the imaginary part of material losses, we do not need to observe the fields up to time $T_{\max}$, hence the value of $\beta$ can be increased beyond $\beta_{\max}$. Since the observed scattered pulse finished before $t = 5 \times 10^{-14} \approx T_{\max}/6$, we can increase $\beta$ to $\beta = 6\beta_{\max}$. We see that all the different values of $\beta$ gives exactly the same results. In Fig. 6(c) the evolution of the number of MVP versus the values of $\beta$ is plotted. Obviously, the larger $\beta$, the fewer MVP.

## IV. CONCLUSION

We presented a novel formulation of the discrete dipole approximation (DDA) for time-domain scattering computations. We used Laplace transform techniques to efficiently solve for the fields scattered by an object, including for pathological cases, such as a scatterer exhibiting resonances (*e.g.*, plasmon resonance, Mie resonance, ...). Because our approach is built on the same general principles as the conventional DDA, it is not restricted to light-scattering by dielectric objects. For instance, our new approach can be used to compute, in the time domain, optical forces [29, 30], or the scattering of an electromagnetic wave by a magnetodielectric object [31–34]. Moreover, the techniques developed in this article make it possible to compute, in the frequency regime, internal fields associated with real resonance frequency. Thus, in the time harmonic domain, our approach should be useful for the study of optical forces on resonant metal nanoparticles [35].

Note that our method can be improved by using higher value of $\beta$, however, in that case one needs to use more sophisticated Laplace transform techniques to decrease truncature and discretization error [36, 37].

| K | 0 | 1 | 2 | 3 | 4 |
|---|---|---|---|---|---|
| $a = \lambda/3$ ($\beta = 0$) | 2166 | 2064 | 2074 | 2124 | 2146 |
| $a = \lambda/3$ ($\beta = \beta_{\max}$) | 1874 | 1832 | 1814 | 1814 | 1798 |
| $a = \lambda/2$ ($\beta = 0$) | 10538 | 9706 | 9632 | 9808 | 10002 |
| $a = \lambda/2$ ($\beta = \beta_{\max}$) | 5158 | 4740 | 4700 | 4732 | 4730 |

TABLE I: Number of MVP to achieve convergence ($\epsilon = 10^{-6}$) versus $K$, for the two different dielectric spheres studied in Sect. III A, for different values of $\beta$. The numbers correspond to the total MVP across all frequencies.

## APPENDIX A: SOLUTION OF THE LINEAR SYSTEM

In the approach introduced in this article, the crucial point is to reduce the number of MVP required to solve iteratively the linear equation of Eq. (5). For large systems, using a good initial estimate of the fields will accelerate the convergence of the method. Accordingly, we use the solution obtained at frequency $m-1$ as the initial estimate for the computation at frequency $m$. In fact the initial estimate for the conjugate gradient method can be refined further by using several frequencies as described in Ref. [9]:

$$\mathbf{E}_{\text{est}}(\omega_m) = \sum_{k=1}^{K<m} a_k \mathbf{E}_{\text{solution}}(\omega_{m-k}). \qquad \text{(A1)}$$

For the $m^{\text{th}}$ frequency, the initial estimate is taken as a linear combination of the $K$ previous frequencies, where the coefficients $a_k$ are found by minimizing:

$$\mathcal{C}[\mathbf{E}_{\text{est}}(\omega_m)] = \|\mathbf{A}(\omega_m)\mathbf{E}_{\text{est}}(\omega_m) - \mathbf{E}_0(\omega_m)\|^2. \qquad \text{(A2)}$$

The minimization procedure leads to a linear system of size $K \times K$ where the coefficients $a_k$ are the unknowns. In Table I we show the influence of $K$ on the number of MVP in the frequency range used for the spheres studied in Sect. III A. The case $K = 0$ correspond to the incident field being used as the initial estimate, *i.e.* $\mathbf{E}_{\text{est}}(\omega_m) = \mathbf{E}_0(\omega_m)$. We can conclude that $K = 2$ or $K = 3$ are reasonable choices in our case, particularly for the larger sphere.

Depending on the geometry of the scattering problem, some iterative methods may perform better than others. In Table II we present the number of MVP for sev-

| Iterative method | GPBICG | QMRCGSTAB | CG | BICG |
|---|---|---|---|---|
| $a = \lambda/3$ ($\beta = 0$) | 2124 | 2684 | $\times$ (10) | $\times$ (5) |
| $a = \lambda/3$ ($\beta = \beta_{\max}$) | 1814 | 2176 | $\times$ (14) | $\times$ (5) |
| $a = \lambda/2$ ($\beta = 0$) | 9808 | $\times$ (27) | $\times$ (8) | $\times$ (3) |
| $a = \lambda/2$ ($\beta = \beta_{\max}$) | 4732 | $\times$ (39) | $\times$ (9) | $\times$ (5) |

TABLE II: Number of MVP to achieve convergence ($\epsilon = 10^{-6}$) versus the iterative method for both spheres studied in Sect. III A, for different values of $\beta$ to compute all the frequencies. A " $\times$ " means that the iterative method failed to converge. In that case the number frequencies at which the iterative method failed is given in brackets. (40 frequencies are used to describe the pulse).

eral common iterative methods, for $K = 3$. We consider the conjugate gradient (CG) and a stabilized version of the bi conjugate gradient (BICG) corresponding to the algorithms given in Ref. [14]. We also consider a quasi-minimal residual variants of the Bi-CGSTAB algorithm called QMRCGSTAB [38] and a method labeled GPBICG which is a refinement of the biconjugate gradient method [10].

For the cases considered here, GPBICG is the only iterative method to always converge, irrespective of the size of the sphere, which confirms the robustness of this method for the DDA [16]. Notice that we do not introduce any preconditioner, however, since the matrix associated with our linear system has ones on the main diagonal, we have by default a Jacobi preconditioner, which is a good preconditioner for the DDA as discussed in Ref. [11]. One might decrease further the number of MVP using a more refined preconditioner but this is outside of the scope of this article.

Notice that we use a special prescription for the polarizability for a sphere which accounts for local-field effects [27]. This form of the polarizability actually increases the number of MVP needed to satisfy the convergence criterion (taking local-field effects into account transforms the scalar polarizability into a space dependent tensor) but the resulting increased accuracy on the electric field inside the sphere is essential when dealing with plasmon or Mie resonances. For instance, in Sect. III B 1 for $\Gamma = 0.1\omega_p$ [$\Gamma = 0.03\omega_p$] the relative error (compared to Mie) on the extinction cross section computed with DDA, using Clausius Mossotti and radiative reaction correction, reaches more than 15% [150%] at low frequencies due to a large permittivity, while it is less than 5% [9%] with our modified polarizability. This is important because with the Laplace transform approach a large error at one frequency will affect the overall time domain computation. The same effect can be seen for the gold particle, but owing to the damping associated to a plasmon resonance, the error at low frequency can be neglected, see Figs. 5(c) and 5(d).


[1] K. S. Yee, IEEE Trans. Antennas Propagat. **14**, 302 (1969).
[2] A. Taflove and M. E. Brodwin, IEEE Transactions on Microwave Theory and Techniques **23**, 623 (1975).
[3] A. Taflove, IEEE Trans. Antennas Propagat. **22**, 191 (1975).
[4] F. M. Kahnert, J. Quant. Spect. Rad. Transf. **79-80**, 775 (2003).
[5] E. M. Purcell and C. R. Pennypacker, Astrophys. J. **186**, 705 (1973).
[6] B. T. Draine, Astrophys. J. **333**, 848 (1988).
[7] B. T. Draine and P. J. Flatau, J. Opt. Soc. Am. A **11**, 1491 (1994).
[8] M. A. Yurkin and A. G. Hoekstra, J. Quant. Spect. Rad. Transf. **106**, 558 (2007).
[9] P. C. Chaumet, K. Belkebir, and A. Rahmani, Opt. Express **16**, 20157 (2008).
[10] J. Tang, Y. Shen, Y. Zheng, and D. Qiu, Coastal Engineering **51**, 143 (2004).
[11] P. J. Flatau, Opt. Lett. **22**, 1205 (1997).
[12] J. Pestana and A. J. Wathen, Journal of Computational and Applied Mathematics **249**, 57 (2013).
[13] P. C. Chaumet, A. Sentenac, and A. Rahmani, Phys. Rev. E **70**, 036606 (2004).
[14] R. D. Da Cunha and T. Hopkins, Appl. Numer. Math. **19**, 33 (1995).
[15] M. A. Yurkin, V. P. Maltsev, and A. G. Hoekstra, J. Quant. Spect. Rad. Transf. **106**, 546 (2007).
[16] P. C. Chaumet and A. Rahmani, Opt. Lett. **34**, 917 (2009).
[17] J. J. Goodman and P. J. Flatau, Opt. Lett. **16**, 1198 (2002).
[18] P. J. Flatau, G. L. Stephens, and B. T. Draine, J. Opt. Soc. Am. A **7**, 593 (1990).
[19] B. Davies and B. Martin, J. of Comp. Phys. **33**, 1 (1979).
[20] P. Moreno and A. Ramirez, IEEE T. Image Process. **23**, 2599 (2008).
[21] P. Gómez Zamorano and F. A. Uribe Campos, Rev. Mex. Fis. **53**, 198 (2007).
[22] P. C. Chaumet and M. Nieto-Vesperinas, Phys. Rev. B **61**, 14119 (2000).
[23] A. G. Hoekstra, M. Frijlink, L. B. F. M. Waters, and P. M. A. Sloot, J. Opt. Soc. Am. A **18**, 1944 (2001).
[24] P. C. Chaumet, A. Rahmani, A. Sentenac, and G. W. Bryant, Phys. Rev. E **72**, 046708 (2005).
[25] P. C. Chaumet, A. Rahmani, and M. Nieto-Vesperinas, Phys. Rev. B **71**, 045425 (2005).
[26] A. Rahmani, P. C. Chaumet, and G. W. Bryant, Opt. Lett. **27**, 2118 (2002), ISSN 0146-9592.
[27] A. Rahmani, P. C. Chaumet, and G. W. Bryant, Astrophys. J. **607**, 873 (2004).
[28] P. G. Etchegoin, E. C. Le Ru, and M. Meyer, J. Chem. Phys. **125**, 164705 (2006).
[29] P. C. Chaumet, K. Belkebir, and A. Rahmani, Phys. Rev. A **81**, 021803(R) (2010).
[30] P. C. Chaumet, A. Rahmani, F. Zolla, A. Nicolet, and K. Belkebir, Phys. Rev. A **84**, 033808 (2011.
[31] P. C. Chaumet and A. Rahmani, J. Quant. Spect. Rad.

Transf. **110**, 22 (2009).
[32] P. C. Chaumet and A. Rahmani, Opt. Exp. **17**, 2224 (2009).
[33] P. C. Chaumet, K. Belkebir, and A. Rahmani, Opt. Express **19**, 2466 (2011).
[34] M. Nieto-Vesperinas and J. J. Saenz, Opt. Lett. **35**, 4078 (2010).
[35] A. S. Zelenina, R. Quidant, and M. Nieto-Vesperinas, Opt.Lett. **32**, 1156 (2007).
[36] G. Honig and U. Hirdes, IEEE Trans. Antennas Propagat. **10**, 113 (1984).
[37] A. Yonemoto, T. Hisakado, and K. Okumura, IEE Proc. Circuits Devices Syst. **150**, 399 (2003).
[38] T. F. Chan, E. Gallopoulos, V. Simoncini, T. Szeto, and C. H. Tong, SIAM J. Sci. Comput. **15**, 338 (1994).

# Bibliography


[1] C. Prada and M. Fink. Eigenmodes of the time reversal operator: a solution to selective focusing in multiple-target media. *Wave Motion*, 20:151–163, 1994.

[2] M. Fink. Time Reversed Acoustics. *Phys. Today*, 50:34–40, 1997.

[3] H. Tortel, G. Micolau, and M. Saillard. Decomposition of the time reversal operator for electromagnetic scattering. *J. Electromag. Waves Appl.*, 13:687–719, 1999.

[4] G. Micolau and M. Saillard. DORT method as applied to electromagnetic subsurface sensing. *Radio Sci.*, 38:1038–, 2003.

[5] A Dubois, K Belkebir, and M Saillard. Localization and characterization of two-dimensional targets buried in a cluttered environment. *Inverse Probl.*, 20(6):S63–S79, 2004.

[6] M. E. Yavuz and F. L. Teixeira. Electromagnetic Fields in Dispersive, Random Inhomogeneous Media. *IEEE Trans. Antennas Propagat.*, 54(8):2305–2315, 2006.

[7] G. Papanicolaou L. Borcea and C. Tsogka. Adaptive interferometric imaging in clutter and optimal illuminatio. *Inverse Problems.*, 22:1405–1436, 2006.

[8] K. Belkebir, R. E. Kleinman, and C. Pichot. Microwave imaging — Location and shape reconstruction from multifrequency scattering data. *IEEE Transactions on Microwave Theory and Techniques*, 45(4):469–476, 1997.

[9] L. Souriau, B. Duchêne, D. Lesselier, and R. E. Kleinman. Modified gradient approach to inverse scattering for binary objects in stratidfied media. *Inverse Probl.*, 12:463–481, 1996.

[10] A. Abubakar and P. M. van den Berg. Iterative forward and inverse algorithms based on domain integral equations for three-dimensional electric and magnetic objects. *Journal of Computional Physics*, 195:236–262, 2004.

[11] D. H. Liu, G. Kang, L. Li, Y. Chen, S. Vasudevan, W. Joines, Q. H. Liu, J. Krolik, and L. Carin. Electromagnetic time-reversal imaging of a target in a cluttered environment. *IEEE Trans. Antennas Propagat.*, 53(9):3058–3066, 2005.

[12] Emeric Mudry, Patrick C Chaumet, Kamal Belkebir, and Anne Sentenac. Electromagnetic wave imaging of three-dimensional targets using a hybrid iterative inversion method. *Inverse Probl.*, 28(6):065007, 2012.

[13] Y. Ruan, P. Bon, E. Mudry, G. Maire, P. C. Chaumet, H. Giovannini, K. Belkebir, A. Talneau, B. Wattellier, S. Monneret, and A. Sentenac. Tomographic diffractive microscopy with a wavefront sensor. *Opt. Lett.*, 37(10):1631–1633, May 2012.

[14] A. J. Devaney. Geophysical diffraction tomography. *IEEE Trans. Geosci. Remote Sensing*, 22:3–13, 1984.

[15] A. Roger. Newton-Kantorovitch algorithm applied to an electromagnetic inverse problem. *IEEE Transactions on Antennas and Propagation*, 29(2):232–238, 1981.

[16] K. Belkebir, J. M. Elissalt, J. M. Geffrin, and C. Pichot. Newton-Kantorovich and modified gradient inversion algorithms applied to Ipswich data. *IEEE Antennas and Propagation Magazine*, 38(3):41–44, 1996.

[17] W. C. Chew and Y. M. Wang. Reconstruction of two-dimensional permittivity distribution using distorted Born iterative method. *IEEE Trans. Med. Imaging*, 9:218–225, 1990.

[18] F. C. Chen and W. C. Chew. Experimental verification of super resolution in nonlinear inverse scattering. *Appl. Phys. Lett.*, 72(23):3080–3082, JUN 8 1998.

[19] A. G. Tijhuis, K. Belkebir, A. C. S. Litman, and B. P. de Hon. Multiple-frequency distorted-wave Born approach to 2D inverse profiling. *Inverse Probl.*, 17(6):1635–1644, December 2001.

[20] R. F. Remis and P. M. van den Berg. On the equivalence of the Newton-Kantorovich and distorted Born methods. *Inverse Probl.*, 16:L1–L4, 2000.

[21] R. E. Kleinman and P. M. van den Berg. A modified gradient method for two-dimensional problems in tomography. *J. Comput. Appl. Math.*, 42:17–35, 1992.

[22] P. M. van den Berg and R. E. Kleinman. A contrast source inversion method. *Inverse Probl.*, 13:1607–1620, 1997.

[23] A. Abubakar, P. M. van den Berg, and B. J. Kooij. A conjugate gradient contrast source technique for 3D profile inversion. *IEICE Trans. Electron.*, E83-C:1864–1874, 2000.

[24] A. Abubakar and P. M. van den Berg. The contrast source inversion method for location and shape reconstructions. *Inverse Probl.*, 18:495–510, 2002.

[25] K. Belkebir, P. C. Chaumet, and A. Sentenac. Influence of multiple scattering on three-dimensional imaging with optical diffraction tomography. *J. Opt. Soc. Am. A*, 23:586–595, 2006.

[26] A. Litman and L. Crocco. Testing inversion algorithms against experimental data: 3D targets. *Inverse Probl.*, 25:020201–5, 2009.

[27] S. Y. Semenov, A. E. Bulyshev, A. Abubakar, V. G. Posukh, Y. E. Sizov, A. E. Souvorov, P. M. van den Berg, and T. C. Williams. Microwave-tomographic imaging of the high dielectric-contrast objects using different image-reconstruction approaches. *IEEE Transactions on Microwave Theory and Techniques*, 53(7):2284–2294, 2005.

[28] K. Belkebir and A. G. Tijhuis. Modified$^2$ gradient method and modified Born method for solving a two-dimensional inverse scattering problem. *Inverse Probl.*, 17(6):1671–1688, December 2001.

[29] D. B. Reid. An algorithm for tracking multiple targets . *IEEE Trans. Auto. Control*, 24:843–854, 1979.

[30] A. E. Fouda and F. L. Fernando. Imaging and tracking of targets in clutter using differential time-reversal techniques. *Waves in Random and Complex Media*, 22:66–108, 2012.

[31] C. D. Moss, F. L. Teixeira, and J. A. Kong. Detection of targets in continuous random media: A numerical study using the angular correlation function. *Microw. Opt. Technol. Lett.*, 33:242–247, 2002.

[32] O. Cmielewski, M. Saillard, K. Belkebir, and H. Tortel. On the characterization of buried targets under a rough surface using the wigner-ville transformation. *IEEE Trans. Geosci. Remote Sensing*, 3:442–446, 2006.

[33] O. Cmielewski, H. Tortel, A. Litman, and M. Saillard. A two-step procedure for characterizing obstacles under a rough surface from bistatic measurements. *IEEE Trans. Geosci. Remote Sensing*, 45:2850–2858, 2007.

[34] H. Ammari, J. Garnier, and K. Solna. A statistical approach to target detection and localization in the presence of noise. *Waves Random Complex Media*, 22(1):40–65, 2012.

[35] M. Fink, C. Prada, F. Wu, and D. Cassereau. Self focusing with time reversal mirror in inhomogeneous media. *Proc. IEEE Ultrason. Symp.*, 2:681–686, 1989.

[36] F. D. Philippe, C. Prada, D. Clorennec, M. Fink, and T. Folegot. Construction of the temporal invariants of the time-reversal operator. *J. Acoust. Soc. Am.*, 126(1):8–13, 2009.

[37] D. Lesselier E. Iakovleva, S. Gdoura and G. Perrusson. Multistatic Response Matrix of a 3-D Inclusion in Half Space and MUSIC Imaging. *IEEE Trans. Antennas Propagat.*, 55(9):2598–2609, 2007.

[38] H. Ammari, E. Iakovleva, D. Lesselier, and G. Perrusson. Music-type electromagnetic imaging of a collection of small three-dimensional inclusions. *Siam Journal of scientific Computing*, 29(2):674–709, 2007.

[39] Devaney, AJ and Marengo, EA and Gruber, FK. Time-reversal-based imaging and inverse scattering of multiply scattering point targets. *J. Acoust. Soc. Am.*, 118(5):3129–3138, 2005.

[40] M. Cheney. The linear sampling method and the MUSIC algorithm. *Inverse Problems*, 17(4):591–595, 2001.

[41] C. Prada and J. L. Thomas. Experimental subwavelength localization of scatterers by decomposition of the time reversal operator interpreted as a covariance matrix. *J. Acoust. Soc. Am.*, 114(1):235–243, JUL 2003.

[42] M. E. Yavuz and F. L. Teixeira. On the sensitivity of time-reversal Imaging techniques to model perturbations. *IEEE Trans. Antennas Propagat.*, 56(3):834–843, 2008.

[43] M. Davy, T. Lepetit, J. de Rosny, C. Prada, and M. Fink. Detection and imaging of human beings behind a wall using the dort method. *Prog. In Electromagn. Res.-PIER*, 110:353–369, 2010.

[44] M. E. Yavuz and F. L. Teixeira. Space-frequency ultrawideband time-reversal imaging. *IEEE Trans. Geosci. Remote Sensing*, 46(4):1115–1124, 2008.

[45] A. Dubois. *Étude de l'intéraction d'une onde électromagnetique avec une structure matérielle en régime temporel: problèmes directs et inverses.* PhD thesis, Université Paul Cezanne Aix-Marseille III, 2005.

[46] T. Zhang, P. C. Chaumet, E. Mudry, A. Sentenac, and K. Belkebir. Electromagnetic wave imaging of targets buried in a cluttered medium u sing a hybrid inversion-dort method. *Inverse Probl.*, 28(12):125008, 2012.

[47] T. Zhang, P. C. Chaumet, A. Sentenac, and K. Belkebir. Three-dimensional imaging of targets buried in a cluttered semi-infinite medium. *Journal of Applied physics*, 114:143101, 2013.

[48] S. M Popoff, A. Aubry, G. Lerosey, M. Fink, A. C Boccara, and S. Gigan. Exploiting the Time-Reversal Operator for Adaptive Optics, Selective Focusing, and Scattering Pattern Analysis. *Phys. Rev. Lett.*, 107(26):263901, 2011.

[49] G. Maire, Y. Ruan, T. Zhang, P. C. Chaumet, H. Giovannini, D. Sentenac, A. Talneau, K. Belkebir, and A. Sentenac. High-resolution tomographic diffractive microscopy in reflection configuration. *J. Opt. Soc. Am. A*, 30(10):2133–2139, 2013.

[50] Yongjin Sung, Wonshik Choi, Christopher Fang-Yen, Kamran Badi zadegan, Ramachandra R. Dasari, and Michael S. Feld. Optical diffraction tomography for high resolution live cell imaging. *Opt. Express*, 17(1):266–277, 2009.

[51] W. Choi, C. Fang-Yen, K. Badizadegan, S. Oh, N. Lue, R. R. Dasari, and M. S. Feld. Tomographic phase microscopy. *Nat. Methods*, 4:717–719, 2007.

[52] R. Dorn, S. Quabis, and G. Leuchs. Sharper focus for a radially polarized light beam. *Phys. Rev. Lett.*, 91:233901–4, 2003.

[53] David Lara and Chris Dainty. Axially resolved complete mueller matrix confocal microscopy. *Appl. Opt.*, 45(9):1917–1930, Mar 2006.

[54] I. Catapano, K. Belkebir, and J. M. Geffrin. A single-view imaging strategy for transient scattered fields. *Inverse Probl.*, 24(1):015008, 2008.

[55] W. C. Chew and J. H. Lin. A frequency-hopping approach for microwave imaging of large inhomogeneous bodies. *IEEE Microwave and Guided Wave Letters*, 5(12):439–441, 1995.

[56] K. Belkebir, S. Bonnard, F. Pezin, P. Sabouroux, and M. Saillard. Validation of 2D inverse scattering algorithms from multi-frequency experimental data. *J. Electromag. Waves Appl.*, 14:1637–1667, 2000.

[57] P. C. Chaumet and K. Belkebir. Three-dimensional reconstruction from real data using a conjugate gradient-coupled dipole method. *Inverse Probl.*, 25:024003–17, 2009.

[58] A. Dubois, K. Belkebir, and M. Saillard. Retrieval of inhomogeneous targets from experimental frequency diversity data. *Inverse probl.*, 21(16):S65–S79, 2005.

[59] A. Dubois, K. Belkebir, I. Catapano, and M. Saillard. Iterative solution of the electromagnetic inverse scattering problem from the transient scattered field. *Radio Science*, 44, 14 2009.

[60] P. C. Chaumet, A. Rahmani, F. Zolla, and A. Nicolet. Electromagnetic forces on a discrete spherical invisibility cloak under time-harmonic illumination. *Phys. Rev. E*, 85:143101, 2012.

[61] P. C. Chaumet, A. Rahmani, F. de Fornel, and J.-P. Dufour. Evanescent light scattering: The validity of the dipole approximation. *Phys. Rev. B*, 58:2310–2315, 1998.

[62] D. Zahn, K. Sarabandi, K. F. Sabet, and J. F. Harvey. Numerical Simulation of Scattering from Rough Surfaces: A Wavelet-Based Approach. *IEEE Trans. Antennas Propagat.*, 48:246–253, 2000.

[63] F. Kleinermann, NJ. Avis, and FA. Alhargan. Analytical solution to the three-dimensional electrical forward problem for a circular cylinder. *Inverse probl.*, 16(2):461–468, 2000.

[64] F. M. Kahnert. Numerical methods in electromagnetic scattering theory. *J. Quant. Spect. Rad. Transf.*, 79-80:775–824, 2003.

[65] Patrick C. Chaumet, Kamal Belkebir, and Adel Rahmani. Discrete dipole approximation for time-domain computation of optical forces on magnetodielectric scatterers. *Opt. Express*, 19(3):2466–2475, Jan 2011.

[66] P. C. Chaumet, K. Belkebir, and A. Rahmani. Coupled-dipole method in time domain. *Opt. Express*, 16:20157–20165, 2008.

[67] M. A. Yurkin and A. G. Hoekstra. The discrete dipole approximation: An overview and recent developments. *J. Quant. Spect. Rad. Transf.*, 106:558–589, 2007.

[68] A. Lakhtakia. Strong and weak forms of the method of moments and the coupled dipole method for scattering of time-harmonic electromagnetics fields. *Int. J. Mod. Phys. C*, 3:583–603, 1992.

[69] A. Rahmani, P. C. Chaumet, and G. W. Bryant. Discrete dipole approximation for the study of radiation dynamics in a magnetodielectric environment. *Opt. Express*, 18(8):8499–8504, 2010.

[70] P. C. Chaumet and A. Rahmani. Coupled-dipole method for magnetic and negative refraction materials. *J. Quant. Spect. Rad. Transf.*, 110:22–29, 2009.

[71] G. Mur. Absorbing boundary conditions for the finite-difference pproximation of the time-domain electromagnetic-field equations. *IEEE Transactions on Electromagnetic Compatibility*, 23:377–382, 1981.

[72] S. T. Chu and S. K. Chaudhuri. Finite-difference time-domain method for optical waveguide analysis. *Progress In Electromagnetic Research*, 11:255–300, 1995.

[73] M. Kerker. *The scattering of light.* Academic Press, INC, London, LTD, 1969.

[74] J. A. Kong. *Electromagnetic Wave theory.* EMW Publishing, Cambridge, Massachusetts, USA, 2000.

[75] J. D. Jackson. *Classical Electrodynamics.* Wiley, 2nd ed. edition, 1975.

[76] M. Born and E. Wolf. *Principles of Optics.* Pergamon, 1959.

[77] E. M. Purcell and C. R. Pennypacker. Scattering and absorption of light by nonspherical dielectric grains. *Astrophys. J.*, 186:705–714, 1973.

[78] A. D. Yaghjian. Electric dyadic Green's functions in the source region. *Proceeding of the IEEE*, 68:248–263, 1980.

[79] P. C. Chaumet and A. Rahmani. Electromagnetic force and torque on magnetic and negative-index scatterers. *Opt. Exp.*, 17:2224–2234, 2009.

[80] P. C. Chaumet, A. Sentenac, and A. Rahmani. Coupled dipole method for scatterers with large permittivity. *Phys. Rev. E*, 70:036606–6, 2004.

[81] P. C. Chaumet, A. Rahmani, A. Sentenac, and G. W. Bryant. Efficient computation of optical forces with the coupled dipole method. *Phys. Rev. E*, 72:046708–6, 2005.

[82] K. Belkebir, P. C. Chaumet, and A. Sentenac. Superresolution in total internal reflection tomography. *J. Opt. Soc. Am. A*, 22:1889–1897, 2005.

[83] J. Li, X. Wang, and T. Wang. On the validity of born approximation. *Progress In Electromagnetics Research*, 107:219–237, 2010.

[84] P. C. Chaumet, T. Zhang, A. Rahmani, B. Gralak, and K. Belkebir. Discrete dipole approximation in time domain through the Laplace transform. *Phys. Rev. E*, 88:063303, 2013.

[85] A. Dubois, J. M. Geffrin, K. Belkebir, and M. Saillard. Imaging of dielectric cylinders from experimental stepped-frequency data. *Appl. Phys. Lett.*, 88(16):164104, 2006.

[86] N. Joachimowicz, C. Pichot, and J.-P. Hugonin. Inverse scattering: an iterative numerical method for electromagnetic imaging. *IEEE Trans. Antennas Propagat.*, 39:1742–1753, 1991.

[87] W. H. Press, B. P. Flannery, S. A. Teukolski, and W. T. Vetterling. *Numerical recipes. The art of scientific computing.* Cambridge University Press, 1986.

[88] P. M. van den Berg and A. Abubakar. Contrast Source Inversion Method: State of Art. *PIER*, 34:189–218, 2001.

[89] P. J. Sementilli, B. R. Hunt, and M. S. Nadar. Analysis of the limit to superresolution in incoherent imaging. *J.Opt. Soc. Am. A*, 10:2265–2276, 1993.

[90] P. C. Chaumet, A. Sentenac, K. Belkebir, G. Maire, and H. Giovannini. Improving the resolution of grating-assisted optical diffraction tomography using a priori information in the reconstruction procedure. *Journal of Modern Optics*, 57(9):798–808, 2010.

[91] L. Tsang, J. Au. Kong, K. H. Ding, and C. O Ao. *A wiley-Interscience Publication.* Scattering of electromagnetic waves, 2001.

[92] Y. Kuga and P. Phu. Experimental studies of millimeter-wave scattering in discrete random media and from rough surfaces - Summary. *J. Electromag. Waves Appl.*, 10:451–453, 1996.

[93] R. Carminati, R. Pierrat, J. de Rosny, and M. Fink. Theory of the time reversal cavity for electromagnetic fields. *Opt. Lett.*, 32:3107–3109, 2007.

[94] M. Saillard, P. Vincent, and G. Micolau. Reconstruction of buried objects surrounded by small inhomogeneities. *Inverse Probl.*, 16:1195–1208, 2000.

[95] C. Prada, S. Manneville, D. Spoliansky, and M. Fink. Decomposition of the time reversal operator: detection and selective focusing on two scatterers. *J. Acoust. Soc. Am.*, 9:2067–2076, 1996.

[96] D. H. Chambers and J. G. Berryman. Analysis of the time-reversal operator for a small spherical scatterer in an electromagnetic field. *IEEE T. Antenn. Propag.*, 52(7):1729–1738, 2004.

[97] M. Saillard G. Micolau and P. Borderies. D.O.R.T. method as applied to Ultrawideband Signals for Detection of Buried Objects. *IEEE Trans. Geosci. Remote Sensing*, 41:1813–1819, 2003.

[98] E. Mudry, P. C. Chaumet, K. Belkebir, G. Maire, and A. Sentenac. Mirror-assisted tomographic diffractive microscopy with isotropic resolution. *Opt. Lett.*, 35(11):1857–1859, Jun 2010.

[99] A. G. Tijhuis, K. Belkebir, A. C. S. Litman, and B. P. de Hon. Theoretical and Computational Aspects of 2-D Inverse Profiling. *IEEE Trans. Geosci. Remote Sensing*, 39(6):1316–1330, June 2001.

[100] M. Lambert, D. Lesselier, and B. J. Kooij. The retrieval of a buried cylindrical obstacle by a constrained modified gradient method in the H -polarization case and for Maxwellian materials. *Inverse Probl.*, 14(5):1265–1283, 1998.

[101] L. Bellomo, S. Pioch, M. Saillard, and E. Spano. Time reversal experiments in the microwave range : description of the radar and results. *Prog. In Electromagn. Res.-PIER*, 104:427–448, 2010.

[102] E. Mudry, E. Le Moal, P. Ferrand, P. C. Chaumet, and A. Sentenac. Isotropic diffraction-limited focusing using a single objective lens. *Phys. Rev. Lett.*, 105(20):203903, 2010.

[103] V. Lauer. New approach to optical diffraction tomography yielding a vector equation of diffraction tomography and a novel tomographic microscope. *J. Microsc.*, 205:165–176, February 2002.

[104] Y. Cotte, F. Toy, P. Jourdain, N. Pavillon, D. Boss, P. Magistretti, P. Marquet, and C. Depeursinge. Marker-free phase nanoscopy. *Nature Photonics*, 7(3):113–âĂŞ117, 2013.

[105] O. Haeberlé, K. Belkebir, H. Giovaninni, and A. Sentenac. Tomographic diffractive microscopy: basics, techniques and perspectives. *Journal of Modern Optics*, 57(9):686–699, 2010.

[106] Y. Ruan. *3D digital imaging with tomographic diffractive microscopy.* PhD thesis, Ecole Centrale Marseille, 2012.

[107] N. Streibl. Three-dimensional imaging by a microscope. *J. Opt. Soc. Am. A*, 2(2):121–127, 1985.

[108] G. Cox and C. J. R. Sheppard. Practical limits of resolution in confocal and non-linear microscopy. *Micros. Res. Tech.*, 63:18–22, 2004.

[109] D. B. Murphy and M. W. Davidson. *Fundamentals of Light Microscopy and Electronic Imaging.* Wiley, 2012.

[110] G. Maire, F. Drsek, J. Girard, H. Giovannini, A. Talneau, D. Konan, K. Belkebir, P. C. Chaumet, and A. Sentenac. Experimental Demonstration of Quantitative Imaging beyond Abbe's Limit with Optical Diffraction Tomography. *Phys. Rev. Lett.*, 102:213905–4, 2009.

[111] R. C. Jones. A new calculus for the treatment of optical systems. *J. Opt. Soc. Am.*, 31(7):488–493, Jul 1941.

[112] Tristan Colomb, Florian Dürr, Etienne Cuche, Pierre Marquet, Hans G. Limberger, René-Paul Salathé, and Christian Depeursinge. Polarization microscopy by use of digital holography: application to optical-fiber birefringence measurements. *Appl. Opt.*, 44(21):4461–4469, Jul 2005.

[113] S. W. Hell and E. H. K. Stelzer. Fundamental improvement of resolution with a 4pi-confocal fluorescence microscope using two-photon excitation. *Optics Communications*, 93(5-6):277 – 282, 1992.

[114] K. A. Serrels and E. Ramsay and R. J. Warburton and D. T. Reid. Nanoscale optical microscopy in the vectorial focusing regime. *Nature Photonics*, 2(5):311–314, 2008.

[115] M. Davy, J. G. Minonzio, J. de Rosny, C. Prada, and M. Fink. Influence of noise on subwavelength imaging of two close scatterers using time reversal method: Theory and experiments. *Prog. In Electromagn. Res.-PIER*, 98:333–358, 2009.

[116] J. M. Geffrin and P. Sabouroux. Continuing with the Fresnel database: experimental setup and improvements in 3D scattering measurements. *Inverse Probl.*, 25(2):024001, 2009.

[117] J. M. Geffrin, P. C. Chaumet, C. Eyraud, K. Belkebir, and P. Sabouroux. Electromagnetic three-dimensional reconstruction of targets from free space experimental data. *Appl. Phys. Lett.*, 92(19):194103, 2008.

[118] P. C. Chaumet, K. Belkebir, and A. Sentenac. Experimental microwave imaging of three-dimensional targets with different inversion procedures. *J. Appl. Phys.*, 106:034901–8, 2009.

[119] C. Eyraud, J.-M geffrin, A. Litman, P. Sabouroux, and H. Giovannini. Drift correction for scattering measurements. *Appl. Phys. Lett.*, 89:244104, 2006.

[120] A. Abubakar M. Li and P. M. van den Berg. Application of the multiplicative regularized contrast source inversion method on 3D experimental Fresnel data . *Inverse Probl.*, 25:024006–23, 2009.

[121] K. Belkebir, I. Catapano, and J. M. Geffrin. The reconstruction of inhomogeneous targets from single view transient data. *Near surface geophysics*, 6:381–390, 2008.

[122] R. W. Freund and N. M. Nachtigal. QMR - a quasi-minimal residual method for non-hermitian linear-systems. *Numerische Mathematik*, 60(3):315–339, 1991.

# Résumé

L'objectif de ce travail de thèse est de détecter et de caractériser des cibles tridimensionnelles dans un milieu désordonné. Ce domaine de recherche est d'intérêt pour de nombreuses applications, telles que le sondage du sous-sol, l'imagerie médicale, la détection non-destructive et l'exploration géophysique, etc. Afin de distinguer les cibles des hétérogénéités du milieu, nous proposons d'utiliser l'une des techniques de retournement temporel, à savoir la méthode DORT (Décomposition de l'Opérateur de Retournement Temporel). La méthode DORT permet de générer des ondes focalisant sélectivement sur chaque cible présente dans un environnement fortement hétérogène. Par ailleurs, la richesse de ces ondes focalisantes est combinée avec un algorithme d'inversion non-linéaire. Ceci nous permet non seulement de localiser, mais aussi de caractériser les cibles (forme et permittivité). La résolution obtenue à l'aide de cette approche est bien meilleure que celles obtenues avec la méthode DORT ou la méthode d'inversion seules, en particulier dans la direction d'illumination. Cette résolution est d'autant meilleure que les données utilisées sont vectorielles. Dans le cas spécifique d'une configuration d'objets enfouis impliquant deux semi-espaces infinis, la caractérisation s'avère problématique. Une solution est apportée en appliquant l'approche de marche récurrente en fréquences. Ces développements théoriques sont également confrontés aux données expérimentales mesurées dans le domaine optique. Une nouvelle Microscopie Tomographique par Diffraction (MTD) est mise en œuvre dans le cadre de cette thèse en tenant compte du caractère vectoriel de la lumière. Ce faisant, une résolution d'environ un quart de la longueur d'onde a été obtenue sur des échantillons en résine déposés sur un substrat de silicium. De plus, nous avons aussi appliqué avec succès la méthode DORT à la MTD afin de focaliser et caractériser de manière sélective plusieurs diffuseurs de tailles différentes.

Lors de ce travail de thèse nous avons également développé des méthodes de caractérisation en régime transitoire. Les différentes méthodes d'inversion élaborées dans ce cadre ont été validées sur des données synthétiques et expérimentales dans le domaine des radio-fréquences.

**Mots clés:** Retournement temporel; focalisation sélective; résolution; microscopie optique; multi-fréquences; régime transitoire; algorithmes d'inversion; diffraction; diffraction inverse; optimisation.

# Abstract

The objective of this thesis work is to detect and to characterize three-dimensional targets in a disordered medium, using electromagnetic excitations. This research domain is of great interest in many applications, such as subsoil probing, medical imaging, non-destructive testing and geophysical exploration, etc. In order to extract the target information from the heterogeneities of the medium, we propose to use one of the time reversal technique, namely the DORT method (French acronym for Décomposition de l'Opérateur de Retournement Temporel). This method permits us to generate different waves that focus selectively on each target in high noisy environment. Moreover, this method is also combined with a non-linear inversion algorithm, which permits not only to localize but also to characterize the targets. The reconstruction resolution appears to be better than the ones obtained with the DORT or the inversion procedure alone, especially in the illumination direction. It is also shown that using full-polarized data is indispensable for achieving better performances rather than in scalar configuration. Moreover, in the half-space configuration, it is mandatory to use the frequency-diversity data to get an accurate reconstruction. These theoretical developments are also confronted to experimental data measured in the optical domain. A full-polarization Tomographic Diffractive Microscopy (TDM) is implemented and a resolution about one-fourth of the wavelength is thus obtained. Furthermore, the DORT method is applied in TDM to realize selective focalization and characterization. In the presence of multiple targets, selective characterization of each scatterer is achieved.

This thesis work also deals with the characterization problem using transient data. Different inversion algorithms are validated using synthetic and experimental hyper-frequency data.

**Key words:** Time reversal; selective focalization; resolution; optical microscopy; multiple frequency; transient regime; inversion algorithms; scattering; inverse scattering; optimization.